ALMA MATER STUDIORUM · UNIVERSITÀ DI BOLOGNA

DOTTORATO DI RICERCA IN
FISICA
Ciclo XXVIII

Settore Concorsuale di afferenza: 02/B1
Settore Scientifico Disciplinare: FIS/03

Conducting Polymers as Novel Tools for Biosensing and Tissue Engineering

Presentata da: Marco Marzocchi

Coordinatore Dottorato:
Prof. Gastone Castellani

Relatore:
Prof. Beatrice Fabroni

Esame finale anno 2014/2015

Contents

Introduction

The field of Bioelectronics deals with the integration of the electronic world of logical circuits, sensors, and actuators, with the world of biology. Thanks to the virtually infinite possibilities offered by a combination of such different fields, it possesses a tremendous potential regarding the improvement of the quality of life of millions of people, with a huge range of possible applications encompassing smart prostheses, regenerative medicine, neural implants, bio-integrated sensors, wearable electronics, and many others.

However, a communication between "soft" living biological elements, that mostly transmit signals via ion concentration gradients in a liquid environment, and "hard" inanimated electronic circuits, that interact mostly through electrical currents generated from moving electrons, can not be achieved easily. As it is often the case with emerging technologies, the development of new materials represented a great step forward towards the bridging of these diverse worlds. In the case of Bioelectronics, the development of conductive polymers and their consequent application to biological studies opened up completely new possibilities, giving birth to the field of Organic Bioelectronics.

Among the many conductive polymers that organic chemistry can provide, poly(3,4-ethylenedioxythiophene) poly(styrenesulfonate), or PEDOT:PSS, nowadays is considered a benchmark material for bioelectronics applications [1], owing to its favorable properties, namely chemical stability, low temperature processing, oxide-free surface in aqueous electrolyte, ionic and electronic transport, and mechanical compliance with living tissues [2–4]. However, conjugated polymers are a relatively new class of materials, and a lot of efforts are being made in the research community in order to develop a complete model accounting for their physical, chemical and electrochemical properties.

The aim of the present work is to give a detailed characterization of the physical and electrochemical properties of PEDOT:PSS thin films, and to prove the potentialities of this material both for the sensing of bioanalytes, through the development of innovative electrochemical sensors, and for tissue engineering applications, through the development of redox-active substrates that can control the replication of living cells.

This study has been carried out at the Department of Physics and Astronomy of the University of Bologna, in collaboration with the Department of Industrial Chemistry of the same University, the Department of Bioelectronics of the École des Mines de Saint-Étienne, France, and the Intelligent Polymer Research Institute of the University of Wollongong, Australia.

In the first Chapter, an overview on the research field of Organic Bioelectronics is presented, with a particolar focus on conjugated polymers and the state-of-the-art of their applications.

In the second Chapter, the properties of conjugated polymers, and in particular of the material under investigation, PEDOT:PSS, are summarized, together with a description of the theoretical models that describe their physical properties.

A deeper insight on the working principles of the electrochemical sensors presented in this work, orgainc electrochemical transistors (OECTs), is given in the third Chapter, underlining the parameters that influence the sensitivity and the efficiency of these devices.

The materials and experimental techniques used for the development and the characterization of the devices under study are then described in the fourth Chapter.

In the fifth Chapter, PEDOT:PSS-based electrochemical sensors are presented, together with the characterization of their performance on the detection of several biochemical compounds of biological relevance. Furthermore, an approach to obtain selectivity, *i.e.* the ability of discriminating between different species within the same solution, on the developed OECTs without the need for chemical functionalization is presented. The last part of this Chapter is then devoted to the description of the results obtained from the integration of OECTs on textiles for wearable electronics applications.

Even though many studies reporting the effect of the oxidation state of con-

ducting polymers on cell adhesion, density and replication can be found in the literature, [5–11], a model regarding the modifications induced in the physical and chemical properties by a change in the oxidation state of PEDOT:PSS and other conducting polymers, which could enlighten the cell-substrate interactions involved in the adhesion process, is still missing. For this reason, the sixth Chapter presents a characterization of the physical and electrochemical properties of PEDOT:PSS thin films as a function of their oxidation state, together with the biological effects of these films on cell growth and in their electrical activity.

The electrochemical characterization of PEDOT:PSS thin films was carried out in collaboration with the research group of Prof. E. Scavetta (Department of Industrial Chemistry, University of Bologna), while the biological measurements were performed in collaboration with the research group of Prof. G. Castellani (Department of Physics and Astronomy, University of Bologna). Finally, primary dermal fibroblasts (hDF) from human donors were gently provided by Prof. S. Salvioli (Department of Experimental, Diagnostic and Specialty Medicine, University of Bologna).

Chapter 1

Organic Bioelectronics

1.1 Development of Bioelectronics

The experiments of Luigi Galvani on bioelectricity, performed in the 18th century, are commonly considered as the starting point of Bioelectronics [1]. This scientific branch can be defined as the study of the interactions between electrical charges (or, from a more engineering-oriented point of view, electronic devices) and biological entities, or, to cite the U.S. National Institute of Standards and Technology (NIST), "the discipline resulting from the convergence of biology and electronics" [12]. Over the last century, electronic devices have been revolutionizing biology and medicine. Defibrillators alone have contributed in saving uncountable lives, while electrocardiographs, electroencelographs and blood analyzers are nowadays part of the standard diagnostic equipment in every hospital. The study of biology also has been transformed by electronics, mainly owing to the development of patch-clamp [13]. This technique allows researchers to measure the ionic current through single ion channels in living cells, and its invention led E. Neher and B. Sakmann to win the Nobel Prize in Physiology or Medicine in 1991 [14]. Given the profound effect that electronics has had on medicine and biology in the past, it is easy to imagine that an integration of these fields with modern electronics will result in equally groundbreaking technological advancements. The ongoing miniaturization of semiconductor devices, as well as the development of novel biocompatible semiconducting materials, is leading to

new opportunities in biomedical research and commercial medical applications. Indeed, these technologies allow the creation of devices that can probe biological systems from the molecule to cell to whole organism levels and thereby open up new areas of basic biological research and new market opportunities for commercialization. Moreover, the integration of bio-sensors, drug delivery systems and mechanical actuators make possible the creation of implantable devices that can sense their environment and actively choose an appropriate response. Many of these applications will be described later in this chapter.

Owing to its huge potential, in terms of scientific research, healthcare development and economic opportunities, the research activity in bioelectronics is growing rapidly. Figure 1.1a shows the number of publications per year from 1985 to 2015 in the Web of Science™ Core Collection Database having "Bioelectronics" or "Organic Bioelectronics" as topic. It should be noted that the absolute number of publications on bioelectronic topics (the ones reported plus the ones published without using the term bioelectronics) is undoubtedly larger; however, this simple analysis provides a representative sample of the related activities in this field. At first, it can be seen that bioelectronics gained scientific interest quite recently, with approximately less than ten papers per year published before 1990, while (not surprisingly) the use of organic semiconductor-based devices for this application is even more recent. The number of publications on bioelectronics had a major increase in 2005, and since then it has increased by more than a factor of two in ten years. Starting from the same year, a growing number of papers about organic bioelectronics have been published, following the diffusion of organic semiconductors in other applications, such as organic light-emitting diodes (OLEDs), organic thin film transistors (OTFTs) and organic photovoltaics (OPV) (Figure 1.1b).

1.2 Materials: Conducting Polymers

Materials represent one of the major limitations to the development of new applications in bioelectronics. Electronic devices must be able to transduce signals between the biotic/abiotic interface, *i.e.* they have to convert ionic signals, typical of the biological world, to electronic signals, which are used by our electronic

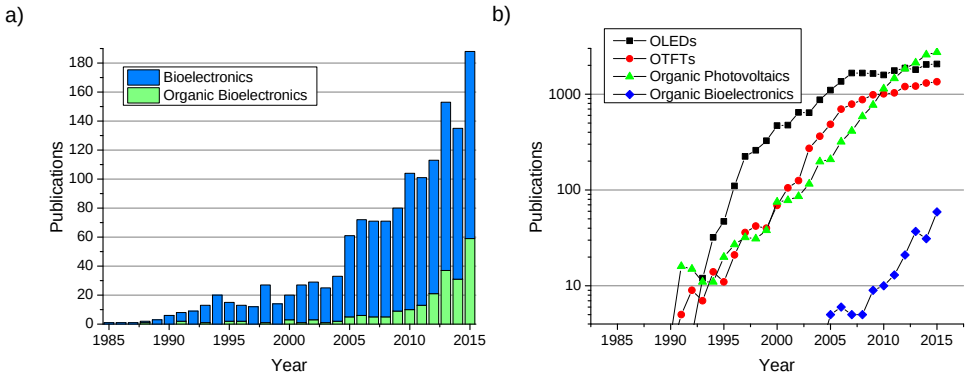

Figure 1.1: Publications per year on (a) Bioelectronics and (b) Organic Electronics from 1985 to 2015. Source: Web of Science™ Core Collection Database.

systems [2, 4]. In traditional inorganic semiconductors and devices, the effectiveness of this conversion is limited by a physical effect known as Debye screening, which is caused by the formation of an electrical double layer on the surface of the sensing material [15]. This electrical screening reduces the distance over which a charge can be sensed in liquid media, and, as a result, limits the use of such sensors in modern biomedical analysis [16]. Moreover, the huge difference in mechanical properties between silicon-based devices and biological tissues is a strong constraint to the development of implantable sensors and prostheses; as an example, the Young's modulus of human brain is about 0.1 MPa, while the modulus of silicon is about 170 GPa, corresponding to a 6-order of magnitude difference [17]. This may lead to local strains at the sample surface during chronic implantations in living tissue that could enhance glial cell inflammation and thus reduce the biocompatibility of the device. In order to go beyond these critical issues, scientific research has been more and more active in developing and testing a wide range of new electronic materials and technologies, such as graphene [18, 19], carbon nanotubes [20, 21], nanoparticles [22, 23], nanostructures [24, 25], or even more "exotic" materials as biomimetic [26], biological [26, 27], and edible [28] materials.

Organic semiconductors have proven to be very promising materials for biosensing and biomedical applications [2, 29]. In particular, a state-of-the-art solution involves the use of conductive polymers. These organic materials were

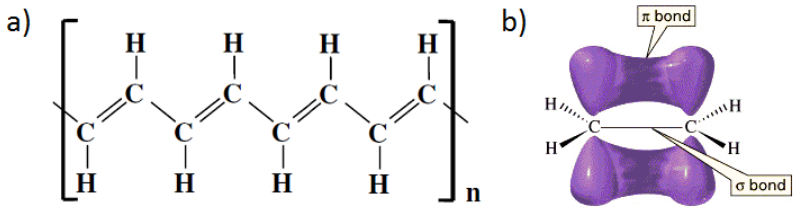

Figure 1.2: (a) Chemical structure of polyacetylene. (b) Schematic view of a π bond.

developed in the 1970s by three collaborating scientists, Alan J. Heeger, Alan G. MacDiarmid, and Hideki Shirakawa [30, 31], who won the Nobel Prize in Chemistry in 2000 for this research [32]. Conductive polymers are conjugated polymers, *i.e.* organic polymers where the carbon atoms are found in an sp^2 hybridization state, with p_z orbitals involved in the formation of π bonds. As a consequence, a succession of alternating single and double bonds between carbon atoms is formed along the polymer backbone [33], as shown in Figure 1.2 for polyacetylene, the simplest conjugated polymer. The electronic delocalization along these π bonds gives rise to electrical conductivity. However, pristine conjugated polymers show conductivities in the range of insulators [34]; the process used to enhance the conductivity of conjugated polymers, making them conductive, is called *doping*, and is essentially a charge transfer reaction resulting in the partial oxidation or reduction of the polymer. The processes related to the electrical conductivity and doping of conjugated polymers are presented more in detail in Chapter 2.

Organic electronics deals with the application of conjugated small molecules and polymers in electronic and optoelectronic devices [35], and its interfacing with biology has been named "organic bioelectronics" [36]. As shown in Figure 1.1, this research field has been rapidly growing during last ten years. The increasing interest in the development of bioelectronic devices based on organic materials instead of "traditional" semiconductors results from many characteristics that make these materials suitable for interfacing biological elements. A comparison between *p*-doped inorganic (Si:B) and organic (PEDOT:PSS) semiconductors is shown in Figure 1.3. Silicon atoms form a lattice through a network of covalent bonds, where each atom shares valence electrons with four neighbors. In contrast, in the organic material covalent bonds are only present within macro-molecular

blocks held together by weak van der Waals interactions and, in the case of doped materials, electrostatic interactions. The prevalence of van der Waals interactions in the organic material defines its "soft" nature and the related key differences with the "hard" silicon, which can be summarized as follows [2, 4, 36]:

- Organic materials offer facile chemical modification. Organic chemistry can be used to modify the structure of the molecular blocks with near-infinite possibilities, since by altering the π-conjugated backbone or the side groups it is possible to change relevant (opto-)electronic, mechanical or biological properties. In a similar fashion, structures that range from single crystals to disordered composites and hydrogels can be produced from the same fundamental conjugated molecular blocks.

- Organic materials are soft, offering good mechanical compatibility with both biological tissues and flexible mechanical substrates.

- In addition to electrons and holes, conjugated polymers can support efficient ion transport at room temperature. Owing to van der Waals interactions, the molecular building blocks of these materials are usually enough largely spaced to allow ions to move efficiently in the film. Moreover, hydrophilic organic films can absorb water and swell, which further enhances ion transport.

- Many organic semiconductors are fully biocompatible, and they can also be decorated with bio-molecular side-groups to selectively promote or inhibit cell viability.

- Van der Waals bonding leads to well-defined interfaces with electrolytes, without dangling bonds or oxides. Organic semiconductors can therefore take advantage of a direct contact with the biological environment.

- Organic materials are often transparent, allowing optical transmission imaging and the use of various microscopy-based techniques when analyzing biological specimens interacting with the device.

- Organic materials can be processed at low temperature, thanks to the weak bonds that hold the molecular blocks together, which can be easily broken

by mild heating (mostly in small molecules) or a solvent (mostly in polymers). As a consequence, an organic film or a crystal can be deposited from vapor or solution on a wide variety of substrates using several low cost techniques.

- Finally the structure of the molecules, and by extension of the film, is strongly coupled with charge distribution. In contrast to silicon, where the presence of electronic charge does not modify the lattice structure appreciably, the removal of an electron from a thiophene chain causes a transition from an aromatic to a quinoid structure (see Figure 1.3). This effect is relevant in biological an electrochemical applications where doping is performed in an electrolyte solution, since the corresponding uptake or release of ions can cause large dimensional changes in the organic film. As a result, electrical doping can be exploited not only to affect the electrical properties of the film, but also to influence its optical and mechanical properties.

The coupling of an organic electronic device with the biological environment can work in two directions: as a sensor or as an actuator (Figure 1.4). When working as a sensor, some characteristic of the device is influenced by a biological reaction or process, and this modification is recorded as a signal; for example, an enzymatic reaction turns off the conductivity of a transistor. Conversely, when working as an actuator, an organic electronic device can operate to induce a biochemical reaction or a biological process; for example, the application of a bias on a conducting polymer electrode stimulates a neuron to generate an action potential [4]. In the production of materials that have to be integrated with biological systems, it is really important to validate their biocompatibility. The suitability of organic materials differs vastly, depending on their synthesis route as well as on the overall nature of the conjugated polymer system, for example its chemical composition, surface charges, or acidity [36]. Depending on the chosen material and its route of synthesis, the polymer film may contain residuals that could be highly toxic for cells such as monomers, detergents, solvents or excessive dopeions. Another parameter that affects the interaction between a cell and the surface is surface topography, which can range from a few nanometers to the micrometer level [37]. Finally, the absorption and organization of proteins on the surface is

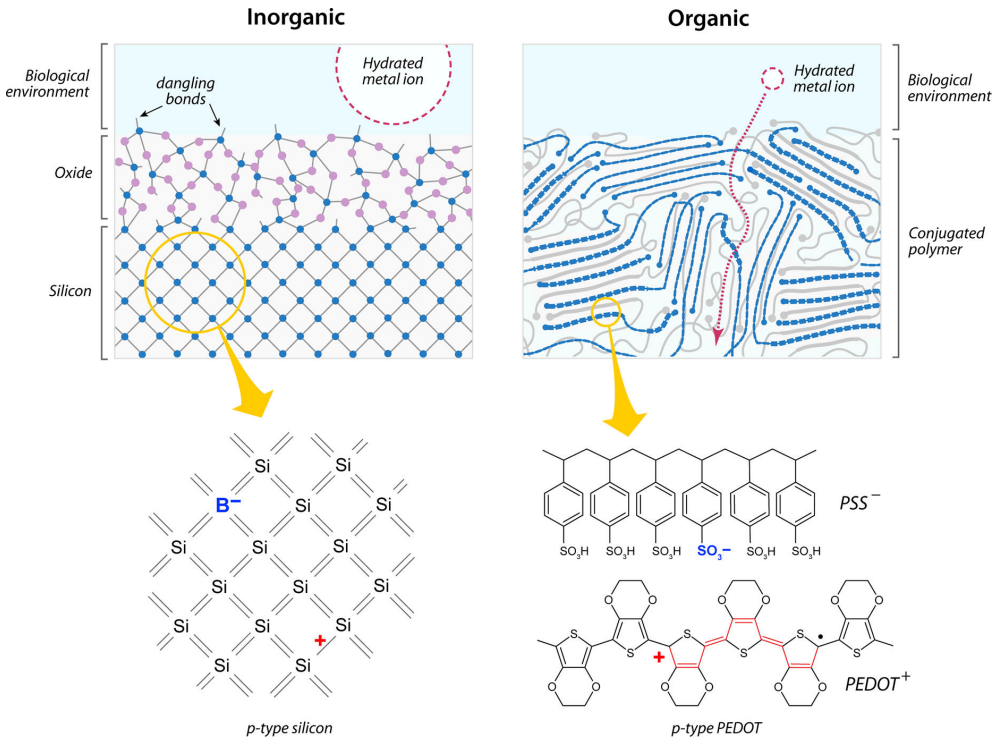

Figure 1.3: Schematics of an inorganic semiconductor, silicon, and an organic semiconductor, PEDOT:PSS, at the interface with an electrolyte. The hydrated ion is used as a reference to define the relative scale. The insets show the effect of *p*-type dopants on the structure of the semiconductors [2].

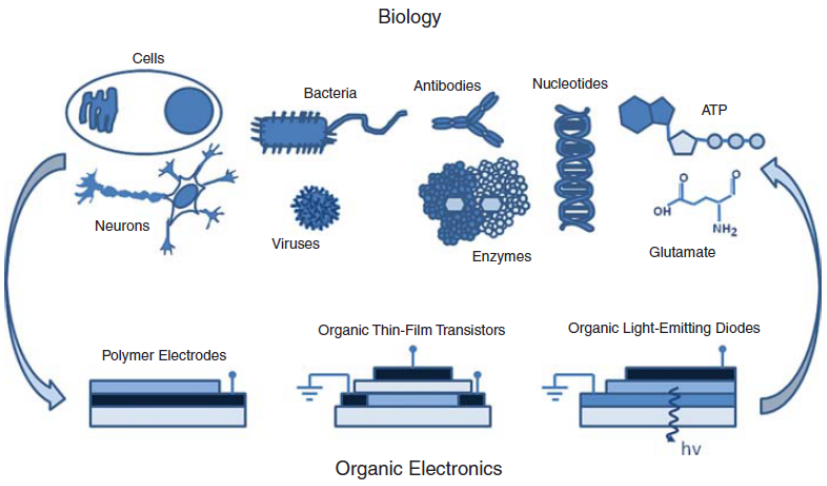

Figure 1.4: Picture representing the interactions between electronic devices and biological elements in organic bioelectronics [4].

also important, as this defines to a great extent cell adhesion and other interfacing properties [38]. The biocompatibility of several different doped and undoped conjugated polymers has been investigated in various studies, both *in vitro* and *in vivo* [39–41]. The most commonly used conjugated polymers in chemical and biological sensors are polyaniline, polypyrrole, polycarbazole, polythiophene, and their derivatives, with applications covering a broad spectrum of chemical and biological sensing [36]. Some examples include humidity and pH sensors, analyte sensing (e.g. glucose, urea, triglycerides, etc.) and more [42], as described in next Section.

1.3 Applications

In this section, some of the most recently-developed electronic devices for biological research are presented.

1.3.1 Biosensors

According to the International Union of Pure and Applied Chemistry (IUPAC) a biosensor is "a device that uses specific biochemical reactions mediated by isolated enzymes, immunosystems, tissues, organelles or whole cells to detect chemical compounds, usually by electrical, thermal or optical signals". In other words, a biosensor is a device consisting of a biological sensing component connected to a transducer that converts the recognizable response into a measurable signal [43]. The history of biosensors began with the fabrication of enzyme electrodes by Leland C. Clark in the 1960s [44]. Since then, researchers coming from numerous scientific disciplines began working on the development of more sophisticated and reliable biosensors. Particularly, the success of glucometers, used to monitor the glucose blood concentration in diabetics, as well as the commercialization of lateral flow assays such as pregnancy tests, have led clinical diagnostics to be the most significant area for the application of biosensors particularly as point-of-care systems [29]. In this thesis, some of the main classes of organic semiconductor-based biosensors will be described: organic field-effect transistors (OFETs), OFET-based sensors, and organic electrochemical transistors (OECTs)

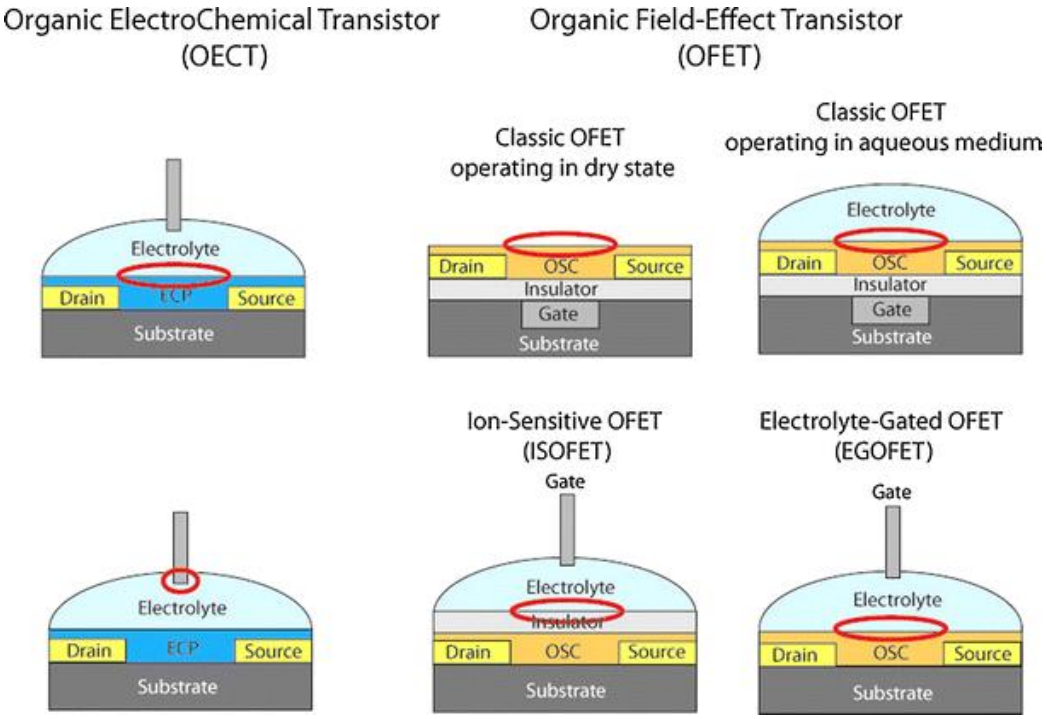

Figure 1.5: OECT and OFET architecture. The red circles indicate the different interfaces involved in the detection of biomolecules [46].

(Figure 1.5). In general, these sensors use π-conjugated organic semiconductors as electronic materials and can be used for biological recognition through proper functionalization or integration of bio-systems such as DNA strains, antibodies, enzymes or capturing proteins. The advantages over other sensing technologies is the capability of delivering a response that is label-free (*i.e.* not requiring a specific marking of the target analyte) using a simple electronic read-out set-up that can be easily miniaturized by also employing printed circuit technologies [29]. Moreover, the use of organic semiconductors as sensing element allows to realize completely flexible devices by using dielectric, conducting, insulating and semiconducting inks on plastic substrates, as shown in Figure 1.6, with no need for ultraclean high-tech fabrication facilities [45].

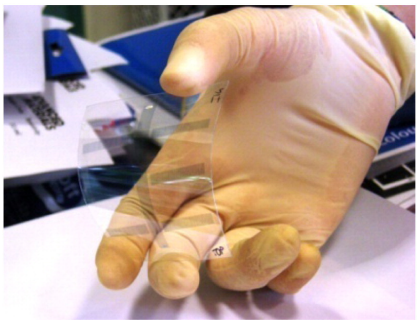

Figure 1.6: Picture of an inkjet-printed transparent and flexible OFET [45].

Organic field-effect transistors (OFETs)

First introduced in the 1980s [47], OFETs have now reached performance levels comparable to that of their polycrystalline inorganic homologues [29], and a number of *p*-type and *n*-type organic semiconducting materials with different chemical and physical properties exhibiting field-effect mobilities higher than 1 $cm^2\ V\ s^{-1}$ can be found. Typical materials include polymers such as poly(3-hexylthiophene) (P3HT) and alkyl-substituted triphenylamine polymers (PTAA), but also oligomers such as pentacene and its soluble derivatives, and α-sexithiophene (α6T) [48].

The structure of an OFET is based on three electrodes, usually metallic, named *source* (S), *drain* (D), and *gate* (G), an organic semiconductor (OSC) film and a dielectric layer (Figure 1.5). The source (grounded) and drain electrodes are connected to the OSC and are used to induce a current I_d by applying a potential V_d. The OSC is also interfaced to the gate electrode through the dielectric layer, that ideally blocks the current I_g between the source and gate electrodes. As a consequence, the application of a gate voltage V_g between these electrodes induces the polarization of the insulator, eventually generating a channel of charges at the interface with the OSC and increasing I_d (*accumulation mode*). More specifically, for *p*-type semiconductors (as the majority of OSCs) a negative voltage is used, so as to generate a channel of positive charges whose geometrical length (L) is the distance between the source and the drain contacts, while its geometrical width (W) is the width of the metal pads. If a positive gate voltage is applied instead, the positive charges inside the OSC are pushed towards the bulk of the semicon-

ductor, depleting the channel of the transistor and decreasing I_d (*depletion mode*). In these devices, a highly resistive OSC is required to have low I_d in the *off* state, *i.e.* when $V_g = 0$, but conversely the current in the *on* state, *i.e.* for $V_g < 0$, must be as high as possible [29]. The switching between these two transport regimes is achieved through the capacitive accumulation of positive charges at the insulator/OSC interface induced by the gate voltage, which is proportional to the gate voltage applied and the capacitance C_i of the insulating layer. So, in order to have a high I_d in the *on* state, a high C_i is required. This can be achieved by using materials with high dielectric constant, ε_r, and low thickness. Moreover, by increasing the capacitance of the dielectric layer it is possible to reduce the operating voltage and the power consumption of the device, wich is one of the major limitations on the performance of these devices [49]. If the electric field generated by the gate voltage is much larger than the field generated by V_d (*gradual channel approximation*), the charges are confined and accumulated only at the insulator/OSC interface, meaning that the charge transport is two-dimensional and independent of the OSC thickness [50]. Conversely, the transport occurring in the *off* state is three-dimensional as it involves the charges present in the whole OSC film [29]. These charges are due to the presence of impurities or structural defects and their quantity must be orders of magnitude lower than the charges generated by V_g.

In OFETs used as chemical sensors, the OSC is directly exposed to the gas or solution to be analyzed, acting both as electronic transport material and sensing element. Basically, the exposure to the analyte modifies the transport properties of the OSC (carrier mobility, *on/off* ratio, threshold voltage), and this changes can be measured and correlated to the analyte concentration. OFETs possess many favorable properties as chemical and biological sensors: label-free detection, repeatability, and high sensitivity. As for the other sensors presented in this chapter, selectivity represents the main limitation to the use of OFETs for sensing applications, although this drawback can be overcome upon proper functionalization [29]. The applications reported in literature for these devices include the detection of nitro-based explosives [51], ammonia [52], nitric oxides [53], peroxides [54], as well as a wide range of biomolecules.

Ion-sensitive OFETs (ISOFETs)

In an ISOFET, the gate electrode and the dielectric layer are not in direct contact as in an OFET, but they are instead separated by an electrolyte solution containing the analyte (Figure 1.5) [55]. In order to control the potentials, a reference electrode is used as gate electrode. Unlike in conventional OFETs, the I_d current is modulated by field-effect doping due to the potential of the electrolyte-insulator interface, which is caused by the presence of ions from the electrolyte solution. These devices can be used to detect ionic species through the functionalization of the dielectric surface or of the gate electrode by means of a selective membrane coating, that only allows the binding of a specific species to the surface. By an appropriate tailoring of the selective membrane, it is possible to detect a wide range of molecules and biological elements; however, the main draw-back of ISOFET-like sensors is the need for a reference electrode, that makes them less prone to be used in array-type sensing systems [29]. An interesting ISFET-like sensing approach that does not need a reference electrode is the so called Charge Modulated (CM) OFET. In this OFET, a large floating-gate is coupled to a control capacitor which allows the biasing of the device, while the sensing area and the channel region are physically separated by an insulator layer. Using this configuration, DNA label-free detection has been reported in the sub nM range [56].

Electrolyte-gated OFETs (EGOFETs)

The structure of an EGOFET is basically the same of an OFET where the dielectric layer has been replaced by an ion-conducting electrolyte solution or polymer electrolyte (Figure 1.5) that is directly responsible for the gating effect of the transistor [46]. The removal of the dielectric layer allows the direct contact between the OSC and the electrolyte, drastically reducing the operating voltage required to switch between the *on* and *off* state [57]. In these devices the polarization of the insulating layer is replaced by the formation of a Debye-Helmholtz double layer at the interface between the electrolyte solution and the OSC layer as well as between the electrolyte and the gate contact [58]. As an example, when a negative gate voltage is applied, negative charges are generated on the surface of the metal gate electrode which repel the anions in the electrolyte that, con-

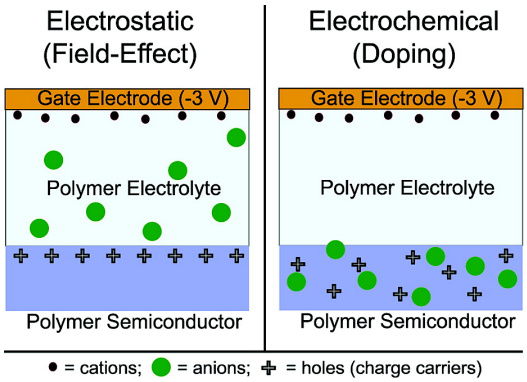

Figure 1.7: Schematic cross-sections of a portion of an EGOFET channel showing the difference in the extent of ion penetration between (a) electrostatic charging and (b) electrochemical doping as operating mechanisms [62].

sequently, are accumulated at the electrolyte/semiconductor interface. Here, the formation of a layer of positive charges is induced electrostatically in the organic semiconductor, increasing its conductivity (assuming a *p*-type conductivity) and generating a second electrical double layer (EDL). Since EDLs are usually very thin (in the order of a few nanometers), their capacitance can be very high (ca. 10 $\mu F\,cm^{-2}$ [59]), lowering the gate and drain voltages required to operate the transistor in the sub-volt regime. One of the main limitations of EGOFETs is their low switching speed between *on* and *off* states, which is due to the low mobility of ions in the electrolyte [60]. In order to improve this parameter, the replacement of a liquid electrolyte with an ion gel gate dielectric has been reported, resulting in significantly shorter polarization times (about 1 ms) [61].

It must be noted that organic semiconductors cannot be considered completely impermeable to the ions from the electrolyte [60]. According to the permeability to these ions, it is possible to define two different operational modes of organic thin film transistors: field-effect charging (as occurs in conventional metal-oxide-semiconductor field-effect transistors, or in OFETs) and electrochemical doping (Figure 1.7) [62]. These two scenarios represent limiting cases for the degree of ion migration into the polymer semiconductor, and a combination of these mechanisms has also been used to explain OFET operation with an electrolyte gate [63, 64]. However, the most accepted explanation of the EGOFET behavior involves a purely electrostatic charging of the organic semiconductor [62, 65]. A

different charging mechanism can affect the performance of the device, as in field-effect charging the intermolecular chain packing within the semiconductor is not disrupted, while this is not the case for electrochemical doping. It is generally accepted that crystalline packing can result in higher carrier mobility. Thus, electrostatic charging of semicrystalline and polymeric semiconductors may result in higher mobilities than the ones that can be obtained with electrochemically doped polymer semiconductors [62].

EGOFET-based sensors have been used for many applications, such as the detection of DNA [66], pH [67], and dopamine [68], as well as the recording of the electrical activity of neuronal networks [69].

Organic electrochemical transistors (OECTs)

As shown in Figures 1.5 and 1.7, organic electrochemical transistors are developed using the same geometry as EGOFETs, but employing a permeable conducting polymer as organic semiconductor, such as polypyrrole (PPy), polyaniline (PANI), polythiophene derivatives, and polycarbazole. Because of the permeability of these polymers, in an OECT the entire volume of the sensing element is in contact with the electrolyte solution (while in EGOFETs only the semiconductor/electrolyte interface is involved). As a consequence, the I_d current modulation upon the application of a gate voltage is obtained through a reversible electrochemical doping/dedoping process that involves a change of conductivity in the whole bulk of the semiconducting layer [70]. This difference compared to field-effect transistors enables the OECT to exhibit high amplification properties in sub-volt operation regimes, preventing water electrolysis and extending the operating times required for *in vitro* and *in vivo* applications [71].

There are two regimes of operation for OECTs: Faradaic and non-Faradaic (capacitive) [72].

Faradaic regime In the Faradaic regime, the application of a gate voltage determines a steady-state current at the gate electrode due to irreversible reduction/oxidation (redox) reactions between the electrode and the electrolyte. This current lowerss the potential drop at the gate interface, increasing the effective gate voltage operating on the channel. As a consequence this

regime has the highest sensitivity, but the fact that the Faradaic mode of operation relies on the irreversible oxidation/reduction of the electrolyte also means that the device characteristics will decay with time and be particularly sensitive to the nature of the electrolyte (feature that can be exploited for the detection of different cations [73]).

Non-Faradaic regime The non-Faradaic mode of operation is an alternative to the Faradaic mode: in this regime, the application of V_g determines exclusively a capacitive current at the gate electrode [60]. In non-Faradaic mode, the electrochemical potential of the gate electrode remains within the stability window of the electrolyte, and polymer doping is coupled to the reversible charging of an ionic double layer at the gate electrode. Therefore, a significant potential drop arises at the gate/electrolyte interface, reducing the effective gate voltage acting on the channel.

In both regimes, the modulation of the conductivity depends on the quantity of active material and on the capacitances at the channel/electrolyte and gate/electrolyte interfaces [72]. As a consequence, the geometrical features of the transistor, and more specifically the ratio between the surfaces of the gate electrode and the active area, A_g/A_{ch}, have a strong impact on the device performance and have been investigated in many works [72,74,75]. Briefly speaking, a trade-off between sensitivity (small gate area) and time response (small channel area) has been observed, requiring a specific tailoring of the device according to its final purpose. More recently, also the channel thickness has proven to affect the sensitivity of these devices [76,77], confirming the (still controversial) hypothesis that the whole volume of the organic semiconductor is involved in the interaction with the electrolyte, as opposite to electrolyte-gated field-effect transistors. More details on the working principles of this class of devices are reported in Chapter 3.

The most important feature of OECTs as biosensors is signal amplification [70], which leads to high sensitivity due to the direct effect of ions in the modulation of the conductivity of the organic semiconductor. Ion-to-electron transduction and high amplification are common necessities for unraveling biological information, increasing the signal-to-noise ratio and lowering the detection limit. One parameter used to quantify amplification is transconductance, defined

as $g_m = \Delta I_d / \Delta V_g$, and OECTs with transconductance up to the mS range, comparable or even superior to solid-state inorganic transistors, have been obtained, outperforming other organic transistors [71]. This result is even more impressive considering that these devices are realized at room temperature from soultion processed materials, and thanks to the soft nature of conducting polymers, they can undergo harsh manipulation without a significant decrease in their electrical performances, as shown in Figure 1.8. Finally, by carefully selecting and varying their geometrical characteristics, it is possible to engineer OECTs with peak transconductance values at zero gate voltage [78]. This result can be exploited in applications that require very low voltages over an extended period of biasing. Moreover, the removal of gate biasing facilitates the integration with circuits and recording systems, which is particularly appealing for lab on a chip applications.

Thanks to their low-voltage requirements and ease of fabrication, functionalization and integration in biological environment, OECTs have been used for sensing a broad range of analytes, such as ions [73,79], H_2O_2 [74], penicillin [80], glucose [81–83], ascorbic acid [76], adrenaline [84], eumelanin [85], dopamine [86,87], glutamate [88], acetylcholine [88], lactate [89], and DNA [90]. It must be noted that a functionalization step, usually requiring the integration of a specific enzyme, is necessary in order to achieve a significant selectivity to the specific molecule of interest (enzymatic sensing). Moreover, OECTs have been successfully coupled to many kinds of live cells. In the case of epithelial cells, OECTs can be used for monitoring barrier tissue integrity from the measurement of the ion flux flowing through the tight junctions formed by these cells [91], as shown in Figure 1.9, with applications for toxicology and diagnostics. Indeed, this system has been used as a model to study the disruption of tight junctions upon the exposure to chemicals [92] and bacteria [93], and it has been recently employed for the study of death dynamics also in cancer cells that do not form tight junctions [94]. On the other hand, OECTs can be integrated with electrogenic cells, such as cardiomyocytes and neurons, for cellular stimulation and for the recording of electrical signals, raising the opportunity of expanding the potential applications of these devices from *in vitro* toxicology and diagnostics to *in vivo* therapeutics [95–97].

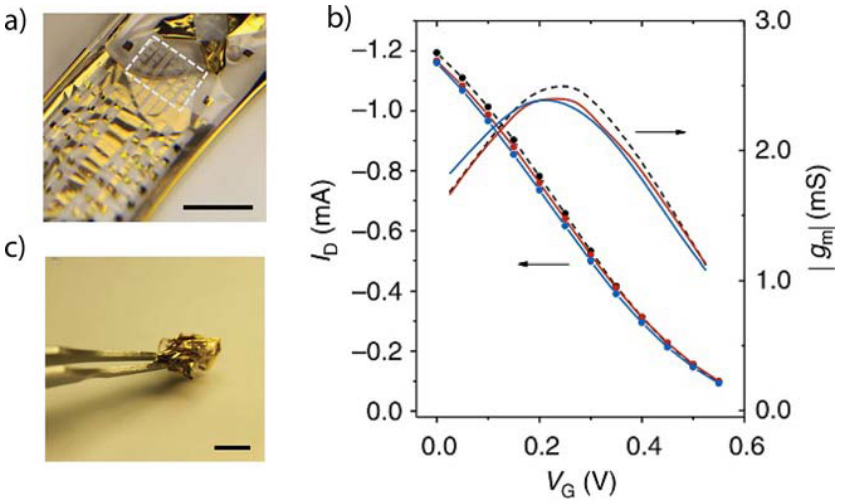

Figure 1.8: High amplification OECTs. (a) An array of OECTs on a thin flexible substrate (scale bar 1 cm). (b) (Left axis) Transfer characteristics of the device before (red) and after (blue) crumpling. (Right axis) Transconductance and time response for devices before (red) and after (blue) crumpling. (c) Crumpling of the array [70].

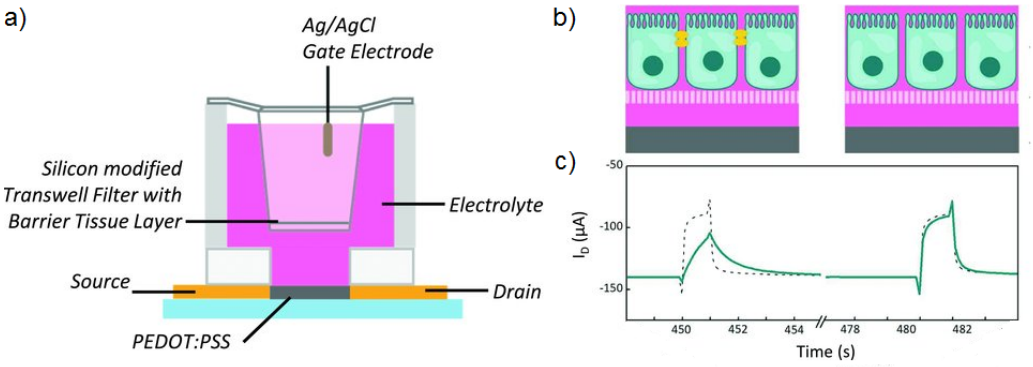

Figure 1.9: OECT-based device for the measurement of tissue barrier integrity. (a) Architecture of the device. (b) Cartoon of epithelial cells with (left) and without (right) tight junctions, sitting on a porous cell culture membrane above a PEDOT:PSS transistor channel. (c) OECT I_d transient response with cells before (left) and after (right) barrier disruption upon the addition of 100 mM H_2O_2 [91].

1.3.2 Neural interfaces and implants

Owing to their combination of biocompatibility and electrical activity, conducting polymers and devices built from conducting polymers were soon coupled to electrogenic cells (cardiomyocytes and neurons) after their development [3]. Neuronal and cardiac cell cultures were indeed among the first experiments to be performed with conducting polymers [5, 98]. The electrical stimulation and recording of nerve tissue and neural activity have provided valuable information about the physiological and pathological functions of the body and the brain. Typically, these recordings are performed with metal electrodes, but the difference in elasticity between neural tissue and metals or silicon may lead to local strains at the sample surface during chronic implantations that could enhance glial cell inflammation, reducing the biocompatibility of the device [17]. Thus, a primary challenge for neural interfaces is to form a good contact with the brain. This can be achieved by using flexible electrodes that conform to the shape of the brain surface [99]. Other critical requirements are to obtain a stable signal over time (*i.e.* the stability and biocompatibility of the semiconducting material), and a sufficiently high amplification to detect the low magnitude signals emitted by neuronal cells [70].

Growth and electrical stimulation of neural tissue

An advantage of conducting polymers compared to other materials for the interfacing of neuronal tissue is that they can be used to electrically stimulate neuronal cells while supporting their morphology. Electrical stimulation has been proven to influence neuronal growth and differentiation, as well as accelerating axonal growth [100, 101]. Moreover, the ease of functionalization of these materials through the doping process can also play an important role in developing new applications. As an example, by doping both PPy and PEDOT using neuronal growth factor (NGF) the attachment and neurite development of PC-12 cells, used as a marker, can be significantly improved [102]. A crucial problem in the focus of neuroscience research is to find a way to promote growth of neuronal cells while suppressing growth of glial cells on the same surface, since the formation of glial cells can affect the efficacy of intracerebrally delivered therapeutic approaches for

neurogenerative disorders (glial sheathing) [103]. Using PPy, it was shown that it was possible to support a higher number of either glial cells or neuroblastoma cells by a change in the doping agent used [104]. On the other hand, the doping agent can also promote neuronal growth and differentiation of precursor cells into a neuronal phenotype [105].

Another advantage of using conducting polymers as electrodes for tissue stimulation is that they can be synthesized *in situ*, in direct contact with live cells, preventing potentially hazardous surgeries for electrode implantation [106]. If the conducting polymer is electrodeposited in a dish containing a living neuronal cell culture, it wraps closely around the cells and their extensions, sometimes engulfing the cell body, eventually producing a cell-templated coating. Neuron-like cells grown on these cell-templated structures seem to re-populate the cell-shaped holes, but do not settle into the exact same position as the original cells used for templating [106]. In a similar fashion, *in vivo* electropolymerization has been used to grow nano- and microscale conductive polymer networks on metal electrodes implanted in mouse brain slices [107]. This process induced a large increase in the effective surface area of the electrode as compared to that of the bare metal, as evidenced by decreased impedance and increased charge capacity.

Recording of neural activity

For the brain, there are three main electrophysiology recording techniques: electroencephalography (EEG) which utilizes electrodes in contact with the skin, electrocorticography (ECoG) which utilizes electrodes in contact with the surface of the brain, and stereoelectroencephalography (SEEG) which utilizes probes that penetrate deep in the brain [108]. Depending on the nature of the signal of interest, the size of the neural population to be interrogated, or the invasiveness of the measurement, EEG, ECoG, or SEEG may be selected [70]. State-of-the-art recordings are currently performed with microfabricated arrays of metal electrodes, which capture the local field potentials (LFPs) generated by the spatio-temporal summation of current sources and sinks (caused by the flux of ions through ion channels localized in the cell membrane) in a given brain volume [109]. Although ECoG probes are easier to use than SEEG probes, recordings performed on the brain

surface pick up a highly integrated, global signal, which corresponds to the summation of different signals generated at different depths. Hence, ECoG probes are not able to accurately detect activities generated by smaller cell assemblies, except those generated right below an electrode [95].

Neurons and brain networks generate small electric potentials, which are difficult to extract from noise when recorded with classical metal electrodes. The use of transistors rather than simple electrodes provides the potential of increased SNR, however, biocompatibility of silicon-based devices is a critical issue for *in vivo* applications. An alternative transistor architecture, the OECT (Section 1.3.1), is gaining more and more attention to overcome the limits of inorganic field-effect transistors. As OECTs capture ion fluxes [110], they constitute the optimal solution to measure electrophysiological signals. Moreover, since OECTs use conducting polymers as sensing element, they offer cytocompatibility and straightforward integration with flexible substrates [111], that can be used for realizing conformable arrays of sensors [99, 112]. Despite these properties, the diffusion of OECTs for neuronal recording in the past had been slowed down by their low electrical performances compared to competing technologies such as inorganic FETs and graphene-based devices. In recent years, a PEDOT-based high-transconductance OECT for ECoG recording has been presented [71] and succesfully tested for *in vivo* applications [95], exceeding the performances of similar transistors. OECTs were also used to monitor cardiac rhythm, eye movement, and brain activity in human volunteers [96, 97]. These results demonstrated that OECTs can be used for recording small electrical signals with amplitude and frequency comparable to neuronal action potentials, with better results than traditional metallic penetrating electrodes without the need for invasive surgery.

1.3.3 Active surfaces for tissue engineering

In previous paragraphs, applications where organic semiconductors are used to sense or stimulate biological activity through an exchange of ions with the surrounding environment have been presented. At a higher level, it is possible to consider the changes induced in the organic film itself as result of this process, and take advantage of these modifications for a different kind of application. Since

the material must be permeable to the electrolyte to have an efficient exchange rate, conducting polymers represent state-of-the-art materials for this purpose. As shown in Figure 1.3, the exchange of ions (doping) in conjugated polymers is associated with a structural rearrangement along the π-conjugated backbone [2]. Moreover, the exchange of ions and the generation of an excess charge induces the uptake of water. This effect can influence a range of properties such as surface energy, roughness, thickness and elastic modulus [6, 113, 114].

The first demonstration of how redox-induced modifications in surface properties can be exploited to control cell behavior was reported by Wong *et al.* by measuring the attachment and spreading of bovine aortic endothelial cells on pristine and reduced polypyrrole [5]. Since then, many studies have shown that a redox switching of the surface of conducting polymers can induce cell stimulation, attachment, differentiation, and morphology changes [6–11, 115]. The origin of these effects is still not clear to date, but experimental evidence has shown that an electrically-induced change in the conformation of fibronectin, an important cell adhesion protein, is involved [116–118]. Nevertheless, different kinds of active surfaces for guiding cell behavior upon an electronic trigger have been developed using conducting polymers in recent years [3], as shown in Figure 1.10.

Redox Switches and Gradients

Electrochemical reduction or oxidization of a conducting polymer induces a modification in charge distribution along the polymer backbone, which is counterbalaced by a counterion usually referred to as "dopant". Depending on the charge available on the backbone, doping ions can be tightly associated or dissociated with the backbone [119]. Thus, the chemical properties of the doping agents, which already have a large effect on the properties of the conducting polymer in its native form [114], are even more important with respect to the surface properties during reversible redox switching [3].

To create wettability switches based on conducting polymers, doping agents representing monomeric surfactants such as dodecylbenzenesulfonate (DBS), perfluorooctanesulfonate (PFOS) and *para*-toluenesulfonate (*p*-TOS) ions are the most widely used, while conjugated polymers such as polyaniline (PANI), poly-

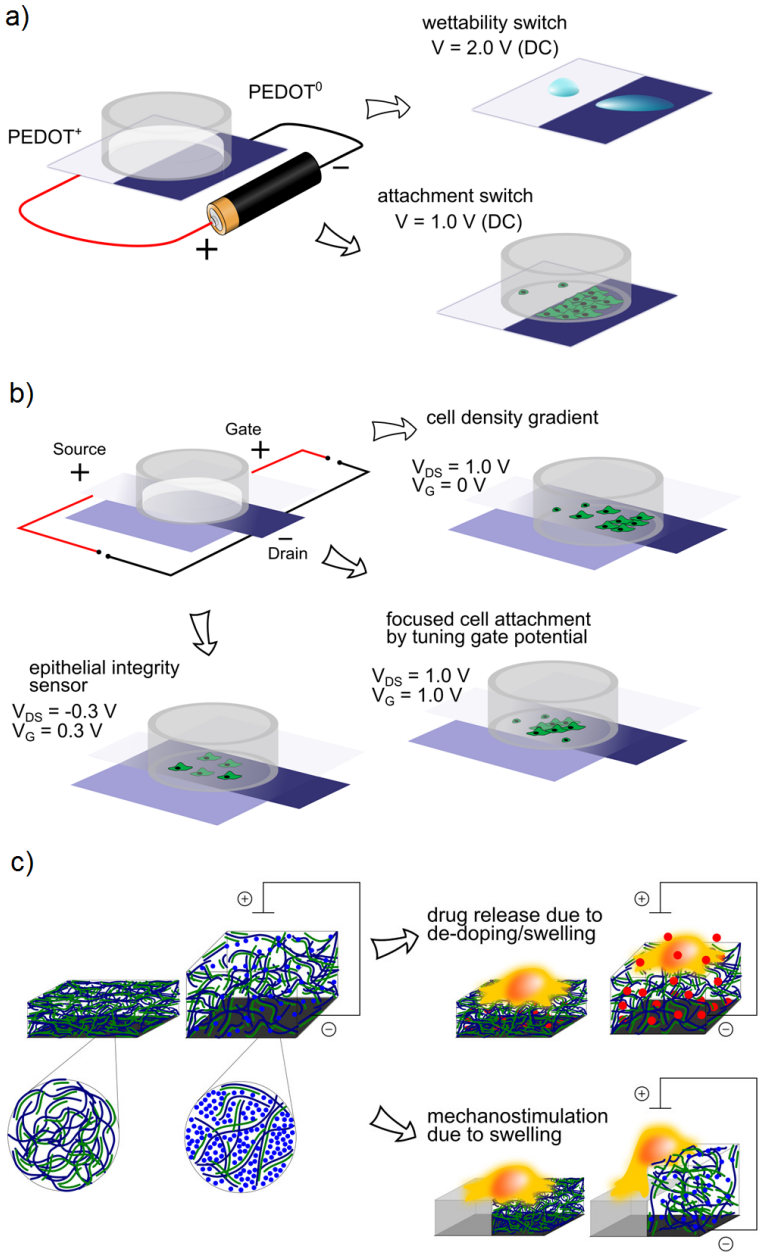

Figure 1.10: Organic bioelectronics used for electrochemical control of surface properties. (a) A two-electrode surface switch is used to control wettability and cell attachment. (b) An OECT is used to create and influence cell density gradients by tuning the gate potential. The same OECT can also be applied as a sensor for epithelial integrity. (c) Swelling behavior in conducting polymers can be used for electronically triggered drug release and mechanostimulation of cells. Adapted from [3].

pyrrole (PPy), poly(3- hexylthiophene) (P3HT), and poly(3,4- ethylenedioxythiophene) (PEDOT) are usually employed as backbones [3, 7, 113, 120]. Although the micro- and nanostructure of the surface has an effect on wettability [121], conjugated polymers are usually not enough nanostructured for inducing a switch between hydrophilic and hydrophobic state solely through a change in their roughness. In this case, the chemical properties of the dopant give a critical contribution in determining the wettability of a surface [114]. Conjugated polymers are generally synthesized through oxidative polymerization, generating an excess of positive charges along their backbone which is balanced by negative counterions. Thus, when the polymer film is in an oxidized state (*i.e.* the backbone is positively charged), the hydrophilic (negatively charged) groups of the counterion are strongly bound with the polymer, while their hydrophobic (not charged) tails are oriented towards the surface, creating a hydrophobic film with large surface energy. In a reduced state (*i.e.* electrically neutral backbone), the electrostatic polymer-counterion bond does not hold anymore. Consequently, the dopant dissociates from the polymer backbone and its hydrophilic groups are favored to interact with water dipoles, creating a more hydrophilic surface (Figure 1.10a, wettability switch) [113].

It is possible to electrically control the surface energy of a conducting polymer film by using a simple two-electrode system, presenting the fully oxidized and fully reduced state of the polymer on each single electrode. Based on the same mechanism, cell attachment switches have been developed that are able to selectively improve or reduce cell attachment depending on the applied potential (Figure 1.10a, attachment switch) [7, 8]. If these electrodes are connected by a continuous stripe of conducting polymer, a linear redox gradient can be estabilished [9]. By adding a gate electrode, this stripe can work as the conducting channel of an OECT (see Section 1.3.1), where the gate voltage is used to modulate the steepness of the electrochemical gradient. Using this device, cell density gradients can be produced, and even tuned, along the channel of the OECT (Figure 1.10b, cell density gradient and focused cell attachment) [122]. Finally, it is also possible to measure current transients by pulsing the gate potential in the presence of a cellular layer grown directly on the channel, so as to measure epithelial integrity [123].

Drug Delivery Systems

Pharmaceutical compounds range from small ions to large and complex proteins and molecules. To achieve a proper response to the treatment, the pharmaceuticals must be delivered inside the body at an optimum rate, and in some cases, at a defined site. For any administered drug system, a lower limit below which the drug has ceased to produce any therapeutic effect, and an upper limit above which the drug exerts various forms of toxicity in the organism, can be identified [124]. Ideally, for a medicinal agent to remain therapeutically effective without toxic effects, its serum concentration should stay within these limts. Drug delivery systems have been developed just to allow slow and gradual intraserum release, and nowadays they represent another application of conducting polymers [36].

The first reported controlled release system based on conducting polymers was reported by Zinger and Miller in 1984 when glutamate anions were released upon the reduction of PPy [125]. This electrically controlled drug release is based on the hypothesis that compounds, entrapped in the polymer during synthesis or fabrication, are released from the polymer matrix due to de-doping and swelling caused by repeated or continuous electrochemical switching (Figure 1.10c, drug release due to de-doping/swelling) [126, 127]. It has been demonstrated that drug release after electrochemical switching of the polymer is not limited to the release of negative doping ions when swelling processes are taken into account [128]. To increase the drug release rate in conjugated polymer membranes, different approaches have been explored, that relate primarily to enhancing the drug diffusion rate inside the polymer electrode in order to promote rapid escape of the drug. This can be achieved by increasing the surface/volume ratio, as an example by producing a sponge-like porous polymer electrode, in which the receiving fluid can intermix with the polymer material [129], or by realizing polymeric nanowires, where the drug-loading capacity depends on the volume of the vacancies and not on the doping level [130]. An alternative route to increase the release rate, as well as to enable the release of more voluminous ionic drug molecules, is to combine the drug-emitting polymer with a hydrogel scaffold [131, 132].

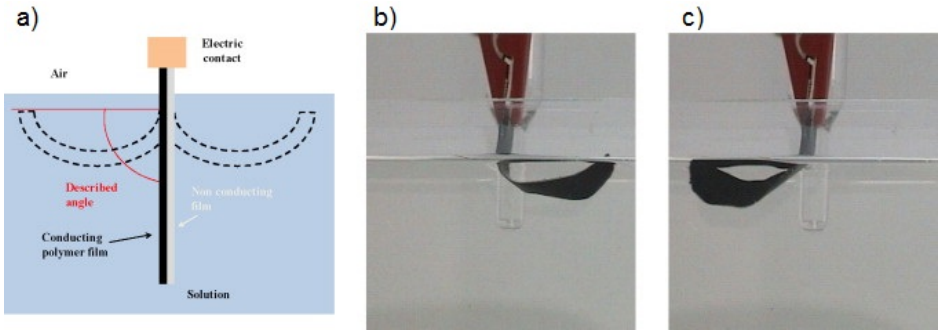

Figure 1.11: A bilayer bending artifical muscle composed of a conducting polymer film and a non-conductive tape. (a) Scheme of the device. (b) Anticlockwise and (c) clockwise movements. Adapted from [139, 140].

Mechanical Transducers

The reversible electrochemical oxidation and reduction of conjugated polymers previously described is associated to ions and solvents uptake from the electrolyte solution, which leads to significant dimensional changes. This phenomenon, called electrochemomechanical deformation, has been used to create soft actuators or transducers for the conversion of electrical power to mechanical work [133]. Suitable materials for the fabrication of conducting polymer-based actuators include polyaniline (PANI), polypyrrole (PPy) and polythiophenes (Pth) [134]. Since PANI actuators are operated in acidic environment [135] and Pth actuators reach comparably low strains in ionic liquid electrolytes [136], PPy actuators are the most widely used in biomedical applications [137], usually with DBS or *p*-TOS as counteranion [138]. In general, the dimensional changes in soft actuators made from conducting polymers are the result of ion and solvent influx. Thus, the strain in PPy actuators has been shown to depend on the size of ions and solvents exchanged in the oxidation and reduction process.

Many devices have been developed based on the electrochemomechanical deformation of electroactive materials [139]. Through the patterning of a conducting polymer on a passive material, such as silicon or SU8, a surface with tunable morphology can be obtained, where the controlled solvent uptake of the polymer can be used for the mechanostimulation of live cells (Figure 1.10c, mechanostimulation due to swelling) [141]. Furthermore, miniaturized conductive polymer

actuators for the generation of high pressure in lab-on-a-chip systems were developed by stacking several layers of modified PPy intercalated with electrolyte layers [142].

An interesting biomimetic approach is the development of artificial muscles using polymer-based stretchable actuators. These devices in their simplest form are composed of a bilayer CP/passive structure: electrochemically driven length variations in the conducting polymer film produce stress gradients across the interface and result in macroscopic bending (Figure 1.11). In a similar fashion, linear movements can be achieved as well [139]. Moreover, since the working potential of conducting polymer films can change as a function of electrolyte concentration, temperature or mechanical stress, these materials can act both as actuators and as environmental sensors at the same time. In this way, they can be used as actuators, sensing the surrounding conditions during movement [143, 144].

A different application, in which electrochemical switching leads to complete reorganization, and eventually causes cracking an swelling of the entire polymer film, has been developed by using a self-doped conductive polymer, PEDOT-S:H [145]. In this polymer, negative charged sulfonate groups are linked to a polythiophene backbone structure via alkyl chains that extend from the backbone. In its reduced state, the polymer associates with protons to balance its internal negative charge. When an electrical potential is applied and the backbone is oxidized, the protons are expelled and the negatively charged groups on the alkyl arms are drawn to the center of the molecule. This results in a major structural change and eventually leads to swelling, cracking and finally disaggregation of the polymer. This material can be used to detach live cells from their substrate while conserving important surface antigens and proteins as compared to enzymatic detachment [3].

Chapter 2

PEDOT:PSS

2.1 Electrical Conductivity in Conjugated Polymers

2.1.1 Role of conjugation

In saturated polymers, all valence electrons are used in covalent σ-bonds. Hence, the energy gap between the valence band and the conduction band is very large and these materials show typical insulating properties. In conjugated polymers (Figure 2.1), the chemical bonding leads to one unpaired electron (the π electron) per carbon atom [146]. Moreover, π-bonding, in which the carbon orbitals are in the sp_2p_z configuration and the orbitals of successive carbon atoms along the backbone overlap, leads to electron delocalization along the polymer backbone. This electronic delocalization provides the "highway" for charge mobility along the backbone of the polymer chain. As a result, the electronic structure in conjugated polymers is determined by the chain symmetry (*i.e.* the number and kind of atoms within the repeat unit), with the result that such polymers can exhibit semiconducting or even metallic properties [33].

The simplest example for modeling electrical conductivity in conjugated polymers is polyacetylene (PAc, molecular formula $[-CH]_n$), the simplest conjugated polymer, shown in Figure 2.1. In PAc, each carbon atom (with four valence electrons) is σ-bonded to two neighbouring carbon atoms and an hydrogen atom, with one π electron per carbon remaining. A simple free-electron molecular orbital model provides the minimum elements needed for describing quantitatively a con-

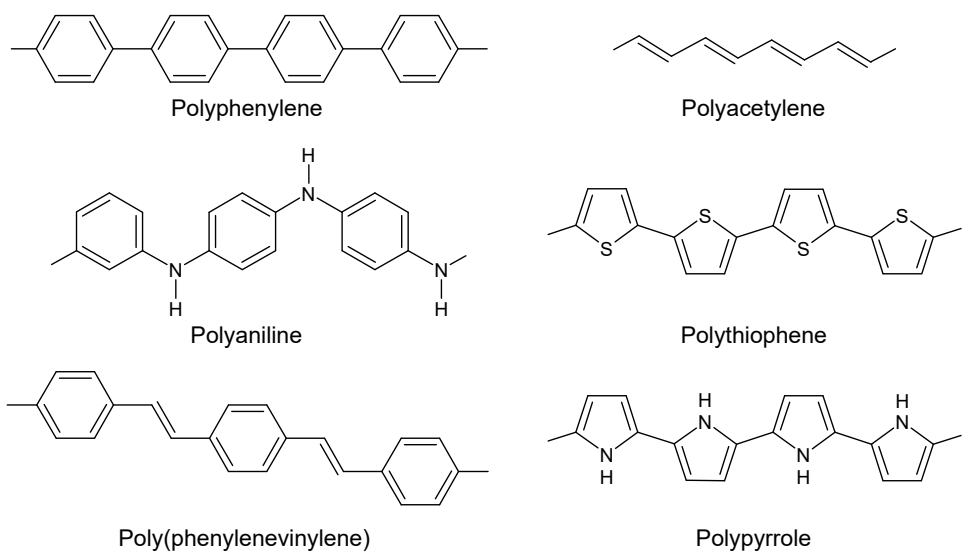

Figure 2.1: Chemical structure of selected conjugated polymers.

ductor, semiconductor or insulator built up of a linear chain of atoms such as in polyacetylene and many other polymers [147]. If we assume a row of N atoms separated by a distance d, the total length of the chain is then $(N-1)d$ or, for large N, approximately Nd. According to the quantum-mechanical model for a free particle in a one-dimensional box (potential equal to zero inside the box and infinity outside) the wave functions correspond to a ladder of eigenvalues [148]:

$$E_n = n^2h^2/8m(Nd)^2 \tag{2.1}$$

where h is the Planck's constant, m the electron mass and n a quantum number, with $n = 1, 2, 3\ldots$

If we assume that the π-electrons from the N p-orbitals are filled into this ladder, with two electrons per molecular orbital, the highest occupied molecular orbital (HOMO) has the energy

$$E_{HOMO} = (N/2)^2h^2/8m(Nd)^2 \tag{2.2}$$

and the lowest unoccupied molecular orbital (LUMO) has the energy

$$E_{LUMO} = (N/2 + 1)^2 h^2/8m(Nd)^2. \tag{2.3}$$

The energy required to excite an electron from HOMO to LUMO is thus:

$$\Delta E = E_{LUMO} - E_{HOMO} = (N + 1)h^2/8m(Nd)^2 \approx h^2/8mNd^2 \tag{2.4}$$

where the approximation is made for large N. The band gap is predicted to decrease as $1/N$ with increasing polymer length, and will thus practically vanish for macroscopic dimensions.

According to this model, macroscopic conjugated polymers should behave like conductors, but experimentally their bandgap does not decrease in the way predicted by Equation 2.4 [149]. Hence there seems to be an upper limit beyond which no change will result from further conjugation into an infinite linear chain. This unexpected result can be explained by taking into account the distortion of the chain, also called Peierls distortion, a common phenomenon in one-dimensional systems [150]. The Peierls theorem states that a one-dimensional system with an incompletely filled band distorts in such a way as to open up a gap at the Fermi level. The degeneracy of π levels, due to the high simmetry of the linear chain, is resolved through a geometrical distortion that reduces the symmetry and induces a rearrangement of the orbital levels. In the case of polyacetylene, this lattice distortion leads to a repeat unit with two carbon atoms closer together and the next two carbon atoms further apart. Hence, the repeat unit can be written as [−CH=CH−] instead of [−CH−]. So, if the carbon-carbon bonds were equally long, π electrons would be spaced out rather evenly along the entire chain; according to Equation 2.4, they would be found in a half-filled continuous band, as it happens for free electrons in metals, and they would be delocalised along the entire chain. But for a chain with alternatingly short and long bonds, the energy band structure changes in a resulting energy gap between a completely filled π band and an empty π^* band, as it happens for electrons in insulators and semiconductors [146]. The energy difference between the highest occupied state (HOMO) in the π band and the lowest unoccupied state in the π^* band is the π-π^* energy gap, E_g.

This bond-alternating structure is common to all conjugated polymers. Because of this distortion, intrinsically conducting polymers have typically low conductivities, whereas their nondistorted structure would have granted a metal-like conductivity. Indeed, the intrinsic conductivity of polyacetylene is low ($< 10^{-5}$ S cm^{-1}); it can be made highly conducting ($\sim 10^{3}$ S cm^{-1}) only by exposing it to oxidizing or reducing agents, a process referred to as "doping" [31].

2.1.2 Charge transport and role of dopant

As mentioned in Section 1.2, the doping process in conjugated polymers is essentially a charge transfer reaction resulting in the partial oxidation (or less frequently reduction) of the polymer. Although conjugated polymers may be charged positively or negatively, studies of the charging mechanism have mostly been devoted to the case of *p*-doping. Depending on the couple polymer-dopant, the doping process can be very effective, increasing the electrical conductivity of the uncharged polymer, almost an insulator, by up to 10-12 orders of magnitude, reaching 1000 S/cm, or even more [34]. A change in the doping state (also called redox status) can also be achieved when ions from an electrolyte enter an organic film, or vice versa. In this case the compensating electronic charge is supplied by a metal contact and the process is called "electrochemical doping".

It must be noted that the term "doping" used in this context can be misleading, since in semiconductor physics it is used for the introduction of an external neutral atom in a host lattice to change its electronic structure [151], while for conducting polymers this process is best viewed as a redox reaction. The insulating neutral polymer is converted into an ionic complex consisting of a polymeric cation (*p*-type doping) and a counterion which is the reduced form of the oxidizing agent, or conversely, a polymeric anion (*n*-type doping) and the oxidized form of the reducing agent as counterion. The ease of oxidation or reduction is thus an important parameter to evaluate if a polymer is a potentially *conducting* polymer. This accounts in part for the choice of π-bonded unsaturated polymers which have small ionization potentials and/or large electron affinities. Indeed, π electrons can be relatively easily removed or added to form a polymeric ion with small effects on the σ bonds which hold the polymer together. Following polyacetylene, this

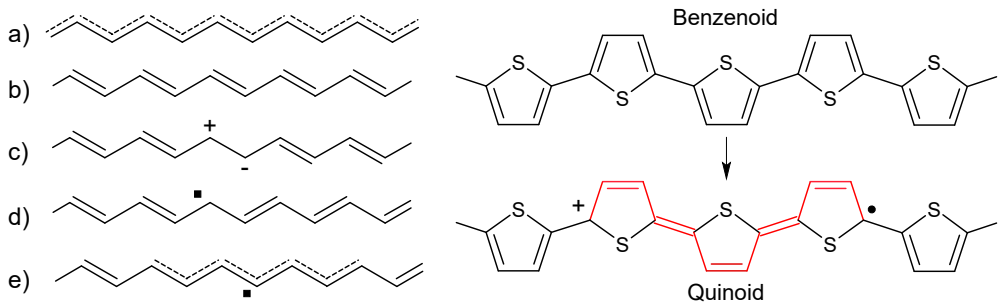

Figure 2.2: On the left, charged states in *trans*-polyacetylene: (a) undimerized structure, (b) dimerized structure due to the Peierls instability, (c) polaron formed by removal of one electron on a carbon atom of the chain, (d) soliton formation, (e) structural relaxation with corresponding delocalized charge distribution. Adapted from [33]. On the right, transition from benzenoid to quinoid structure in polythiophene upon the introduction of a positive charge.

basic principle has been applied with success to a large number of other organic polymers [152]. The increase in electrical conductivity results from the generation of charge carriers and from the ability of those charge carriers to move along the π-system. Consequently, doped conjugated polymers are good conductors for two reasons [33]:

- Doping introduces carriers into the electronic structure. Since every repeat unit is a potential redox site, conjugated polymers can be doped to a relatively high density of charge carriers;
- The attraction of an electron in one repeat unit to the nuclei in the neighboring units leads to carrier delocalization along the polymer chain and to charge carrier mobility, which is extended into three dimensions through interchain electron transfer.

Charges that are introduced in polymers are stored in novel states, called *polarons*, *bipolarons* or *solitons* [153]. These states include a charge and a lattice distortion. Indeed, in organic molecules the equilibrium geometry is different between ground and ionized state, as in the transition between benzenoic-like and quinoid-like structure in polythiophene shown in Figure 2.2. Differently from inorganic solids, where the removal of an electron from the lattice generates a hole

on top of the valence band (Figure 2.3a), in an organic polymer chain it can be energetically favorable to localize the charge and to generate a local distortion (relaxation) of the lattice around it. This process causes the presence of localized electronic states in the gap due to a local upward shift $\Delta\varepsilon$ of the HOMO and downward shift of the LUMO (Figure 2.3b). If this variation in the energy of the HOMO and LUMO levels is higher than the energy required for lattice distortion, E_{dis}, the charge localization process is favored relative to the band process, and a polaron is formed with energy $\Delta\varepsilon - E_{dis}$. It has been reported in literature, from calculation based on the Hückel theory, that in conjugated polymers polaron formation coupled with lattice deformation is always energetically favorable respect to ionization [152].

In the case of an electron polaron, the added electron is stored in a newly created level drawn from the conduction band. In the case of a hole polaron, an electron is removed from a newly created level moved up from the valence band. In both cases a half-filled level is created with spin $1/2$. The energy difference between the band edge and the newly created states depends on the band gap and on the chain length [146]. It must be noted that when a polaron is formed, the valence band remains full and the conduction band empty, since the half-occupied level is localized in the gap (2.3b). As a consequence, there is no appearance of metallic character. However, with a high concentration of counterions the polaron can move in the field of close counterions, so its mobility along the chain can be high. This implies that the doping must be strong to achieve high carrier mobilities.

If a second electron is removed from the polymer chain, two possibilities arise: the electron can be removed from the polaron itself, forming a bipolaron, or from anywhere else on the chain, forming a second polaron. The electronic band structure corresponding to the presence of a bipolaron is depicted in Figure 2.3c. A bipolaron is defined as a non-independent pair of charges of the same polarity associated with a strong local lattice distortion. A bipolaron has two levels in the energy gap: in the case of a negative bipolaron both levels are fully occupied, while for a positive bipolaron both levels are empty. In either case, while a polaron has spin $1/2$, the spins of bipolarons sum to zero. Since these charges have the same sign, the energy gained from lattice deformation must be higher than the energy coming from the Coulomb repulsion of these charges [154]. More-

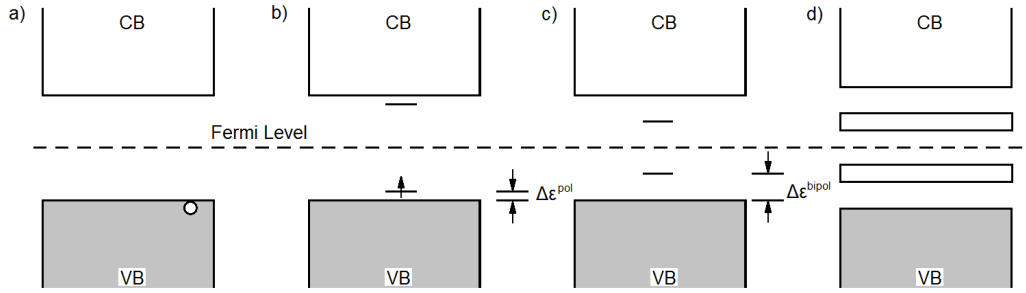

Figure 2.3: Illustration of the band structure of a polymeric chain in the case of the formation of: (a) a delocalized hole; (b) a polaron; (c) a bipolaron; (d) bipolaron bands in high doping conditions. The Fermi level is taken as reference level. Adapted from [152].

over, the lattice distortion increases upon this second ionization process (E_{dis} for bipolarons is higher than for polarons), implying that the reduction of ionization energy, $\Delta\varepsilon$, must change accordingly, keeping in mind that bipolaron formation is energetically favored only if $\Delta\varepsilon > E_{dis}$. As a consequence, the electronic states appearing in the gap for a bipolaron are further away from the band edges than for a polaron, as shown in Figure 2.3c. Calculations for many conjugated polymers have indicated that the distortion energy required to form one bipolaron and to form two polarons is very similar [155–157]. On the other hand, the decrease in ionization energy is much more important in the bipolaron case ($2\Delta\varepsilon^{bip}$) than for two polarons ($2\Delta\varepsilon^{pol}$), as shown in Figure 2.3. This is the reason why a bipolaron is thermodynamically more stable than two polarons, despite the Coulomb repulsion due to the presence of two similar charges, which is also screened by the presence of dopants [152].

Experimental and theoretical investigations of the evolution of the electronic and transport properties as a function of doping level on different conjugated polymers have been conducted since the early 80s [152]. Experimental data from optical absorbance spectra [157] and electron spin resonance (ESR) [158] show that at low doping (about 1 mol %), an increasing number of polaronic states (spin 1/2) are formed. At higher dopant concentrations (about 10 mol %), polarons gradually disappear due to the formation of spinless bipolarons. By further increasing the dopant concentration (about 30 mol %), the bipolaronic states within the en-

ergy gap eventually overlap, leading to the formation of two bipolaron bands and a widening of the original bandgap (since the new states are extracted from valence and conduction bands), as shown in Figure (2.3d). The generation of these bands considerably improves the conductivity of the material at high dopant concentrations.

Solitons are a third type of excited species, which only occurs in degenerate polymers, *i.e.* polymers that possess two different geometrical structures in the ground state with exactly the same energy. The most common example for a degenerate polymer is *trans*-polyacetylene (PAc) [159]. Indeed, as it can be seen in Figure 2.2, an interchange of single and double bonds along the chain of PAc results in the same structure. As a result, when an electron is extracted from a polaron along the chain, the two positive charges are not coupled as it would happen in non-degenerate polymers. Since the geometric structure that appears between the two charges has the same energy as the geometric structure on the other sides of the charges, there is no increase in distortion energy when the two charges separate, and consequently they are free to mowe away from each other. By looking at the PAc structure in Figure 2.2d, it is apparent that a single charge on a PAc chain constitutes a boundary between two degenerate segments with specular geometry. Such a charge associated with a boundary is called a soliton, because it has the properties of a solitary wave which can propagate without deformation and dissipation [160]. The presence of a soliton is associated to a localized electronic state in the center of the bandgap. This level can be filled with one electron (neutral soliton, spin 1/2), with two electrons (negatively charged soliton, spin zero) or it can be empty (positively charged soliton, spin zero). In a long chain, the spin density in a neutral soliton (or charge density in a charged soliton) is not localized on one carbon but spreads over several carbons [159], which gives the soliton a width as shown in Figure 2.2e. Solitons can propagate along the chain and contribute to charge transfer through "intersoliton hopping", where an electron can jump between localized states on adjacent polymer chains through a phonon-assisted hopping process [161].

Unlike PAc, most conjugated polymers possess a nondegenerate ground state that corresponds to a single aromatic-like geometric structure, while a quinoid-like resonance structure is allowed but with a higher total energy (Figure 2.2).

Ab initio calculations have been used to show that the quinoid structure has a lower ionization potential and a larger electron affinity than the aromatic structure [162]. This explains the local chain geometry relaxation to a quinoid structure that appears upon doping around the dopant charges.

Two aspects have to be stressed. First, in polymeric materials, the overall charge transport is due to the combination of charge transport along the single polymer chains an charge hopping between different chains. The latter process is likely to be the rate-limiting step which determines the conductivity observed macroscopically [152]. Interchain interactions and the development of a model for the interchain exchange of polarons, bipolarons and solitons are thus of prime importance. Second, polymers are rather amorphous and inhomogeneous, and the effects of disorder on charge transport have therefore to be properly taken into account.

2.1.3 Temperature dependence of charge transport

To give a physical description of the charge transport in conjugated polymers, it is useful to consider the temperature dependence of parameters such as conductivity and thermopower of those polymers.

In a metal the conductivity, σ, remains finite as the temperature approaches zero. This is due to the fact that there are delocalized states at the Fermi level, which allow conductivity without termal activation. Furthermore, in metals the conductivity decreases with increasing temperature, due to phonon-electron interactions. In semiconductors, the situation is the opposite as for metals: at temperatures near zero they act as insulators and an exponential increase in conductivity with temperature is a typical behaviour, because conduction is caused by the hopping of charges between localized states [163].

Polyacetylene is a good example to demonstrate the changes in conductivity and thermopower as a function of temperature and doping (Figure 2.4). At low doping level the conductivity approaches zero for $T = 0$ and increases exponentially with increasing temperature [164]. Hence, a typical semiconducting behavior is observed. The newly created charge carriers that are due to the small amount of dopants added are strongly localized to defect sites within the electronic gap.

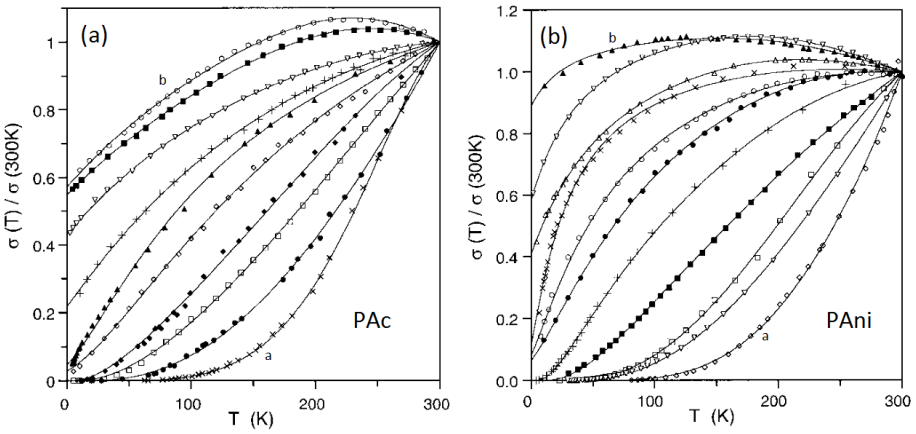

Figure 2.4: Normalized conductivity temperature dependence for (a) iodine-doped PAc and (b) camphor sulphonic acid-doped polyaniline with increasing dopant concentrations from the curve a (minimum) to the curve b (maximum) in both graphics. The fits are to Equation 2.6 for polymers with σ non-zero as $T \rightarrow 0$ and to Equation 2.7 for $\sigma \rightarrow 0$ as $T \rightarrow 0$ [164].

With increasing doping level a low temperature semiconductor-metal transition occurs resulting in nonzero conductivities at $T = 0$, with a continuous increase in conductivity with increasing temperature. The fact that conductivity remains above zero for $T = 0$ shows that the material contains delocalized states at the Fermi level. In highly doped polyacetylene samples the term $d\sigma/dT$ changes its sign in correspondance to a so-called cross-over temperature [164], above which the conductivity decreases with increasing temperature. This is a characteristic feature of many highly doped conducting polymers (see Figure 2.4).

A second important parameter for the understanding of conductivity in conjugated polymers is the termoelectric power, or thermopower, which is a measure of the rate of diffusion of charge carriers in response to a thermal gradient [165]. Thermopower is a transport property that is usually less affected by materials imperfections than the conductivity, and so can help identify the intrinsic conduction processes [166]. When a temperature difference is applied to a solid, mobile charge carriers migrate from the hot side to the cold side, like a gas that expands during heating. If only one type of carrier is able to migrate, or migrates stronger than the other one, an electric field is created within the material (Seebeck effect). The thermopower is defined as the proportionality constant between the strength

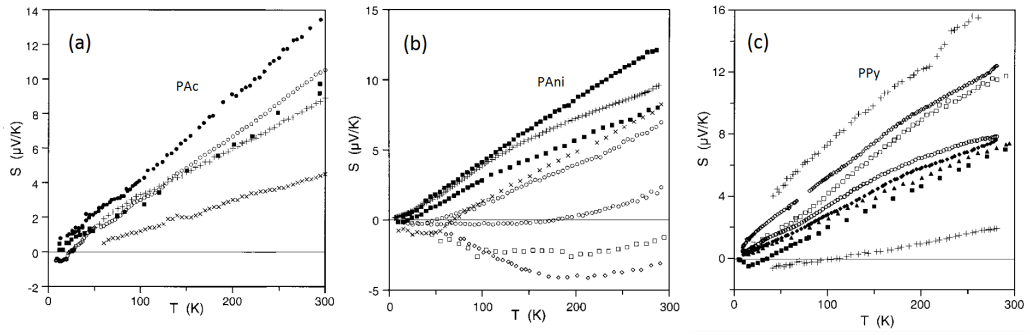

Figure 2.5: Thermopower for (a) highly doped PAc, (b) PAni, (c) PPy [164].

of that field and the temperature gradient [163]. A positive sign for thermopower indicates that holes are responsible for the charge transport, while a negative sign means that charge is transported through electrons. In the case of doped polyacetylene (PAc), polyanyline (PAni) and polypyrrole (PPy), thermopower shows positive sign [164].

For PAc, at very low doping levels the room temperature thermopower is very large and it decreases with the increasing of the doping level, until for fully doped samples the thermopower shows remarkably good agreement with the proportionality to temperature expected for metallic diffusion. The magnitude of the room temperature thermopower is somewhat larger than for typical conventional metals, which is the trend generally expected for metals with low carrier density. Thermopower measured for PAc, PAni and PPy is shown in Figure 2.5. This metallic behavior is in contrast to the crossover from non-metallic to metallic temperature dependence seen in the conductivity of PAc. This metallic thermopower character suggests that the conductivity crossover can not arise from a change in the nature of the electronic states with increasing temperature, because this variation should also be seen in thermopower, which is very sensitive to electronic structure [164].

The conflicting behavior of conductivity and thermopower is easily resolved in a heterogeneous model in which metallic (ordered) and non-metallic (disordered) components are both present [167]. Contributions from the metallic and non-metallic regions are present simultaneously, but their relative weighting is different for conductivity and thermopower, so the crossover from metallic to non-metallic behavior in conductivity will not in general coincide with a corresponding

change in thermopower. Because thermopower contributions are weighted by the thermal rather than the electrical resistance, and heat is carried by lattice vibrations as well as the charge carriers, the thermopower is more likely to show the intrinsic behavior of the crystalline metallic regions, while conductivity is affected by both metallic and non-metallic components [166, 167].

2.1.4 Heterogeneous model

In contrast to a semiconductor solid, the structure of a conjugated polymer is far less regular [146]. Polymers contain individual molecules with different chain lengths, varying amounts of defects and chain ends; furthermore, they can be amorphous or partially crystalline. Additional differences occur due to aging, and finally the polymer chains can have orientation in the three space directions resulting in anisotropic electronic properties. As a consequence, the disorder in conjugated polymers has a strong effect on the electronic properties. However, order itself is not a sufficient condition for charge transport, since even in a highly ordered system, macroscopic charge transport is not possible unless the charges can hop or diffuse from one chain to another.

System with a disorder length scale (the distance from an arbitrary point of the material beyond which the crystal lattice loses its periodic character) equal to or smaller than the elctronic correlation length are described as *homogeneously disordered*; systems in which the disorder length scale is large compared to the elctronic correlation length are described as *heterogeneously disordered* instead [168]. Heterogeneous disorder has been proposed for various types of polyacetylene, and also for PEDOT:PSS a heterogeneous disorder model is appropriate [169]. It has been pointed out that the concepts of homogeneous and heterogeneous disorder on their own are not sufficient to describe the carriers behaviour in conjugated polymers [168]. Nonetheless, these models can give a first understanding for the charge transport in intrinsically conductive polymers and the calculated data based on these models give good fits for the experimental results [164].

The localization effects in the inhomogeneously disordered conducting polymer are proposed to originate from rod-like quasi one-dimensional chains [164, 170]. It has long been recognized that crystallization in polymers typically in-

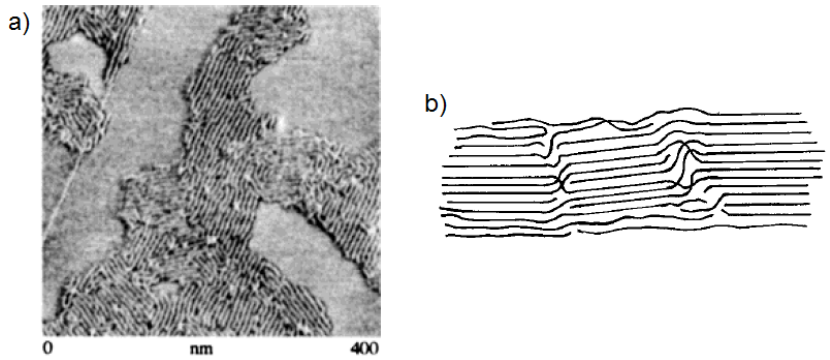

Figure 2.6: (a) Scanning force microscopy (SFM) image of polymer chains on a surface showing separate regions of well-aligned chains [171]. (b) Sketch of morphology of polymer chains in highly conducting PAc showing heterogeneous disorder [164].

volves small crystallites of aligned chains interspersed with regions where the chains are disordered, and this is also the case for conducting polymers. Percec *et al.* [171] have succeeded in visualizing the crystallization on a two-dimensional substrate of a nonconducting polymer consisting of cylindrical units of relatively large diameter, as illustrated in Figure 2.6. Well-defined crystalline regions surrounded by discontinuities are clearly seen: similar boundaries in conducting polymers would tend to dominate the resistance of a sample since the charge carriers must traverse the "barriers" surrounding the crystallites.

The resistance in a heterogeneous model such as that illustrated in Figure 2.6 for conduction in polymers can be written as the sum of the resistances of the crystalline parts (subscript c) and barrier parts of the conduction path along the fibers. Taking account of the fact that the metal-semiconductor transition may occur in the barrier region, with both non-metallic (subscript n) and disordered metallic (subscript d) portions present in parallel, this model gives the conductivity as [164]:

$$\sigma^{-1} = \rho = f_c\rho_c + \left[(f_n\rho_n)^{-1} + (f_d\rho_f)^{-1}\right]^{-1} \tag{2.5}$$

where f_i are geometric factors defined by $f_i = \frac{L_i A}{L A_i}$. Here L and A are the effective total length and cross-sectional area of the sample, L_i is the length of path consisting of material i with intrinsic resistivity ρ_i, and A_i is the effective cross-sectional area for conduction in each type of material. For the case of a fibrillar polymer

where the fibers have similar properties and the nature of the electronic states does not change with temperature, the temperature dependence of the geometric factors is supposed to be small. However, intrinsic resistivities ρ_i do depend on temperature and moreover they also depend on the doping level. Consequently, various models for conductivity depending on temperature and doping level have been proposed in literature [164, 172].

For highly conducting organic polymers, the non-metallic temperature dependence found for the conductivity can be ascribed to fluctuation-induced tunneling between extended metallic regions [173]. If we use this mechanism for the barrier resistance (the second term in Equation 2.5), and the crystalline conductivity (the first term) as that of a quasi-one-dimensional metal [174, 175], we obtain the expression [176]:

$$\sigma^{-1} = f_c\rho_m \exp\left(-\frac{T_m}{T}\right) + \left\{\left[f_n\rho_t \exp\left(\frac{T_t}{T+T_s}\right)\right]^{-1} + [f_d\rho_d]^{-1}\right\}^{-1} \tag{2.6}$$

which gives a good account of the conductivity of the metallic polymers (σ non-zero as $T \rightarrow 0$), as shown by the fits in Figure 2.4. In Equation 2.6, T_m gives the energy of phonons that can backscatter charge carriers (about 1400 K for PAc [175] and 1000 K for the other polymers [164]), ρ_m and ρ_t are the resistivities associated respectively to the quasi-one dimensional metal and to the tunneling barrier and T_t and T_s are the tunneling parameters (that depend on materials and geometry of the tunneling junction) [177]. The disordered metal resistivity ρ_d is taken as approximately constant as it is normally dominated by elastic disordered scattering. The residual resisitivity of the crystalline regions can be taken as negligible in comparison with the other terms [176]. From a different point of view, we can say that basically in highly doped conjugated polymers localized and extended states exist in parallel. A critical energy E_c exists that separates localized states from extended states. The resulting electronic behaviour depends on the position of the Fermi energy E_F relative to the mobility edge E_c: if the Fermi level lies within the extended states, then the conductivity remains non zero even as T approaches 0, since no thermal activation is required for charge transport [146].

For low conductivity polymers, for which the conductivity vanishes as T ap-

proaches 0, the disordered metal term and significant tunneling at very low temperatures are absent. Instead, the temperature dependence is dominated by hopping-type behaviour as in disordered semiconductors. The appropriate form of Equation 2.5 can be written as [178]:

$$\sigma^{-1} = f_c \rho_m \exp\left(-\frac{T_m}{T}\right) + f_n \rho_0 \exp\left(\frac{T_0}{T}\right)^{\gamma} \tag{2.7}$$

where ρ_0 and T_0 are constant values that depend on the considered polymer. For $\gamma = 0.25$, the second term is Mott's variable-range hopping (VRH) law in three dimensions [179], while for $\gamma = 0.5$ it represents either quasi-1D hopping, or 3D hopping in the presence of electron-electron interactions [180], or tunneling between mesoscopic metallic islands, in which the charging energy is significant [181].

For a random network of coupled one-dimensional metallic wires, Prigodin and Efetov [172] predicted four different conductivity modes depending on teperature. Starting from low temperatures, the material shows a VRH conductivity. Then, the next transport mode is the hoppig over nearest states, followed by regions of localized correlations, and finally band transport is reached. For a one-dimensional system the variable range hopping is described by Mott's temperature law [179]:

$$\sigma(T) = \sigma_0 \exp\left[-\left(\frac{T}{T_0}\right)^{1/2}\right] \tag{2.8}$$

with $T_0 = e^2/\varepsilon L$, where e is the electron charge, ε is the dielectric constant, and L is the localization length, defined as the distance from a site for the electron wave function to decay to $1/e$ of its value [163]. The $T^{1/2}$ dependece at low temperatures is typically due to electron-electron interactions [182]. The low-temperature $T^{1/2}$ terms (the low-temperature conductivity with the residual conductivity subtracted) are shown for several conducting polymers in Figure 2.7, compared to an inorganic doped semiconductor, Si:B, and a typical 3D conventional amorphous metal, a Fe-Ni-P-B alloy. The $T^{1/2}$ terms for PPy are only slightly larger than those for Si:B and the amorphous metal, but that shown for polyaniline (PAni) is much larger, and all those for polyacetylene (PAc) are huge by comparison with the others [164]. An enhanced magnitude of these $T^{1/2}$ terms is expected in the

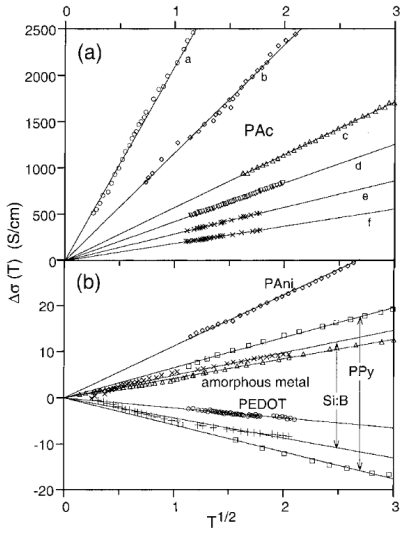

Figure 2.7: Temperature-dependent conductivity $\Delta\sigma(T)$ (i.e. residual conductivity subtracted) showing the $T^{1/2}$ behavior at low temperatures for (a) highly conducting PAc doped with iodine, (b) PAni doped with CSA, (c-d) a typical amorphous metal (Fe-Ni-P-B), (e-f) PEDOT, with the range of the PPy and Si:B data also indicated [164].

heterogeneous model discussed above if the metal-semiconductor transition occurs in the barrier regions and the crystalline regions are highly conducting. These highly conducting regions lead to an enhancement of the overall conductivity and a larger absolute value for the $T^{1/2}$ interaction term. At very low temperatures, the temperature dependent metallic resistivity for highly conducting regions (first term in Equation 2.6) becomes negligible, and the $T^{1/2}$ interaction term dominates the temperature dependence of conduction through the barrier regions.

2.2 PEDOT:PSS

2.2.1 PEDOT

During the second half of the 1980s, a new polythiophene derivative, poly(3,4-ethylenedioxythiophene) (PEDOT) [146], was developed at the Bayer AG research laboratories in Germany. PEDOT is an intrinsically conductive conjugated polymer, composed by a chain of 3,4- ethylenedioxytiophene (EDOT) monomers,

as shown in Figure 2.8, prepared using standard oxidative chemical or electrochemical polymerization methods. PEDOT is found as an insoluble polymer, yet exhibiting some very interesting properties [183]:

Reversible doping state PEDOT can be repeatedly doped and undoped. It is almost transparent and light blue in the oxidized state and can be easily changed into opaque and dark blue appearance in the neutral state. Thus its color changes visibly when its doped state changes and may be suitable for optical applications, such as electrochromic displays [184].

Excellent stability PEDOT has improved chemical and thermal stability. Thermal studies show that a continuous degradation occurs above 150°C and complete decomposition above 390°C [185]. Electrical conducting properties appear to remain almost unaltered after aging in environmental conditions. Its high stability is attributed to favorable ring geometry and the electron-donating effect of the oxygen atoms at the 3,4- positions stabilizing the positive charge in the polymer backbone.

Low band gap (high conductivity) PEDOT has a band gap of about 1.5-1.6 eV [186]. The lower band-gap relative to polythiophene is thought to originate from the influence of the electron-donor ethylene dioxy groups on the energies of the frontier levels of the π system. Experimental results show that, after doping, PEDOT exhibits reduced absorption in the visible: the oscillator strength shifts from around 1.5 eV (lowest $\pi - \pi^*$ transition) to below 1 eV in the metallic state. Thus it shows a high electrical conductivity in its doped state [187].

Electrochemical properties Compared to other conducting polymers, electrochemically synthesized films of PEDOT have a low redox potential and excellent stability in their doped state. From cyclic voltammetries, it is found that the redox peaks at approximately 0 mV (oxidation) and -400 mV (reduction) remain almost unaffected during cycling. However, only under an applied negative potential of -700 mV the neutral films were found to be stable. Open circuit potential measurements show that the neutral films are rapidly oxidized [188].

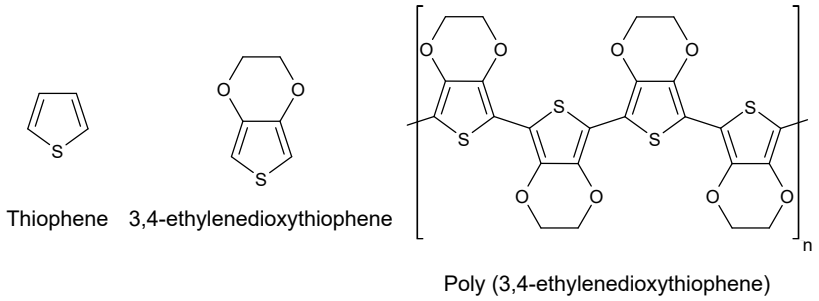

Figure 2.8: Chemical structure of thiophene, 3,4- ethilenedioxythiophene (EDOT) and poly(3,4- ethilenedioxythiophene) (PEDOT).

2.2.2 PEDOT:PSS dispersions

One of the reasons why PEDOT has become a succesful conductive polymer is the availability as a polymer dispersion [146]. Although the PEDOT polycation is not soluble in any solvent, used in combination with poly(styrenesulfonic acid) (PSS) as a counterion a polyelectrolite complex (PEC) can be prepared that forms a stable dispersion, which can be produced on an industrial scale and used in many deposition techniques. Chemical structure of PEDOT:PSS is shown in Figure 2.9.

PSS was the first polyelectrolyte used for a PEC with PEDOT in 1990 and has remained the industrial standard ever since. PSS is commercially available in a large range of molecular weights with different polydispersities. PSS as a counterion for PEDOT is always used in excess, that is, as host polyelectrolyte (HPE), as shown in Figure 2.9. The molar ratio of tiophene groups to sulfonic acid groups in standard PEDOT:PSS dispertions is in the range of 1:1.9 to 1:15.2, which corresponds to a weight ratio range of 1:2.5 up to 1:20. Since only one charge is found for every three to four tiophene rings, the charge excess of PSS is between 6-fold and 46-fold [146]. Due to the delocalization of positive charges in PEDOT, the resulting weak polar groups and the different spacing of charges in PEDOT compared to PSS, it is reasonable to assume that the structure of PEDOT:PSS is based on random interactions between their polymer chains, with no order on the molecular or supermolecular level (the so-called “scrambled-egg arrangement) [146]. PSS is used in combination with PEDOT for basically two reasons: the first is to act as a counterion, balancing the positive charges on the PEDOT backbone,

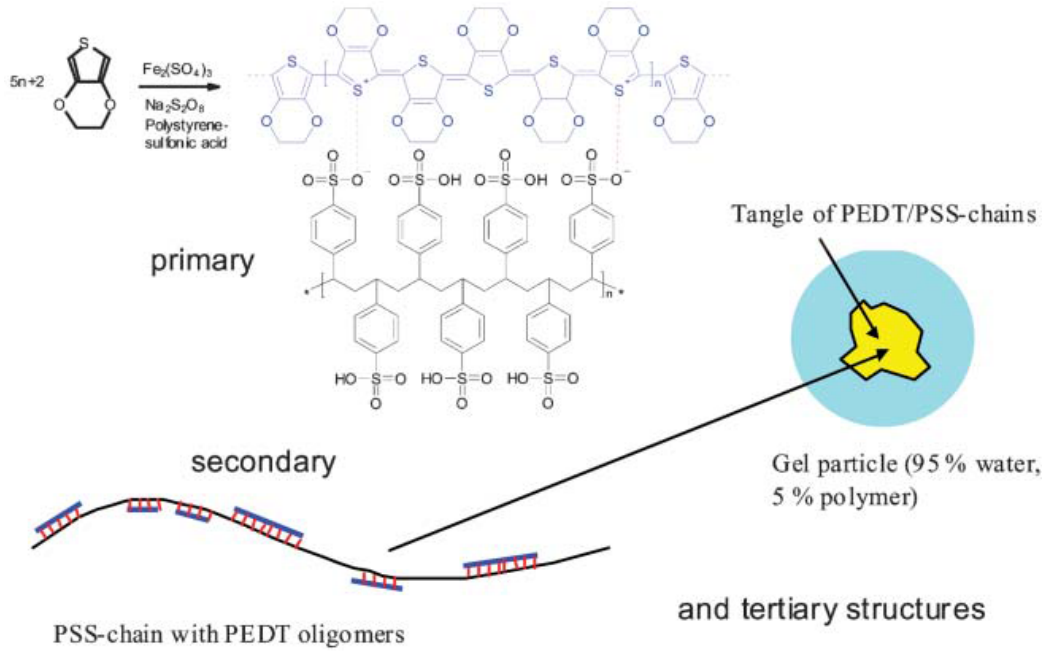

Figure 2.9: Structure of poly(3,4-ethlenedioxytiophene) poly(styrenesulfonate) (PEDOT:PSS). Adapted from [189].

and the second is to keep PEDOT segments dispersed in water owing to its high hydrophilicity [189]. Their combination leads to a loosely crosslinked and highly swollen polymer gel, composed by gel particle consisting of about 90 - 95% by water, with maximum solids content depending on the PEDOT to PSS ratio, growing with an increasing PSS content [189]. In order to understand the physical and chemical properties of PEDOT:PSS, it must be noted that PEDOT chains appear to be much shorter than PSS chains: several measurements with PEDOT:PSS or substituted PEDOT derivatives suggest that the molecular weight of the PEDOT molecules is not exceeding 1 to 2.5 kDa (about 6 to 18 repeating units), resembling an oligomeric nature of these segments [189], while the average molecular weight of commercially available PSS is usually 70 kDa at least [190].

Being composed of two polymers with different electrical and chemical properties, the PEDOT to PSS ratio can influence some of the physical parameters of the polymer film, namely bulk conductivity, sheet resistance, solids content, and surface roughness. More specifically, higher relative concentrations of insulat-

ing PSS lead to less conductive and flatter films, due to a decrease in the size of PEDOT particles in the PEDOT:PSS suspension [189, 191, 192]. These results are also in accordance with the observed correlation between particle size and film conductivity, from which it can be seen that smaller particles give films with smaller conductivity [189]. The average particle size of PEDOT:PSS dispersions is typically in the range of 10 to 100 nm [146].

2.2.3 Deposition of PEDOT:PSS

PEDOT:PSS dispersed in water can be deposited in principle by all common techniques employed for the deposition of waterborne coatings. Common deposition techniques to obtain uniform coatings are slit coating, drop casting, bar coating, spin coating, electrospinning and spraying. In case a structured deposition is required, other techniques are commonly employed such as screen printing, inkjet, nozzle printing and various form of contact printing (roll to roll), that is, relief, flexographic, gravure and offset printing [193]. Other ways for structured deposition of PEDOT:PSS have been realized by modifying the wetting properties of the surface, that is by depositing water repellants [194] or by introducing photolithographical techniques [195].

The pristine PEDOT:PSS dispersion in water has to be adjusted to meet the requirements of the specific deposition technique and to obtain uniform films. Important properties that determine the film quality are the viscosity, the surface tension and the adhesion to the substrate [146]. This can be done by using different grades of PEDOT:PSS, which differ in solid content, the ratio of PEDOT to PSS and the gel particle distribution, or by the addition of water soluble or dispersible additives. Several ready-to-use formulations optimized for specific applications and deposition techniques are commercially available, for example by Heraeus GmbH (under the commercial name Clevios™) [196] and Sigma-Aldrich [197].

Among the other techniques, the deposition of PEDOT:PSS dispersions by spin coating has proven to be an easily accessible technique to obtain uniform films in a thickness range from 10 to 1000 nm. Typical spin curves are illustrated in Figure 2.10. Another appealing technique for the deposition of PEDOT:PSS thin films is electrochemical polymerization, at first developed for polypyrrole

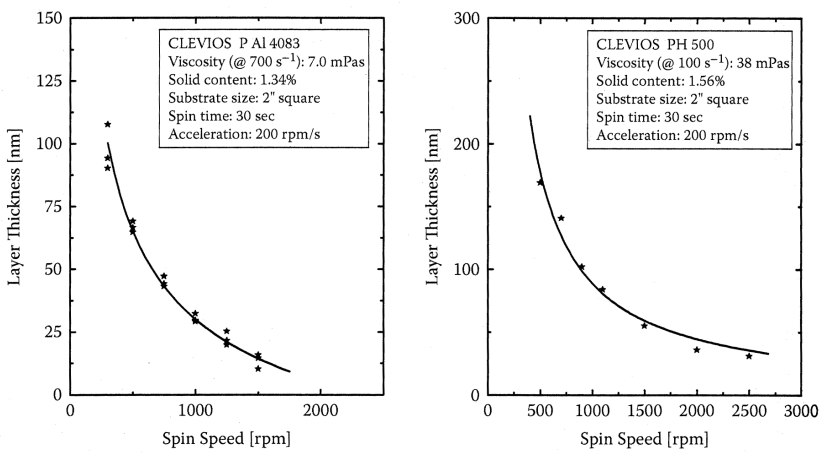

Figure 2.10: Spin curves of CLEVIOS™ P AI 4083 and CLEVIOS™ PH 500. Adapted from [146].

[198], and then extended to a wide range of conjugated polymers. This technique allows a more precise control on the quantity of material that is deposited on the substrate, and provides an easy way to functionalize the material by introducing inorganic [199] or bio-molecules [200]. The electropolymerization of PEDOT:PSS has been proven to produce films and micro-structured systems with facile electrochemistry, high-ionic conductivities, good electrochemical stability and a capacitance suitable for practical use in electrochemical supercapacitors [201–203].

2.3 PEDOT:PSS Thin Film Properties

2.3.1 Thermal and light stability

One major advantage of PEDOT:PSS films is their thermal stability. This property has been studied by thermogravimetrical analysis (TGA) of thick layers at Bayer Laboratories [146]. In Figure 2.11a is shown the weigth loss over time while the sample is heated at a constant rate in helium. Between 100°C and 200°C the weigth loss is solely determined by evaporation of remaining water, while at about 250°C the sample weigth decreases significantly. Data from ion currents taken simultaneously show that this is caused by the fragmentation of PSS groups. At

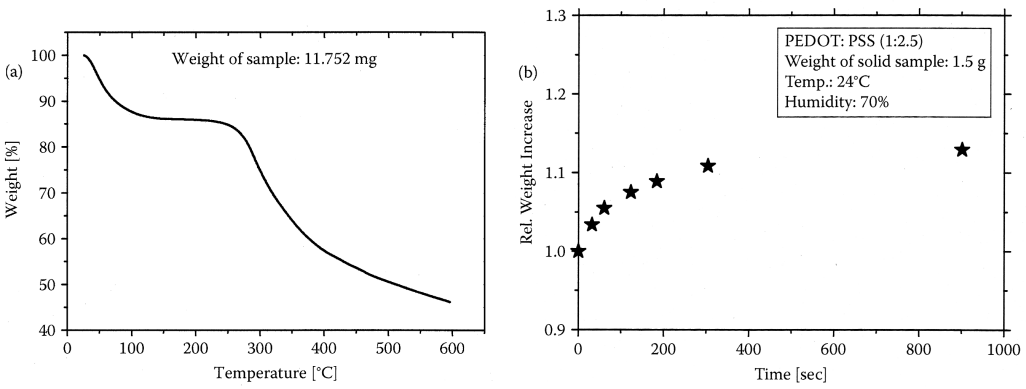

Figure 2.11: (a) Weigth loss of a sample of PEDOT:PSS with a weigth ratio of PEDOT to PSS as 1:20 monitored while heating at a constant rate of 5 K/min. (b) Weigth increase of a PEDOT:PSS sample owing to the absorption of water as a function of time. Adapted from [146].

temperatures $T > 350°C$ other fragments due to carbon oxidation are detected. Following the analytical data obtained by TGA the material is considered to be thermally stable up to 200°C.

When PEDOT:PSS films are exposed to light, the wavelength of radiation affects the kinetic of degradation significantly [146]. In particular, conductivity of PEDOT:PSS films especially decreases for absorbed UV photons with $\lambda < 320$ nm, indicating that, like most polymers, pure PEDOT:PSS films degrade over time when exposed to UV light. This fact limits the use of conducting polymers in outdoor applications when proper protection means are not taken. Figure 2.12a displays the resistivity of thin films of pristine PEDOT:PSS (with a ratio of PEDOT to PSS as 1:2.5) exposed to the light of a Xe lamp. The films show a steep increase of resistivity when left unprotected in air, whereas films encapsulated by a thin glass plate to avoid the contact with ambient air exhibit only a slow increase, very similarly to the films stored in air in the absence of light. These results demonstrate that the degradation is due to an air-induced oxidation of PEDOT, accelerated by the simultaneous absorption of UV light. This process can be significantly slowed down when the films are properly encapsulated, that is, by covering PEDOT:PSS with glass plates or protective polymer coatings. Also the deposition of thick PEDOT:PSS layers or the addition of stabilizing agents

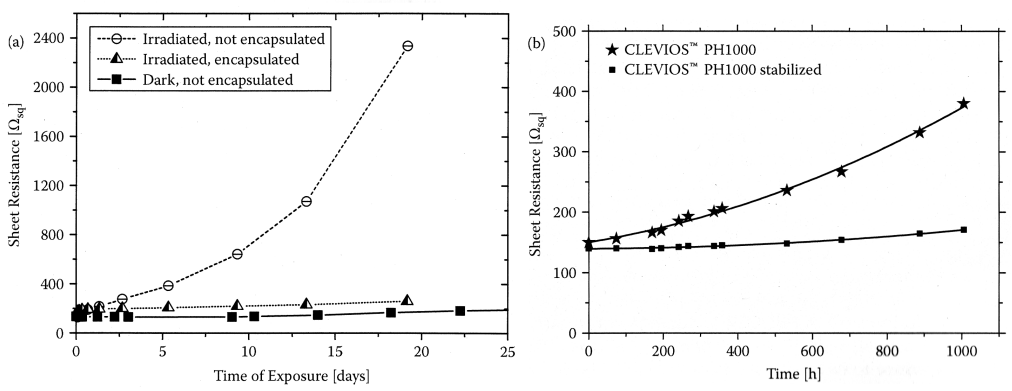

Figure 2.12: (a) Sheet resistance of films of PEDOT:PSS including 5% ethylene glycol as a function of time. (b) Sheet resistance of PEDOT:PSS films exposed to a Xe lamp as a function of time, compared to a non-exposed sample. Adapted from [146].

reduces the increase of resisitivity over time (see Figure 2.12b) [146].

2.3.2 Water uptake

PEDOT:PSS is strongly hygroscopic and takes up moisture when handled under ambient conditions [146]. The 15 wt% water loss of predried PEDOT after baking, as depicted in Figure 2.11a, can therefore be attributed to absorbed water. The water absorption of a predried PEDOT:PSS sample of 1.5 g is monitored over time in Figure 2.11b. The sample consists of flakes peeled off from the underlying substrate with a thickness of several tens microns. Within the first 3 minutes the weigth of the sample increases by 10% when brought in contact with ambient air. Thin layers of PEDOT:PSS films up to a thickness of about 100 nm almost instantaneously absorb water from the environment. The picked up water is incorporated into the films and hence the layer thickness increases accordingly. The swelling of the films depends on the relative humidity level and on the PEDOT to PSS ratio. An increase of layer thickness is especially pronounced for films with a high PSS content and can reach up to 30% [146].

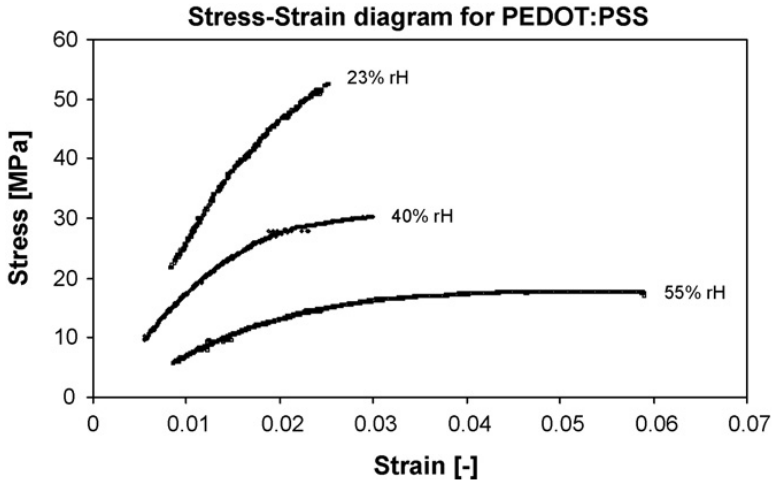

Figure 2.13: Stress-strain diagrams for typical results obtained at different relative humidities [204].

Relative humidity	Tensile strength (MPa)	Young's modulus (GPa)	Fracture behavior
23% rH	53.2	2.8	Brittle (smooth surface)
40% rH	33.7	1.9	Intermediate (rough surface)
55% rH	22.2	0.9	Plastic (shear lips)

Table 2.1: Overview of the mechanical properties of a 25 μm thick tensile specimen made of PEDOT:PSS [204].

2.3.3 Mechanical properties and morphology

The mechanical properties have been investigated by tensile strength tests on free-standing PEDOT:PSS films [204]. All mechanical characteristics were found to be strongly dependent on the relative humidity (rH) level. The dependence on relative humidity can be seen in Figure 2.13, which shows typical stress-strain curves obtained at different conditions, while an overview of the results is summarized in Table 2.1.

X-ray diffraction (XRD) analysis [169] and morphology observations made with scanning probe microscopy techniques [192] indicate that, owing to the film-forming properties of PSS, PEDOT:PSS films are amorphous. This is in contrast to chemically *in situ* polymerized PEDOT films, which do not contain PSS and exhibit crystalline ordering and fibril-like structures.

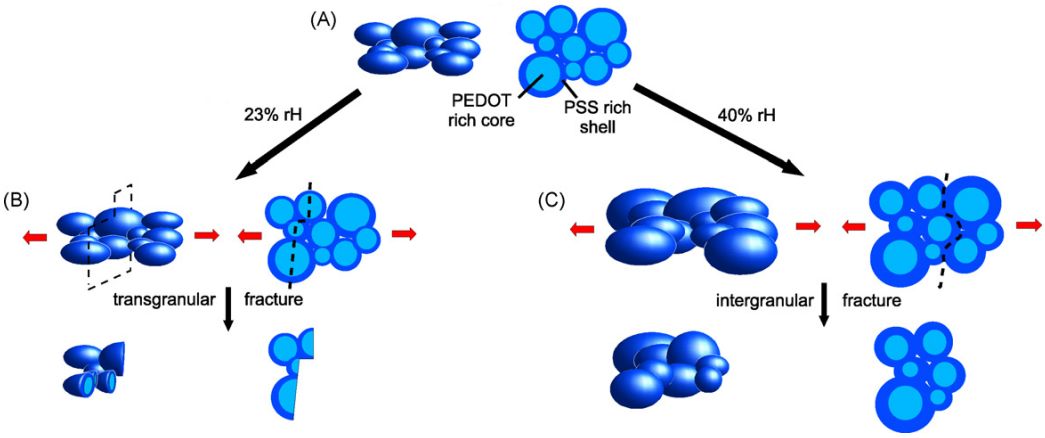

Figure 2.14: (a) Solid film consisting of lentil-like shaped grains of PEDOT:PSS. (b) Transgranular brittle fracture with smooth fracture surfaces. (c) Intergranular plastic fracture with rough surface [204].

Accordingly to tensile tests, SEM and AFM analysis, the following morphological and micromechanical model for PEDOT:PSS films (shown in Figure 2.14) is commonly accepted in literature [204]. PEDOT:PSS films are made from grains with an average diameter of about 3040 nm, composed by a PEDOT-rich core and a PSS-rich shell (Figure 2.14a). The coherence of the material is achieved by hydrogen bonds between PSS in the shell. At low relative humidities these hydrogen bonds are very strong and therefore upon fracture the crack grows through individual grains (transgranular fracture) which results in brittle macroscopic fractures (Figure 2.14b). Higher relative humidities then lead to water uptake by the hydrophilic and hygroscopic PSS rich shell and thus to a swelling of the material and larger distances between grains. Larger distances between shells mean reduced cohesion due to weakened hydrogen bonds and therefore reduced mechanical strength. Upon tensile loading at higher relative humidities individual grains can then slide by each other. This results in a rough surface and an intergranular fracture, that can originate macroscopically plastic failures (Figure 2.14c).

2.3.4 Light absorption spectra and energy levels

The light absorption spectrum of PEDOT:PSS is almost identical to the absorption of *in situ* chemically polymerized PEDOT without PSS. PEDOT:PSS thin films

are highly transparent in the visible spectral range, with almost flat transmission curves, slightly tilted to higher absorption in the red giving the films a light-blue appearance [146].

In Figure 2.15 is shown the absorbance spectrum for a 100 nm thin film of PEDOT:PSS. It consists of a broad feature above 400 nm increasing all the way up to 3200 nm, which can be interpreted as a free charge contribution to the absorption or alternatively as excitations of the mid-gap states (polarons or bipolarons) [205]. At shorter wavelengths (inset in Figure 2.15a) there are two pronounced absorbance peaks at 193 and 225 nm and a broader shoulder at slightly longer wavelengths (250-280 nm), which can be attributed to the $\pi - \pi^*$ transitions of the benzene rings of PSS.

As discussed in Section 2.1.2, the generation of charged states (polarons and bipolarons) along the polymer backbone is coupled to the formation of energy levels within the energy gap. As a consequence, the absorption spectrum of PEDOT and PEDOT:PSS strongly depends on the PEDOT oxidation state. Figure 2.15 depicts the optical absorption spectra for PEDOT:PSS films deposited on ITO as electrode in an electrochemical cell as a function of photon energy at different bias [206]. The peak at 2.2 eV (560 nm), corresponding to the $\pi - \pi^*$ transitions in neutral PEDOT, reduces as the applied bias is increased, while the absorption at lower energies increases due to the formation of polaronic (1.4 eV) and bipolaronic (0.5 eV) states. These new energy levels are broadened due to the amorphous nature of the film, the length distribution of PEDOT segments, and the interactions of charge carriers at high doping levels [146].

2.3.5 Electrical conductivity

PEDOT:PSS is an intrinsically conducting polymer with metal-like properties. The thiophene rings form a π-system, being heavily p-doped. Owing to the oxidative polymerization reaction one net free positive charge per three to four tiophene rings is created. PSS does not contribute to charge transport directly, but acts as a template to keep PEDOT in the dispersed state and provides film-forming properties. The dissociated sulfonate groups balance the charges of the cationic PEDOT by forming a stable salt [146].

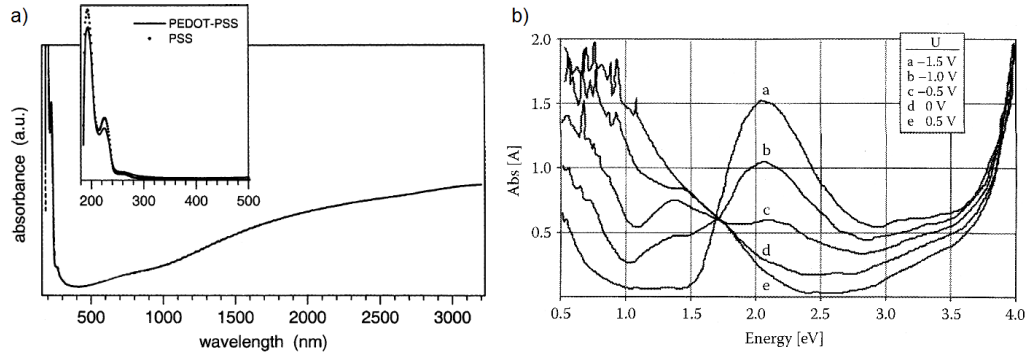

Figure 2.15: (a) Absorbance of a thin film of PEDOT:PSS (110 nm). In the inset, absorbance of PEDOT:PSS and PSS in the spectral range from 185 to 500 nm. Adapted from [205]. (b) Optical absorption spectra of a PEDOT:PSS electrode in an electrochemical cell for different applied voltages. Adapted from [206].

The conductivity, σ, is defined by the product of elemental charge e, charge carrier mobility, μ, and density of charge carriers, n. In case of hole- and electron-conducting materials, both charge carriers species contribute according to the equation [163]:

$$\sigma = e \cdot \mu_p \cdot n_p + e \cdot \mu_n \cdot n_n \tag{2.9}$$

In case of PEDOT:PSS, only holes contribute to the charge transport. Injected free electrons immediately recombine at oxidized PEDOT sites, hence the transport of electrons does not contribute to the overall current [146]. The density of holes in PEDOT:PSS can be simply calculated using a geometrical consideration. For highly conductive PEDOT:PSS, the ratio of PEDOT to PSS is 1:2.5 by weigth. The density of solid films is approximately 1 g/cm^3. Owing to the molecular weigth of the monomeric units of PEDOT and PSS, that is 140 and 182 g/mol respectively, the density of EDOT monomers can be estimated to be approximately 10^{21} cm^{-3}. From electrochemical measurements, the level of oxidation per monomer unit is known to be approximately one charge per three EDOT units. Consequently, the density of holes in PEDOT:PSS films can be estimated to be $n_p = 3 \cdot 10^{20}$ cm^{-3}. For highly conductive films a conductivity of 1000 S/cm has been obtained. The hole mobility in PEDOT:PSS can be calculated to be approximately $\mu_p = 20$ cm^2/Vs for the given conductivity and the estimated hole

density.

Following the concept of charge transport in amorphous organic semiconductors, the conduction mechanism of conjugated polymers is commonly discussed in terms of charge hopping between adjacent sites. Segments of conjugated polymers are preferentially forming electronic active sites due to their ability of being easily oxidized and reduced. Charge transport between adjacent sites depends on their relative energetic position, distance and orientation [146].

One of the first studies on the conductivity in PEDOT:PSS films has been made by Aleshin *et al.* [169]. They studied the conductivity and magnetoresistance of PEDOT:PSS as a function of temperature, and found that both parameters increase with increasing temperature. The dependence of conductivity was discussed using Mott's variable range hopping (VRH) model [179]:

$$\sigma(T) = \sigma_0 \exp\left[-\left(\frac{T_0}{T}\right)^{\gamma}\right] \tag{2.10}$$

where σ_o is the conductivity at infinite temperature, $k_b T_0$ is the energy barrier between localized states and the exponent γ is equal to $1/(1 + D)$, D being the dimensionality of the system assuming that the density of the states near the Fermi level $N(E_f)$ is either constant or varies smoothly with energy. Hence, for 3-D systems $\gamma = 1/4$ and $T_0 = 16/[k_b N(E_f) L^3]$, while for 1-D systems $\gamma = 1/2$ and $T_0 = 16/[k_b N(E_f) L_{\parallel} L_{\perp}^2]$. Here, L is the localization length, defined as the distance from a site for the electron wave function to decay to $1/e$ of its value [163]. The parallel and perpendicular terms are referred to the direction of the system [179].

There have been several reports focusing on the temperature dependence of the conductivity of PEDOT:PSS [169, 207, 208]. All the results are discussed within the framework of the VRH model and are summarized in Table 2.2. From these data, the following results can be inferred:

- The pH value of the solution affects conductivity. Highest conductivities are obtained for low pH values.
- Conductivity increases with temperature within the entire regime observed (0 - 300 K).

pH	Conductivity enhancing agent	σ(300K) (S/cm)	T_0 (K)	γ	Reference
0	/	12	720	0.48	[169]
1.23	/	20.6	610	0.52	[169]
2.0	/	6	910	0.46	[169]
4.31	/	0.092	2800	0.45	[169]
5.2	/	0.077	3400	0.43	[169]
12.2	/	0.055	3500	0.44	[169]
~ 2	/	0.4	2927	~ 0.5	[207]
~ 2	DMSO	143	1153	~ 0.5	[207]
~ 2	EG	200	903	~ 0.5	[207]
~ 1.8	/	0.0011	3.2×10^6	0.25	[208]
~ 1.8	Sorbitol (5 wt%)	4.18	2720	0.53	[208]
~ 1.8	Sorbitol (10 wt%)	5.2	2314	0.52	[208]

Table 2.2: Temperature dependence of PEDOT:PSS films conductivity, discussed in terms of the Variable Range Hopping model.

- Almost all data are best modeled with an exponent $\gamma = 0.5$, except when conductivity is very low. This suggests that conductivity is of the 1-D type for highly conductive samples and of the 3-D type for the low conductive ones.

- The parameter T_0 decreases with increasing conductivity. This is in accordance with the VRH model claiming that the localization length L will increase as conductivity increases.

Finally, the distribution of PEDOT:PSS particles in solution determines the morphology of thin films and consequently their conductivity. In fact, the addition of water miscible high boiling solvents like ethylene glycol (EG), dimethyl sulfoxide (DMSO) or sorbitol can boost conductivity by two to three orders of magnitude owing to morphological changes in the film [192]. This procedure is known as *secondary doping*.

2.3.6 Conductivity enhancing agents

The term "secondary doping" was introduced by MacDiarmid and Epstein, referring to an additive that further increases the conductivity of an already doped

polymer by up to several orders of magnitude [209]. While primary doping has a reversible effect, which is exploited as an example in OECTs to switch the device between on and off states (see Section 1.3.1), the effect of secondary doping is permanent and remains even when the additive is removed [146]. However, since secondary doping does not actually change the doping level of PEDOT [210], these additives are often referred to as *conductivity enhancing agents* (CEA) instead of secondary dopants [211].

Conductivity enhancing agents are usually added to the PEDOT:PSS water dispersion prior to deposition, but can also be used in a post-treatment step after film formation. An heating step, even if not compulsory, has been proved to further increase the film conductivity [212]. The heat treatment also has the effect of removing many of the CEA from the final film.

An extensive list of chemicals presented in literature in combination with PEDOT:PSS and their effects on conductivity can be found in Reference [146]. The most effective substances reported (which are, indeed, also the most used for the treatment of PEDOT:PSS) are dimethyl sulfoxide (DMSO), copper(II) chloride, ethylene glycol (EG), and dodecylbenzenesulfonate (DBSA), corresponding to an increase in conductivity of several orders of magnitude. It has also been reported recently that the conductivity of PEDOT:PSS films can be increased up to about 4000 S/cm, a value comparable to that of indium-tin oxide, upon a post-treatment with sulphuric acid [213]. However, the use of sulphuric acid strongly limits the application to bioelectronics. More than a single parameter, it has been observed that a combination of different factors, namely high solubility in water, high boiling point, and high dielectric constant, is required to a good secondary dopant for PEDOT:PSS [212].

Although some of these additives have been used for more than a decade for the processing of PEDOT:PSS, their role on PEDOT:PSS increase in conductivity is still under debate, and many hypotheses have been formulated [192, 207, 212, 214]. A first important observation is that the increase in conductivity is not proportional to the additive concentration [212, 215], as shown in Figure 2.16a. After reaching a limit concentration, further additions do not correspond to an increase in conductivity anymore. Although the initial concentration of the CEA in the processable solution is quite low (usually no more than a few % in vol-

ume), their concentration increases during the drying of the film thanks to their lower vapor pressure compared to water [212]. As a result, a small quantity is enough for affecting the whole film. Another important observation is that after film formation, the presence of the secondary dopant is not necessary to maintain the enhancement in conductivity [146]. From these findings it appears quite clear that the effect of CEA takes place during film formation (*i.e.* during the solvents evaporation).

Changes are observed both for the surface and for the bulk of the material. On the surface, while for a pristine PEDOT:PSS sample PSS is found in excess, the surface composition becomes more similar to the bulk when a secondary dopant is used, with an increase of the PEDOT to PSS ratio [212]. This finding is confirmed from STM [216] and AFM measurements [212], wich show respectively an increase in more conductive and harder areas on the surface of PEDOT:PSS for increasing additive concentration. However, since conductivity is a property which involves the whole bulk of the material, these changes must not be limited to surface only, but extend to the bulk composition.

When a solid film of PEDOT:PSS is deposited from aqueous dispersion, polymer chains do not reach an equilibrium state, but are instead "frozen" in nonequilibrium [208]. The presence of the high-boiling solvent allows the blend to rearrange, which means that the PEDOT olygomers find a new thermodynamically favorable position. The same mechanism can explain the increase in conductivity observed upon thermal annealing of the films after deposition. Since the polymer chains are charged, it is reasonable to assume that the high polarity of the secondary dopant is necessary to interact with the ionic charges of the polyanion and the polycation [146]. This process has also been described as a screening effect between $PEDOT^+$ and PSS^- chains, which allows the chains to orientate [207, 214]. After this rearrangement, even if the CEA is then thermally removed, the film remains in its new thermodynamically favorable state [208]. The increase of crystallinity of the PEDOT:PSS film however is not pronounced enough for being observed in x-ray diffraction spectra [214].

Charge transport in PEDOT:PSS films takes place through a hopping mechanism. The charge is transported between PEDOT-rich conductive regions, separated by insulating, PSS-rich regions, which represent the main obstacle to trans-

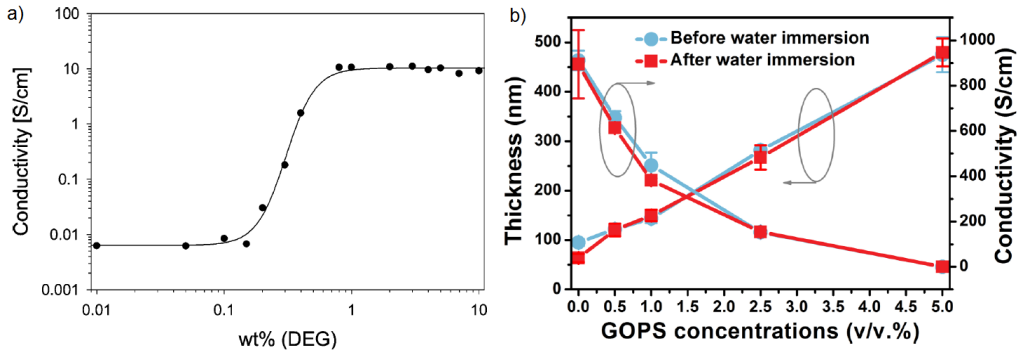

Figure 2.16: (a) Plot of the conductivity of a PEDOT:PSS film versus the amount of diethylene glycol introduced to the water emulsion [212]. (b) Thickness (left *y* scale) and conductivity (right *y* scale) change of PEDOT:PSS films with increasing cross-linker (GOPS) concentration before and after water immersion [215].

port electric current within the material [208]. As a consequence, an increase in the ordering of the PEDOT segments in the film results in the formation of highly conductive pathways, which are created only if the high boiling solvent is present long enough to allow the thermodynamical rearrangement to occur. Eventually, this organization on the nanometer scale is responsible for the observed macroscopic conductivity increase.

A different class of additives is composed by cross-linkers. These substances enhance the formation of covalent bonds between polymer chains, changing their physical properties. Due to the high hidrophilicity of PSS, the exposure of PEDOT:PSS to water is usually followed by delamination of the film. It has been reported that the stability of PEDOT:PSS films in aqueous solutions can be improved by the addition of the cross-linker 3-glycidoxypropyltrimethoxysilane (GOPS) [88, 215]. As shown in Figure 2.16b, although the addition of GOPS induces a good mechanical and electrical stability, it also yields thicker films with lower conductivity. Indeed, thick films likely contain a larger amount of PSS units, which are not removed by water due to the presence of the GOPS cross-linker. As a consequence, the excess of hydrophilic PSS would absorb larger amounts of water and cause irreversible morphological changes in the film, thus resulting in a decrease in conductivity [215, 217].

Chapter 3

OECTs Working Principles

3.1 Device Model

First demonstrated by White *et al.* in 1984 [218], organic electrochemical transistors (OECTs) are receiving renewed attention [29, 60], in particular as sensors for the detection of chemical and biological analytes, as shown in Section 1.3.1. An OECT consists of a conductive channel, which is basically a thin film of a semiconducting polymer in its doped (conducting) state deposited onto a supporting substrate; source (S), drain (D) and gate (G) contacts, which are usually metallic, and finally an electrolyte medium in contact with the channel and the gate (see Figure 3.1a). These devices exploit the reversible doping/dedoping effect induced on the conducting polymer-based conductive channel by the application of a gate voltage V_g through an electrolyte solution. Thanks to the high difference in conductivity between doped and undoped states of conjugated polymers [119], the effect of the gate voltage is to induce a pronounced switch between an "on" (*i.e.* conductive) and an "off" (*i.e.* non conductive) state of the polymer. This change in conductivity can be observed by measuring the modulation of the current flowing between source (grounded) and drain electrodes, I_d, generated by an applied source-drain voltage V_d, upon the application of the gate voltage.

In general, OECTs can work in accumulation or depletion mode. However, in most of the applications found in literature OECTs are used in depletion mode, meaning that the conducting polymer is used in its pristine doped state, and is

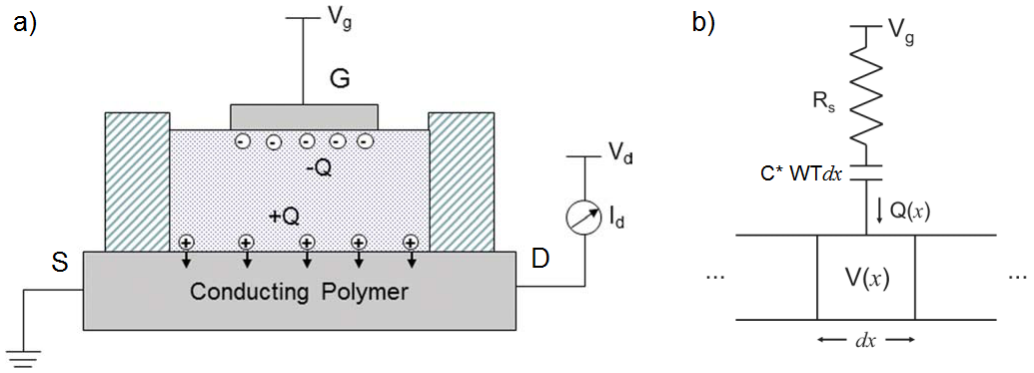

Figure 3.1: (a) Schematic of an OECT cross-section (case $V_g > 0$). (b) Modelization of an OECT through the coupling of ionic and electronic circuits. Adapted from [219, 220].

then switched to undoped by the application of V_g during the operation. Thus, in this Chapter the working principles of an OECT are described for depletion mode. Furthermore, because most of conducting polymers are hole transporters, the nomenclature used in this analysis is referred to p-type doping, with negligible contribution to electrical conductivity from electrons and anions. However, the same method can be applied to n-doped materials with only minor modifications. Being the semiconductor p-doped, the application of a positive gate voltage (relative to ground, *i.e.* the source electrode) causes the injection of cations from the electrolyte into the organic semiconductor film. This in turn de-dopes the organic semiconductor and thus decreases the source-drain current I_d, as shown in Figure 3.2a.

OECTs can be modeled as the sum of two electrical circuits, one accounting for the electronic transport within the organic semiconductor, and the other regarding the ionic transport of ions through the electrolyte and across the electrolyte/semiconductor interface (Figure 3.1b) [220].

3.1.1 Electronic circuit

The electronic circuit is used to describe hole transport in the organic semiconductor between source and drain electrodes, which is approximated by a resistive

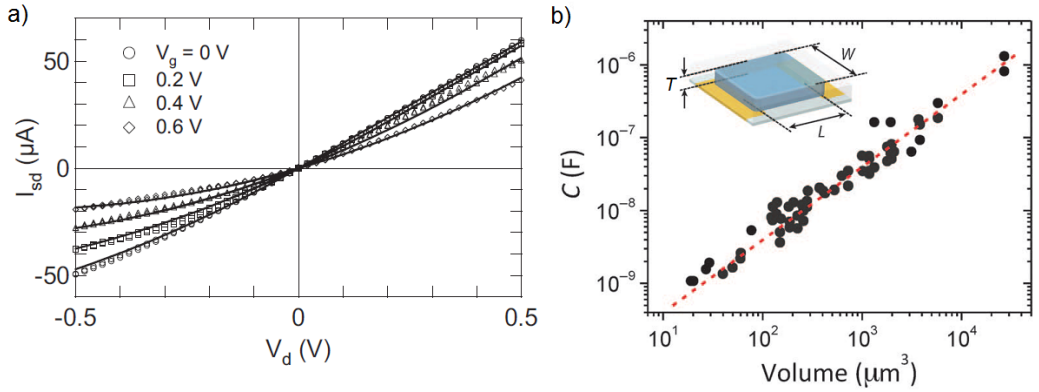

Figure 3.2: (a) Experimental steady-state current-voltage characteristics for a PEDOT:PSS OECT fitted to modeled steady-state characteristics (solid lines). (b)PEDOT:PSS capacitance for devices of varying geometry. Inset: channel dimensions. Adapted from [77, 220].

element following Ohm's law:

$$J(x) = q\mu p(x)\frac{dV(x)}{dx} \tag{3.1}$$

where J is the current flux, q is the elementary charge, μ is the hole mobility, p is the hole density, and dV/dx is the electric field through the semiconductor. In order to simplify the calculations and derive an alytical solution, μ is taken as a constant (neither dependant from the electrical field nor from carrier concentration).

Since we are considering a hole conductor working in depletion mode, we are interested in the de-doping of the organic semiconductor that takes place when a positive gate voltage is applied. In such a case, cations are repelled from the gate electrode into the organic semiconductor, and to maintain charge neutrality, for each ion entering the film a hole extracted for the source is not replaced from injection at the drain electrode. If we take into account that each injected cation compensates one acceptor, we can then write the concentration of charge carriers in a volume v of the organic material as:

$$p(x) = p_0\left(1 - \frac{Q}{qp_0v}\right) \tag{3.2}$$

where p_0 is the hole density in the organic semiconductor before the de-doping process and Q is the total charge of the cations injected in the organic film from the electrolyte. To simplify the calculations, two further assumptions have to be made: negative ions are assumed to have no effect on the conductivity of the organic semiconductor, and charge density is assumed to be uniform across the thickness of the organic semiconductor, an approximation that limits the validity of this model to thin films [220].

3.1.2 Ionic circuit

The ionic circuit accounts for the motion of ions through the electrolyte and the charge transfer and accumulation at the gate electrode-electrolyte and semiconductor-electrolyte interfaces. As a result, it can be modeled as a resistor (R_s) and a capacitor (C_d) in series [221]. The resistor describes the conductivity of the electrolyte and is a measure of its ionic strength, while the capacitor is composed by the series of two capacitors corresponding to the polarization occurring at the interfaces just mentioned. Because of the high capacitance of conducting polymers [222], many device properties such as response time and sensitivity will depend on the gate capacitance, which is affected by the geometry and the material of the electrode. As described in Section 1.3.1, the current flowing at the gate electrode is made up of two contributions, the first coming from the capacitive charging of an electrical double layer at the electrolyte-gate interface (non-Faradaic process), and the second coming from electrochemical reactions taking place at the gate electrode (Faradaic process). The model here reported only considers a non-Faradaic regime of operation [72]. The Faradaic contribution to the operation of the OECT is discussed in Section 3.4.1.

The ionic circuit is thus represented by an RC circuit, and the application of a gate voltage is then followed by the charging of the capacitor C_d:

$$Q(t) = Q_{tot}[1 - \exp(-t/\tau_i)] \tag{3.3}$$

where $Q_{tot} = C_d \Delta V$ is the total charge passing through the circuit, ΔV is the voltage applied across the electrolyte, and the ionic transit time is described by

$\tau_i = C_d R_s$. It has been recently demonstrated by Rivnay *et al.* that for organic semiconductors which are permeable to ions, such as PEDOT:PSS and other conjugated polymers, capacitance per unit area, which is usually considered for modeling OFET behavior, is not an effective parameter for describing OECT operation. In their work, a strong correlation between channel capacitance and thickness is observed (Figure 3.2b) and a volumetric capacitance, $C^* = C_d/v$, where v is the volume of the channel, is suggested as a more suitable parameter [77]. From the same experimental results, it is observed that the zero offset in the linear fit of C *vs.* v suggests the absence of ion accumulation at the surface, indicating a negligible ion injection barrier from the electrolyte into the conducting polymer film.

3.2 Steady-state Behavior

If we take hole mobility as a constant, the electrical behavior of the organic semiconductor only depends on a change in its carrier concentration. In order to obtain a solution for the OECT behavior, the effective dopant density (Eq. 3.2) must be spatially known throughout the organic film. In the following discussion, the geometrical dimensions of the organic film are named L (lenght), W (width) and T (thickness), as shown in the inset of Figure 3.2b, with the spatial variable x ranging from 0 to L along the length of the channel. If a differential fraction of the film, dx, is considered in position x, then the charge injected in the corresponding volume $WTdx$ by a gate voltage V_g can be expressed as:

$$Q(x) = C^*(V_g - V(x))WTdx \tag{3.4}$$

where $V(x)$ is the spatial voltage profile within the organic film. By combining Equations 3.1, 3.2, and 3.4 it is possible to obtain the governing equation for OECT characteristics at steady-state [220]:

$$J(x) = q\mu p_0 \left(1 - \frac{Q(x)}{qp_0 v}\right)\frac{dV(x)}{dx} = q\mu p_0 \left(1 - \frac{V_g - V(x)}{V_p}\right)\frac{dV(x)}{dx} \tag{3.5}$$

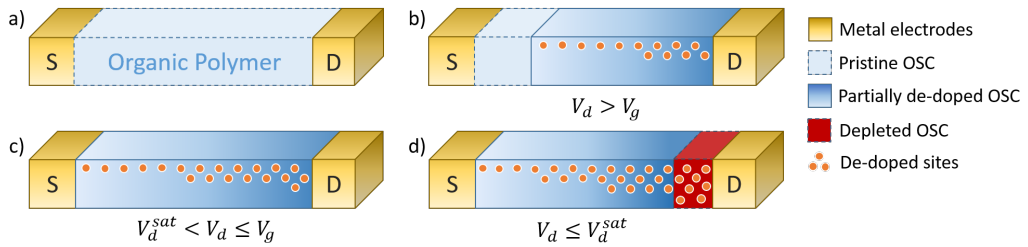

Figure 3.3: Doping levels in a p-type OECT channel for $V_g > 0$ (depletion mode). (a) Scheme of the channel in its pristine (fully doped) state. (b) For $V_d > V_g$, the gating affects the doping of the organic semiconductor only where $V(x) < V_g$. (c) For $V_d^{sat} < V_d \leq V_g$, cations are injected all along the channel. (d) For $V_d \leq V_d^{sat}$, in the channel area where $V(x) \leq V_d^{sat}$ the density of injected cations fully counterbalances the hole density of the organic semiconductor, generating a depletion region.

where V_p is the pinch-off voltage (also called threshold voltage), defined as $V_p = qp_0/C^*$, *i.e.* the voltage required to accumulate a charge density equal to the intrinsic dopant density of the semiconductor.

At steady-state, $J(x)$ must be spatially constant along the channel, so for an ideal geometry with constant cross-section of the semiconductor it can be expressed as $J(x) = J = I/WT$. Thanks to this condition, the source-drain current I_d can be obtained from Eq. 3.5 for various regimes of operation, keeping in mind that $0 \leq |V(x)| \leq |V_d|$ and that de-doping only occurs when $V(x) < V_g$. If I_d is known, it is possible to extract the transconductance g_m of the device, defined as $g_m = \partial I_d/\partial V_g$. Transconductance is the figure-of-merit that quantifies the efficiency of the gating effect.

Different regimes for I_d can be identified depending on the values of V_g and V_d. Firstly, the case $\mathbf{V_g > 0}$ is considered (Figure 3.3).

$V_d > V_g$**:** When the drain voltage is higher than the gate voltage, de-doping occurs only in the region of the device where $V(x) < V_g$, while in the region where $V(x) > V_g$, $p(x) = p_0$ (Figure 3.3b). This regime is described by:

$$I_d = G\left(V_d - \frac{V_g^2}{2V_p}\right) \tag{3.6}$$

where the current is linear with drain voltage. The onset of linear behavior

occurs when $V_d = V_g$. Transconductance then becomes equal to:

$$g_m = -\mu C^*(WT/L)V_g \tag{3.7}$$

independent from V_d and linear with V_g.

$0 < V_d < V_g$**:** In this regime, partial de-doping occurs through all the channel length (Figure 3.3c), and the current flowing between source and drain electrodes can be written as:

$$I_d = G\left(1 - \frac{V_g - 1/2V_d}{V_p}\right)V_d \tag{3.8}$$

where $G = q\mu p_0 WT/L$ is the conductance of the organic semiconductor film. The transconductance

$$g_m = -\mu C^*(WT/L)V_d \tag{3.9}$$

is independent from V_g and linearly depends on V_d.

$V_d < 0$**:** For negative drain voltages, those portions of the organic film where the local density of injected cations becomes equal to the intrinsic dopant density can be completely de-doped (Figure 3.3d). This condition is reached in proximity of the drain electrode when $V_d = V_d^{sat} = V_g - V_p$, that is to say when the potential difference between gate electrode and drain electrode (the position in the channel at lowest potential with respect to the gate) equals the pinch-off voltage. If the drain voltage goes below V_d^{sat}, the area of the channel where $V(x) < V_d^{sat}$ will be depleted, with a slight and gradual increase in the extension of the depletion region towards the source electrode for decreasing V_d. However, in the limit of long channel, this widening of the depletion region is negligible, and for $V_d \leq V_d^{sat}$ the current saturates to:

$$I_d^{sat} = -G\frac{(V_p - V_g)^2}{2V_p} = -G\frac{V_d^{sat2}}{2V_p} \tag{3.10}$$

so the drain current will only depend on the saturation drain voltage for a

particular gate voltage. At saturation, transconductance is then given by:

$$g_m = -\mu C^*(WT/L)(V_p - V_g) \tag{3.11}$$

Complete de-doping could hypothetically be also achieved at $V_d > 0$, occurring at first when $V_g = V_p$, however this condition is typically not of significant interest because of the high gate voltages required [220].

For the case $\mathbf{V_g < 0}$, two regimes can be observed. If $V_g < V_d$, cations are not injected from the electrolyte into the film, so de-doping does not occur and the current I_d is linear with V_d and independent from V_g. If $V_g > V_d$, de-doping only occurs in the region of the device where $V(x) < V_g$, leading to an expression analogous to Equation 3.6.

3.3 Transient Behavior

As OECTs can be modeled using a combination of an ionic and an electronic circuit, their transient behavior will be determined by an ionic and an electronic effect: the injection of a cation from the electrolyte into the organic film and the removal of a hole at the drain electrode (considering $V_d < 0$, as in many sensing applications), respectively. In order to keep the calculation tractable, it is convenient to neglect the spatial variation of the drain voltage and hole density, considering an average ionic current and hole density along the channel. The combination of the current associated with the removal of holes due to de-doping and the current due to the drain voltage (Ohm's law) can be expressed as:

$$J(t) = q\mu p(t)\frac{V_d}{L} + qfL\frac{dp(t)}{dt} \tag{3.12}$$

where f is a proportionality constant accounting for the spatial non-uniformity of the de-doping process, comprised between 0 and 0.5 [220].

Keeping in mind that for ideal geometrical conditions $J(t) = I(t)/WT$ and combining Equations 3.12 and 3.2, the transient drain current can be made ex-

plicit:

$$I(t) = G\left(1 - \frac{Q(t)}{qp_0v}\right)V_d - f\frac{dQ(t)}{dt} \tag{3.13}$$

where $Q(t)$ is the transient charge (ions) injected from the electrolyte. For simplicity, the transient behavior is only described for the case where de-doping occurs all along the organic film without saturation effects. A constant gate potential is considered, and an average voltage drop between the organic film and the gate electrode is chosen, $\Delta V = V_g - 1/2V_d$. Using these assumptions and Equation 3.3, the transient behavior for a simplified OECT can be described as:

$$I(t, V_g) = I_{ss}(V_g) + \Delta I_{ss}\left(1 - f\frac{\tau_e}{\tau_i}\right)\exp(-t/\tau_i) \tag{3.14}$$

where $I_{ss}(V_g)$ is the steady-state source-drain current at a gate voltage V_g and ΔI_{ss} is the difference between the base current and I_{ss} for an applied V_g. In this Equation, two time constants, τ_e and τ_i, are introduced to account for the effectiveness of electronic (holes) and ionic (cations) transport, respectively. As shown in Figure 3.4a, the decrease in the source-drain current upon the application of a positive gate voltage can follow a monotonic decay or a spike-and-recovery shape, according to the ratio between electronic and ionic time scales, $f\tau_e/\tau_i$. Qualitatively, a monotonic decay ($f\tau_e < \tau_i$) indicates that hole transport and extraction is sufficiently fast and the transient response is thus controlled from the ionic injection process. Conversely, a spike-and-recovery indicates that hole transport in the organic film occurs at a relatively slow rate and the transient current is dominated by hole extraction.

The characteristic electronic time constant (τ_e) is a measure of the hole transit time, and is related to hole mobility, applied drain voltage and channel length, $\tau_e = L^2/(\mu V_d)$ [220]. The characteristic time constant for ionic transport in the electrolyte (τ_i), as described in the electronic circuit model, is determined by the solution resistance and capacitance of the ionic double layer, $\tau_i = R_sC_d$, which can be estimated as $\tau_i \sim l/C^{1/2}$, where l is distance between the organic film and gate electrode and C is the ionic concentration [221]. Consequently, the time constant ratio appearing in Equation 3.14 can be expressed as $\tau_e/\tau_i \sim L^2C^{1/2}/(l\mu V_d)$. From this relationship, it is apparent that the geometrical configuration of the device,

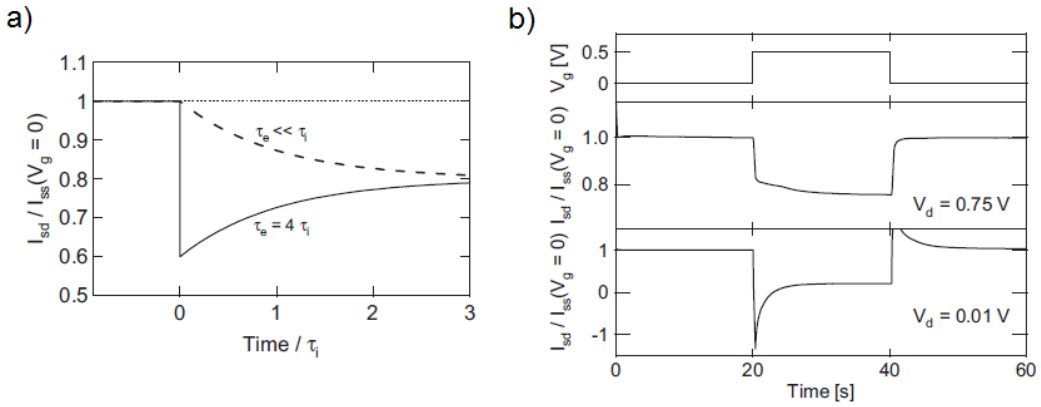

Figure 3.4: (a) Modeled source-drain current transient for a constant drain voltage with an arbitrary ΔI and fixed geometric factor ($f = 1/2$). Transient demonstrates two different possible characteristics responses, monotonic decay ($\tau_i > f\tau_e$, dashed line) or spike-and-recovery ($\tau_i < f\tau_e$, solid line). (b) Experimental source-drain current transient with constant applied gate voltage. Two characteristic responses can be observed with variation in V_d. Adapted from [220].

such as the organic film length or the distance between channel and gate electrode, together with the drain voltage (Figure 3.4b), are responsible for the character of the transient response [220]. The effect of the geometry of OECTs on their effectiveness when used as sensors will be discussed in Section 3.4.2.

3.4 Sensing with OECTs

3.4.1 Electrochemical sensing

The model discussed in Section 3.2 does not take into account the effect of electrolyte composition and its ionic strength on the OECT operation. However, OECTs have been succesfully used for the sensing of various analytes, such as glucose [81–83], ascorbic acid [76], adrenaline [84], dopamine [86,87], and many other molecules [70]. Indeed, the presence of a reactive species in the electrolyte solution generates a shift in the electrochemical potential of the solution, which can be seen as a shift in the gate voltage, $V_g^{eff} = V_g + V_{offset}$, where V_g^{eff} is the *effective* gate voltage acting on the channel, while V_{offset} is an offset voltage that is dependent on the analyte concentration (Figure 3.5) [223].

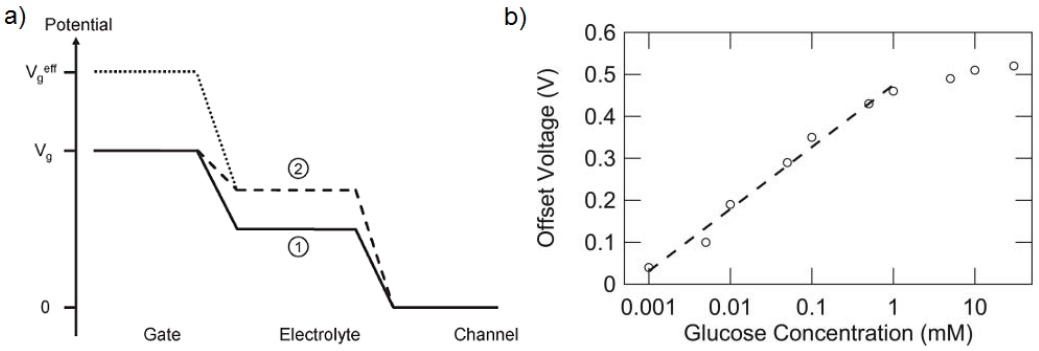

Figure 3.5: (a) Potential diagram of an OECT. In the absence of analytes (solid line), the electrolyte potential (1) is determined by the relative capacitances at the gate and channel interfaces. When an analyte is added to the solution (dashed line), the electrolyte potential (2) is increased according to the Nernst equation. The effective gate voltage (dotted line) is the gate voltage required to produce the same electrolyte potential (2) in the absence of Faradaic effects. (b) Dependence of the offset voltage on glucose concentration. The dashed line is a fit to the experimental data up to a glucose concentration of 1 mM. Adapted from [223].

An example of the dependence on analyte concentration of V^{offset} is shown for a PEDOT:PSS OECT with a Pt gate electrode for increasing glucose concentrations in Figure 3.5b. The logarithmic trend points out that the change of the electrolyte electrochemical potential follows Nernst equation:

$$E_N = E_0 + \frac{kT}{ne} \ln\left(\frac{[Ox]}{[Red]}\right) \tag{3.15}$$

where $[Ox]$ and $[Red]$ are the concentrations of oxidized and reduced species, respectively, E_0 is the formal potential, k is Boltzmann's constant, T is the temperature, e is the electronic charge, and n is the number of electrons transferred during the reaction [221]. It is worth noting that an OECT based on a different organic semiconductor may not show Nernstian relationship since the solid/electrolyte interface may have different properties [73]. The physical meaning of V^{offset} can be understood by comparing the OECT with conventional electrochemical sensors. While in conventional electrochemistry a change in the working electrode potential is measured with respect to a constant reference electrode, in an OECT the gate voltage is fixed, and the electrolyte potential varies relatively to that of the

gate, as shown in Figure 3.5a.

The electrolyte potential, V_{sol}, depends on the capacitances associated to the gate-electrolyte and channel-electrolyte interfaces [219, 223]. The total charge Q injected at the transistor channel can be written as the sum of smaller charges stored in a differential volume $dv = WTdx$:

$$Q = \sum C^*_{ch} WT dx \, (V_{sol} - V(x)) \tag{3.16}$$

where C^*_{ch} is the capacitance per unit volume of the channel, $C^*_{ch} = C_{ch}/v$, as described in Section 3.2, and W and T are, respectively, the channel width and thickness. For dx small enough, this Equation can be approximated with:

$$Q = C_{ch} V_{sol} - C^*_{ch} WT \int_{x=0}^{L} V(x)\, dx \tag{3.17}$$

where L is the total length of the channel. Two capacitors in series accumulate the same charge Q, so the same charge can also be written referring to the gate electrode interface:

$$Q = C_g \, (V_g - V_{sol}). \tag{3.18}$$

By combining Equations 3.17 and 3.18 the dependence of V_{sol} on the capacitances of the system can be finally made explicit:

$$V_{sol} = V_g \frac{C_g}{C_g + C_{ch}} + \frac{C^*_{ch} WT}{C_g + C_{ch}} \int_{x=0}^{L} V(x)\, dx \tag{3.19}$$

which for $V_d \ll V_g$ (*i.e.* negligible variation of $V(x)$ along the channel) can be simplified as:

$$V_{sol} = \frac{V_g}{1 + \gamma} \ \text{(no analyte)} \tag{3.20}$$

where $\gamma = C_{ch}/C_g$.

When a redox-active analyte is added to the electrolyte, it exchanges charge with the the gate electrode (Faradaic regime), shifting the electrolyte potential at a new value described by the Nernst equation [223]:

$$V_{sol} = \frac{V_g}{1 + \gamma} + \frac{kT}{2e} \ln A + \text{const.} \tag{3.21}$$

where A is the analyte concentration, and the constant contains the concentrations of protons and oxygen involved in the redox reaction (which are taken as constant during the process) and the formal potential E_0. This change in the electrolyte potential is illustrated in Figure 3.5a with a dashed line. We can then define an effective gate voltage:

$$V_g^{eff} = V_g + (1+\gamma)\frac{kT}{2e}\ln A + \text{const.} \tag{3.22}$$

so that the electrolyte potential can now be expressed in the same form as Equation 3.20,

$$V_{sol} = \frac{V_g^{eff}}{1+\gamma} \text{ (analyte)}. \tag{3.23}$$

V_g^{eff} is the equivalent voltage that needs to be applied in the absence of Faradaic effects at the gate electrode in order to result in the same source-drain current, as illustrated in Fig. 3.5 (dotted line). By comparing $V_g^{eff} = V_g + V_{offset}$ with Equation 3.22, it is clear that the offset voltage is represented by the last two terms in this Equation and describes the Faradaic contribution to the effective gate voltage. Following Nernst equation, this contribution shifts the electrochemical potential of the solution and is scaled by the capacitance ratio.

In conclusion, the shift in the electrolyte potential due to the Faradaic contribution of a redox-active analyte can be taken into account by substituting the gate voltage with an effective gate voltage, V_g^{eff}, in the non-Faradaic model described in Section 3.2. The incorporation of the effective gate voltage in this model yields a quantitative relationship between the source-drain current and the analyte concentration. As an example, in the saturation regime the source-drain current can be expressed by combining Equations 3.10 and 3.22:

$$I_d^{sat}(A) = -\frac{G}{2V_p}\left[V_g + (1+\gamma)\frac{kT}{2e}\ln A + C\right]^2 \tag{3.24}$$

where A is the analyte concentration and the constant C contains the difference between the constant term of Equation 3.22 and the pinch-off voltage V_p. From this Equation, the sensitivity of the device can be calculated as $\partial I_d^{sat}/\partial A$.

3.4.2 Influence of the geometry

Thanks to the electrochemical gating, in OECTs the geometrical configuration of the gate electrode relative to the channel can be tuned with only small limitations. This allows planar device architectures in which the area, shape, and relative position of the channel and gate electrode can be varied independently [74].

As shown in Equation 3.24, the effect of the presence of an analyte on the current flowing in the channel of an OECT depends on the ratio between the channel-electrolyte capacitance and the gate-electrolyte capacitance, γ. The gate electrode is usually metallic, so its capacitance only depends on the area exposed to the electrolyte. Regarding the channel capacitance, it was shown recently to depend on the volume of the conjugated polymer used, PEDOT:PSS [77]. This can be explained by considering that PEDOT:PSS is porous: although a double layer on the surface still exists, the effective area of the double layer scales with the volume of the channel, and thus is much bigger than the physical area of the film [73]. As a consequence, the sensitivity of the transistor to analytes is related to the materials chosen, the ratio of the channel to gate area [74,75,219], and also to the thickness of the semiconductor channel [76,77]. Since no ion penetration takes place at the metal gate electrode, the ratio γ can be tuned by changing the gate area and the channel volume. For a fixed channel thickness, γ is then controlled by the ratio A_{ch}/A_g.

A typical quantity used to assess the sensing capability of a transistor is the normalized current modulation, $\Delta I/I_0 = |I - I_0|/I_0$, where I is the *off* current ($V_g > 0$) and I_0 is the *on* current ($V_g = 0$). A plot of $\Delta I/I_0$ for different concentrations of H_2O_2 and different γ is shown in Figure 3.6a [74] for a PEDOT:PSS OECT with a Pt gate electrode. For low concentrations, a background $\Delta I/I_0$, which is independent of concentration, is measured. This regime is followed by a second one in which $\Delta I/I_0$ increases with concentration, and the sensitivity changes with γ. Finally, a third regime is observed, in which $\Delta I/I_0$ saturates and does not increase anymore with concentration. This behavior was proven not to depend on the absolute area of the electrodes, but only on their ratio [74].

Several observations can be made from the data reported in Figure 3.6a. At first, the value of $\Delta I/I_0$ at low concentrations decreases with γ, which means

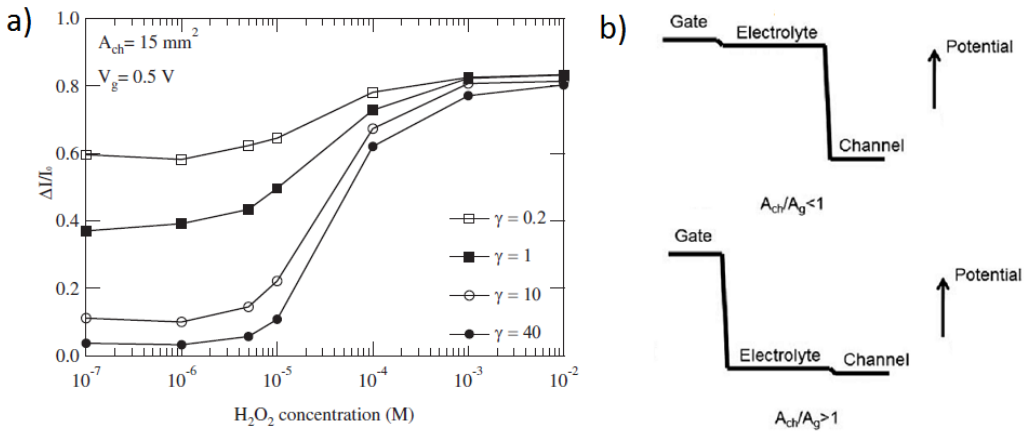

Figure 3.6: (a) Response of OECTs with different values of γ as a function of H_2O_2 concentration for V_d 0.2 V and V_g 0.5 V. (b) Potential distribution between the gate electrode and the channel for two device geometries. Adapted from [74, 219].

that devices with small gates show a small current modulation in the absence of an analyte. Then, the sensitivity, *i.e.* the slope of the curve at intermediate concentrations, increases with γ, which means that devices with small gates are more sensitive. At high concentrations, $\Delta I/I_0$ saturates at the same current and for the same concentration independent of γ. Finally, the detection range does not seem to depend on the channel/gate area ratio.

These results can be understood by considering the two working regimes of an OECT, which are the Faradaic and non-Faradaic regimes previously described and summarized in Equation 3.21, which defines the electrolyte potential V_{sol}. In this Equation, the first term accounts for the non-Faradaic capacitive gating effect while the other terms are related to the nernstian charge transfer reaction. In accordance with the non-Faradaic term, the potential drop between the gate and the solution will be small for large gate area (small γ), while conversely there will be a large difference between gate and solution for small gate (large γ), as shown in Figure 3.6b. Consequently, the current modulation, which depends on the potential drop between the electrolyte and the channel, increases strongly for increasing gate areas, as well as its dependence on the gate voltage. Therefore, if a small gate is used, a modulation of the gate voltage will only cause a small

modulation of I_d. These observations are consistent with the low concentration regions in Figure 3.6a and imply that the response at low analyte concentration is due to the non-Faradaic contribution to V_{sol} [74].

Since for large gate areas the potential drop between gate electrode and electrolyte is very small, the addition of an analyte that causes an increase in V_{sol} (Figure 3.5a) will have only a minor effect. Conversely, in an OECT with a small gate, where geometry favors a small V_{sol} in the absence of analyte, the modulation caused by the addition of analyte will be proportionally larger. Therefore, devices with smaller gates show the highest sensitivity [74, 219].

Finally, Figure 3.6a shows that the onset of saturation for high analyte concentration is almost independent from γ. This result can be explained by considering that saturation is reached when the electrolyte potential becomes comparable to the gate bias because of the Faradaic contribution. At this limit, $V_{sol} \approx V_g$, meaning that the potential drop between the gate electrode and the channel almost entirely affects the electrolyte/channel interface. If further analyte is added to the solution, V_{sol} can not increase significantly and the gating effect on the semiconductor film does not change. This conclusion is confirmed by the fact that the saturation value of $\Delta I/I_0$ increases with gate bias [74].

To summarize, in OECTs with large γ (small gate area or large channel volume) the electrolyte potential is close to the channel potential at low analyte concentration, inducing a low current modulation. If the analyte concentration increases, the electrolyte potential (and then current modulation) increases as well, until the gate potential is reached and saturation occurrs. Conversely, in devices with small γ (large gate area or small channel volume) the electrolyte potential is close to the gate potential even at low analyte concentration, so it cannot increase significantly. For this reason, OECTs with small gate present a lower background signal and a higher sensitivity compared to OECTs with large gate area.

Chapter 4

Materials and Methods

In this Chapter the details about the materials studied and the experimental techniques employed for device preparation and their characterization are presented. In the first Section, the data regarding the different formulations of PEDOT:PSS used, together with the procedures adopted for thin film deposition and OECT preparation, are given. In Section 4.2 and 4.3, the instrumentation and techniques used for the characterization of, respectively, physical and electrochemical properties of PEDOT:PSS thin films are presented. Finally, Section 4.4 reports the experimental setup and procedures employed for culturing living cells on PEDOT:PSS.

4.1 PEDOT:PSS

An overview on the chemical structure of PEDOT:PSS, together with its physical and chemical properties, has been given in Chapter 2. However, many different formulations are commercially available for specific applications. In this work, two different formulations of PEDOT:PSS were used, Clevios™ CPP105D and Clevios™ PH1000. Both of them are waterborne dispersions of PEDOT:PSS mixed with some additives for optimizing specific properties. The former is a low conductive formulation, which is optimized to be deposited on hydrophobic substrates, while the latter is optimized to be highly conductive. The physical properties of these dispersions are presented in Table 4.1.

	CPP105D	**PH1000**
Solid content	1.0 – 1.4%	1.0 – 1.3%
Viscosity (mPa s)	10 – 50	15 – 50
pH value	2.6 – 3.0	1.5 – 2.5
Density at 20°C(g/cm^3)	0.909	1

Table 4.1: Physical properties of Clevios™ CPP105D and Clevios™ PH1000 [196].

4.1.1 Deposition techniques

These PEDOT:PSS formulations were deposited on glass substrates by spin coating. Ethylene glycol 20 v/v% and dodecylbenzene sulfonate (DBSA) 0.05 v/v% were added to PH1000 to improve its electrical conductivity and the ease of the spin coating deposition. A cross-linking agent, 3-glycidoxypropyl trimethoxysilane (GOPS) 1 v/v%, was added to both CPP105D and PH1000 to improve their resistance to delamination when exposed to water [224]. These two suspensions were treated in ultrasonic bath for 10 minutes and filtered using 1.2 μm cellulose acetate filters, then spin coated over clean glass slides. The samples were subsequently dried at 140°C for 30 min to remove water and other solvents.

For the deposition of PEDOT:PSS on woven cotton and lycra, 1% (w/v) of GOPS was added to a solution obtained by mixing two parts of Clevios™PH1000 and one part of ethylene glycol. About 40% (w/w) of the solvent was evaporated in order to obtain a liquid with the suitable viscosity for being used as ink for screen printing. The obtained PEDOT:PSS suspension was then printed on the fabric: the pristine textile was covered by using insulating tape as a mask. The PEDOT:PSS ink was applied on the edge of the textile and was moved onto it by the use of a fill blade. The tape was then removed and the textile was dried in an oven at 90°C for 30 min. A thin layer of PDMS was eventually applied on the PEDOT:PSS track in order to keep dry the electrical contacts between the organic semiconductor and the metallic electrodes of the electronic readout.

In addition to these techniques, thin films of PEDOT:PSS were produced by electrochemical deposition. As mentioned in Section 2.2.3, this technique allows a precise control on the quantity of material that is deposited on the substrate, and provides an easy way for functionalization [199]. A strong limitation imposed by

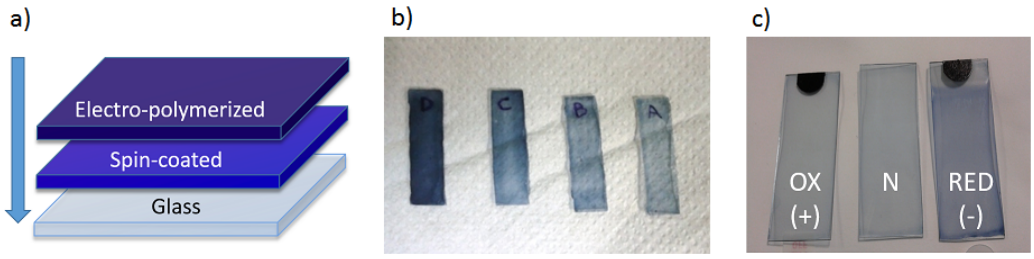

Figure 4.1: Sample preparation. (a) PEDOT:PSS layers in electropolymerized samples. (b) PH1000 films obtained at different spin coating speeds. (c) CPP105D films in their pristine form (N), and after oxidation (OX) and reduction (RED).

this technique is the requirement of an electrically conducting substrate; to overcome this constraint without adding a metal layer, so as to obtain all-organic electropolymerized films, a thin film of spin coated CPP105D was used as conducting layer for electrochemical deposition (4.1). This material was chosen instead of the metals commonly used for this purpose, such as gold or ITO, to obtain transparent films, which can be employed in low-cost and flexible devices. Moreover, a decrease in the delamination of electropolymerized PEDOT:PSS was observed when deposited on CPP105D-coated glass slides instead of metal electrodes, due to the good adhesion of CPP105D to glass.

Electropolymerized PEDOT:PSS was synthesized onto a previous deposited PEDOT:PSS (CPP105D) thin film prepared as described above, with the only exception that no cross-linker was added to the suspension, since this addition increased dramatically the electrical resistance of the conducting polymer. To increase the electrical conductivity, the coated glass slide was immersed for 5 minutes in ethylene glycol and was dried again at 140°C for 40 minutes.

Deaerated water containing 10 mM EDOT and 0.1 mM PSS was used as monomer solution. Oxidative electrodeposition was carried out by cyclic voltammetry (see Section 4.3) (E_{low} = 0 V; E_{high} = +1.5 V; scan rate = 0.1 V s^{-1}) employing a three electrode cell equipped with a saturated calomel electrode (SCE) as reference electrode, and a Pt wire as counter electrode. The PEDOT:PSS spin coated film acted as working electrode, after ensuring the electrical contact to the potentiostat with conductive silver paint. By varying the number of polymerization cycles, it was possible to control the amount of deposited PEDOT:PSS.

Name	Deposition technique	Substrate
CPP105D	Spin coating	Glass
PH1000	Spin coating	Glass
ED4	Electrochemical polymerization (potentiodynamic, 4 cycles)	Glass + CPP105D
ED8	Electrochemical polymerization (potentiodynamic, 8 cycles)	Glass + CPP105D

Table 4.2: Different types of PEDOT:PSS used for characterization and cell culture experiments.

As a result, the four kinds of PEDOT:PSS listed in Table were obtained. Two of them were obtained by spin coating, and they are identified using the commercial name of their PEDOT:PSS dispersion, while the remaining two materials, ED4 and ED8, were obtained by electrochemical potentiodynamic polymerization of PEDOT:PSS by applying, respectively, 4 and 8 cycles of polymerization.

4.1.2 Electrochemical oxidation

The oxidation state of PEDOT:PSS can be electrochemically modified upon the application of a voltage in electrolyte solution. When a negative potential is applied to PEDOT:PSS, positive ions (C^+) from the electrolyte can penetrate the polymer film, which undergoes the electrochemical reaction [225]:

$$PEDOT^+ : PSS^- + C^+ + e^- \rightarrow PEDOT^0 + PSS^- : C^+. \tag{4.1}$$

The effect of the positive ions is to break the electrostatic interaction between PEDOT and PSS, reducing hole concentration and bringing PEDOT to its neutral and non-conductive form. Conversely, when a positive voltage is applied to PEDOT:PSS, the transition from polaronic states to bi-polarons is induced, increasing its conductivity. Indeed, the redox process induces a sharp change in color from dark blue (reduced PEDOT) to almost transparent (oxidized PEDOT), due to the presence of polaronic and bipolaronic states within the $\pi - \pi^*$ energy gap. The effectiveness of the redox process can be thus monitored through optical measurements (Section 4.3.2).

The oxidation state of the PEDOT:PSS films was changed using the three-

electrode cell setup described in previous Section. The PEDOT:PSS films were connected to a potentiostat and used as working electrodes in phosphate buffered saline solution (PBS). The samples were kept at a continuous bias *vs.* SCE for 1 h to obtain an oxidized (positive voltage applied) or reduced (negative voltage applied) form of PEDOT:PSS. This time interval was chosen after analyzing the trend of current *vs.* time during polarization, so as to ensure a complete and stable polarization. The samples were then rinsed in distilled water and dried at room temperature. It must be noted that the use of a reference electrode during the biasing of the samples was proven to be essential to achieve a reproducible oxidation state of PEDOT:PSS, since without this reference, the actual chemical potential of the polymer films is basically random.

Please note that, since the pristine oxidation state of PEDOT is actually partially oxidized, in this thesis the neutral state of PEDOT ($PEDOT^0$) is referred to as "reduced", whereas the fully oxidized state as "oxidized", as generally found in literature. Where not differently specified, the potentials used to reduce and oxidize PEDOT:PSS thin films were -0.9 V and +0.8 V, respectively.

4.2 Physical Characterization

4.2.1 Surface morphology and thickness

One of the most effective tools available to observe features at the micro- and nano-scale on the surface of a sample is the atomic force microscope (AFM). The device functioning is summarized in Figure 4.2. This microscope utilizes a micrometrical tip (its size is about 10-20 μm) mounted on a flexible cantilever as a probe. One end of the cantilever is fixed to a support, while the other end (where the tip is located) is free to move. When the tip approaches the sample, van der Waals forces between the surface and the tip induce a deflection on the cantilever. The potential energy of the tip is then approximated by the Lennard-Jones potential shown in Figure 4.3. To detect the slight deflection of the cantilever, a laser beam is focused on its back and reflected on a photodiode divided in four sectors. From the measurement of the variation of the relative intensities detected by the sections of the photodiode it is possible to precisely know which is the amount of

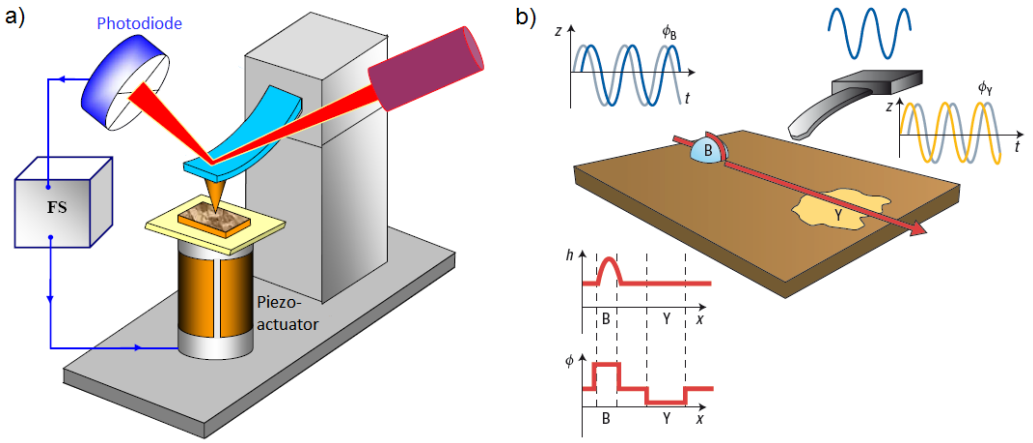

Figure 4.2: (a) Schematic picture of an atomic force microscope. The feedback system (FS) controls the tip-surface distance through a piezoelectric actuator accordingly to the cantilever deflection. (b) Scheme of the heigth and phase imaging operation. The cantilever oscillation depends on the topography and its composition. The phaseshift signal changes with variation in the dissipated energy on the sample surface. Adapted from [226, 227].

vertical and lateral deflection of the cantilever.

Imaging of the surface of the PEDOT:PSS films was carried out using a Park NX10 AFM operating in non-contact mode, in air and in liquid (PBS) in ambient conditions. In non-contact mode, the tip is kept oscillating close to its resonant frequency, ω_0. For a free oscillating tip, the heigth z from the sample surface is described by the equation [226]:

$$z(t) = z_0 + A_0 \cos(\omega t - \phi) \tag{4.2}$$

where z_0 is the mean height of the cantilever, A_0 is the free-oscillation amplitude, ω is the oscillation frequency and ϕ is a phase constant which is set at 90°for the free oscillating tip. Non-contact is achieved when the tip is kept far enough from the sample surface to stay in the attractive regime (*i.e.* the force acting on the tip is attractive, $F = dU/dz > 0$, see Figure 4.3) for the whole amplitude of the oscillation. When the tip approaches the sample, the interaction with the sample lowers the amplitude of the oscillation to a new value, $A(z)$, with $A(z) < A_0$. This value is used as set-point to control the heigth of the tip using a feedback system,

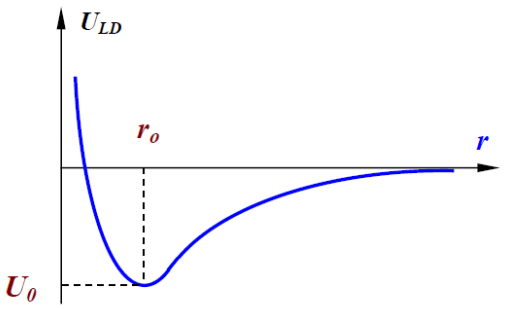

Figure 4.3: Lennard-Jones potential qualitative form [226].

which allows to measure the heigth of the sample.

From surface morphology, many statistical parameters can be obtained describing the geometry of the surface. In this work, surface roughness was quantified from the root mean square roughness, R_q, which is calculated as:

$$R_q = \sqrt{\frac{1}{n}\sum_{i=1}^{n} y_i^2} \tag{4.3}$$

where n is the number of pixels of the AFM image, and y_i are the heigth values of each pixel. RMS roughness was evaluated from images of lateral size 20 μm.

The same technique was also used to evaluate film thickness. After deposition, the films were gently scratched away in part from their substrate, and the step heigth was then measured in non-contact mode.

4.2.2 Mechanical properties

Using an atomic force microscope it is possible also to obtain information about the mechanical properties of a thin film, such as its stiffness and Young's modulus. For a system with a single degree of freedom, the stiffness is defined as $k = F/\delta$, where F is the force applied and δ is the displacement produced by the force along the same degree of freedom; Young's modulus (also called elastic modulus), instead, is defined as the ratio of the tensile stress $\sigma(\varepsilon)$ and the extensional strain

ε in the elastic regime of the stress-strain curve:

$$E(\varepsilon) \equiv \frac{\sigma(\varepsilon)}{\varepsilon} = \frac{F/A_0}{\Delta L/L_0} = \frac{FL_0}{A\Delta L} \tag{4.4}$$

where A_0 is the actual cross-sectional area through which the force is applied, ΔL is the amount by which the length of the object changes, and L_0 is the original length of the object. While Young's modulus is an intensive property of a material, the stiffness is a property which depends both on the material and the geometrical structure of the sample; as a consequence, these quantities are different, but related. As an example, for a for an element in tension or compression, the axial stiffness is given by $k = AE/L$.

The determination of stiffness and Young's modulus can be achieved with an AFM through the acquisition of force-distance curves, where a tip with an appropriate force constant k is used for the indentation of the film. By measuring the deflection δ of the tip, the applied force can be obtained from Hooke's law, $F = k\delta$. Furthermore, if the displacement z of the z-scanner of the AFM is known (*i.e.* the change in tip heigth imposed by the AFM during the indentation), then the indentation length d is given as $d = z - \delta$ (with δ always lesser than z, whereas $\delta = z$ only for an infinitely-hard surface).

Once F and d are known, the stiffness can be easily calculated as $k = F/d$, while Young's modulus is given by the Sneddon model for a conical indenter with apex angle 2θ on an elastic half-space [228]:

$$F = \frac{2E}{\pi(1-\nu^2)} d^2 \tan\theta \tag{4.5}$$

where ν is the Poisson's ratio, defined as the negative ratio of transverse to axial strain. For isotropic materials, $0.2 \leq \nu \leq 0.5$ [229].

The stiffness and Young's modulus of PEDOT:PSS samples were measured in liquid environment (PBS) before and after the oxidation process described in Section 4.1.2. The force-distance curves were acquired using a Park NX10 AFM with Park PPP-NCHR cantilevers ($k = 42$ N/m). For the calculation of Young's modulus, ν was taken as 0.34 [204].

4.2.3 Wettability and surface energy

The wettability is the ability of a solid surface to reduce the surface tension of a liquid in contact with it, causing its spreading on the surface. The wettability of a material can be quantified directly by measuring the contact angle formed by a droplet of liquid placed on it, as shown in Figure 4.4. If the liquid used is water, the surface is then called *hydrophilic* if the contact angle is $\theta < 90°$, or *hydrophobic* if $\theta > 90°$.

The wettability of a surface is related to its surface energy, γ, which represents the excess energy (per unit area) at the surface of a material compared to the bulk, and therefore contains information about surface properties such as surface charge, roughness, and the energy of intermolecular bonds. For liquids, the surface energy density is also called surface tension.

More specifically, contact angle, as shown in Fig. 4.4, is related to three parameters: the surface energy of the solid surface (γ_{sv}), the surface tension of the liquid (γ_{lv}), and the energy associated to the solid-liquid interface (γ_{sl}). These quantities are related according to Young's equation [230]:

$$\gamma_{lv} \cos\theta = \gamma_{sv} - \gamma_{sl} \tag{4.6}$$

One of the approaches that can be used to determine γ_{sv} and γ_{sl} by using contact angle data is the equation of state for interfacial tensions [231],

$$\gamma_{sl} = f(\gamma_{lv}, \gamma_{sv}) \tag{4.7}$$

which expresses the interfacial energy as a function of the surface energies of the solid and liquid phases. The existence of such equation in this form was demonstrated by Neumann *et al.*, which also gave an empirical formulation as [231]:

$$\gamma_{sl} = \gamma_{lv} + \gamma_{sv} - 2\sqrt{\gamma_{lv}\gamma_{sv}}\exp[-\beta(\gamma_{lv} - \gamma_{sv})^2]. \tag{4.8}$$

where β is a constant experimentally determined as 0.000115 $(\mathrm{m}^2/\mathrm{mJ})^2$. Combin-

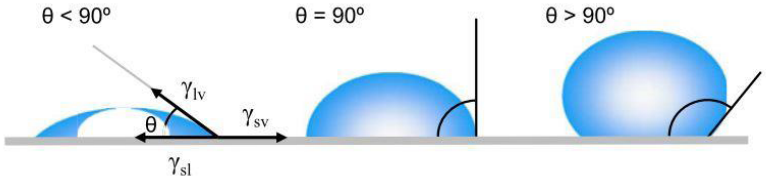

Figure 4.4: Contact angle bewteen a liquid droplet and a smooth and homogeneous surface [233].

ing Equation 4.8 with Young's equation finally yields:

$$\cos\theta = -1 + 2\sqrt{\frac{\gamma_{sv}}{\gamma_{lv}}}\exp[-\beta(\gamma_{lv} - \gamma_{sv})^2] \tag{4.9}$$

where the only unknown is the solid surface energy, γ_{sv}, that can be calculated numerically once θ is measured, since γ_{lv} is known for water [232].

In this work, hydrophilicity and surface energy of the PEDOT:PSS films were determined by water contact angle measurements (surface tension of 72.8 mJ/m^2), which were performed with a custom setup, consisting in a graduated syringe aligned to a video camera, using the sessile drop technique. The contact angles were measured using an image analysis software (*ImageJ*) and then converted into surface energy values employing Equation 4.9.

4.2.4 Electrical measurements

A useful parameter for comparing the electrical properties of devices which are different in size is sheet resistance, R_s, defined as $R_s = \rho/T$, where ρ is the resistivity and T is the thickness of the film. The sheet resistance of the polymer films was measured using a 4-probe custom setup, where four aligned and evenly spaced (spacing 2.7 mm) conductive tips were connected to a Keithley 2400 SourceMeter, which was used as a current generator for the two external tips and as a voltage meter for the two inner tips. Using this configuration, the resitivity of the film can be calculated:

$$\rho = 2\pi F s \frac{V}{I} \tag{4.10}$$

where s is the probe spacing and F is a geometrical correction factor. For an infinite and thin film (length and width of the sample $\gg s$, $T \ll s$), this expression is approximated by:

$$\rho = \frac{\pi T}{\ln 2} \frac{V}{I}. \tag{4.11}$$

Consequently, the sheet resistance becomes:

$$R_s = \frac{\rho}{T} = \frac{\pi}{\ln 2} \frac{V}{I}. \tag{4.12}$$

Hence, a geometrical correction factor of $\pi/\ln 2$ was applied to all measurements [234]. Once R_s and T are known, the conductivity can be easily obtained as $\sigma = 1/(R_s T)$.

The electrical characterization of PEDOT:PSS-based OECTs was carried out using the setup shown in Figure 4.5. Two Keithley 2400 SourceMeters controlled by a personal computer via a homemade LAB-VIEW software were simultaneously employed to apply the source-drain (V_d) and source-gate (V_g) potentials and to measure the respective currents (I_d, I_g). In some experiments, the sourcemeter source output was connected to the working-electrode output of an eDAQ EA161 potentiostat, which was set as high-impedance voltmeter, for measuring the source electrode potential *vs.* a saturated calomel reference electrode (SCE).

Instead of using a reservoir for containing the electrolyte solution as in many OECTs found in literature, we immersed the active area of the OECT in solution using an electrochemical cell as container (Figure 4.5). This configuration offers several practical advantages: it simplifies the addition of analytes to the electrolyte solution; it allows the use of a magnetic stirrer for improving the diffusion of analytes after their addition; it makes easy to remove oxygen, which interferes with the electrochemical sensing process, from the electrolyte solution by saturating the cell with nitrogen gas.

OECT characterization involved the acquisition of charcteristic curves ($I_d - V_d$) and transfer curves ($I_d - V_g$). The transconductance was obtained from the transfer curves as $g_m = \partial I_d / \partial V_g$. In order to measure sensitivity and limit of detection (LOD) to various analytes, the drain current was recorded as a function of time at fixed V_d and V_g, which were chosen accordingly to the analyte. The analyte

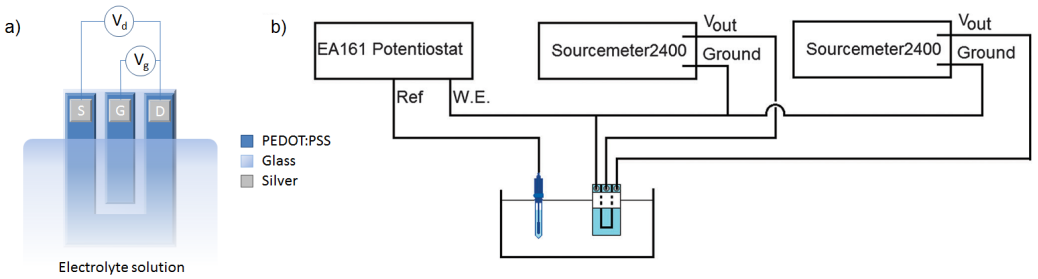

Figure 4.5: (a) Geometry of the OECT. (b) Schematic of the instrumental setup employed to perform OECT characterization. One SourceMeter was used to apply V_d and measure I_d on the PEDOT:PSS channel; the second SourceMeter (common ground terminal) was used to apply V_g to the gate electrode and to measure I_g. A potentiostat was used for the measurement of the electrochemical potential of PEDOT:PSS during OECT operation.

was then added at different concentrations, causing a change in the drain current. The measured variation in I_d was then used to obtain a calibration curve, I_d *vs.* concentration, from which the sensitivity was extracted as the slope of the curve, $\Delta I/\Delta C$, while the LOD was evaluated as the lowest addition that led to a change in I_d.

4.3 Electrochemical Characterization

In addition to the study of the physical properties described in previous Section, electrochemical techniques can be used for gaining information about the kinetics and charge transport involved in the electrochemical redox reactions exploited both in OECTs and in cell culture substrates studied in this work. The electrochemical characterization of PEDOT:PSS thin films was carried out by cyclic voltammetry (CV) and spectrophotometry. These techniques both involve the use of a three electrode cell where three electrodes, named working, reference and counter electrode, are in contact with an electrolyte solution. The sample, a thin film of PEDOT:PSS in our case, is used as the working electrode, which potential is measured with respect to the reference electrode of known potential. The counter electrode is used to generate the current required to keep the working electrode at the desired potential without affecting the reference electrode.

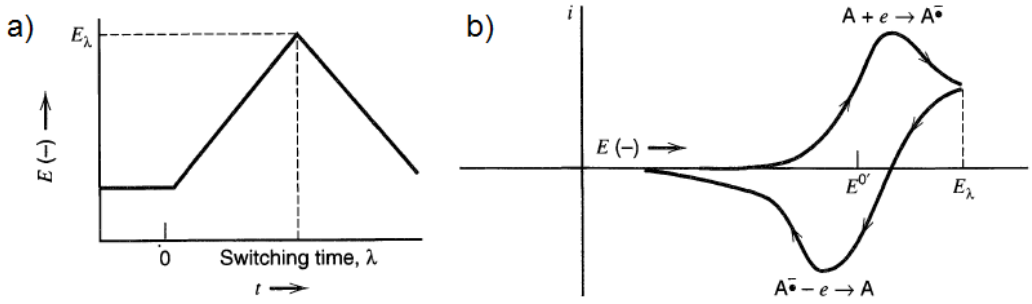

Figure 4.6: (a) Cyclic potential sweep; (b) Resulting cyclic voltammogram. Adapted from [221].

The electrochemical characterization of PEDOT:PSS thin films was carried out in collaboration with the research group of Prof. E. Scavetta (Department of Industrial Chemistry, University of Bologna).

4.3.1 Cyclic voltammetry

In a CV, the electrochemical potential of the sample is swept linearly over time at a fixed scan rate v until a switching potential, E_λ, is reached at a time $t = \lambda$. Then, the direction of the scan rate is switched until the electrochemical potential of the sample is brought back to its starting value E_i. Thus the potential during each cycle is given by:

$$E = E_i - vt \qquad (0 < t \leq \lambda) \tag{4.13}$$

$$E = E_i - 2v\lambda + vt \qquad (t > \lambda) \tag{4.14}$$

This sweep reversal method is extremely powerful and is among the most widely practiced of all electrochemical methods [221]. In a cyclic voltammetry, the shape of the curve ($I - t$ or, more commonly, $I - E$, as shown in Figure 4.6b) is given by a superposition of a capacitive current, due to the charging of the electrical double layer at the electrode-electrolyte interface, and a Faradaic current, due to mass transfer in the electrochemical reaction $O + ne \rightleftarrows R$ occurring at the electrode. The charging current during a potential sweep can be expressed as [221]:

$$I_c = vC_d[1 - \exp(-t/R_sC_d)] \tag{4.15}$$

where R_s is the electrical resistance of the solution, and C_d is the double layer capacitance. This current, which is time-dependent, saturates for $t \gg R_s C_d$ at a steady-state current $I_{c,ss} = vC_d$, with a linear dependence on the scan rate $v = dE/dt$. If a triangular wave is applied instead of a single sweep, then the steady-state current changes from vC_d during the forward (increasing E) scan to $-vC_d$ during the reverse (decreasing E) scan, because of the change in sign of dE/dt.

The Faradaic current is regulated by two laws, Fick's law of diffusion for the case of a planar electrode 4.16, and Nernst equation 4.17:

$$\frac{d[O]}{dt} = D\frac{d^2[O]}{dx^2} \tag{4.16}$$

$$\frac{[O]_{x=0}}{[R]_{x=0}} = \exp\left[\frac{nF}{RT}(E(t) - E_0)\right]. \tag{4.17}$$

Fick's law of diffusion governs the mass transport process towards the electrode, where D is the diffusion coefficient and the parameter x denotes the distance from the electrode surface. Nernst equation defines the surface concentrations of the oxidized and reduced form of the redox reagents as a function of $E(t)$ and E_0, respectively the applied and the formal potential [15]. In Equation 4.17, t is the time, n is the number of electrons transferred per molecule of O reacting at the electrode surface, F is the Faraday constant, R is the constant for an ideal gas, and T is the absolute temperature.

For a reversible diffusion-controlled process, *i.e.* a reaction where the reaction rate is limited by the rate of transport of the reactants to the surface of the electrode [221], the current response at each potential for a reversible cyclic voltammogram may be calculated, with $E(t) = E_i - vt$ [15], using a mathematical procedure called semi-integration ($d^{1/2}y/dx^{1/2}$) or convolution [235]:

$$I(t) = -nFA[O]_{bulk}\sqrt{D}\frac{d^{1/2}}{dt^{1/2}}\left(\frac{1}{1 + \mathrm{e}^{\frac{nF}{RT}(E_i - vt - E_0)}}\right) \tag{4.18}$$

where A is the electrode area.

Finally, the hypothesis of diffusion-controlled process can be verified using the Randles-Ševčik equation, which relates the peak current, I_p, with the square-root

of the scan rate [15]:

$$I_p = 0.446nFA[O]_{bulk}\sqrt{\frac{nFvD}{RT}}. \tag{4.19}$$

In this work, cyclic voltammetries have been carried out in a three electrode cell containing a phosphate buffer solution 0.1 M pH 5.5 as electrolyte. The electrochemical potentials were measured with respect to an aqueous saturated calomel electrode (SCE), a Pt wire was used as the counter electrode and a PEDOT:PSS thin film deposited on a glass slide was used as the working electrode. The electrochemical responses were acquired by employing an eDAQ EA161 potentiostat controlled by personal computer.

4.3.2 Spectrophotometry

As described in Section 4.1.2, the redox state of PEDOT:PSS films can be assessed with optical absorption measurements. The experimental setup used for spectrophotometry is illustrated in Figure 4.7. A monochromator selectively controls the wavelength of the light going through the sample (a thin film of PEDOT:PSS deposited on a glass slide), which is kept in a cuvette containing an electrolyte solution. A photodiode array is then used to detect the light after absorption from the sample, while a potentiostat controls the oxidation state of PEDOT:PSS in real-time. As a result, the absorption spectra of the sample at different oxidation states are acquired, highlighting the formation of conducting states at different energies along the polymer backbone.

This technique was also used for monitoring the time stability of the redox state after polarization while the PEDOT:PSS films were immersed in three different aqueous media: distilled water, PBS, and Dulbecco's modified Eagle's medium (DMEM) supplemented with fetal bovine serum. These media were used because of their different composition, since PBS contains small ions only while DMEM also contains quite large organic molecules, like amino acids, vitamins and glucose.

These spectroelectrochemical experiments were carried out using a Hewlett-Packard 8453 diode array spectrophotometer with an *in situ* electrochemical cell

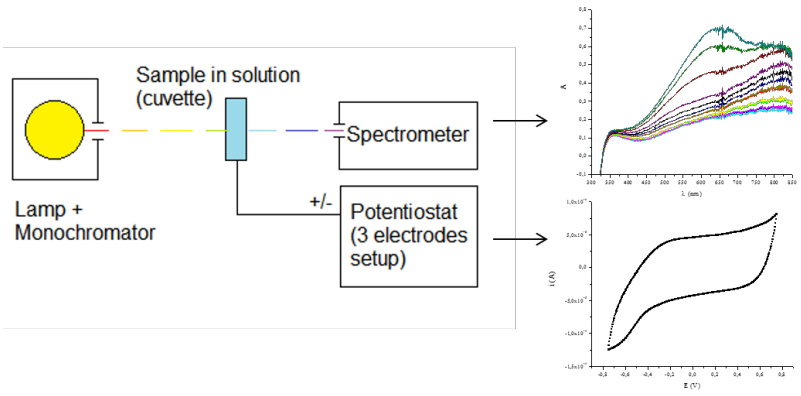

Figure 4.7: Scheme of the spectrophotometry setup.

(home-made) during the application to the sample of a linear potential ramp, starting from -0.7 V to +0.7 V at a scan rate of 0.05 Vs^{-1}. Furthermore, the stability of the induced redox state was continuously monitored for 1 h after removing the applied bias by collecting Vis-NIR (300-1000 nm) spectra for 60 minutes every minute after the end of polarization. Finally, the observation of the time stability of PEDOT:PSS was extended to 48 h in cell culture medium only, a time scale which is comparable to the duration of cell growth experiments.

4.4 Cell Proliferation

The effects induced by a change in the redox state of PEDOT:PSS on the cell adhesion and growth process were studied by culturing two different cell lines, primary human dermal fibroblasts (hDF), and human glioblastoma multiforme cells (T98G). These types of cells have been chosen in order to assess the effects of the substrates parameters on adherent, high-replicating and tissue-forming cells with very similar genotypic and phenotypic properties, but normal (hDF) and tumor-like (T98G). The biological experiments on cell growth and patch clamp, together with the analysis of their outcome, were carried out in collaboration with the research group of Prof. G. Castellani (DIFA, University of Bologna).

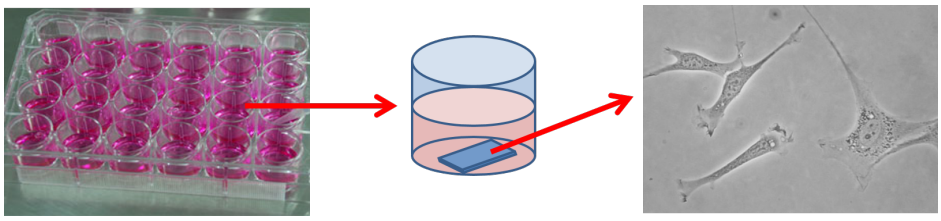

Figure 4.8: Positioning of the PEDOT:PSS samples for cell culture. After biasing, the samples are cut and placed on the bottom of a multiwell plate.

4.4.1 Cell culture

Glioblastoma multiforme cells (T98G), derived from a human tumor, were maintained in Roswell Park Memorial Institute (RPMI) medium, supplemented with 10% fetal bovine serum, 1% L-glutamine, 10% sodium pyruvate, and antibiotics (1% penicillin and 1% streptomycin). Primary dermal fibroblast (hDF), gently provided by Prof. S. Salvioli (DIMES, University of Bologna), were obtained from two donors (age 24 and 23 years) by skin biopsies according to standard culture method. All the donors gave their informed consent before biopsy was performed.

hDF were maintained in Dulbecco's modified Eagle's medium (DMEM), supplemented with 10% fetal bovine serum, 1% L-glutamine, and antibiotics (1% penicillin and 1% streptomycin). hDF of 3-15 passages number were used.

Both cells population were kept in culture standard conditions in incubator at 5% CO_2 humidified atmosphere at 37°C. Before each experiment, the cells were detached by trypsin (0.02%) in ethylenediaminetetraacetic acid (EDTA) and resuspended in culture medium at room temperature.

4.4.2 Proliferation curves

Cell culture 24-well plates were prepared as follow (Figure 4.8): PEDOT:PSS substrates in non-biased, oxidized, and reduced form were cut using a diamond tip and three replication for each form were placed in nine different wells of the plate; then, the plates were sterilized under UV per 20 minutes. Before cell seeding, PEDOT:PSS was washed using sterile culture medium to buffer the pH altered by the substrates. No bias was applied during cell seeding or growth.

T98G and hDF cells were counted by an hemocytometer and seeded in a density of 0.010×10^6 and 0.015×10^6 with 500 µL of supplemented RPMI and DMEM, respectively, in each well prepared as described and in three wells without PEDOT:PSS, that is, on a sterile hydrophilic polystyrene tissue culture surface (control) physically treated for improving cell adhesion. Cells were allowed to adhere and spread for 24 h prior the observation.

Cell proliferation was studied by growing T98G and hDF in a CO_2 incubation system integrated within a motorized stage allowed to perform time-lapse imaging acquisition even for tens of hours. Images were acquired in phase-contrast at 100× of magnification for a time interval up to 72 h (4 days) by the inverse automatized optical microscopy Nikon Eclipse-Ti.

4.4.3 Patch clamp setup

The patch clamp technique is an electrophysiology technique that allows the study of ion channels in cells. In patch clamp recording, a glass micropipette is used as a recording electrode, while another electrode is located in the bath around the cell as a reference electrode [13]. Thanks to its small size the micropipette, whose diameter is usually in the micrometer range, is used to enclose a surface area of the cell (or "patch"). Then, a voltage can be applied between the micropipette electrode and the reference electrode in order to record the current flowing through the ion channels of the cell (voltage clamp), or in a similar fashion, the current can be kept constant to measure changes in the membrane potential (current clamp). In this work, whole-cell configuration was used. With this technique, the electrode is used to rupture the membrane patch, providing access from the interior of the pipette to the intracellular space of the cell and allowing the measurement of multiple channels simultaneously, over the membrane of the entire cell [236].

Resting membrane potential and voltage-dependent membrane current recordings were measured both with patch clamp technique in whole-cell configuration at RT (22-24°C) with an HEKA EPC-10 amplifier driven by the Patch Master software. Before the recordings, cells were detached using trypsin-EDTA (0.02%), suspended in 1:3 culture medium and kept out of the incubator in a Falcon tube. Within 6h 30 µl of suspended cells were seeded on a polystyrene 35-mm Nunc

Petri dish, used as control (*CTRL*), and on PEDOT:PSS (ED8) substrates in not biased, oxidized and reduced forms obtained after polarization at +0.8 V and -0.9 V, respectivley. Before seeding, PEDOT:PSS samples were washed out twice with PBS and placed into a Petri dish. After 15 min cells were checked under the microscope to verify their attachment to the substrates, then a wash out with the bath solution was performed and about 2 ml of the same solution was left for recordings.

The bath solution (extracellular electrolyte solution), the same for T98G and hDF, contained (in mM): 133 NaCl, 4 KCl, 2 $MgCl_2$, 2 $CaCl_2$, 10 4-(2-hydroxyethyl)-1-piperazineethanesulfonic acid (HEPES) and 10 glucose (pH 7.4, NaOH). The electrode solution (pH 7.2, KOH) contained, for T98G cells (in mM): 10 NaCl, 120 K-aspartate, 2 $MgCl_2$, 4 $CaCl_2$, 10 HEPES, 10 ethylene glycol tetraacetic acid (EGTA), 3 Mg-ATP, 0.2 GTP-Tris, and for hDF cells (in mM): 145 KCl, 1 $MgCl_2$, 1.8 $CaCl_2$ and 10 HEPES. The patch micropipette tip resistances ranged between 3 and 7 MΩ when filled with electrode solution.

4.4.4 Voltage-clamp

Current traces were acquired at digitizing rates of 20 kHz and filtered at 2.9 kHz with an eight-pole low-pass Bessel filter. Voltage steps (20 mV, 150 ms) from -30 to +110 mV were delivered at intervals of 1 s; to inactivate other voltage-activated K^+ currents, the holding potential V_h was set to 0 mV. Specific built-in software algorithms minimized on-line the fast capacitance transients, and performed a tracked leakage subtraction of the current amplitude every 10 ms; this software setting allowed the automatic measurement of cell capacitance. Current amplitude values were considered after reaching the steady-state level, and were averaged to produce a single value for each measurement. To quantify the plasma membrane permeability to potassium ions a solution containing 10 mM concentration of tetraethylammonium chloride (TEA) was prepared from an adjusted bath solution (123 mM NaCl) and was applied by perfusion with a rate of about 1-1.5 ml/min.

4.4.5 Current-clamp

Resting membrane potential was acquired through the balanced bridge technology of the EPC-10 amplifier, at digitizing rates of 10 kHz and filtered at 2.9 kHz with an eight-pole low-pass Bessel filter. Before switching into the current clamp modality the compensation of the capacitance transients in the voltage clamp mode was performed. The membrane current was clamped at 0 pA in order to balance the ionic flows inward and outward the cell. To evaluate the resting membrane potential and in the same time the quality of the seal and the goodness of the recording, a stimulation protocol consisting of current steps (20 pA, 150 ms) from -120 to +120 pA delivered at intervals of 1 s was used. The resting membrane potential value of each cell was obtained by averaging the data from the baseline, i.e. the region of the voltage traces (from 0 to 100 ms) corresponding to the current holding of 0 pA. All values are expressed as mean ± SEM. Student's *t* test was used to compute the probability values (p) in two-group comparison. A p threshold of 0.05 was considered for statistical significance.

Chapter 5

PEDOT-based Electrochemical Sensors

In this Chapter, PEDOT:PSS-based electrochemical sensors, namely amperometric sensors and organic electrochemical transistors (OECTs), are presented. Their performance was characterized using several biochemical compounds of biological relevance, and the results are summarized in Section 5.5. An approach to obtain selectivity on OECTs without the need for chemical functionalization is then presented, followed by the description of the results obtained from the integration of OECTs on textiles for their application as wearable sensors.

5.1 Amperometric Sensors

The simplest electrochemical sensor based on PEDOT:PSS realized in this work is the amperometric sensor. These devices were realized by spin-coating a thin film of Clevios™ PH1000 on a glass slide, as described in Section 4.1.1, at a speed of 700 rpm for 10 seconds. The coated slides (area 1 cm^2) were then used as the working electrode in a three electrode electrochemical cell, with a Pt wire as counter electrode and a saturated calomel electrode (SCE) as reference electrode.

Amperometric sensing is realized in a three-electrode electrochemical cell by applying a known potential E to the device with respect to the reference electrode, and by measuring the current I flowing between the sensor and the counter elec-

trode. The potential E can be swept over a specific range (voltammetry) or kept constant, in order to measure the temporal variations in the current I upon the addition of an analyte (chronoamperometry).

5.1.1 Electrochemical response to dopamine

In order to probe the amperometric operation of the device, it was tested for the detection of 3,4-dihydroxyphenyl ethylamine, commonly known as dopamine (DA). DA is an important neurotransmitter in the mammalian central nervous system, and a loss of DA-containing neurons may result in some serious diseases such as Parkinson's disease; thus, the determination of the concentration of DA is an important problem in analytical biochemistry [199]. DA detection is obtained thanks to the electrochemical reaction:

$$2\,\mathrm{PEDOT}^{+} + \mathrm{DA} \rightarrow 2\,\mathrm{PEDOT}^{0} + \mathrm{oxidized\,DA} \tag{5.1}$$

To investigate the electrocatalytic oxidation towards DA, PEDOT:PSS thin films deposited on glass slides were characterized by cyclic voltammetry (CV) ranging from -0.2 V to +0.6 V (*vs.* SCE) in 0.1 M PBS (pH 5.5) for an increasing analyte concentration from 0 to 3.0 mM (Figure 5.1a). In the absence of DA, no significant peak is observed and the rectangular shape of the curve suggests that PEDOT:PSS has the typical behavior of a capacitor in such potential range. Upon the addition of DA to the supporting electrolyte, a redox wave that is ascribed to the dopamine oxidation appears in the anodic side, together with a peak of lower intensity in the cathodic current at $E = 0.15$ V. Both the anodic peak current I_{pa} and potential E_{pa} increase with DA concentration. In Figure 5.1b the trend of I_{pa} *vs.* concentration is presented, showing that the peak current is directly proportional to the concentration of dopamine with a slope equal to $8.0\,10^{-5}$ A mM^{-1} and a R^2 of 0.975. Such results confirm the oxidation of DA when PEDOT is biased at a sufficiently high positive potential.

As shown in Figure 5.2a, the CV curves of DA were measured with PEDOT:PSS electrodes at different scan rates, ranging from 5 mV s^{-1} to 200 mV s^{-1}. This Figure clearly shows that the peak currents for the anodic oxidation and cathodic reduction of 1 mM DA in 0.1 M PBS gradually increase with an increase

in the scan rate. The relationship between the anodic peak currents I_{pa} and the root square of the scan rate $v^{1/2}$ is displayed in Fig. 5.2b, showing a linear proportionality over the considered range, with a slope of $1.13\,10^{-3}$ A $V^{-1/2}$ $s^{1/2}$ and $R^2 = 0.9825$. As suggested by Randles-Ševčik equation (Eq. 4.19), this result indicates that the electrochemical oxidation at the PEDOT:PSS electrode depends on the DA diffusion from bulk solution to electrode surface [221]. However, when the scan rate increases, also the peak potentials for the oxidation and reduction of DA shift to more positive and negative potentials, respectively, suggesting a kinetic limitation in the reaction between the redox sites of PEDOT and dopamine. These results demonstrate that the overall electrochemical process is mixed-controlled by mass transport and charge transfer kinetics.

5.1.2 Chronoamperometric sensing

DA determination was realized by chronoamperometry under magnetic stirring at $E = 0.45$ V with sequential additions of DA to the electrolyte solution (Figure 5.3a), using PEDOT:PSS-coated glass electrodes. The analyte concentration was gradually increased in aliquotes of 0.1, 1, 10, 100 and 200 µM (five additions for each aliquote) while measuring the current flowing between the PEDOT:PSS electrode and a Pt working electrode. The response of the device is stable and

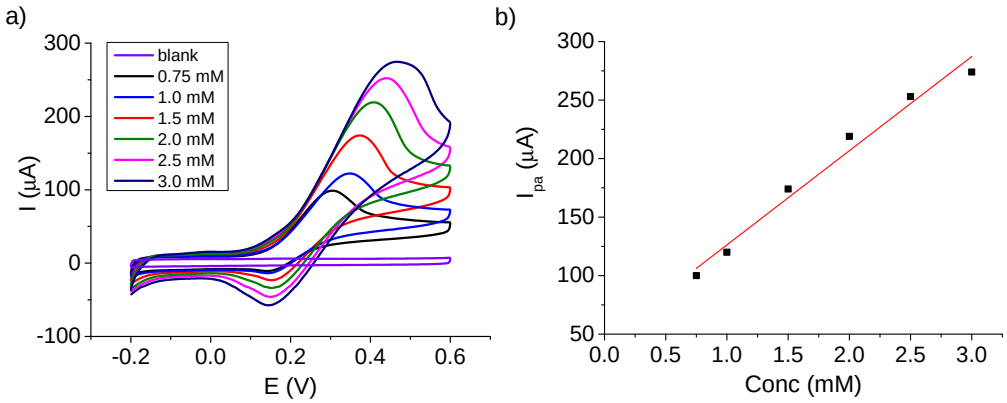

Figure 5.1: (a) Cyclic voltammetries recorded at a PEDOT:PSS electrode for increasing dopamine concentrations in PBS 0.1M, scan rate 10 mV s^{-1}. (b) Plot of anodic peak current *vs.* dopamine concentration.

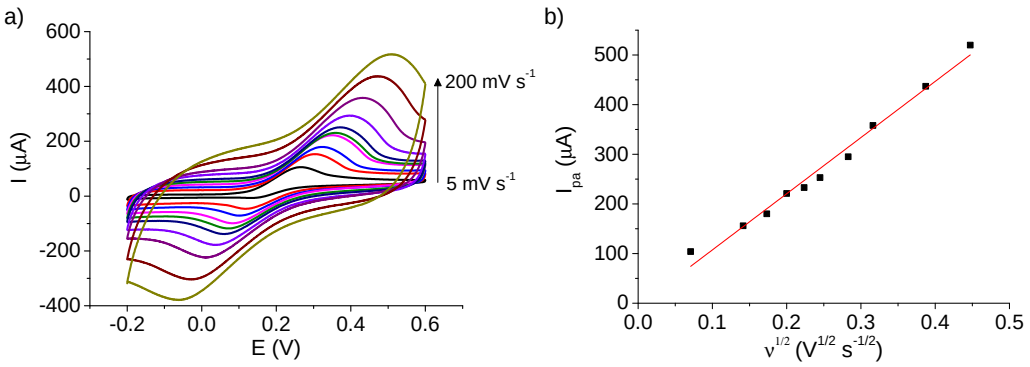

Figure 5.2: (a) Cyclic voltammetries recorded at a PEDOT:PSS electrode for increasing scan rate in PBS 0.1M with dopamine concentration 1 mM. (b) Plot of oxidative peak current *vs.* square root of scan rate.

rapid, with the average response time being about 10 s. Calibration curves were obtained by plotting the steady state current, measured after subtraction of the base line current, *vs.* DA concentration, as shown in Figure 5.3b. A linear relationship between the registered current and DA concentration was observed over all the examined range (0.1 μM - 1.3 mM), with a slope (sensitivity) of 1.92 10^{-4} A mM^{-1} and R^2 = 0.998. The limit of detection (LOD), determined at a signal-to-noise ratio of 3, is 0.4 μM.

5.2 Development of a Novel All-PEDOT OECT

Electrochemical sensors offer many advantages with respect to other techniques such as the use of quick and easy procedures, but the determination is rather expensive because it requires a potentiostat and, consequently, a complex readout electronics for acquiring the signal, together with a reference electrode that also hinders the miniaturization of these devices [76].

Organic electrochemical transistors (OECTs) represent a valid option to overcome these issues (see Section 1.3.1). The transistor configuration ensures a high sensitivity, since it combines a sensor and an amplifier. As a consequence, small changes in the potentials due to the analyte may lead to a pronounced variation of the channel current. Transistor-based sensors offer many advantages, including

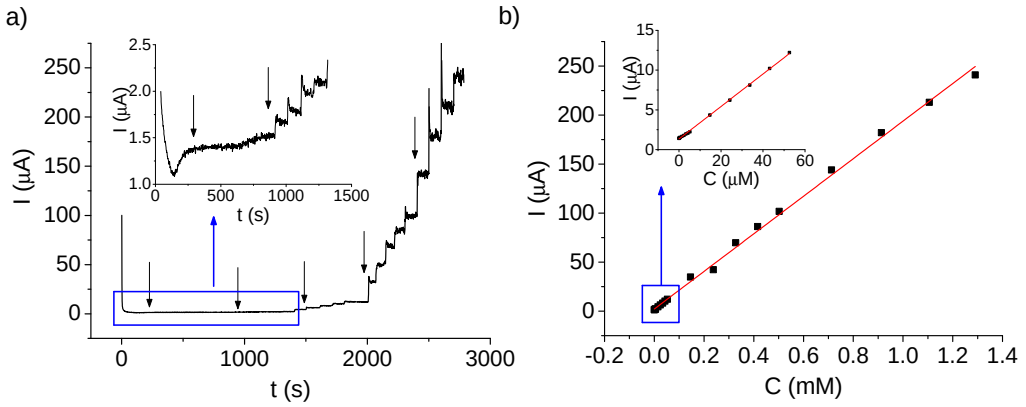

Figure 5.3: (a) Chronoamperometric response at 0.45 V *vs.* SCE of a PEDOT:PSS electrode in 0.1 M PBS solution to successive dopamine additions. The black arrows indicate an increase in the dopamine concentration in the added solution, ranging from 0.1 μM to 200 μM per addition; (b) Calibration curve of I *vs.* dopamine concentration.

high sensitivity, feasibility for miniaturization, and a simple electrical readout.

In this work, PEDOT:PSS was used as material for both the semiconducting channel and the gate electrode. This feature allows an easier and less expensive fabrication compared to devices using metals as the gate electrode, requiring a single deposition technique for the whole device. Moreover, the absence of metallic elements makes the device particularly suitable for flexible electronics applications.

OECTs were fabricated by spin-coating Clevios™ PH1000 (see Section 4.1.1) on a glass substrate with the geometry shown in Figure 5.4. The active area of the OECT was then immersed in the electrolyte solution (PBS 0.1 M pH 5.5) using an electrochemical cell as container. The working regime of our OECT was optimized by studying the electrochemical behavior of PEDOT:PSS, and by comparing transistors with two different thicknesses T (with $T_{ch} = T_g$ in each transistor).

5.2.1 Electrochemical characterization

Although OECTs completely made with a conductive polymer have been described in literature already [237,238], only a few papers proposed them as chem-

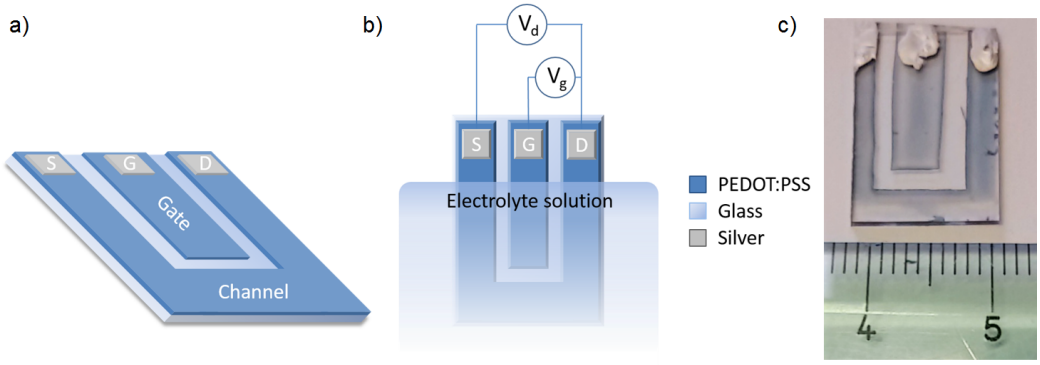

Figure 5.4: (a,b) Schematics showing the geometry of the OECTs used in this work. *S*, *G* and *D* refer to the source, gate and drain electrodes, respectively. (c) Picture of an OECT.

ical sensors using an enzymatic transduction [83, 239], and their characterization is still lacking.

The electrochemical properties of the PEDOT:PSS electrodes of our OECTs were studied by cyclic voltammetry (Figure 5.5). When the CVs were performed between -0.2 and +0.6 V *vs.* SCE, a typical capacitive curve with rectangular shape was observed, suggesting that PEDOT:PSS behaves like a capacitor in such a potential range (see Fig. 5.5a, dotted line). In these conditions, the signal was stable for hundreds of cycles. The range of investigated potential was then expanded (-1.6 to +0.8 V) so as to highlight the PEDOT:PSS redox processes (Fig. 5.5a, solid line). Within this range, the stability of the recorded current slightly decreased, with a reduction of the peak current of about 3% for each cycle, but it was possible to observe the redox waves of PEDOT:PSS clearly.

The redox wave labeled with *I* in Fig. 5.5a is ascribed to PEDOT:PSS oxidation, involving the formation of polaronic and bipolaronic states originating from the neutral form of PEDOT. This process is caused by the electrochemical doping due to the injection of holes in the π-conjugated system of the polymer backbone. On the other hand, the process I' is ascribed to the reduction of polaronic and bipolaronic states to form neutral PEDOT. From this measurement, the charge that flows during the cathodic process can be calculated in order to evaluate the concentration of the oxidized sites C_{ox} as a function of the applied electrochemical potential (Figure 5.5b, blue curve).

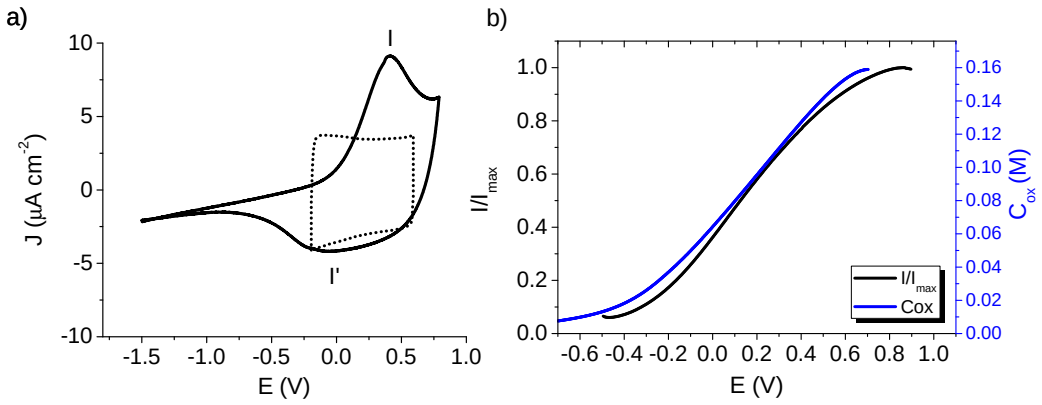

Figure 5.5: (a) CVs (0.02 Vs^{-1}) of PEDOT:PSS recorded in PBS 0.1 M pH 5.5 in two different potential ranges. (b) Plot of I/I_{max} and C_{ox} reported *vs.* the electrochemical potential of the source, E. I/I_{max} was recorded applying 0.3 V between the working electrode and the drain electrode of the transistor.

The dependence of I_d on the electrochemical potential of the channel was examined by recording the current (V_d = 0.3 V) while the electrochemical potential of the source, E_s, was changed using a potentiostat (setup in Fig. 4.5b). It must be noted that since $E_d = E_s + V_d$, by controlling the electrochemical potential of one between the source and drain electrodes it is possible to change the electrochemical potential of the whole channel. Two voltage ranges were chosen for E_s, the first between -0.2 V and +0.6 V, and the second between -0.5 V and +0.9 V. Figure 5.7a reports the values of normalized current I_d/I_{max} (where I_{max} is the maximum recorded drain current) *vs.* E_s and *vs.* time in the -0.2 V to +0.6 V range, highlighting a very stable response. Thus, this range represents an optimal working condition for our OECTs and it was used for the further optimization of the device as a sensor.

The examined voltage range was then extended to -0.5 V / +0.9 V for including the beginning of the redox processes on the cathodic side (Fig. 5.5, black curve). As expected, the neutral form of PEDOT:PSS, which is formed for $E_s \leq 0.4$ V, exhibits the lowest conductivity. With increasing E_s, holes are injected into the PEDOT:PSS backbone, and the oxidation of the polymer occurrs. Consequently, the conductivity of the material increases as indicated by the increase of I/I_{max}. It is noteworthy that the shapes of I/I_{max} *vs.* E_s and C_{ox} *vs.* E_s are very similar,

highlighting how oxidized sites play a key role in the PEDOT:PSS conductivity in the examined range of the electrochemical potential.

The observed strong correlation between I_d, C_{ox} and E_s can thus be used for estimating the electrochemical potential of the channel without the need for a reference electrode. Indeed, the variation of the electrochemical potential of the channel due to the reaction between PEDOT:PSS and an analyte can be directly determined by measuring the shift in the drain current that is induced by the doping/dedoping of the conducting polymer. An appropriate gate voltage, V_g, can be used to enhance the speed and the intensity of this variation of I_d, improving the sensitivity and the limit of detection of the device.

The optimization of the performance of the OECT was studied by using ascorbic acid (AA) as reducing analyte; this choice is, on the one hand, because of the importance of this species in many applicative contexts and, on the other hand, because this analyte is considered a benchmark to test and compare the performances of different electrode systems based on an electrochemical transduction [240].

Since the whole transistor is made of PEDOT:PSS, AA oxidation can take place either at the channel or at the gate electrode, depending on the applied gate voltage. Indeed, if PEDOT is sufficiently oxidized, the following reactions occur:

$$\text{Reaction 1}: \ 2\,\text{PEDOT}^+ + \text{AA} \rightarrow 2\,\text{PEDOT}^0 + \text{oxidized AA} \tag{5.2}$$

$$\text{Reaction 2}: \ \text{PEDOT}^0 \rightarrow \text{PEDOT}^+ + \text{e}^- \tag{5.3}$$

As a result, for positive V_g, E_g is higher than E_s (keeping in mind that $E_d < E_s$ for $V_d < 0$), so AA oxidation mainly takes place at the gate electrode and PEDOT oxidation takes place at the channel. On the other hand, for negative values of V_g, E_g is lower than E_d and so the AA mainly reacts with the channel, while PEDOT is oxidized at the gate electrode.

Figure 5.6a shows the I_d *vs.* time plot whereas different amounts of AA were added to the electrochemical cell. Since the potentials were not applied versus a reference electrode, as would happen by employing a potentiostat, E_g and E_d can change during the AA oxidation leading to a variation of I_d. The added AA reacts at the gate electrode, reducing PEDOT:PSS and lowering its electrochemical potential E_g. Consequently, the applied potential difference V_g between the gate and

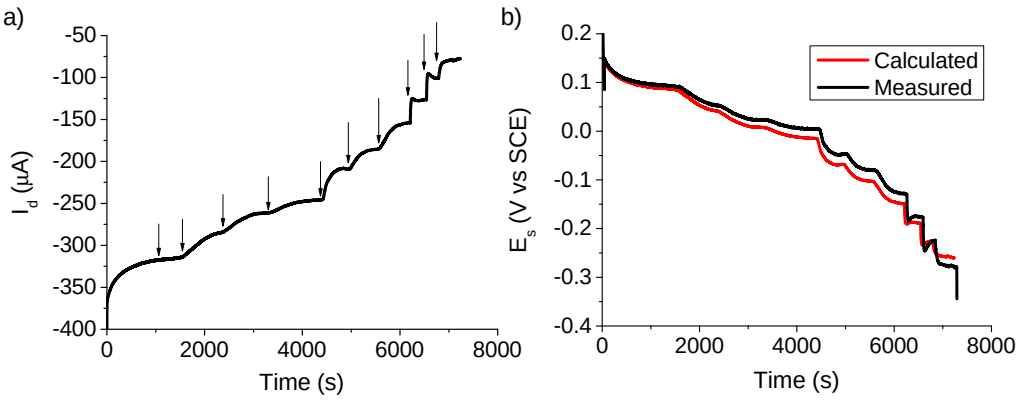

Figure 5.6: (a) $I_d(t)$ curve obtained for an OECT (thickness = 870 nm) after the addition of different amounts of AA (V_g = +0.4 V; V_d = −0.3 V). The additions are labeled with an arrow. (b) Electrochemical potential of the channel (source electrode) during the experiment reported in (a). The black line corresponds to the measured potential, while the red line to the potential that is estimated from I_d by employing a calibration plot.

the source is maintained through the oxidation of PEDOT:PSS sites, increasing the gate current. The higher I_g leads to a higher dedoping of the channel, which results in a decrease of I_d. Because the electrochemical potential of the channel follows Nernst equation (see Section 3.4.1), the drain current is linearly dependent on the logarithm of AA concentration, $\log C_{AA}$.

At the same time, the electrochemical potential of the channel was monitored by measuring the electrochemical potential of the source electrode, E_s, with respect to a reference SCE electrode. The same potential was also calculated from I_d through the inversion of the calibration curve of I_d as a function of E_s shown in Fig. 5.5b. A comparison between the measured and the calculated curves (Figure 5.6b) shows that the two curves are almost superimposable, demonstrating that the variation in the drain current of an OECT is caused by the modification of the electrochemical potential of the PEDOT:PSS channel. Moreover, this result implies that I_d can be effectively used to evaluate the electrochemical potential of the channel, and so that OECTs can be used as electrochemical sensors without the need for a reference electrode or a potentiostat.

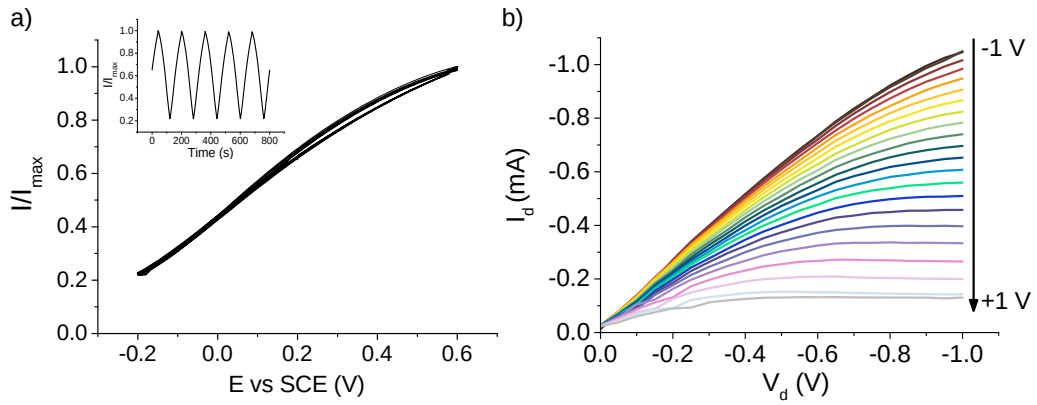

Figure 5.7: (a) I_d/I_{max} *vs.* E on five cycles. In the inset, the corresponding I_d/I_{max} *vs.* t plot is shown. (b) Output curves recorded in PBS 0.1 M pH 5.5, with incremental gate voltage from -1 V to +1 V (step 0.1 V).

5.2.2 Effect of the gate potential

The gate potential is a critical parameter in the OECT operation for sensing. In an OECT, the electrochemical potential of the channel, and consequently I_d, can be controlled by the gate electrode that promotes the doping and de-doping processes. This ability of the device to operate as a transistor was assessed by the acquisition of its output characteristics at increasing V_g (Figure 5.7b).

In addition to the doping state of the channel, V_g controls the electrochemical potential of both the gate and the channel, and consequently governs if the electrochemical reaction between the analyte and PEDOT:PSS occurs at the first or at the latter. Therefore, a characterization of the sensing efficiency of the device at different values of V_g is very important for the optimization of an OECT-based sensor.

As shown in Figure 5.8, different response curves to AA additions were obtained at a constant V_d of -0.3 V by applying different gate voltages from -0.9 V to +0.5 V. When the drain current is stabilized, a stationary regime is established between the rates of the electrochemical processes and the other PEDOT reactions. After AA addition, this regime is altered and a change of I_d is observed. After some time, I_d reaches a new stationary regime that is determined by the reaction thermodynamics together with the kinetics of the gate electrode.

These curves were used to measure the trends of E_s and I_d *vs.* $\log C_{AA}$. The

V_g (V)	Slope E_s (mV decade^{-1})	Slope $\lvert I_d \rvert$ (µA decade^{-1})	Rise time (s)	Gain
No gate	-35 ± 2	-2.5 ± 0.1	227	
0.5	-105 ± 4	-6.0 ± 0.5	70	11
0.25	-77 ± 5	-4.4 ± 0.3	110	32
0	-29 ± 1	-1.8 ± 0.2	259	110
-0.3	-25 ± 7	-1.3 ± 0.2	332	37
-0.6	-64 ± 3	-3.3 ± 0.2	64	11
-0.9	-100 ± 1	-4.5 ± 0.1	20	5.2

Table 5.1: Performance of the OECT operating at different V_g. The rise time has been evaluated as the time required by I_d to rise from the base-line to 90% of its final value after an increment in AA concentration of 0.1 mM, while the gain is given as $\Delta I_d/\Delta I_g$.

slopes of the linear fits of these parameters are reported in Table 5.1. For all the examined gate potentials, both E_s and the absolute value of I_d (which is negative for $V_d = -0.3$ V) decrease for an increase in AA concentration. On the one hand, if AA oxidation takes place at the channel of the transistor ($V_g < 0$), the reaction between PEDOT and AA directly leads to a reduction of PEDOT and thus to a decrease of E_s. On the other hand, if the reaction takes place at the gate ($V_g > 0$), the consecutive increase of the oxidative gate current leads to the dedoping of the channel, again decreasing E_s.

E_s and I_d result linearly dependent on $\log C$, and for both parameters the values of the slopes are the lowest when the applied V_g is -0.3 V. Furthermore, the value observed for $V_g = 0$ is exactly -29 mV decade^{-1}, the value expected for the thermodynamics of an electrochemical process that involves two electrons [221]. Similarly, if no potential is applied to the gate, and consequently its electrochemical potential is not forced to be equal to the source potential, the slope is equal to -35 mV decade^{-1}, still very close to -29 mV decade^{-1}. Such results point out that for low values of applied gate potential the OECT response is controlled by the thermodynamics of the reaction between PEDOT:PSS and AA. The slopes of E_s and I_d *vs.* $\log C_{AA}$ then increase with the absolute value of V_g, suggesting an amplification on the variation in I_d generated by the gate voltage. Indeed, the best sensitivities in terms of I_d were obtained for the maximum applied gate voltages, +0.5 and -0.9 V.

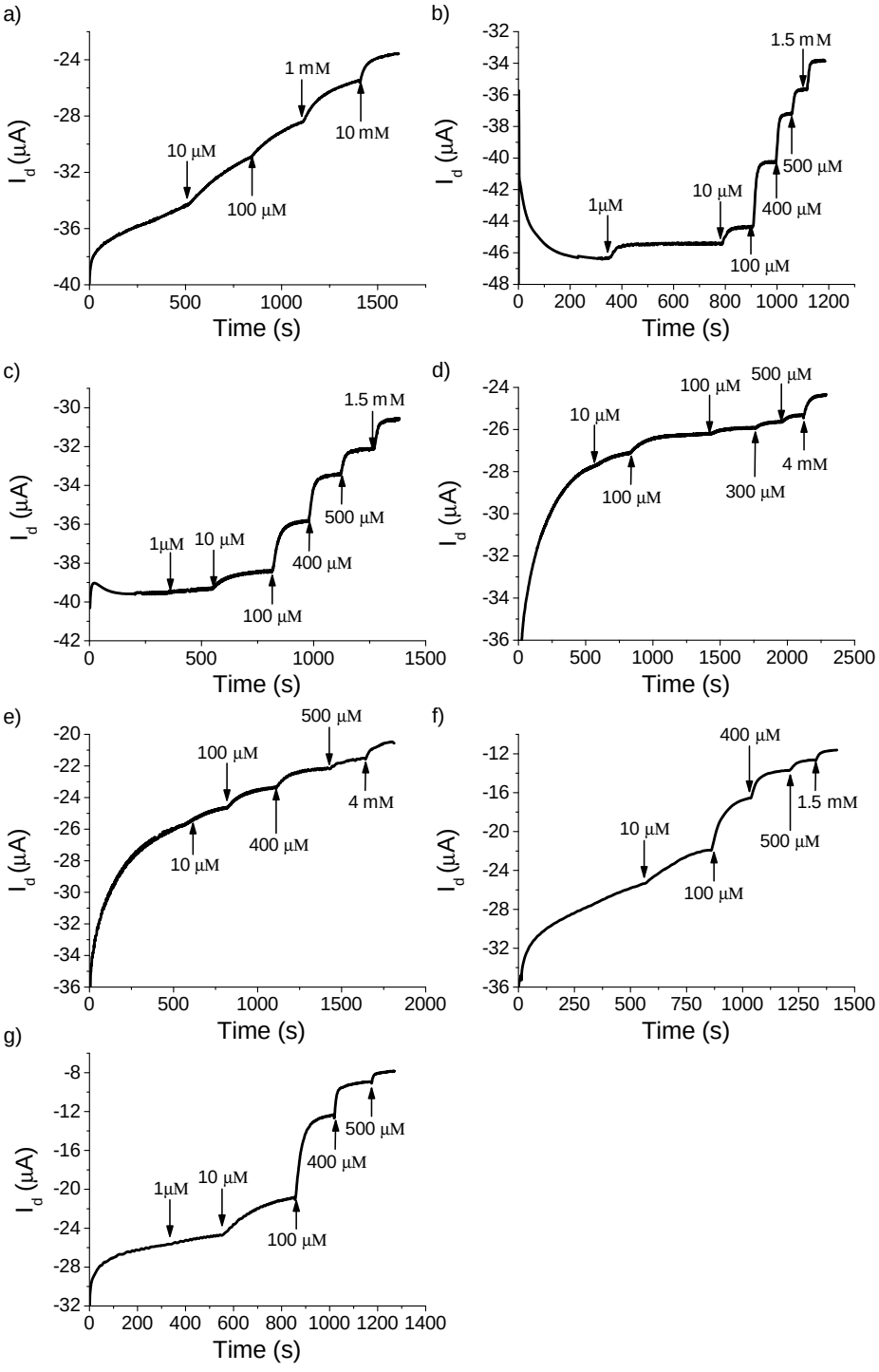

Figure 5.8: Curves of I_d *vs.* time obtained for different V_g with AA additions. (a) No V_g applied; (b) $V_g = -0.9$ V; (c) $V_g = -0.6$ V; (d) $V_g = -0.3$ V; (e) $V_g = 0$ V; (f) $V_g = +0.25$ V; (g) $V_g = +0.5$ V. The concentration increments in the electrolyte solution due to AA additions are reported with arrows.

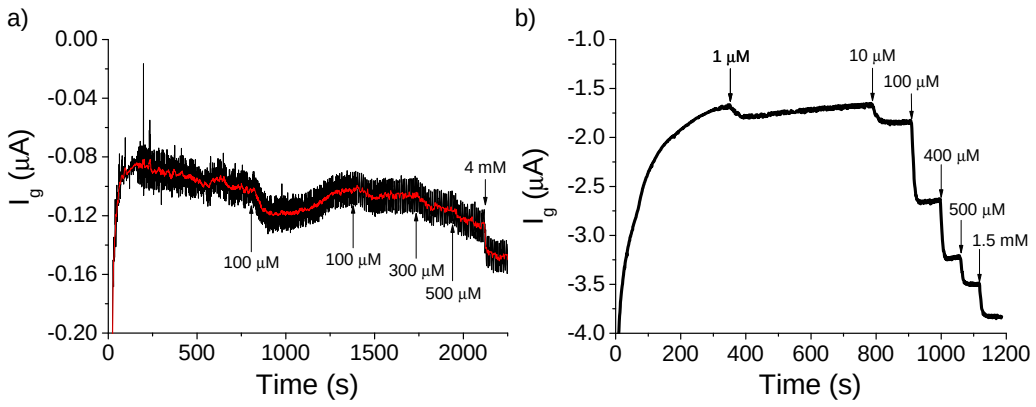

Figure 5.9: I_g *vs.* time recorded at (a) $V_g = -0.3$ and (b) $V_g = -0.9$ V while different amounts of AA were added to the electrolyte solution. The concentration increments of AA in the electrolyte solution are reported with arrows.

This effect can be explained by considering that an increase in V_g leads to an increase of the gate current, suggesting that also the rate of redox reactions of PEDOT increases. Thus, the different behaviors observed at low and high gate voltages is clearly visible in the $I_g(t)$ curves shown in Figure 5.9. At low voltage (-0.3 V), I_g is low and a very weak variations are observed upon AA addition. The device is only ruled by the reaction between AA and PEDOT, which occurs until the thermodynamic equilibrium is reached. On the other hand, at high voltage (-0.9 V), I_g is about 20 times higher, and after the addition of AA a significant change in the current is observed. The current is stable after each addition, suggesting that the thermodynamic equilibrium is not reached and the device is controlled also by a kinetic effect.

An evaluation of the stability of I_d *vs.* time as a function of V_g is important for the optimization of OECT operation. From Figure 5.8, it is apparent that the drift in the drain current is higher when the gate voltage is not applied, or similarly 0 V are given. The drift is then only slightly reduced for low potentials (-0.3 and +0.25 V), and then the signal becomes more stable at high gate potentials (-0.6, -0.9 and +0.5 V), quickly reaching a constant value after each addition. However, different rise times are observed depending on the sign of the applied gate potential, with a slower response for positive gate potentials (Table 5.1). A high rise time points out a slower response of the device, which induces a larger uncertainty on the

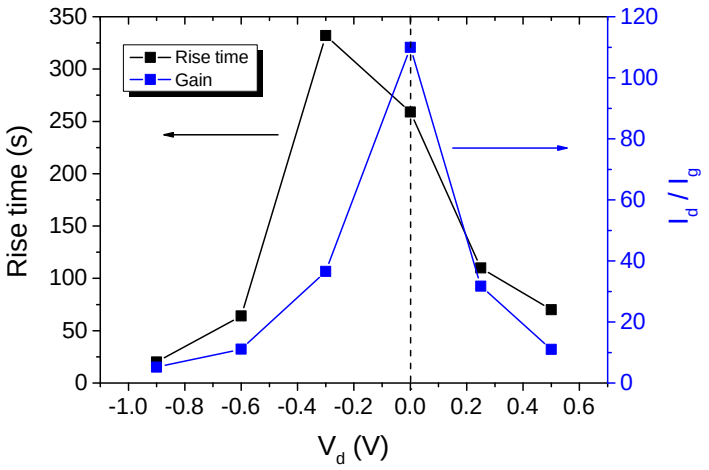

Figure 5.10: Rise time (black curve) and current gain (blue curve) relative to a 10 μM addition of AA in an OECT polarized using different gate voltages.

determination of I_d after each addition.

Finally, current amplification, $G = \Delta I_d / \Delta I_g$, was obtained from the analysis of the curves reported in Figure 5.8. This quantity was calculated at low AA additions (10 μM), since at high concentrations the gate current becomes comparable to the drain current, introducing a contribution in the measurement of I_d that cannot be quantified precisely. As shown in Table 5.1, the current gain is higher at low V_g, with a sharp maximum at $V_g = 0$ which is due to the very low gate current observed in that condition, and then decreases for increasing gate voltage.

Figure 5.10 shows an interesting comparison between these two figures-of-merit, rise time (black curve) and current amplification (blue curve), highlighting a trade-off between these parameters: at low V_g, the gate current is very low, increasing the amplification of I_d; however, the small gate current is reflected on a slower response, since the ion flux that causes the de-doping of the PEDOT:PSS channel is smaller. Conversely, at high gate voltages the gate current is higher, reducing the current amplification but increasing the speed of the de-doping process.

Since $V_g = -0.9$ V ensures both high sensitivity and high signal stability, this setting has been chosen for the sensing of several reducing analytes.

5.2.3 Effect of the thickness

As recently pointed out by Rivnay *et al.*, in OECTs all the volume of the organic semiconductor is involved in the electrochemical reactions that control the operation of the device [77]. In order to investigate the effect of the PEDOT:PSS film thickness on the device response, two transistors with the same geometry were prepared by spin coating PEDOT:PSS at 3000 rpm for 10 s and at 500 rpm for 3 s, obtaining thicknesses equal to 170 nm for the thinnest and 870 nm for the thickest.

The $I_d(t)$ curves obtained with these OECTs are reported in Figure 5.11, and the relative limit of detection, sensitivity, linearity range and rise time are compared in Table 5.2. The lowest limit of detection and the fastest response are obtained using the thinnest transistor, while the normalized sensitivities, expressed as the slope of the linear fit of the quantity $1 - I/I_{max}$ *vs.* $\log C_{AA}$, are very similar. Finally, the variation of I_d is linear with $\log C_{AA}$ in a wider range for the thickest transistor.

These results can be understood by considering that the reduction process of PEDOT:PSS is taking place in the channel, as a consequence of the AA oxidation that takes place at the gate in order to keep the gate voltage constant. I_d depends on the variation of charge carriers concentration that involves all the volume of the PEDOT:PSS channel. Therefore, if the PEDOT:PSS thickness decreases, less PEDOT sites have to be reduced in order to obtain the same change in conductivity. Since the number of sites that are reduced per unit time depends on the surface of PEDOT:PSS exposed to the electrolyte, which is the same for both transistors, the variation of I_d is then faster for the thinnest film. Similarly, the quantity of analyte required to induce a measurable change in conductivity is smaller, explaining the difference in the limit of detection.

The sensitivity, given as the slope of $1 - I/I_{max}$ *vs.* $\log C_{AA}$, appears to be independent from the thickness of PEDOT:PSS, instead. Indeed, as described in Section 3.4.2, the sensitivity of an OECT is related to the ratio of the gate and channel volumetric capacitances, $\gamma = C^*_{ch}/C^*_g$. Since both the gate and the channel are made in PEDOT:PSS, γ only depends on the relative volumes of the channel and the gate. Moreover, the geometry of the tested device is the same,

Thickness (nm)	LOD (µM)	Sensitivity (decade^{-1})	Linear range (µM)	Rise time (s)
170	0.4	0.267 ±0.004	10 ÷100	145
870	1	0.299 ±0.005	10 ÷1000 M	434

Table 5.2: Performance of OECTs with different thicknesses.

implying that the ratio of the channel and gate areas, A_{ch}/A_g, is the same as well, so that γ only depends on the the ratio of the thicknesses T_{ch}/T_g. Even though the OECTs under examination have different thicknesses, the channel and gate electrode on the same transistor do have the same thickness. Thus, in our OECTs γ, and consequently the sensitivity, does not scale with the thickness.

Finally, the linear fits shown in the insets of Figure 5.11 point out that in the thickest transistor I_d follows a linear trend with the logarithm of AA concentration over a wider range. More specifically, while the onset of the linear behavior is approximately the same (10^{-5} M), in the thickest transistor the linear region extends up to a concentration 10 times higher than that of the thinnest (10^{-3} M and 10^{-4} M, respectively). For a positive gate voltage, as in the case of these measurements, this upper limit depends on the quantity of available sites in the gate electrode that can be reduced by AA, which of course depends on its volume. At high analyte concentrations, the rate of the reaction between PEDOT:PSS and AA (Equation 5.2) is not enough to oxidize all the AA molecules that interact with the gate electrode, and as a consequence the induced variation in I_d is lower than the ideal case. From a different point of view, at high AA concentrations the electrochemical potential of the electrolyte, E_{sol}, is already close to the electrochemical potential of the gate electrode E_g, and further additions of analyte do not induce a significant variation in their relative positions. Again, the relative variation of E_{sol} with respect to E_g depends on the relative quantities of available sites in the gate electrode and AA molecules added. As a result, the highest concentration limit for saturation of the thickest device shown in Fig. 5.11 is due to its higher number of active sites that can undergo reduction from the analyte.

To summarize, thin devices ensure both high sensitivity and high signal stability, as well as a better limit of detection compared to thick devices. For these reasons, the sensing of several analytes presented in this Chapter was carried out

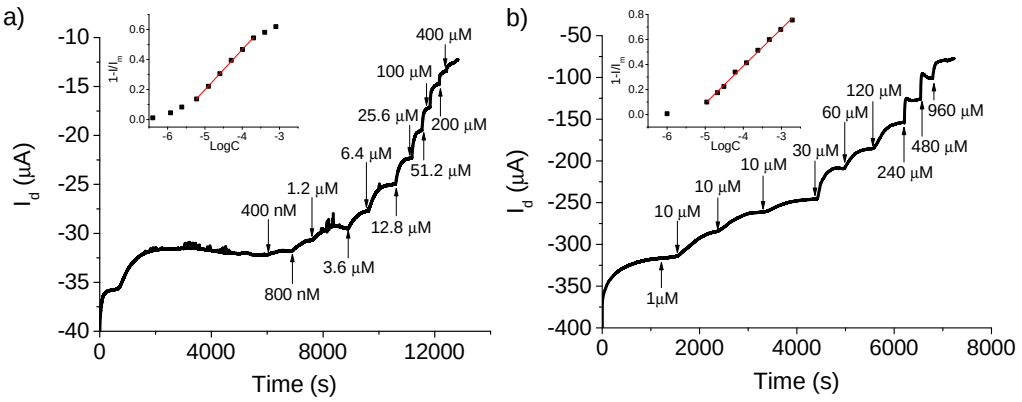

Figure 5.11: I_d *vs.* time curves for OECT with thickness (a) 170 nm and (b) 870 nm after the addition of different amounts of AA (V_g = +0.4 V; V_d = −0.3 V). The additions are labeled with an arrow where the increase of concentration is reported. In the insets, the quantity $1 - I/I_{max}$ *vs.* $\log C_{AA}$ relative to each curve is reported.

using OECTs with thin layers (< 200 nm) of PEDOT:PSS.

5.3 Sensing of Biochemical Analytes

In this Section, the calibration and the results of the realized OECTs for the sensing of various analytes are presented. For all the measurements, the geometry of the device is the one shown in Fig.5.4, while the experimental setup is described in Section 4.2.4. For each analyte, several quantities at known concentration were added to the electrolyte under magnetic stirring while measuring the gate and drain currents of the OECT at constant potentials V_g and V_d. From the recording of $I_d(t)$, a calibration curve was obtained from which the limit of detection (LOD), the linear range of $1 - I_d/I_{max}$ *vs.* $\log C$, and the sensitivity were calculated. The LOD was calculated as the concentration that leads to a signal 3 times higher than experimental noise, evaluated as the standard deviation of the blank signal, while the sensitivity was calculated as the slope of the linear fit of $1 - I_d/I_{max}$ *vs.* $\log C$.

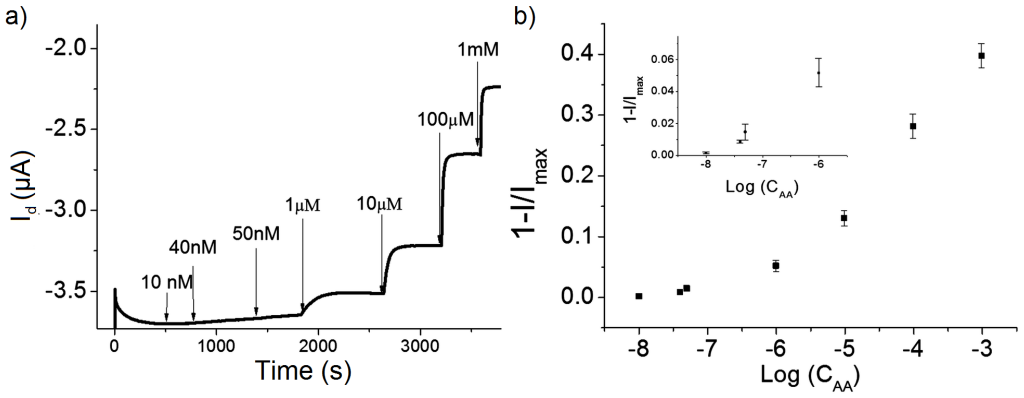

Figure 5.12: (a) I_d *vs.* time curve ($V_g = -0.9$ V; $V_d = -0.3$ V) obtained after the addition of different AA amounts. The additions are labeled with arrows where the increase of concentration is reported. (b) $1 - I/I_{max}$ *vs.* $\log C_{AA}$ plot.

5.3.1 Ascorbic acid

L-Ascorbic acid (AA), or vitamin C, is a very important biological compound that plays a key role in many metabolic reactions [76]. Moreover, as mentioned before, this analyte is often used as a benchmark to compare the performances of different electrochemical sensors [240].

Figure 5.12 reports the I_d *vs.* time curve that has been obtained by adding different AA amounts to the electrolyte solution. The plot of $1 - I/I_{max}$ *vs.* $\log C_{AA}$ (Fig. 5.12b) shows two different regions wherein a linear correlation can be established. The first region corresponds to the range 10^{-8} to 10^{-6} M, and the slope of the linear fit is equal to $(2.6 \pm 0.3) \times 10^{-2}$ decade^{-1}. The second region is comprised between 10^{-6} and 10^{-3} M with a slope of (0.12 ± 0.01) decade^{-1}. The LOD, evaluated considering the linear plot in the low concentration range (10^{-8} to 10^{-6} M), results equal to 13 nM. The LOD estimated for our OECT is lower than the values reported in literature for amperometric sensors used for AA determination [76].

In human tissues, AA concentration is usually found between 0.04 and 4 mM [241], while vitamin C-rich food contains $0.005 \div 2$ mM [242]. So, the OECT is sensitive enough for AA analysis in food and biological samples. Indeed, this sensor was used to measure the amount of AA in the Aspirina C (Bayer) medicinal product. A 3.2 g tablet was dissolved in 50.0 mL of water, then 0.050 mL of such solution was added to 10.0 mL of PBS solution wherein the OECT was immersed.

The variation of I_d was recorded and used to evaluate the AA amount in the tablet through the calibration curve represented in Fig. 5.12b. The measured amount of AA is equal to (0.27 ± 0.03) g, in good agreement with the value declared by the producer (0.24 g).

5.3.2 Dopamine

As mentioned in Section 5.1.1, dopamine (DA) is an important neurotransmitter in the mammalian central nervous system, and the determination of its concentration in a biological environment is an important problem in analytical biochemistry [199].

In the presence of a redox-active species such as dopamine in the supporting electrolyte, the gating effect is amplified, owing to the reaction described in Equation 5.1, which takes place at the gate electrode for a negative V_g. In order to continuously monitor the response of the OECT to additions of dopamine, the real-time I_d response was measured at the fixed voltages $V_g = -0.9$ V and $V_d = -0.3$ V. Figure 5.13a shows the $I_d(t)$ curve of a device characterized in PBS solution during the additions of various concentrations of dopamine. The device exhibits response to the addition of 50 nM dopamine, and the respective change of I_d increases with the increase of analyte concentration with a logarithmic behavior.

From the analysis of $1 - I/I_{max}$ *vs.* $\log C_{DA}$, a linear range is found between 10^{-6} and 10^{-4} M, with a slope of (0.11 ±0.01) decade^{-1}, very similar to the value obtained for ascorbic acid, and a LOD of 50 nM, which is almost one order of magnitude lower than the LOD obtained with PEDOT:PSS amperometric sensors (see Section 5.1.2). However, dopamine concentration in human plasma is usually below 0.13 nM [243], so further optimization of the device is required for being used in real applications.

For the treatment of Parkinson's disease, dopamine cannot be used because it cannot cross the protective blood-brain barrier; for this reason its precursor, L-3,4-dihydroxyphenylalanine, also known as L-DOPA or levodopa, is used to increase dopamine concentration in the brain [244]. The administration of levodopa to patients increases its concentration in blood to much higher levels than dopamine,

reaching levels on the order of 1 mM during the first hours following its intake [245].

Levodopa was added at increasing concentrations in the electrolyte solution of our OECT, inducing a variation in I_d (Figure 5.13b). As for dopamine, a linear region for $1 - I/I_{max}$ *vs.* $\log C_{DA}$ is found between 10^{-5} and 10^{-3} M, with a slope of $(7.5 \pm 0.2) \times 10^{-2}$ decade^{-1} and a LOD of 5 µM, which is far beyond the target limit for real applications.

5.3.3 Gallic acid

Gallic acid (GA) is a phenolic acid commonly used as a standard for determining the polyphenol content of various analytes, which is reported in gallic acid equivalents (GAE) [246]. Phenolics are found in all plants and are present in some of the most consumed food products in the world, such as tea, coffee, wine, and olive oil [247, 248]. They are responsible for many important properties of these substances, including color, bitterness, astringency, and antioxidant capacity. More specifically, their ability to inhibit oxidative stress gained a huge interest in the fields of food sciences and nutraceuticals [249, 250].

The application of our OECT to the sensing of antioxidant species such as

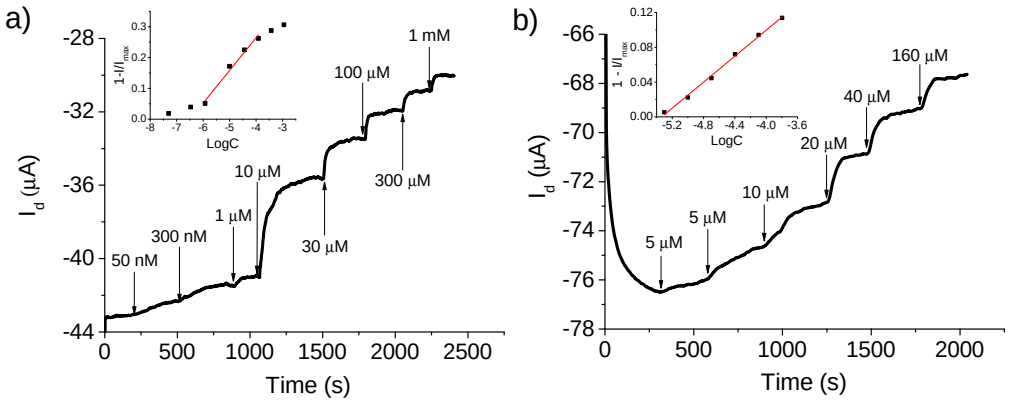

Figure 5.13: I_d *vs.* time curve ($V_g = -0.9$ V; $V_d = -0.3$ V) obtained after the addition of different dopamine (a) and levodopa (b) amounts. The additions are labeled with arrows where the increase of concentration is reported. In the insets, $1 - I/I_{max}$ *vs.* $\log C_{DA}$ is plotted.

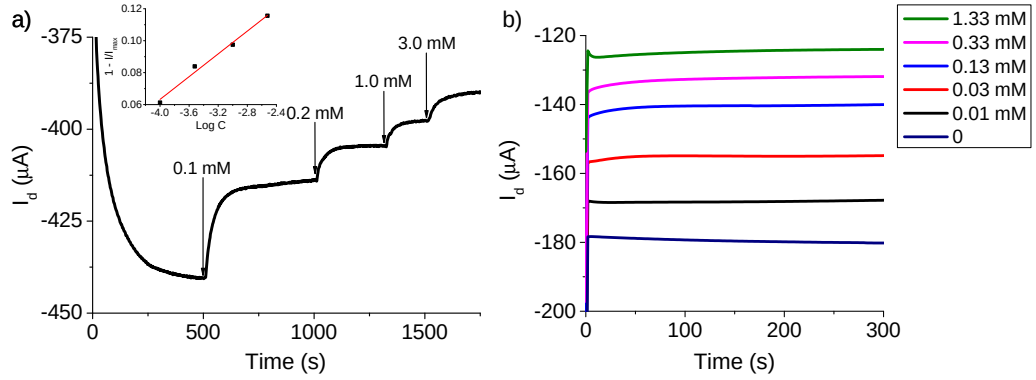

Figure 5.14: (a) I_d *vs.* time curve ($V_g = -0.9$ V; $V_d = -0.3$ V) obtained after the addition of different gallic acid amounts. The additions are labeled with arrows where the increase of concentration is reported. In the inset, $1 - I/I_{max}$ *vs.* $\log C_{GA}$ is plotted. (b) I_d of the device with electrolyte solution containing different concentrations of gallic acid. Gallic acid was not added at increasing concentration to the same solution, but each solution was prepared separately and then tested using the same OECT.

polyphenols was tested by using gallic acid as a model analyte. At first, several subsequent additions were made in the electrolyte solution, in order to obtain a calibration curve from the analysis of $I_d(t)$ (Figure 5.14a), obtained at the fixed voltages $V_g = -0.9$ V and $V_d = -0.3$ V. The linear fit of $1 - I/I_{max}$ *vs.* $\log C_{GA}$ gave a slope of $(3.5 \pm 0.3) \times 10^{-2}$ decade^{-1}, and a linear response range was found between 10^{-6} and 10^{-2} M with a limit of detection of 1 μM.

The sensor was then tested for a real application, the determination of the concentration of antioxidant agents (mainly polyphenols) in wine. A new calibration curve was obtained by using several different test solutions made of PBS and GA at a specific concentration, in a range suitable with the concentrations that are typically found in wines (about 1 mM for white wines and 10 mM for red wines [251, 252]). Each solution was tested separately by recording the I_d current of the same OECT operating at fixed voltages ($V_g = -0.9$ V and $V_d = -0.3$ V) using that solution as electrolyte. The device was then rinsed and the measurement was repeated for a different solution. The solutions were not tested for increasing concentration, as in the usual calibration curves, but the order of testing was chosen randomly. As shown in Figure 5.14b, a good correlation was found also

Wine	OECT (mg/L)	Folin-Ciocâlteu (mg/L)
White Tavernello	240 ± 60	217
Bianco del Rubicone	50 ± 12	273
Red PAM	1400 ± 300	1317
Pinot (rosé)	32 ± 12	178
Sangiovese	600 ± 200	800
Red Toscano	900 ± 200	1044

Table 5.3: Total phenolic content of four wines expressed as gallic acid equivalent measured with an OECT and the Folin-Ciocâlteu method.

in this case for I_d *vs.* $\log C_{GA}$, with a linear response between 10^{-3} and 1 M and a slope for $1 - I/I_{max}$ *vs.* $\log C_{GA}$ equal to (0.12 ±0.02) decade^{-1}.

Finally, the device was used for the determination of the total polyphenol concentration in six different wines, and the obtained values were compared to the results obtained using the Folin-Ciocâlteu method, one of the standard analytical techniques used for the determination of the polyphenol content in a solution [253]. The results obtained with our OECTs, shown in Table 5.3, are in good agreement with the reference technique in four samples, demonstrating that OECTs can be effectively used for sensing the concentration of antioxidant species in red wine, where the polyphenol concentration is higher. However, the results for white wines, whose polyphenol concentration is lower, show an underestimation of the polyphenol content, meaning that an optimization for this range of concentrations is still required. Once improved, this application could be easily extended to other solutions, such as olive oil, tea and coffee, with only slight modifications of the device.

5.3.4 Oxidizing agents

In previous paragraphs, the OECT has been used for sensing reducing agents such as dopamine, ascorbic acid and polyphenols. Also the applications of OECTs as biochemical sensors that can be found in literature are in their vast majority related to the revelation of reducing analytes [29, 46, 60, 70], which de-dope the PEDOT:PSS channel of the transistor, inducing a measurable decrease in the drain current.

However, PEDOT:PSS-based OECTs can also be used for the detection of

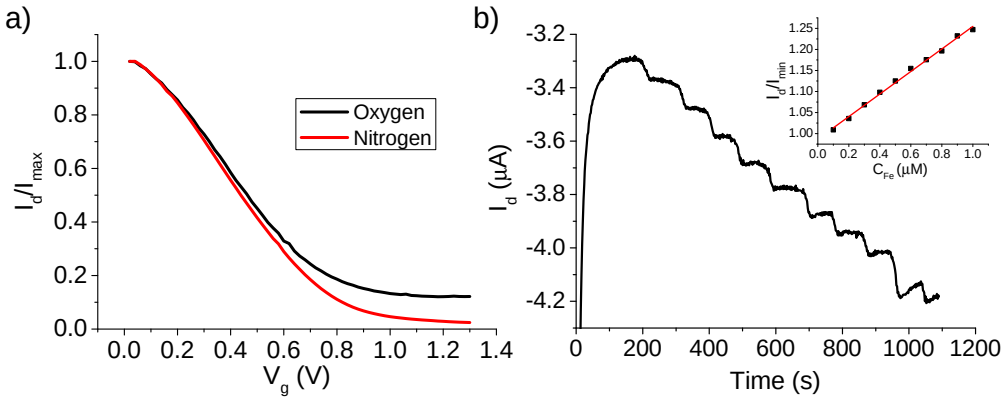

Figure 5.15: (a) Transfer curves of an OECT taken in air (black curve) and in nitrogen-saturated atmosphere (red curve) normalized to the maximum I_d, which corresponds to $V_g = 0$. (b) I_d *vs.* time curve of the device ($V_g = 0.7$ V, $V_d = -0.3$ V). Fe^{3+} was added several times to obtain a calibration curve of I_d *vs.* C (inset). Each addition corresponds to an increase of 0.1μM in Fe^{3+} concentration.

oxidizing species. Indeed, if a positive V_g is applied to turn off I_d, and then an oxidizing agent is added to the electrolyte, the reduced $PEDOT^0$ in the channel can react with the analyte and turn back to its conductive state $PEDOT^+$, increasing I_d.

Since in ambient conditions oxygen is present in solution at a relatively high concentration, its contribution to PEDOT oxidation can interfere with the detection of the analyte, because of the reaction:

$$4\,\mathrm{PEDOT}^0 + \mathrm{O_2} + 4\mathrm{H}^+ \rightarrow 4\,\mathrm{PEDOT}^+ + 4\mathrm{H_2O} \tag{5.4}$$

This contribution increases the time required to reach an equilibrium state, causing a significant drift in the drain current. The effect of oxygen on the operation of the OECT can be observed by comparing transfer curves taken in ambient conditions (*i.e.* with oxygen) and in a nitrogen-saturated atmosphere (*i.e.* with very low residual oxygen in solution), as shown in Figure 5.15a. From these curves, the ratio I_{dmax}/I_{dmin} can be evaluated in order to quantify the efficacy of the gating effect in the transistor. As a result, this ratio increases from ~10 to ~40 by removing the oxygen from the electrolyte solution. For this reason, the detection of oxidizing agents with OECTs was carried out in nitrogen-saturated atmosphere.

In order to verify the ability of OECTs of sensing oxidizing agents, their response was preliminarily calibrated using the ion Fe^{3+} as model analyte. The operating voltages were chosen as $V_d = -0.3$ V and $V_g = 0.7$ V, so as to maintain a low drain current, but keeping the device in a region at high transconductance (the slope of the transfer curve in Figure 5.15a). When Fe^{3+} is added to the electrolyte solution, holes are injected into the PEDOT channel, according to the process:

$$PEDOT^0 + Fe^{3+} \rightarrow PEDOT^+ + Fe^{2+} \tag{5.5}$$

increasing PEDOT conductivity and, consequently, I_d.

The curve of $I_d(t)$ relative to the addition of Fe^{3+} is shown in Figure 5.15b. From the corresponding calibration curve (inset), a linear dependence of the normalized current I_d/I_{min} *vs.* C was found, highlighting a non-Faradaic nature of the sensing process.

Following the preliminary calibration with Fe^{3+}, OECTs were used for the sensing of 2,2-diphenyl-1-picrylhydrazyl, or DPPH. This molecule is a stable radical, often used in tests for the determination of antioxidant power to simulate free radicals [254]. Its interaction with PEDOT is analogous to Fe^{3+}:

$$PEDOT^0 + DPPH \rightarrow PEDOT^+ + DPPH^- \tag{5.6}$$

The calibration curve was obtained using the same potentials used for the measurement of Fe^{3+}, $V_d = -0.3$ V and $V_g = 0.7$ V. The acquired $I_d(t)$ curve and the relative calibration curve are reported in Figure 5.16. As shown in the calibration plot in Fig. 5.16b, two regimes can be identified for I_d/I_{min} *vs.* C: a linear trend for concentrations between 0.5 μM and 5 μM, and a logarithmic trend for higher concentrations. This difference in the OECT operation depending on the analyte concentration can be explained as a transition between a low concentration regime where the number of injected holes is directly proportional to the analyte concentration, following Faraday law on electrolysis, and a high concentration regime following Nernst equation, where the electrochemical potential of the channel depends on the logarithm of analyte concentration.

In the linear range, the sensitivty was calculated as (2.62 ± 0.04) A mol^{-1},

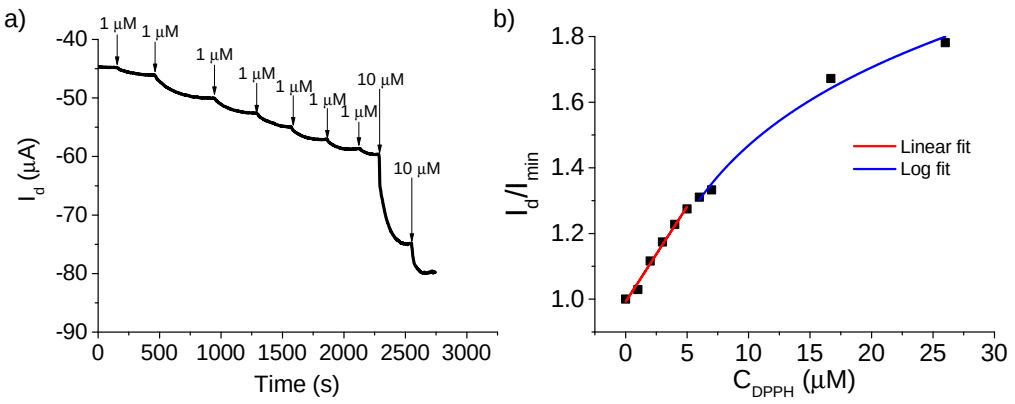

Figure 5.16: (a) I_d *vs.* time curve of the device (V_g = 0.7 V, V_d = −0.3 V) after the addition of different amounts of DPPH. The additions are labeled with arrows where the increase of concentration is reported. (b) Calibration curve of DPPH. Two regimes were identified, a linear dependence at low concentrations (red fit) and a logarithmic dependence at higher concentrations (blue fit).

with a LOD equal to 0.5 µM. In the logarithmic range, the sensitivity was found as (0.78 ± 0.05) decade^{-1}, while the LOD was evaluated as 1 µM.

5.3.5 Selectivity

As described in previous paragraphs, PEDOT:PSS-based OECTs can be used to detect a wide range of redox-active species in solution, without any functionalization. Even though this feature opens up a wide range of possible applications, it also represents the main limitation for the use of OECTs on real samples, since these devices are not able to discriminate between the analyte of interest and other interferent substances. A preliminary study was carried out to overcome this issue by taking advantage of two effects involved in the electrochemical reactions involved in OECTs.

The first observation is that each substance which is present in the solution to be analyzed reacts at a different electrochemical potential. Thus, by performing a scan of the applied gate voltage, which is used to control the electrolyte potential with respect to the channel as well, it is possible to highlight the contribution of each interferent. This is especially evident from the analysis of transconductance, $g_m = \partial I_d/\partial V_g$, that expresses the effect of the applied gate voltage on the drain

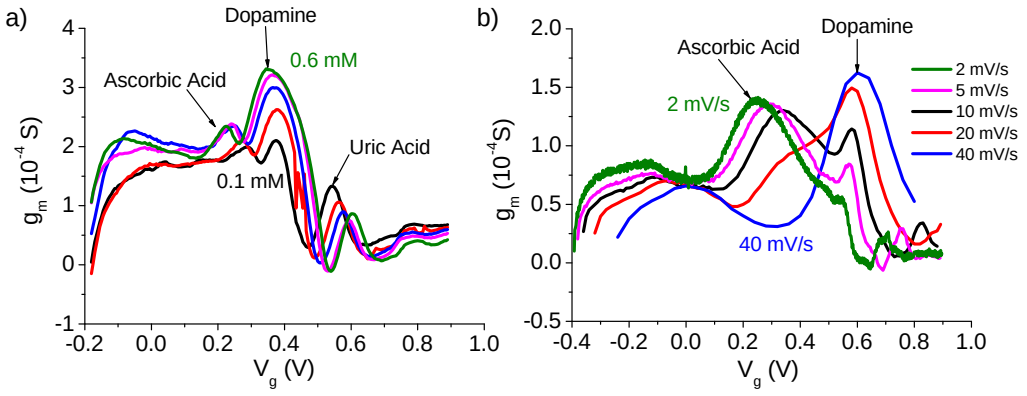

Figure 5.17: Transconductance *vs.* V_g of an OECT with analyte and interferents in the electrolyte solution. (a) Ascorbic acid 0.2 mM, uric acid 0.2 mM and dopamine from 0.1 (black curve) to 0.6 mM (green curve). (b) Ascorbic acid 1.5 mM and dopamine 0.1mM at different scan rates, from 2 mV/s (green curve) to 40 mV/s (blue curve).

current and can be easily obtained as the derivative of the transfer curve of the transistor.

An example is shown in Figure 5.17a, where a solution containing two interferents, ascorbic acid 0.2 mM and uric acid 0.2 mM, and an analyte (dopamine) in variable concentration from 0.1 to 0.6 mM is analyzed. Three separated peaks can be clearly identified, pointing out the contribution coming from each molecule. The position and height of the peaks of the interferents are ideally independent from analyte concentration. However, the peak of uric acid is influenced by the different amount of reduced PEDOT found in the channel when different dopamine concentrations are used; since the scan direction of V_g goes in the direction of increasing potential, the oxidation of ascorbic acid and dopamine takes place before the oxidation of uric acid, changing the electrochemical potential of the PEDOT:PSS channel and thus the drain current. The peak of dopamine, as expected, increases with increasing concentration, suggesting that this method can be used for the detection of an analyte in the presence of interferents.

A second observation that was verified is that the reaction of PEDOT with different chemical species follows different kinetics, and consequently the effect of the interferents will depend on the speed of the gate voltage scan. Figure 5.17b

shows the transconductance *vs.* V_g of an OECT with an electrolyte solution containing the analyte (dopamine 0.1 mM) and an interferent (ascorbic acid 1.5 mM) taken at different scan rates for te gate voltage, from 2 mV/s to 40 mV/s. Since the peak of AA is located at a lower potential, it reacts with PEDOT before dopamine, reducing significantly the increase in the gating effect due to the analyte. However, the redox reaction between PEDOT and AA is slower than the reaction occurring between PEDOT and dopamine, so when the scan rate is increased, less and less AA can interfere in the process, increasing the effectiveness of dopamine. This effect is reflected in the decrease in the peak of AA, which is accompanied by a strong increase in the peak of dopamine.

The two effects illustrated in this paragraph represent two promising methods that, with further optimization, could lead to the realization of selective sensing with OECTs without the need for functionalization.

5.4 Wearable Sensors

In recent years the interest on the development of wearable electronic devices has grown notably. Wearable technology is today applied to the production of different special garments such as protective clothing, soldier uniforms, and activity trackers. Furthermore, there is a tremendous interest in developing wearable technology for physiological monitoring, in order to obtain a novel class of personalized point-of-care devices that could be extensively and effortlessly integrated into the daily life of a patient in the form of wireless body sensors [255, 256]. In this Section, the development of a wearable sensor based on the all-PEDOT:PSS OECT previously described by integration with textile substrates is presented.

5.4.1 Geometry and fabrication

Using a PEDOT:PSS formulation similar to the one used for the fabrication of OECTs on glass substrates, the channel and gate electrode were deposited on woven cotton and lycra, with a spatial resolution of about 1 mm. The details on the PEDOT:PSS formulation used and the deposition process are reported in Section 4.1.1. As shown in Figure 5.18, the PEDOT:PSS tracks display a well

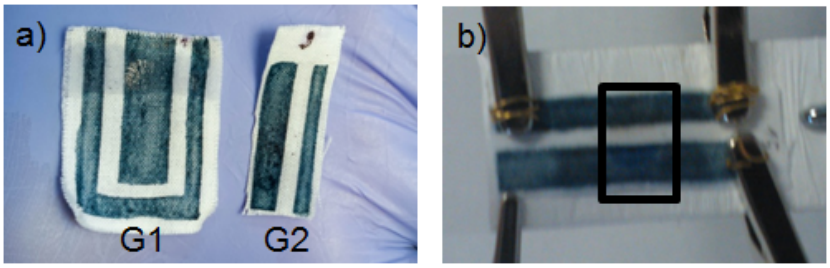

Figure 5.18: (a) Picture of two OECTs realized with geometry G1 (left) and G2 (right). (b) In transistors with geometry G2, the analyte is added in the area between the gate and the channel only (black square), which is delimited by a thin film of PDMS.

defined shape that is clearly visible onto the fabrics.

The devices were realized in two geometries, named G1 and G2, which are shown in Figure 5.18a. These geometries were developed for two different applications. The geometry G1 is suitable for the immersion in the electrolyte solution in an electrochemical cell and was used to reproduce the devices realized on glass described in previous Section. The geometry G2 was used instead for testing the OECT performance in dry conditions, where the electrolyte solution was added in droplets of 10 μL of volume in the area between the gate electrode and channel to simulate the wetting of fabric due to sweat (Figure 5.18b). The sheet resistance of PEDOT:PSS-modified textile was tested using the 4-probe technique and resulted equal to (38 ± 7) Ω/□.

In order to produce a wearable device, washability must be taken into account. This property was evaluated for our printed OECTs by measuring their sheet resistance after several washing cycles. In Figure 5.19a the sheet resistance of the channel as a function of the number of washing cycles is reported. The electrical properties of PEDOT-modified textile change after the early washing steps, but after two cycles it reaches a value (about 70 Ω/□) that remains constant after the following washings.

5.4.2 Sensing in ideal conditions

At first, the sensing ability of a textile OECT with a similar geometry (G1, Figure 5.18a) to the one developed for chemical sensors on glass substrates was tested.

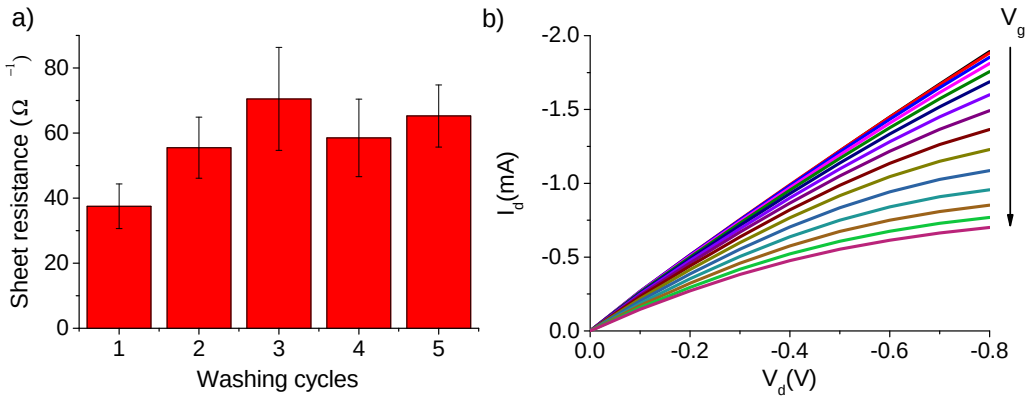

Figure 5.19: (a) Sheet resistance of a PEDOT:PSS track obtained by screen printing as a function of the number of washing cycles. (b) Characteristic curves recorded for a G1 transistor with V_g from -0.7 V to +0.7 V (step 0.1 V).

This layout enables to immerse the active area of the transistor in a solution, whereas the electrical terminals are kept dry. This represents an ideal condition for electrochemical experiments, where the analyte is uniformly distributed in the electrolyte solution and the sensing area of the device is completely in contact with the electrolyte. As previously described, the application of a positive gate voltage decreases the current I_d, beacause of PEDOT reduction in the channel. This can be seen in the output curves presented in Figure 5.19b.

The sensing features of textile OECTs in G1 geometry were tested by evaluating its response to ascorbic acid (AA), dopamine (DA) and adrenaline (AD). The transistors were soaked in PBS solution under stirring, and the gate and drain were biased at -0.9 V and -0.3 V, respectively. These values were chosen as a consequence of the study on the effect of the gate voltage on the sensing performance of our OECTs presented in Section 5.2. Figure 5.20a shows the I_d *vs.* time plot recorded while different amounts of adrenaline were added in the electrochemical cell. The adrenaline can be detected by the sensor because it is a oxidizable compound and, consequently, it can react with the positively-biased PEDOT:PSS at the channel:

$$\text{PEDOT}^{+} + \text{AD} \rightarrow \text{PEDOT}^{0} + \text{oxidized AD} \tag{5.7}$$

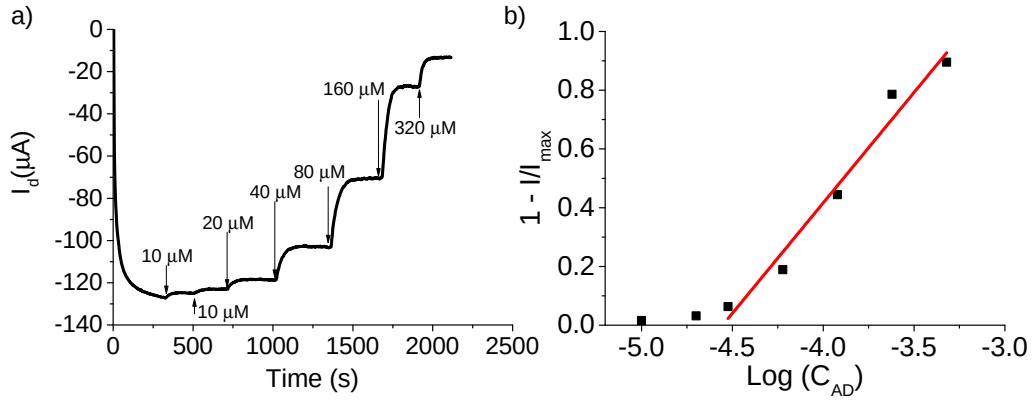

Figure 5.20: (a) I_d *vs.* time curve ($V_g = -0.9$ V; $V_d = -0.3$ V) obtained after the addition of different adrenaline amounts. The additions are labeled with arrows where the increase of concentration is reported. (b) I/I_{max} *vs.* $\log C_{AD}$ plot.

Analyte	**Linear range (M)**	**Slope (decade^{-1})**	**LOD (M)**
Ascorbic acid	$10^{-4} - 10^{-2}$	0.37 ± 0.03	10^{-6}
Adrenaline	$3 \times 10^{-5} - 10^{-3}$	0.75 ± 0.07	10^{-5}
Dopamine	$10^{-6} - 10^{-5}$	1.0 ± 0.2	10^{-6}

Table 5.4: Parameters of calibration plots of different analytes on OECTs with layout G1.

which causes a decrease in channel conductivity.

The measured $1 - I/I_{max}$ values are plotted as a function of the logarithm of AD concentration in Figure 5.20b. In the range $3{\times}10^{-5}$ - $1{\times}10^{-4}$ M the trend is linear with a slope of (0.75 ± 0.01) decade^{-1}. For lower concentrations the trend is not linear, but a response to the adrenaline addition can be observed down to 10^{-5} M. The signal of I_d *vs.* time is stable and shows no drift upon each addition, and the response time results equal to 70 s, highlighting that the device can sense the variation of adrenaline concentration almost in real time. Similar responses have been also obtained for ascorbic acid and dopamine, demonstrating that the sensor can work for detecting redox active compound. The parameters related to the calibration plot of all these compounds are reported in Table 5.4.

OECT devices used in ideal conditions (*i.e.* completely immersed in an electrolyte solution) exhibit a stable response wherein the channel current is linearly dependent upon the logarithm of the concentration of redox-active molecules in a

concentration range that is characteristic of the analyzed compound. These results demonstrate that all-PEDOT:PSS textile OECTs can reliably and quantitatively detect chemical compounds. The sensitivity of these devices is higher than the one observed for a similar OECT obtained on a glass substrate (see Section 5.3), although the LOD is still too high for the detection of these compounds in sweat, which is in the order of 10^{-9}M.

5.4.3 Sensing in simil-real conditions

Since in real-life applications the wearable sensor can not be immersed in a solution that contains the target compound, another device geometry, G2 (Figure 5.18a), was used to assess OECT performance in real-life conditions. The OECT in the geometry G2 was tested by adding 10 µL of PBS in the area between the gate electrode and channel to simulate the wetting of fabric due to sweat. The characteristic curves obtained are analogous to the ones obtained for OECT with G1 geometry shown in Figure 5.19b, demonstrating that a little amount of added electrolyte solution is enough to ensure both the electrical contact between the two PEDOT:PSS tracks and the occurrence of the redox processes required for transistor operation.

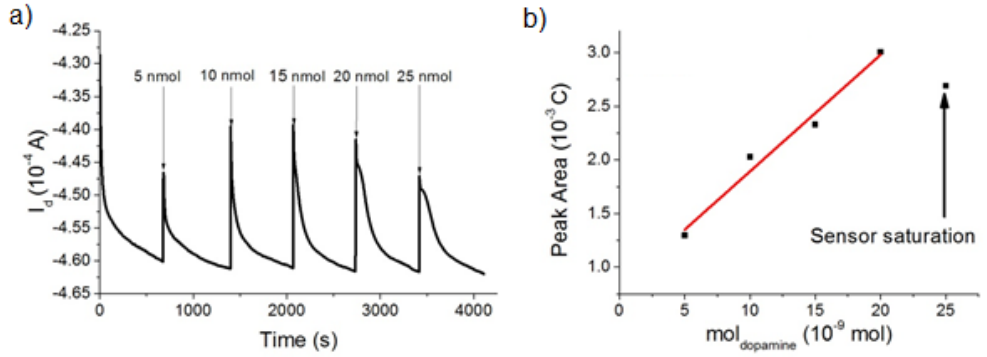

Figure 5.21: (a) I_d *vs.* time curve (V_g = −0.9 V; V_d = −0.3 V) obtained after the addition of different amounts of dopamine. The additions are labeled with arrows where the increase of concentration is reported. (b) Total charge flowing in the channel, obtained from the area below each peak in (a), as a function of the quantity of injected dopamine.

The sensing ability of OECT in geometry G2 was investigated by adding small amounts of analyte solutions on the operating device. Figure 5.21 shows the I_d *vs.* time plot obtained when dopamine was used as redox active compound. The OECT responds to an increase in the concentration of redox active molecules with a decrease of I_d as previously observed for the ideal conditions. However, after the signal variation, I_d is not stable, showing a fast recovery after each addition. Consequently, the signal curve exhibits several peaks in correspondence of every dopamine addition.

This behavior can be explained by considering that the quantity of dopamine that is added onto the sensor is very low. So, the analyte is consumed in the electrochemical reactions at the basis of sensor transduction, leading to a substantial decrease of its concentration and a corresponding increase of I_d. As a confirmation of this hypothesis, the charge flowing at the gate electrode after every dopamine addition was calculated, finding results that are very close to the ones expected from dopamine electro-oxidation if two exchanged electrons for each molecule are considered. Therefore, the decrease of I_d can be explained by a real change in the dopamine concentration on the surface of the sensor.

Since the volume of the solution that contains the analytes in the sensing area of the transistor is not known, the total amount of dopamine molecules in the electrolyte solution was determined instead of dopamine concentration. This quantity was then correlated to the charge flowing on the channel of the transistor relative to each addition, calculated as the integral of $I_d(t)$ for each peak, finding a linear relationship between charge and injected dopamine (Figure 5.21b). The slope of this calibration plot resulted equal to (1.10 ±,0.06 C M^{-1}).

This preliminary results point out that wearable OECT sensors used in conditions that are more close to real-life applications, with a very low volume of electrolyte solution on one side of the fabric only, can detect the variation of redox-active compounds. However, the different mechanism involved in the PEDOT/analyte redox reaction in this experimental condition still requires further investigation for the determination of reliable calibration curves.

5.5 Conclusions

In this Chapter, the development and the characterization of all PEDOT:PSS-based OECTs for the sensing of several redox-active compounds of biological interest is presented. The results for the sensitivity, expressed as the slope of the linear fit of $1 - I_d/I_{max}$ *vs.* $\log C$, the limit of detection (LOD), evaluated as the minimum analyte addition causing a variation in I_d three times higher than its standard deviation (noise), and the range of linearity of $1 - I_d/I_{max}$ *vs.* $\log C$ for each tested analyte are reported in Table 5.5.

These results demonstrate the capability of our all PEDOT:PSS-based OECTs to detect redox-active species. However, they also highlight the issue of the lack of selectivity of these devices. In order to overcome this problem, it is possible to take advantage of the different potentials and kinetics of the redox reaction bewteen these molecules and PEDOT:PSS. Following this method, OECTs were used for discriminating between the different components of an electrochemical solution containing the analyte of interest, dopamine, and two interferents, ascorbic acid and uric acid, proving that selectivity can be achieved in OECTs without further functionalization.

Being completely made using polymeric material, OECTs have been realized

Analyte	**Linear range (M)**	**Slope (decade^{-1})**	**LOD (M)**
Ascorbic acid			
Low concentration	$10^{-8} - 10^{-6}$	0.026 ± 0.003	10^{-8}
High concentration	$10^{-6} - 10^{-3}$	0.12 ± 0.01	10^{-8}
Textile OECT	$10^{-4} - 10^{-2}$	0.37 ± 0.03	10^{-6}
Dopamine			
OECT on glass	$10^{-6} - 10^{-4}$	0.11 ± 0.01	5×10^{-8}
Textile OECT	$10^{-6} - 10^{-5}$	1.0 ± 0.2	10^{-6}
Levodopa	$10^{-5} - 10^{-3}$	0.075 ± 0.002	$5\,10^{-6}$
Gallic acid			
Standard $I_d(t)$	$10^{-6} - 10^{-2}$	0.035 ± 0.003	10^{-6}
Random additions	$10^{-3} - 1$	0.12 ± 0.02	10^{-5}
Adrenaline (textile)	$3 \times 10^{-5} - 10^{-3}$	0.75 ± 0.07	10^{-5}
DPPH	$5 \times 10^{-6} - 3 \times 10^{-5}$	0.78 ± 0.05	10^{-6}

Table 5.5: Parameters of the calibration curves obtained with OECT on the compounds tested in this work.

on cotton and lycra in order to develop wearable biochemical sensors for real-time analysis of sweat. Also in this configuration, detection of redox-active analyte has been achieved, both in ideal experimental conditions, with an experimental setup identical to the one used for the characterization of "traditional" OECTs, and in conditions more similar to real-life applications. However, further studies are still needed for improving the sensitivity and selectivity of these devices, as well as for the development of a more effective theoretical model regarding OECT operation for sensing applications.

Chapter 6

Cell Culture Substrates

Thanks to their favorable properties, namely chemical stability, low temperature processing, oxide-free surface in aqueous electrolyte, ionic and electronic transport, and mechanical compliance with living tissues, conjugated polymers (CPs), are promising materials for tissue engineering applications [2–4]. Among them, PEDOT:PSS has become a reference material for the interfacing of electronics and living tissues. Over the past few years, many studies involving the effect of the oxidation state of CPs on cell adhesion, density and replication have been carried out [115]. The redox state of the underlying CP has been proven to alter the folding of fibronectin, one of the most important adhesion proteins present in the extracellular matrix [116]. However, it is still not clear if this effect is the only cause of the observed modifications in cell growth. Moreover, a model regarding the modifications induced in the physical and chemical properties by a change in the oxidation state of PEDOT:PSS and other conducting polymers is still missing.

It is known that cell-substrate interaction depends on the surface properties of the substrate itself: wettability [7], surface roughness [257–259], and electrical conductivity [260, 261] are key parameters in regulating this interaction, but their specific role in the adhesion process, together with the effect of electrochemical kinetics and protein-substrate interactions, are still not completely understood. For this reason, a characterization of the electrochemical and physical properties of PEDOT:PSS as a function of its oxidation state was carried out on four different types of PEDOT:PSS, and the results are presented in the rest of this Chapter.

The characterization of the material was integrated by cell culture experiments using two different cell lines, primary human dermal fibroblasts (hDF), and human glioblastoma multiforme cells (T98G). These types of cells were chosen in order to assess the effects of the substrates parameters on adherent, high-replicating and tissue-forming cells with very similar genotypic and phenotypic properties, but normal (hDF) and tumor-like (T98G).

Using the procedures described in Section 4.1.1 and 4.1.2, four types of PEDOT:PSS were deposited on glass substrate in order to obtain films with the same chemical composition, but different physical properties. The samples were kept at a continuous bias *vs.* SCE for 1 h to obtain an oxidized (positive voltage applied) or reduced (negative voltage applied) form of PEDOT:PSS. This time interval was chosen after analyzing the trend of current *vs.* time during polarization, so as to ensure a complete and stable polarization. Where not differently specified, the potentials used to reduce and oxidize PEDOT:PSS thin films were -0.9 V and +0.8 V, respectively.

6.1 Electrochemical Characterization

Since cell growth experiments require long-term interaction (usually days, or even weeks) between the physical substrate of the cells and an aqueous electrolyte solution, the assessment of the chemical and electrochemical kinetics of the substrate is crucial. For this reason, the stability of our PEDOT:PSS films was studied through cyclic voltammetry and spectrophotometry. These measurements were carried out in different aqueous media for the redox voltages +0.8 V / -0.9 V *vs.* SCE to identify the stability of the electrochemical modification of the oxidation state of PEDOT:PSS.

6.1.1 Cyclic voltammetry

As for OECTs (see Section 5.2.1), the electrochemical properties of PEDOT:PSS were studied by cyclic voltammetry (CV) using a three electrode cell (see Section 4.3.1). The CV responses were found to be very stable between -0.2 and +0.6 V. Nevertheless, it was possible to carry out a reliable electrochemical characteri-

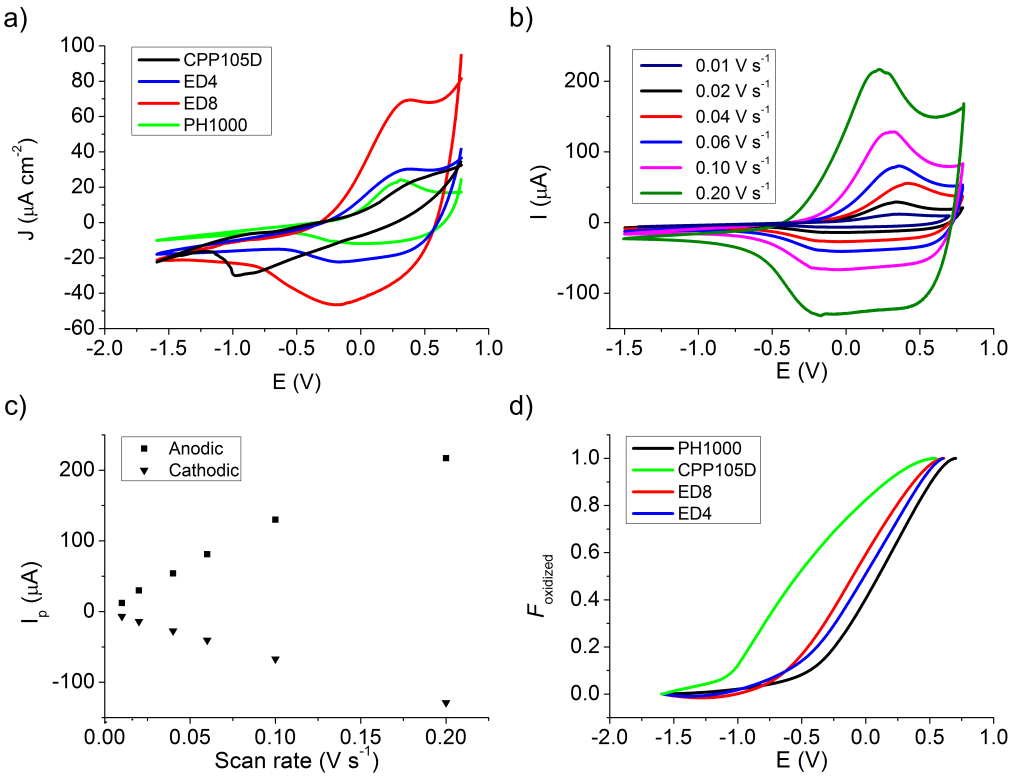

Figure 6.1: (a) CVs recorded for different PEDOT:PSS substrates (scan rate 20 mV s^{-1}). (b) Cyclic voltammograms of PH1000 taken at different scan rates. (c) Peak current versus scan rate of (b). (d) Fraction of oxidized PEDOT:PSS ($F_{oxidized}$) for the different substrates as a function of the applied voltage.

zation using a wider range of the applied potential, up to the maximum values achievable before an irreversible degradation process set in. The CVs (Figure 6.1a) which were obtained for the four types of PEDOT:PSS samples under examination display a couple of peaks that are well defined for PH1000, ED4 and ED8, whereas the redox waves of CPP105D are less defined and their baseline is tilted, probably due to a higher electrical resistance (see Section 6.2.3).

The peak currents are directly proportional to the scan rate in the range 0.010-0.100 V/s for all the samples (Figures 6.1b and c show the results for PH1000). Since according to Randles-Ševčik equation (Equation 4.19) for a diffusion-controlled process the peak current must be proportional to the square-root of the scan rate [15], this result highlights that diffusion is not the limiting step of the

electrochemical doping/de-doping process, and thus that the whole film thickness is involved in the electrochemical reaction. Therefore, the charge flowing during the CV scans corresponds to the electrons that are needed to change the redox state of the whole PEDOT:PSS volume.

As a consequence, the degree of the electrochemical doping of the film can be calculated for each material as a function of the electrochemical potential. From Fig. 6.1d, which reports the fraction of oxidized PEDOT sites over the number of total active sites, $F_{oxidized}$, it is possible to see that the active sites that take part in the redox processes are almost completely reduced ($F_{oxidized} \approx 0$) at -0.9 V. On the other hand, the anodic limit for polarization is found at +0.8 V, since it is observed that higher potential values lead to a strong overoxidation of the conductive polymer.

Assuming that only one charge interacts with each active site of the conductive polymer, it is also possible to calculate the concentration of sites that change their redox state by measuring the charge that flows during the cathodic scan of a cyclic voltammetry, which is easily obtained as the integral of $I(t)$. This concentration results equal to 0.55, 0.54, 0.21, and 0.16 mol dm^{-3} for ED4, ED8, CPP105D, and PH1000, respectively. From these concentrations the charge carrier density can be calculated for each material, obtaining 3.31, 3.25, 1.26 and 0.96×10^{20} cm^{-3}, respectively. The larger values of electrochemically polymerized PEDOT:PSS can be ascribed to its higher PEDOT/PSS ratio [262].

6.1.2 Spectrophotometry

The experimental setup used for spectrophotometry measurements is shown in Figure 4.7. This technique was used to record the visible and near-infrared (NIR) spectra recorded on PEDOT:PSS films biased at different potentials (Figure 6.2). From these spectra, three redox states of PEDOT:PSS can be identified. The spectrum of native PEDOT:PSS displays a large band at about 900 nm that is ascribable to polaron absorption. [263]. The spectrum recorded when PEDOT:PSS was biased at +0.8 V does not show any peak at 900 nm, meaning that such potential is sufficient to oxidize polarons, forming bipolarons that, being located deeper in the energy gap with respect to polarons, cause a shift of the absorption peak to higher

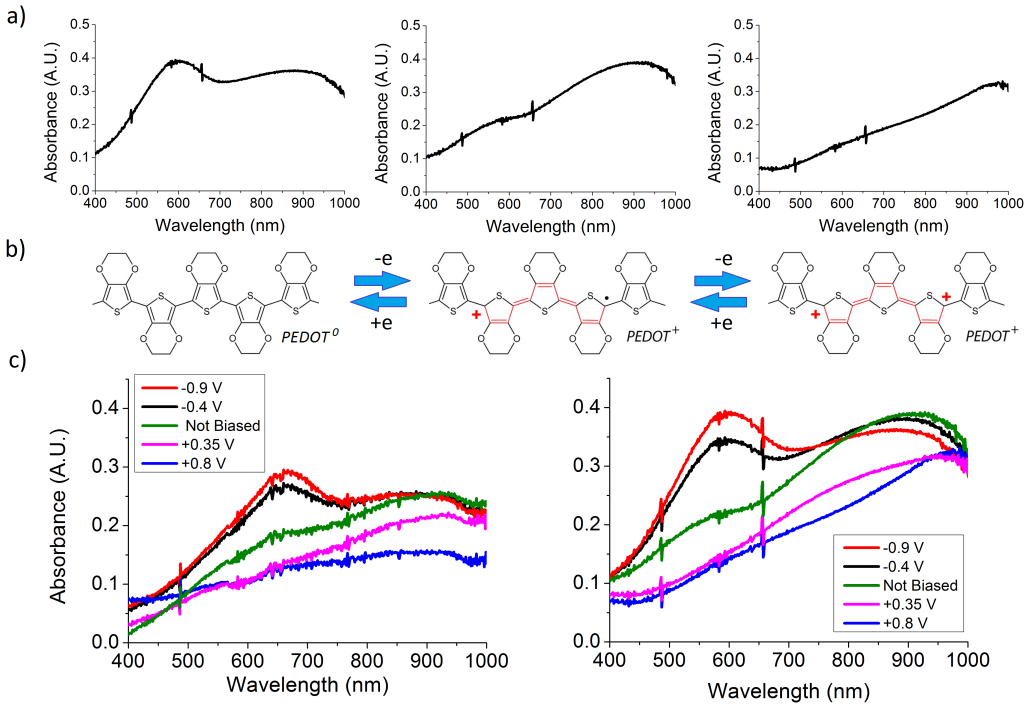

Figure 6.2: (a) Visible and NIR spectra of ED8 in its reduced (-0.9 V, left), not-biased (middle) and oxidized (+0.8 V, right) forms. (b) Schematics of the redox process in PEDOT from its reduced (left) to its fully oxidized (right) state. (c) Visible and near IR spectra of PH1000 (left) and ED8 (right) in their native state and biased at -0.9, -0.4, +0.35, and +0.8 V.

wavelengths. The formation of bipolarons turns PEDOT:PSS into its highly conductive form (Figure 6.2b), that is almost transparent [146]. Indeed, the spectrum recorded for PEDOT:PSS biased at +0.35 V displays a shoulder at about 800 nm, suggesting an intermediate state where not all the polarons have been oxidized into bipolarons.

On the other hand, the spectrum recorded when PEDOT:PSS was biased at -0.9 V shows two peaks. The first one, at about 600 nm, is assigned to the transition $\pi - \pi^*$ of the polymer in its neutral state, highlighting the reduction of the polarons caused by the injection of electrons into the material, as shown in Figure 6.2b. However, the band at 900 nm points out that charged polarons are still present in PEDOT:PSS, suggesting that the reduction of this material is incomplete at -0.9 V. This effect has already been observed in literature, and it was ex-

plained as the result of a slow and spontaneous oxidization of PEDOT due to the presence of an aqueous medium [264]. Finally, the spectrum recorded at -0.4 V also shows a peak at 600 nm (Figure 6.2c), but its intensity is slightly lower with respect to the spectrum obtained at -0.9 V, suggesting that a lower percentage of PEDOT is in its neutral form.

Having assessed the redox effects inducedd on PEDOT:PSS thin films by the applied potential, PEDOT:PSS substrates were prepared using three applied bias values that generated three different sets of samples: one containing mainly neutral PEDOT, one containing mainly polarons and one wherein PEDOT is present in its high conductive state. To maximize the difference in performance of these three types of substrates, PEDOT:PSS was thus used either in its pristine state or biased at -0.9 and +0.8 V.

6.1.3 Time stability of the redox state

The time stability of the electrochemically-generated redox state of PEDOT:PSS thin films plays a key role in their effective use as cell growth substrates. To ensure the long-term stability of the redox state, the films were biased for 1 h in PBS and, consequently, they were removed from the electrolyte solution, washed using distilled water and then the modifications that occurred after the applied bias was removed were recorded by collecting visible and NIR spectra.

Since these films are realized for being applied to cell cultures, *i.e.* for being used in liquid environment, they were immersed in three different aqueous media during the stability measurements: distilled water (H_2O), phosphate buffer solution (PBS) and Dulbecco's modified Eagle's medium (DMEM) supplemented with fetal bovine serum. These media were used because of their different composition, since PBS contains small ions only while DMEM also contains quite large organic molecules, like amino acids, vitamins and glucose. The stability of the induced redox state was continuously monitored for 1 h after removing the applied bias, with a new spectrum acquired every 2 minutes. An example of the collected spectra is shown in Figure 6.3 for ED4.

The spectrum of negative-biased substrates displays a decrease of the absorbance peak at 600 nm that is due to the transition $\pi - \pi^*$ of the neutral form of

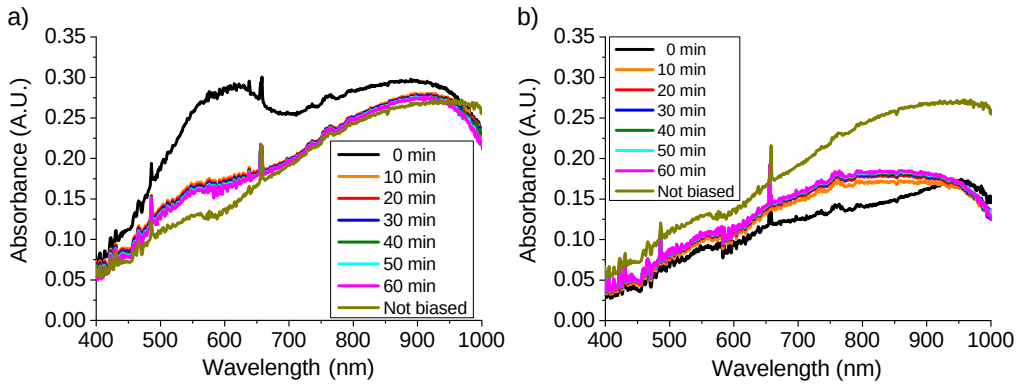

Figure 6.3: Spectra of ED4 substrates in their pristine state and biased at (a) -0.9 V and (b) +0.8 V recorded each 10 minutes for 1 h while immersed in PBS after being biased.

PEDOT, that is generated by the polarization at -0.9 V. The amount of neutral PEDOT that is still present in the sample at the time t is proportional to the quantity $Abs_{600}\%(t)$, that is calculated as:

$$Abs_{600}\%(t) = \frac{A_{600}(t) - A_{600}^{native}}{A_{600}(0) - A_{600}^{native}} \tag{6.1}$$

Where $A_{600}(0)$ and $A_{600}(t)$ are, respectively, the absorbance at 600 nm of the biased PEDOT:PSS at the beginning of the measurement and after being immersed for a time t, while A_{600}^{native} is the absorbance at 600 nm of native PEDOT:PSS.

When PEDOT:PSS is biased at +0.8 V, a highly conductive state is formed and the film becomes transparent with almost flat spectra. After the end of the polarization the peak at about 900 nm increases due the formation of polarons or bipolarons. The amount of highly conductive PEDOT:PSS that has turned in the average oxidized state can be estimated by the recovery of absorbance at 900 nm, $Abs_{900}\%(t)$, that is calculated as:

$$Abs_{900}\%(t) = \frac{A_{900}^{native} - A_{900}(t)}{A_{900}^{native} - A_{900}(0)} \tag{6.2}$$

where $A_{900}(0)$ and $A_{900}(t)$ are, respectively, the absorbance at 900 nm of the biased PEDOT:PSS at the beginning of the measurement and after being immersed for a

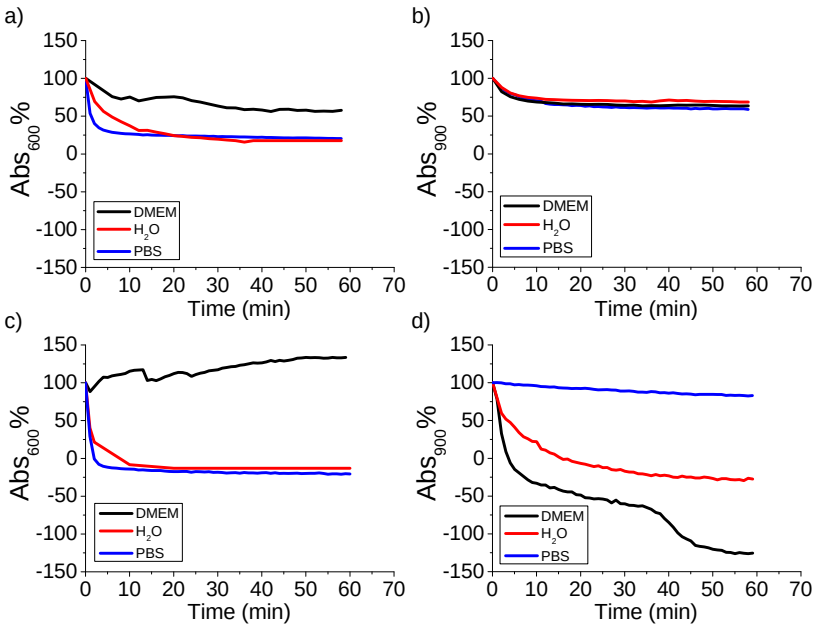

Figure 6.4: Trends of $Abs_{600}\%(t)$ and $Abs_{900}\%(t)$ for (a) reduced ED4, (b) oxidized ED4, (c) reduced PH1000, and (d) oxidized PH1000. The samples were biased at -0.9 and +0.8 V, and then immersed in DMEM, H_2O, and PBS. The spectra of reduced/oxidized ED8 and CPP105D (not shown) show a behavior analogous to ED4.

time t, while A_{900}^{native} is the absorbance at 900 nm of native PEDOT:PSS.

Figure 6.4 reports the evolution in time of these quantities for ED4 and PH-1000, where $Abs_{600}\%(t)$ expresses the residual redox state of reduced PEDOT:PSS relative to the absorbance peak measured just after biasing, and $Abs_{900}\%(t)$ similarly expresses the residual fraction of oxidized sites in oxidized PEDOT:PSS. Figure 6.4 shows that the reduced forms of PEDOT:PSS revert to their pristine state in a few minutes when exposed to distilled water and PBS, while in DMEM their absorbance drops at about 60% of its starting value and then stabilizes. The oxidized forms are more stable in time than the reduced ones for any tested medium for substrates ED4 (Figure 6.4a, b), ED8, and CPP105D, in accordance with results obtained on PEDOT by other groups [264, 265]. After 1 h, the residual oxidation of all the samples is about 60% of the initial state, with the only exception of PH1000 (Figure 6.4c, d). DMEM acted strongly on the redox state of oxidized PH1000, leading to a spontaneous reduction of PEDOT.

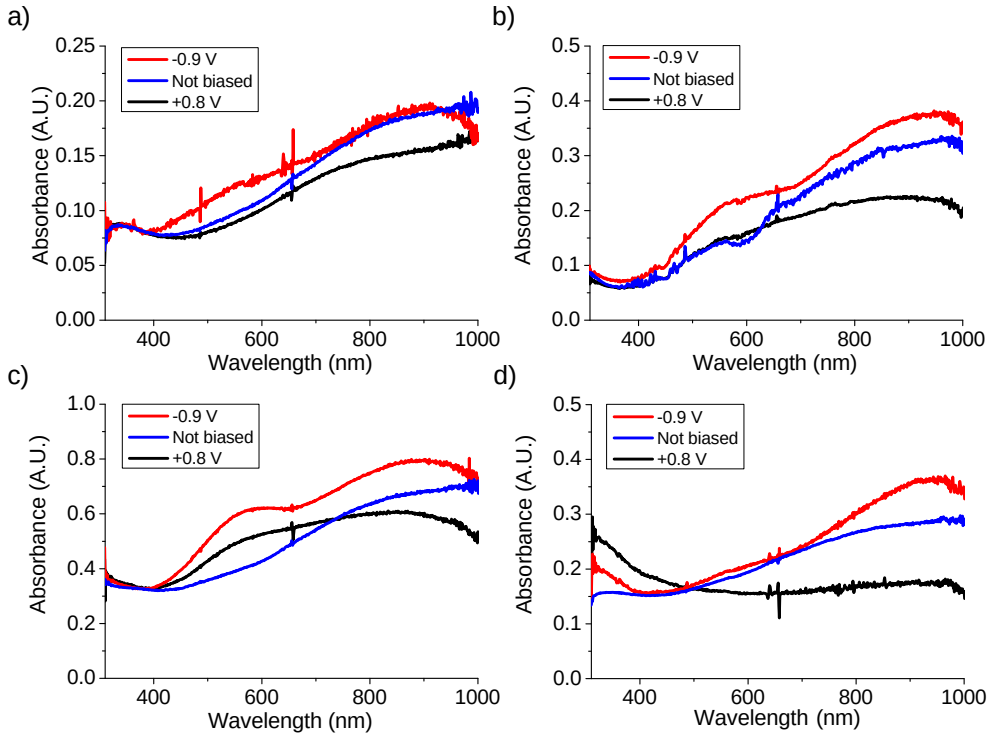

Figure 6.5: Absorption spectra of reduced, not biased and oxidized CPP105D (a), ED4 (b), ED8 (c) and PH1000 (d) after 48 h of immersion in DMEM.

The same measurement in DMEM was repeated by monitoring the spectra of PEDOT:PSS for 48 h to assess the stability of this polymer in cell culture medium for a time period comparable to the duration of biological experiments. As a result, the difference in the absorption spectra of oxidized and reduced samples was still observable, with a residual oxidation of about 90% of the starting value for the oxidized samples and about 30% for the reduced ones, attesting the effectiveness of the redox process. Moreover, the spectrum of oxidized PH1000 showed an absorbance peak between 300 and 400 nm after 48 h of immersion in DMEM which was not present at the beginning of the measurement, suggesting the occurrence of a chemical modification induced by the cell culture medium.

From these observations it is possible to conclude that, although the generated redox states are not completely stable in time, a sharp difference between the oxidized and reduced films is still present after the removal of the redox voltage

for all the four types of PEDOT:PSS samples here investigated, meaning that the application of a continuous bias during cell growth is not necessary to grant an effective difference in the redox state of PEDOT:PSS.

6.2 Physical Characterization

The physical properties of PEDOT:PSS films as a function of their oxidation state were investigated using several experimental techniques. The results are presented in this Section.

6.2.1 Atomic force microscopy

An atomic force microscope was used to investigate the surface morphology of the four kinds of PEDOT:PSS thin films in ambient conditions and in PBS 0.1 M. 1 μm × 1 μm maps of the surface topography of the samples were acquired in non-contact mode. Four maps, representative of the four types of PEDOT under investigation, are presented in Figure 6.6, and the root mean square roughness, R_q, and thickness, measured as described in Section 4.2.1, of the different films of PEDOT:PSS are reported in Table 6.1.

CPP105D has the flattest surface (R_q of about 6 nm), while ED8 shows the highest roughness (R_q about 33 nm). The comparison between CPP105D, ED4, and ED8 shows that it is possible to increase the surface roughness of PEDOT:PSS by controlling the number of polymerization cycles. This increase in surface roughness is due to the formation of PEDOT-rich globular structures of increasing size, as can be seen from Figure 6.6. A comparison between these samples shows that the thickness of the samples is basically not affected by the first four cycles of polymerization, while the following four cycles increase the thickness

Sample	R_q **(nm)**	**Thickness (nm)**
CPP105D	6 ± 1	260 ± 60
PH1000	13 ± 3	440 ± 30
ED4	22 ± 4	240 ± 80
ED8	33 ± 2	480 ± 120

Table 6.1: RMS roughness and thickness of the samples under study.

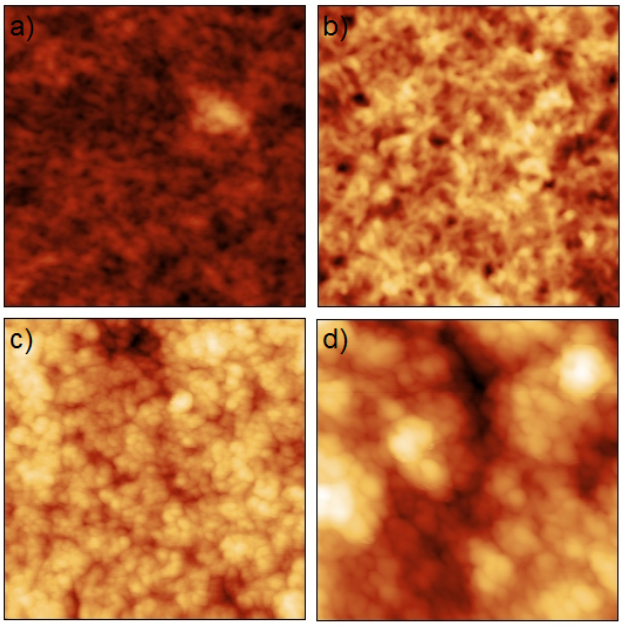

Figure 6.6: AFM topography images of the PEDOT:PSS samples under study: (a) PH1000, (b) CPP105D, (c) ED4, and (d) ED8. Scan size: 1 μm × 1 μm. z scale: 35 nm for panels (a-c) and 90 nm for panel (d).

of PEDOT:PSS by about 100% of its starting value. This effect can be explained by assuming that polymerization starts inside the volume of CPP105D, used as conductive electrode, during the first cycles of this process, and then the electropolymerized PEDOT:PSS starts growing on the surface of the electrode only after a certain number of cycles, increasing the overall film thickness.

The surface morphology of the four types of PEDOT:PSS was investigated as a function of their oxidation state, finding no significant variation between oxidized, reduced and pristine films. The same measurements were repeated in PBS, again finding no difference with respect to the results obtained in air regarding surface morphology. These results point out that there is no orientation effect of the dopant molecules induced by the reduction and oxidation of PEDOT:PSS, and that the different rates of cell growth observed on PEDOT:PSS with different oxidation states [10, 115] are not related to a change in surface roughness.

In addition to surface morphology, atomic force microscopy was used for the investigation of the mechanical properties of PEDOT:PSS through the acquisition

of force-indentation curves, as shown in Figure 6.7a. These curves were taken in PBS 0.1 M on substrates that were previously reduced and oxidized, and on substrates that were not treated with redox reactions ("not biased"). From these data, the stiffness and Young's modulus of ED8 were extracted (see Section 4.2.2); the values obtained are reported in Table 6.2. The not biased and oxidized samples show very similar mechanical properties, which is not surprising since pristine PEDOT:PSS is partially oxidized already, while the reduced samples are notably softer, with a stiffness and Young's modulus less than 50% compared to the other films. This decrease in the hardness of PEDOT:PSS is related to the removal of the electrostatic binding of PEDOT to PSS due to the uptake of cations during the reduction process:

$$\mathrm{PEDOT^+ : PSS^- + C^+ + e^- \rightarrow PEDOT^0 + PSS^- : C^+}. \tag{6.3}$$

Because of this reaction, PEDOT:PSS mechanical structure changes from its original "quasi-crystalline" form, where PEDOT and PSS are bound together, to a gel-like structure, where PSS is more free to move and to absorb cations and water molecules.

This hypothesis is confirmed by our observation that, when an external potential is applied to polymer films in an electrolyte solution, they undergo expansion and contraction (electromechanical actuation) due to the diffusion of electrolyte ions in and out of the polymer, in order to compensate for a charge imbalance on the polymer backbone, as seen in literature for doped polypyrrole [114]. This result is presented in Figure 6.7b. ED8 thin films were immersed in PBS and their electrochemical potential was switched alternately between an oxidizing (+0.8 V) and reducing (-0.8 V) value every 60 s (red line). At the same time, the variation in film thickness, Δz, was monitored with AFM by positioning the tip in contact with the film surface and recording every 2 s the displacement of the z scanner required to keep a constant deflection of the cantilever (black circles). As shown in Figure, the thickness of the film increases when a reducing potential is applied, due to the swelling of cations and water molecules that are absorbed by PSS, causing a decrease in film stiffness. Then, when an oxidizing potential is applied, these cations are released from the film, causing a deswelling of the absorbed water and

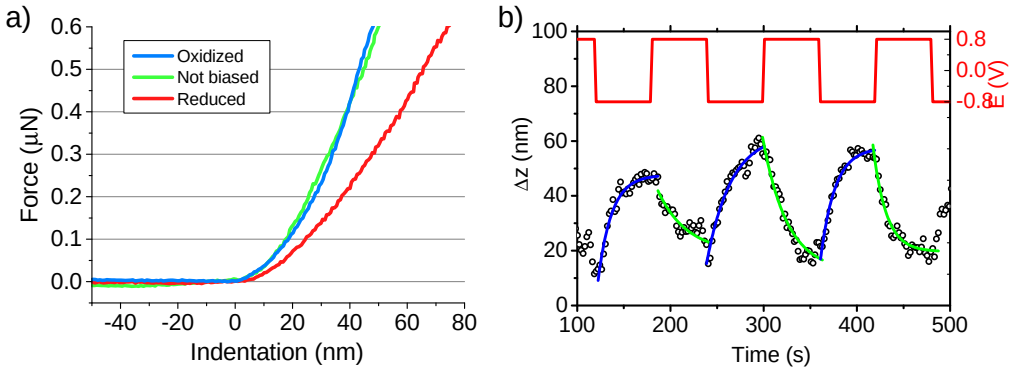

Figure 6.7: (a) Force-indentation curves measured on oxidized, reduced and not biased ED8. (b) Variation of the thickness of an ED8 thin film in PBS 0.1 M as a function of time and of the applied bias (red line). Exponential fits of swelling and deswelling are plotted with blue and green lines, respectively.

Oxidation state	**Stiffness (N/m)**	**Young's modulus (GPa)**
Oxidized	17 ± 7	1.3 ± 0.4
Pristine	16 ± 7	1.40 ± 0.13
Reduced	7.3 ± 1.6	0.56 ± 0.17

Table 6.2: Stiffness and Young's modulus of electropolymerized PEDOT:PSS (ED8) in PBS 0.1 M.

a strengthening of the PEDOT-PSS binding.

This swelling/deswelling process induces a significant variation in film thickness ($\Delta z/z \sim 10\%$) and follows an exponential kinetics (blue and green curves represent the exponential fits of $\Delta z(t)$ for a reducing and oxidizing potential, respectively). The exchange of cations with the electrolyte solution can explain the instability of the redox state of PEDOT:PSS shown in Figures 6.3 and 6.4. When a PEDOT:PSS film is reduced in PBS, it accumulates an excess of cations (mainly Na^+) because of the negative applied bias; then, the film is immersed in a different solution with no bias applied, causing its electrochemical potential to increase in order to reach an equilibrium state with the electrolyte solution, thus releasing a significant fraction of the absorbed cations. Conversely, when a previously-oxidized PEDOT:PSS film is immersed in an electrolyte solution, it undergoes partial reduction through an intake of cations.

6.2.2 Wettability and surface energy

Water contact angle measurements were carried out on the samples just after deposition (pristine) and after 1 h of polarization in PBS. As a control, some of the samples were immersed in PBS for 1 h with no bias applied. The results are reported in Figure 6.8. From the measurement of the contact angle, the surface energy of each surface was numerically calculated through the equation of state for interfacial tensions (see Section 4.2.3) [231]; the results are presented in Table 6.3. All the samples are hydrophilic (contact angle is always below 90°). However, regarding the not biased form of PEDOT:PSS, there is a clear difference between CPP105D-based films (both ED4 and ED8 are polymerized using CPP105D films as working electrode) and PH1000, which shows a lower hydrophilicity.

The comparison between the contact angles measured before and after the exposure to PBS points out a very strong difference. This effect can be explained by considering that PSS in excess is partially removed when the films are immersed in water [215]. This excess of PSS is expected to be mostly accumulated on the surface of the films [266], and because of the presence of HSO_3^- groups, it can be

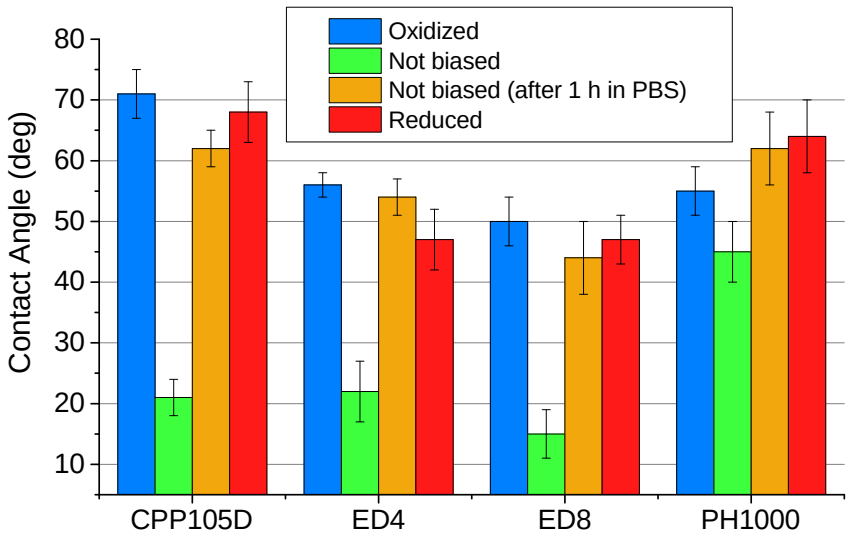

Figure 6.8: Water static contact angle measured on the PEDOT:PSS samples under study in their oxidized, not biased and reduced form. The not biased samples were measured as-deposited and after being immersed in PBS for 1 h.

	Surface energy ($mJ\,m^{-2}$)			
Sample	**Reduced**	**Not biased**	**Not biased after 1 h in PBS**	**Oxidized**
CPP105D	43 ± 3	68 ± 1	47 ± 2	41 ± 3
ED4	56 ± 3	68 ± 2	51 ± 2	50 ± 1
ED8	56 ± 2	70 ± 1	57 ± 3	54 ± 2
PH1000	45 ± 4	57 ± 3	47 ± 3	51 ± 2

Table 6.3: Surface energies of the samples under study.

dissolved by water thanks to the formation of hydrogen bonds, making the surface of the film hydrophilic. Since the PSS in excess is poorly interacting with PEDOT, its removal in water has no significant effect on the electrical and electrochemical properties of PEDOT:PSS, and is not detected by other techniques.

On the other hand, a change in the oxidation state of PEDOT:PSS does not seem to influence the hydrophilicity and the surface energy of this material, conversely to what was observed for instance on PEDOT:Tosylate [7]. Thanks to their relatively small dimensions compared to PSS (171 vs 70,000 Da), tosylate anions can be completely removed from the polymer matrix and undergo ion exchange when immersed in an electrolyte solution [267], while this effect is hindered for PSS due to steric effects. As a consequence, the exchange of PSS anions is mechanically impeded, as well as the switching of charged sulfonate groups from PEDOT to the surface. This explanation is confirmed by the fact that PEDOT:PSS exchanges cations (Na^+, K^+, etc.) with the electrolyte solution to maintain electrical neutrality [225], while PEDOT exchanges its counterion when small dopant molecules, like tosylate or perchlorate, are used [267]. Moreover, since the outer part of the film is mainly composed by an excess of PSS, the variation of the redox state of inner PEDOT does not affect the surface processes. As a result, the surface energy of the films is weakly influenced, if not at all, by the applied polarization, even if charge distribution in the PEDOT cores is effectively modified.

These results suggest that, regarding PEDOT:PSS, surface energy and wettability cannot be considered key parameters for controlling cell growth.

6.2.3 Electrical properties

The sheet resistance (R_s) of PEDOT:PSS thin films was measured using a 4-probe setup before and after the application of a redox voltage to the samples for 1 h. The results are reported in Figure 6.9. PH1000 films have the lowest sheet resistance (R_s about 0.36 kΩ/□). ED4 and ED8 show slightly higher values (R_s about 1.1 and 0.8 kΩ/□, respectively), but still comparable, while the sheet resistance of CPP105D is at least ten times higher compared to the other materials.

When an oxidizing voltage is applied to the PEDOT:PSS electrode, the polymer film changes from its pristine partially oxidized state to a more conductive fully oxidized state thanks to the formation of bipolarons along the polymer backbone. However, if the positive bias is over +0.6 V, PEDOT:PSS undergoes overoxidation, which breaks the conjugation along the chain and thus induces a dramatic increase in electrical resistance, as observed in all our tested samples. On the other hand, the application of a negative voltage induces a transition from the conductive state $PEDOT^+$ to a its non conducting state $PEDOT^0$, where the dopant PSS^- is not bound anymore to PEDOT because of the electrostatic interaction with positive ions from the electrolyte solution, causing an increase in R_s

Once that the sheet resistance R_s, the thickness t and the carrier density p are known, it is possible to evaluate the conductivity σ and carrier mobility μ_p of the

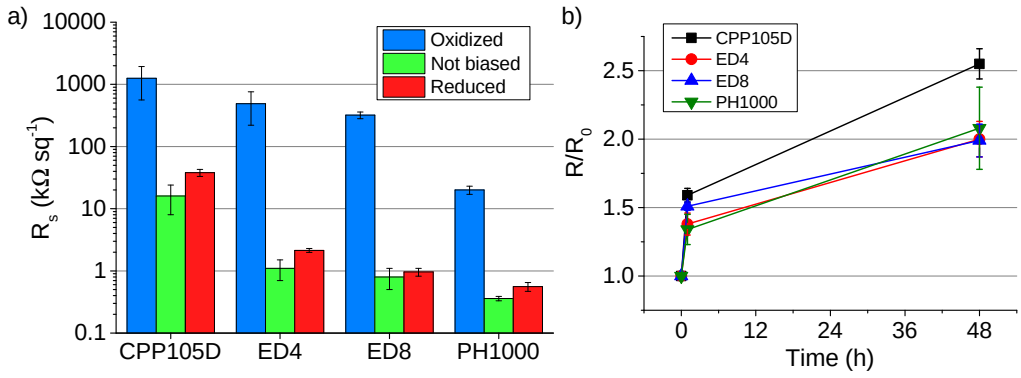

Figure 6.9: (a) Sheet resistance measured on the four sets of PEDOT:PSS samples here investigated in their oxidized, not biased, and reduced form. (b) Sheet resistance of not biased PEDOT:PSS kept in DMEM for up to 48 h. The values are normalized to the sheet resistance of as-deposited PEDOT:PSS.

Sample	Thickness (nm)	Carrier conc. (10^{20} cm^{-3})	R_s (kΩ/□)	σ (S cm^{-1})	μ_p (cm^2/V s)
CPP105D	260 ± 60	1.26 ± 0.13	16 ± 5	2.4 ± 0.9	0.12 ± 0.04
PH1000	440 ± 30	0.96 ± 0.10	0.36 ± 0.03	63 ± 7	4.1 ± 0.4
ED4	240 ± 80	3.3 ± 0.3	1.1 ± 0.2	38 ± 15	0.7 ± 0.3
ED8	480 ± 120	3.3 ± 0.3	0.80 ± 0.17	26 ± 9	0.50 ± 0.16

Table 6.4: Electrical parameters of the different PEDOT:PSS films.

PEDOT:PSS films from the equations $\sigma = 1/R_s\, t$ and $\sigma = q\mu_p p$. The values obtained are reported in Table 6.4; the evaluated σ and μ_p are in good agreement with typical values for PEDOT:PSS [146, 268, 269]. It is noteworthy that, despite the low carrier density, PH1000 shows the highest electrical conductivity, indicating a higher mobility compared to the other formulations.

Finally, the effect of the exposure to cell culture medium (DMEM) was tested on not biased samples for up to 48 h, finding that the surface resistance increases by about a factor of 2 in this time period (Figure 6.9b). This change mostly takes place within the first hour, indicating that is probably due to a spontaneous reorganization of the polymer chains induced by the interaction with the electrolyte (which lowers carrier mobility) rather than a degradation effect.

6.2.4 Energy-dispersive X-ray spectroscopy

In order to measure the amount of cations absorbed during the redox process, the composition of our PEDOT:PSS thin films, expressed in terms of relative atomic concentration (n. atoms of each element / n. total atoms) was perliminarily determined using energy-dispersive X-ray spectroscopy (EDX). Because of the interference of Ca^+ and K^+ ions found in the glass substrate, poly(methyl methacrylate) (PMMA), an organic polymer composed by H, C and O atoms only, was used as substrate for PEDOT:PSS deposition.

ED8 thin films were analyzed in their not biased state and after being polarized in their oxidized and reduced state for 1 h in PBS. The concentrations of the four most concentrated elements found in these films are presented in Table 6.5. Apart from C, O, and S, which are part of the chemical structure of PEDOT:PSS, a small but significant concentration of Na atoms is observed in reduced and oxidized

Sample	**[C] (%)**	**[O] (%)**	**[S] (%)**	**[Na] (%)**
Substrate	77.27	22.73	0	0
Oxidized	69.27	28.82	1.02	0.65
Not biased	75.34	24.2	0.29	0
Reduced	74.03	24.65	0.53	0.79

Table 6.5: Atomic concentrations of the four most present elements measured in oxidized, not biased and reduced films through EDX spectroscopy. To avoid interferences, PMMA was used instead of glass as substrate for PEDOT:PSS deposition.

films. Conversely, no Na is present in the not biased samples, which have never been immersed in PBS, meaning that the Na atoms present in polarized films have been absorbed from the buffer solution during the redox process.

While the signal corresponding to C and O atoms is due to both PEDOT:PSS and its substrate, S atoms can only be found in PEDOT and PSS. For this reason, Na atomic concentration was normalized with respect to S, so as to remove the effect of irregularities in the thickness of the substrate and of PEDOT:PSS. As shown in Figure 6.10a, the applied voltage has a strong effect on the amount of absorbed ions, whose concentration in oxidized samples is about half the concentration found in the reduced ones. When a reducing (negative) voltage is applied to PEDOT:PSS, cations are forced to enter the polymer film, bonding with the negative charges of the PSS chains (Figure 6.10b). This result is in accordance with the results on the swelling and stiffness of PEDOT:PSS films coming from AFM measurements in liquid (Figure 6.7).

The presence of cations in the oxidized samples can be explained by taking into account the buffer solution uptake due to the high hydrophilicity of PSS and the porous structure of the polymer films. Moreover, the partial overoxidation of the films biased using a positive voltage (which can be seen from the electrical measurements in Figure 6.9a) involves the incorporation of cations along the polymer chain, breaking its conjugation.

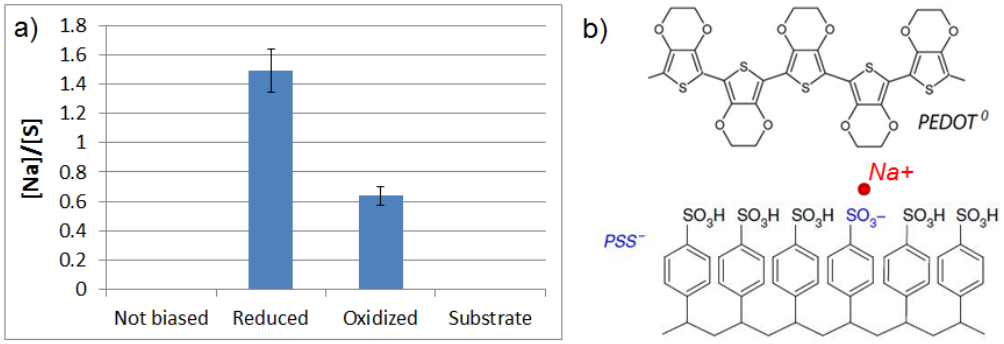

Figure 6.10: (a) Normalized concentration of Na atoms in ED8 films with different oxidation state. (b) Na incorporation due to the uncompensated negative charge on PSS in reduced PEDOT:PSS.

6.3 Biological Effects of the Oxidation State

6.3.1 Cell growth

To assess the viability and the different efficacy of PEDOT:PSS thin films as substrates for controlled tissue growth applications, the proliferation rate of two different cell lines, human glioblastoma multiforme cells (T98G), and primary human dermal fibroblasts (hDF), was tested on the polystyrene substrate of cell culture plates (control), on the four types of pristine PEDOT:PSS substrates (not biased), and on oxidized (+0.8 V) and reduced (-0.9 V) films. The samples were biased for 1 h in PBS and then disconnected from the generator prior to cell seeding. The proliferation curves of both cells population have been obtained by normalizing the mean number of adherent cells counted from fixed focal fields (set when the first image section has been acquired, that is, 24 h from seeding) after 24, 48, and 72 h.

The measured cell growth rates on the different samples are shown in Figure 6.11. The obtained results can be summarized as follows:

- The growth rate of normal cells (hDF) measured at 72 h from seeding on each type of PEDOT:PSS tested is not significantly different compared to the others (not biased, reduced, and oxidized), with the only exception of oxidized (+0.8 V) PH1000, where a significant increase in hDF growth compared to the not biased sample was observed (Figures 6.11a and 6.12).

- The growth rate of tumor cells (T98G) showed a significant increase on all the tested substrates that had been reduced (-0.9 V). Indeed, the statistical analysis highlighted that, at 72 h from seeding on all the four types of reduced PEDOT:PSS substrates, the cell proliferation rate is significantly enhanced compared to the not biased and oxidized ones, irrespective of the type of film used (Figures 6.11b and 6.12). Furthermore, within the experimental errors, the T98G proliferation rate is the same on all the not biased PEDOT:PSS substrates, with the only exception of ED4.

As indicated by the physical parameters of PEDOT:PSS, the techniques used for film deposition create surfaces characterized by different RMS roughness, thickness, surface energy and wettability. Differently, the proliferation rate analysis, for both normal and tumor cells, did not show significant differences between the four types of pristine substrates, therefore indicating that the morphology of the PEDOT:PSS surfaces does not influence the growing capability of these cells.

It is interesting to note that even if the hydrophilicity of the PH1000 pristine form is significantly lower compared to CPP105D-based films, also in this case, the proliferation rate of both cells population is not affected.

From the data acquired, we can also observe that the application of an external redox potential does not affect surface morphology, surface energy, and hydrophilicity, while the sheet resistance is strongly increased only by the application of an oxidizing potential in all substrates. Nevertheless, since the proliferation rates are not modified by any of the oxidized substrates except for the hDF growing on PH1000, we can exclude a causal relationship between sheet resistance and proliferation capability on biased PEDOT:PSS. On the basis of these evidence, it seems that the electrochemical status is an independent perturbing key factor able to induce a detectable modification of biological systems like the one used.

Furthermore, the interesting finding that hDF proliferation rate increases only when seeded on oxidized PH1000, while the reduced form of any PEDOT:PSS type tested is able to induce an increase only in T98G cells, suggests a different mechanism by which biased substrates might influence the replication processes of different types of cells.

The study of the electrochemical stability (Section 6.1.3) points out that only

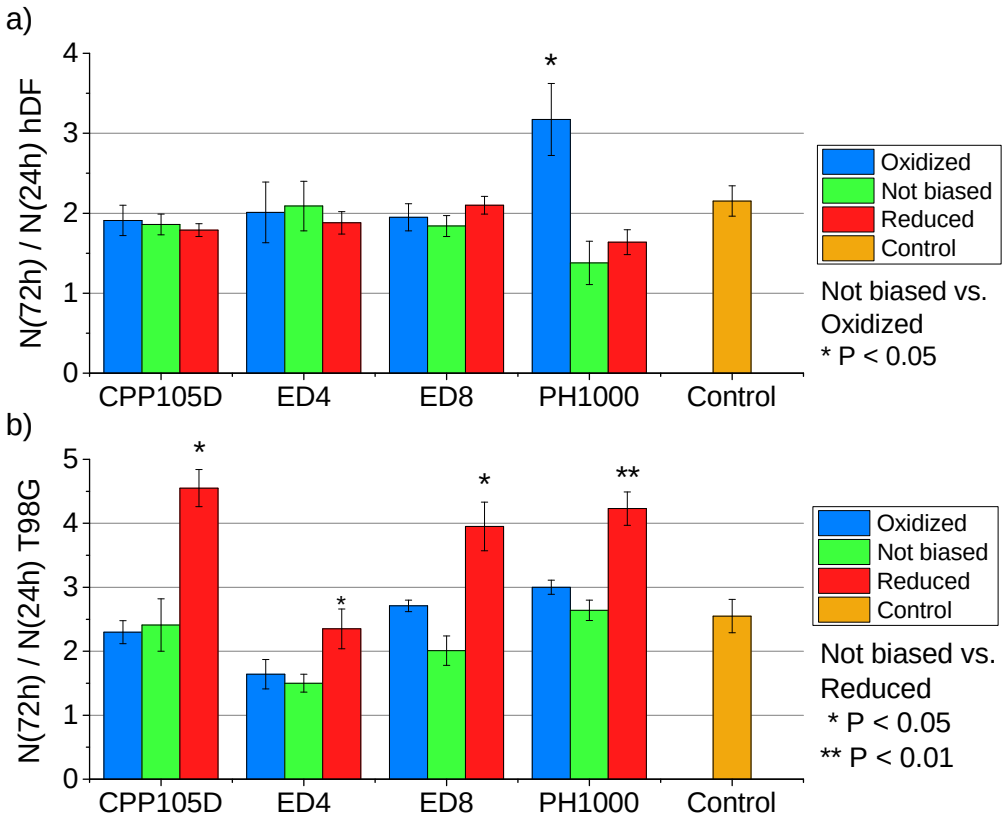

Figure 6.11: Effect, after 72 h from seeding, on the proliferation rate of the PEDOT:PSS substrates altered by an oxidation (+0.8 V) or reduction (-0.9 V) process. (a) Proliferation rate of hDF cells plated on not biased PEDOT:PSS CPP105D (n = 4), ED4 (n = 4), ED8 (n = 6), PH1000 (n = 4), and polystyrene wells substrate (control, n = 6) measured as the mean (±SEM) number of adherent cells counted from different focal fields at 100×of magnification at 24/48/72 h and normalized to the values obtained from each substrate at 24 h. (b) Proliferation rate of T98G cells plated on not biased PEDOT:PSS CPP105D (n = 7), ED4 (n = 6), ED8 (n = 6), PH1000 (n = 6), and polystyrene wells substrate (control, n = 5), measured as described in panel (a). The p values are calculated by a Student t test.

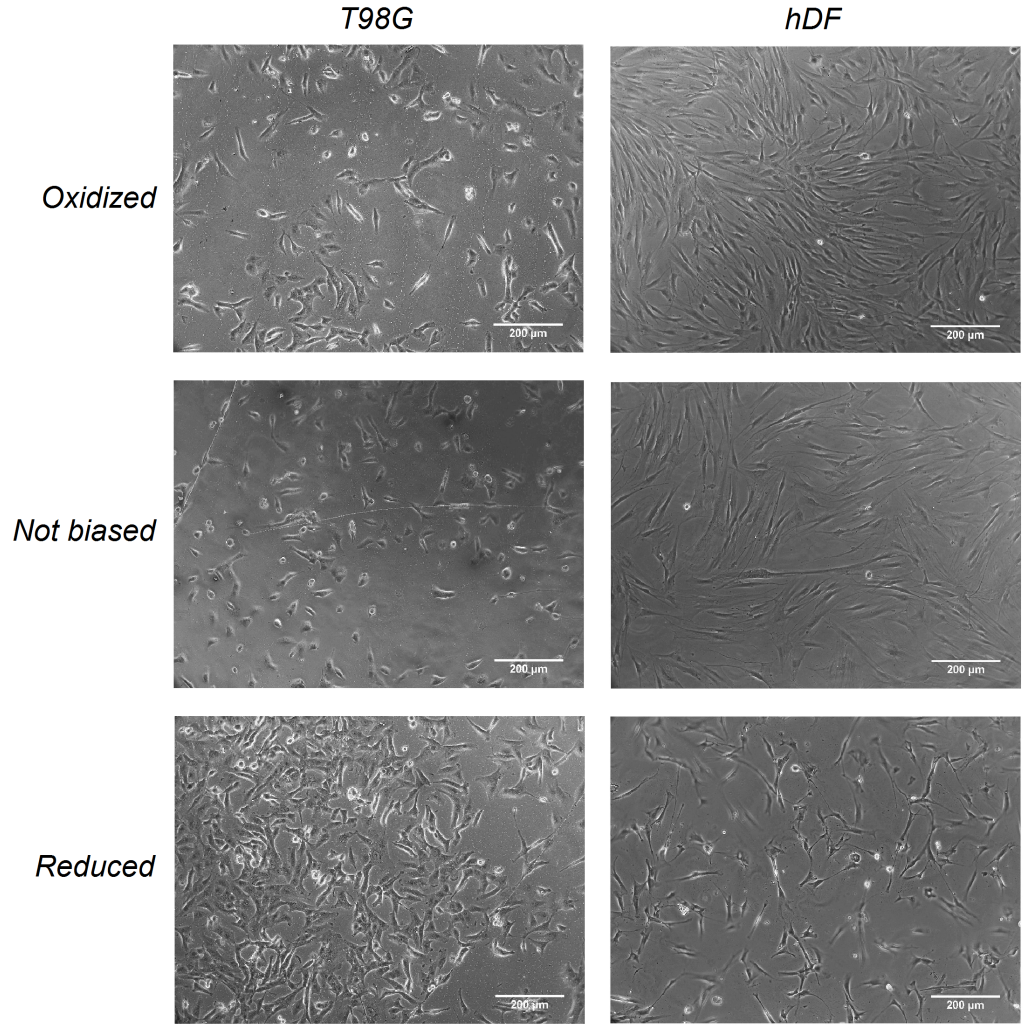

Figure 6.12: Representative example of T98G and hDF phase contrast microscopy images at 100× of magnification on oxidized (+0.8 V), not biased and reduced (-0.9 V) PH1000 after 72 h from cell seeding. Scale bar 200 µm.

the oxidized form of PH1000 spontaneously undergoes reduction when exposed to the cell growth medium (DMEM), as shown in Figure 6.4. Similarly, all the reduced PEDOT:PSS samples spontaneously undergo partial oxidation when immersed in cell culture medium. This state-change might be explained as an exchange of charge (i.e., ions and charged molecules) with the cell culture medium, responsible for the creation of a gradient in the ionic concentration which influences both the local chemical composition of the environment and the charge distribution of the extracellular matrix. Indeed, in addition to electrochemical stability, also AFM measurements of stiffness and swelling (Section 6.2.1), as well as EDX spectroscopy (Section 6.2.4), confirm the electrochemically-controlled swelling/deswelling mechanism through the intake of cations and water during the reduction of PEDOT:PSS, which are then released during oxidation.

6.3.2 Ion channel activity

The ability to change the local ion concentration can have strong effects on cell replication both by changing the local pH and surface charge, that could possibly influence the folding of adhesion proteins observed by other groups on oxidized and reduced conjugated polymers [116], and through the modification in the behavior of cellular ion channels. In fact, the activity of K^+ ion channels is related to cell proliferation and apoptosis, and is of great importance for cellular replicative mechanisms. They regulate several interrelated parameters which are involved in cell growth and replication, such as the adjustment of cell volume, the concentration of Ca^+ inside the cell and the resting membrane potential [270–272].

Moreover, studies performed on a human breast adenocarcinoma cell line demonstrated that multiple families of voltage dependent K^+ currents become active during the mitotic cycle [273, 274], and that the K^+ channels expression or activity change across stages of the cell cycle [272, 275]. All these findings highlight the importance of K^+ ion channels in modulating the replication of tumor cells. In order to gain a better understanding about the effects of the cations release mechanism at a cellular scale, the activity of ion channels and membrane polarization on PEDOT:PSS at different oxidation states was studied through patch clamp techniques.

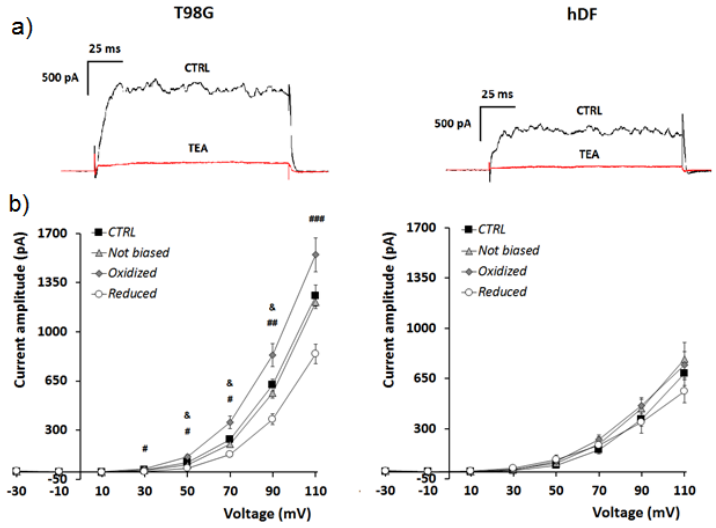

Figure 6.13: (a) Outward currents recorded in whole-cell configuration on control Petri dish in standard conditions (black line) and after TEA perfusion (red line) on T98G and hDF. (b) Current-voltage relationships ($I-V$) recorded in T98G and hDF on Petri dish (*CTRL*) and PEDOT:PSS (ED8) substrates.

Transmembrane whole-cell currents were recorded in voltage-clamp mode (see Section 4.4.3) from T98G and hDF cells plated on polystyrene Petri dish (*CTRL*) and on PEDOT:PSS (ED8) films in their not biased, oxidized and reduced states. In order to evaluate the effect of the K^+ current on the overall current recorded, the non-selective K^+ channel inhibitor tetraethylammonium chloride (TEA) was used at the saturating concentration of 10 mM. As a result, the ionic currents decreased dramatically after TEA perfusion (Figure 6.13a), indicating that the current recorded is mostly due to the ions fluxes through outward K^+ channels. Hence, K^+ channels are almost the only responsible for the electrical properties of both cells.

The following step was then to measure the ion currents, recorded at several voltage steps ($I-V$), from T98G and hDF cells plated on the control substrate and on not biased, oxidized and reduced PEDOT:PSS substrates. The results of the statistical analysis of these measurements are plotted in Figure 6.13b. A first observation is that, as for cell growth, the effect of PEDOT:PSS oxidation state is cell-dependent, with T98G showing different reactions on different samples,

while hDF are basically not affected by the oxidation state of the polymer. Regarding T98G, the currents recorded on not biased films are very similar to the ones recorded on the control Petri dish. On the other hand, a significant increase in the currents is observed on oxidized samples, while conversely the current decreases on reduced samples. Since K^+ channels are passive channels, *i.e.* K^+ ions are transported out from the cell through a diffusion process due to a gradient between internal (high) and external (low) K^+ concentration, this effect could be originated by a change in local concentration of K^+ ions.

6.3.3 Membrane polarization

The electrophysiological properties of cells, such as the channels activity and the intensity of ion fluxes, are strongly correlated to the resting membrane potential (V_r). This potential expresses the difference between the electrochemical potentials inside and outside the cell membrane, and is thus related to the ion concentrations according to Nernst equation. Consequently, a change in the local ion concentration should be reflected in a change in V_r.

For this reason, the resting potentials of T98G and hDF cellular membranes, whose whole-cell current was clamped at 0 pA (voltage-clamp mode), were recorded from cells plated on polystyrene Petri dish (*CTRL*) and on PEDOT:PSS (ED8) films in their not biased, oxidized and reduced states (Figure 6.14). Once again, the effect of the oxidation state of the substrate is cell-dependent. Accordingly to cell growth and ion currents measurements, the membrane potential of hDF cells is basically not affected by the redox state of the substrate. Nevertheless, a depolarization effect is apparent from a comparison between cells adherent to the control Petri dish and cells on PEDOT:PSS (irrespective of the oxidation state), both in hDF and, more effectively, in T98G. Moreover, V_r is different between the tumor and the normal cells independently from the substrate.

Interestingly, the reduced substrate, the one able to modify the cellular function of adhesion and proliferation more consistently than the others, is also in this case the most effective. Indeed, the V_r recorded on T98G cells undergo to a depolarization from negative to positive values. Human fibroblasts plated on reduced substrates show the same trend, but their depolarization is much less pronounced

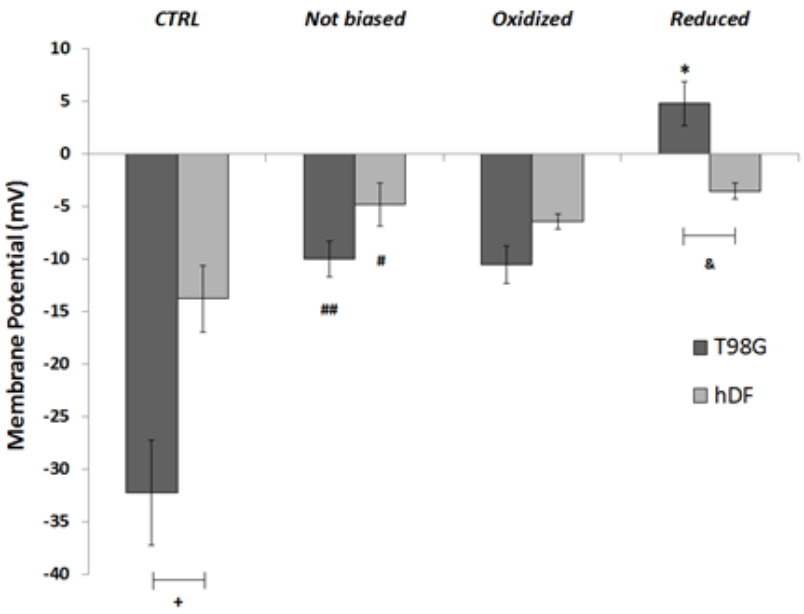

Figure 6.14: Resting whole-cell membrane potential recorded in T98G and hDF on Petri dish (*CTRL*) and PEDOT:PSS (ED8) substrates.

compared to T98G, and not significantly different from that observed on not biased films.

Conclusions

In this work, the development and characterization of two classes of all PEDOT:PSS-based devices are presented: electrochemical sensors, in the form of organic electrochemical transistors (OECTs), and redox-active substrates capable of controlling the replication of living cells.

Thanks to their low-voltage requirements and ease of fabrication, functionalization and integration in biological environment, OECTs are ideal devices for the sensing of a broad range of redox-active compounds of biochemical and biological interest. During the research activity presented in this thesis, all PEDOT:PSS-based OECTs were realized, and their sensing efficiency was optimized in terms of sensitivity and limit of detection (LOD) through the investigation of the effect of device geometry, thickness, and operating voltages. An electrochemical characterization of these devices was carried out as well, in order to clarify the processes involved in the device operation. As a result from this characterization, the drain current I_d resulted directly proportional to the electrochemical potential of the transistor channel, implying that these devices can be used as electrochemical sensors without the need for a reference electrode or a potentiostat.

Furthermore, the operation of these devices as electrochemical sensors was tested on several analytes, namely ascorbic acid, dopamine, gallic acid, adrenaline, and 2,2-diphenyl-1-picrylhydrazyl (DPPH). A calibration curve of $1-I_d/I_{max}$ *vs.* $\log C$ was obtained for each analyte, confirming that the electrochemical potential of the channel (and thus I_d) follows a Nernstian dependence on the analyte concentration. From these curves the range of logarithmic response, sensitivity and LOD were evaluated for each analyte, obtaining in most cases performances suitable for real applications. Indeed, the realized devices were tested for the determination of ascorbic acid in the Aspirina C (Bayer) medicinal product, and

the quantification of the polyphenol content in six wines, obtaining a significant agreement between actual and measured value in most of the cases.

The lack of selectivity, *i.e.* the ability of discriminating between different species within the same solution, is a common problem for sensors based on electrochemical transduction, and represents the main limitation of our OECTs for the analysis of real solutions. For this reason, preliminary studies on the effect of gate voltage and scan rate were carried out, exploiting the difference in redox potential and reaction kinetics between different molecules. In both cases, the different components of a test solution were identified without the need for functionalization of the devices, which constitutes a very promising result for the application of these devices to real applications.

Thanks to the use of a conducting polymer as active material, the OECT technology was succesfully transferred on textile substrates, woven cotton and lycra. Different geometries were realized, and the devices show good electrical properties and gating effect, not differently from the "traditional" OECTs realized on glass substrates.

Using the same material, a different kind of devices, redox-active substrates for applications in tissue engineering, was developed and characterized. Four types of PEDOT:PSS thin films were realized by a change in their deposition technique, and their oxidation state was consequently modified through electrochemical oxidation and reduction for 1 h in buffer solution upon the application of +0.8 V and -0.9 V, respectively.

The physical and electrochemical properties of these films were then characterized using several experimental techniques: cyclic voltammetries, spectrophotometry, AFM, water contact angle, surface resistance measurements, and EDX spectroscopy.

From this characterization, the limits for a stable and reproducible oxidation and reduction of PEDOT:PSS films were found as -0.9 V for reduction, and +0.8V for oxidation. The stability with time of the redox state was then assessed, finding that even though a strong decrease in the fraction of oxidized/reduced states is observed during the first minutes of exposure to an electrolyte solution, a significant residual quantity of these states is maintained for at least 48 h, demonstrating that these substrates can be used on several days-long biological experiments even

without a continuous applied bias. The mechanical and electrical properties of the spin-coated and electrodeposited films were investigated, obtaining physical parameters such as stiffness and Young's modulus, surface roughness, electrical conductivity, surface energy, and charge carrier mobility and concentration.

Furthermore, an exchange of ions with the solution, related to the redox state of PEDOT:PSS films, was observed from AFM and EDX measurements, showing that during the reduction process PEDOT:PSS absorbs cations from the electrolyte solution, process that is accompanied by a decrease in film stiffness and an increase in film thickness due to the swelling of water; these cations can then be released again upon the spontaneous oxidation of the film.

Finally, the effect of a change in the redox state of these PEDOT:PSS films on cell growth was assessed using two cell lines, human dermal fibroblasts (hDF) and human tumoral glioblastoma multiforme cells (T98G). The result was found to be strongly cell-dependent, suggesting that each cell type has its own peculiar response to the same environment: hDF proliferation rate was significantly enhanced specifically by oxidized PH1000, the only substrate that we have observed to strongly exchange charge with the cell culture medium, while T98G cells proliferation rate was significantly enhanced on reduced samples, irrespective of the material used as substrate.

These results point out that the cell proliferation rate has a clear dependence on the electrochemical state of its substrate, while it is not affected by other parameters such as surface roughness, surface conductivity and surface energy. As a confirmation, no significant difference in the cell growth rate is observed between the not biased forms of the four types of PEDOT:PSS films here used as substrates, even if they show different surface parameters. A possible explanation involves the exchange of ions between oxidized/reduced PEDOT:PSS and the electrolyte solution, changing the local ionic concentration and thus the cellular activity. This hypothesis was investigated with further biological experiments, *i.e.* by recording the K^+ channel activity and membrane polarization on hDF and T98G cells seeded on PEDOT:PSS at different redox states, finding similar trends with respect to cell growth experiments. The results of these measurements, even if not conclusive, point out that the effect of the redox state of conjugated polymers on cell growth is not related to a single physical or chemical parameter of the material itself, but

involves the interaction of these materials with the biological solution.

Bibliography

[1] G. G. Malliaras. Organic bioelectronics: A new era for organic electronics. *Biochim. Biophys. Acta*, 1830:4286–4287, 2013.

[2] J. Rivnay, R. M. Owens, and G. G. Malliaras. The rise of organic bioelectronics. *Chem. Mater.*, 26:679–685, 2014.

[3] S. Löffler, B. Libberton, and A. Richter-Dahlfors. Organic bioelectronic tools for biomedical applications. *Electronics*, 4(4):879–908, 2015.

[4] R. M. Owens and G. G. Malliaras. Organic electronics at the interface with biology. *MRS Bull.*, 35:449–456, 2010.

[5] J. Y. Wong, R. Langer, and D. E. Ingber. Electrically conducting polymers can noninvasively control the shape and growth of mammalian cells. *Proc. Nati. Acad. Sci. USA*, 91:3201–3204, 1994.

[6] H. Zhang, P. J. Molino, G. G. Wallace, and M. J. Higgins. Quantifying molecular-level cell adhesion on electroactive conducting polymers using electrochemical-single cell force spectroscopy. *Sci. Rep.*, 5:13334, 2015.

[7] C. Saltó, E. Saindon, M. Bolin, A. Kanciurzewska, M. Fahlman, E. W. H. Jager, P. Tengvall, E. Arenas, and M. Berggren. Control of neural stem cell adhesion and density by an electronic polymer surface switch. *Langmuir*, 24:14133–14138, 2008.

[8] K. Svennersten, M. H. Bolin, E. W. Jager, M. Berggren, and A. Richter-Dahlfors. Electrochemical modulation of epithelia formation using conducting polymers. *Biomaterials*, 30:6257–6264, 2009.

[9] A. M. D. Wan, D. J. Brooks, A. Gumus, C. Fischbach, and G. G. Malliaras. Electrical control of cell density gradients on a conducting polymer surface. *Chem. Commun.*, 35:5278–5280, 2009.

[10] F. Greco, T. Fujie, L. Ricotti, S. Taccola, B. Mazzolai, and V. Mattoli. Microwrinkled conducting polymer interface for anisotropic multicellular alignment. *ACS Appl. Mater. Interfaces*, 5:573–584, 2013.

[11] K. M. Sivaraman, B. Özkale, O. Ergeneman, T. Lühmann, G. Fortunato, M. A. Zeeshan, B. J. Nelson, and S. Pané. Redox cycling for passive modification of polypyrrole surface properties: Effects on cell adhesion and proliferation. *Adv. Healthcare Mater.*, 2:591–598, 2013.

[12] G. M. Walker, J. M. Ramsey, R. K. Cavin, D. J. C. Herr, C. I. Merzbacher, and V. Zhirnov. A framework for bioelectronics: Discovery and innovation. *National Institute of Standards and Technology*, 2009.

[13] O. P. Hamill, A. Marty, E. Neher, B. Sakmann, and F. J. Sigworth. Improved patch-clamp techniques for high-resolution current recording from cells and cell-free membrane patches. *Pflügers Archiv*, 391(2):85–100, 1981.

[14] Nobelprize.org. Nobel Media AB 2014. The Nobel Prize in Physiology or Medicine 1991. `http://www.nobelprize.org/nobel_prizes/medicine/laureates/1991`.

[15] F. Scholz. *Electroanalytical Methods - Guide to Experiments and Applications*. Springer, 2nd edition, 2010.

[16] S. Ingebrandt. Bioelectronics: Sensing beyond the limit. *Nat. Nanotechnol.*, 10:734–735, 2015.

[17] J. Yang and D. C. Martin. Impedance spectroscopy and nanoindentation of conducting poly(3,4-ethylenedioxythiophene) coatings on microfabricated neural prosthetic devices. *J. Mater. Res.*, 21(5):1124–1132, 2006.

[18] S. K. Vashist and J. H. T. Luong. Recent advances in electrochemical biosensing schemes using graphene and graphene-based nanocomposites. *Anal. Chim. Acta*, 84:519–550, 2015.

[19] J. Q. Liu, Z. Liu, C. J. Barrow, and W. R. Yang. Molecularly engineered graphene surfaces for sensing applications: a review. *Anal. Chim. Acta*, 859:1–19, 2015.

[20] N. Yang, X. P. Chen, T. L. Ren, P. Zhang, and D. G. Yang. Carbon nanotube based biosensors. *Sens. Actuators, B*, 207:690–715, 2015.

[21] A. Saha, J. Chengmin, and A. A. Marti. Carbon nanotube networks on different platforms. *Carbon*, 79:1–18, 2014.

[22] P. D. Howes, R. Chandrawati, and M. M. Stevens. Colloidal nanoparticles as advanced biological sensors. *Science*, 346(6205):1247390, 2014.

[23] A. Majdalawieh, M. C. Kanan, O. El-Kadri, and S. M. Kanan. Recent advances in gold and silver nanoparticles: synthesis and applications. *J. Nanonsci. Nanotechnol.*, 14(7):4757–4780, 2014.

[24] X. Duan and C. M. Lieber. Nanoscience and the nano-bioelectronics frontier. *Nano Research*, 8(1):1–22, 2015.

[25] S. Krishnamoorthy. Nanostructured sensors for biomedical applications a current perspective. *Curr. Opin. Biotechnol.*, 34:118–124, 2015.

[26] V. Scognamiglio, A. Antonacci, M. D. Lambreva, S. C. Litescu, and G. Rea. Synthetic biology and biomimetic chemistry as converging technologies fostering a new generation of smart biosensors. *Biosens. Bioelectron.*, 74:1076–1086, 2015.

[27] N. Amdursky, D. Marchak, L. Sepunaru, I. Pecht, and M. Sheves. Electronic transport via proteins. *Adv. Mater.*, 26(42):7142–7161, 2014.

[28] C. J. Bettinger. Materials advances for next-generation ingestible electronic medical devices. *Trends Biotechnol.*, 33(10):575–585, 2015.

[29] L. Torsi, M. Magliulo, K. Manoli, and G. Palazzo. Organic field-effect transistor sensors: a tutorial review. *Chem. Soc. Rev.*, 48:8612–8628, 2013.

[30] H. Shirakawa, E. J. Louis, A. G. MacDiarmid, C. K. Chiang, and A. J. Heeger. Synthesis of electrically conducting organic polymers: halogen derivatives of polyacetylene, $(CH)_x$. *J. Chem. Soc. Chem. Commun.*, pages 578–580, 1977.

[31] C. K. Chiang, C. R. Fincher, Y. W. Park, A. J. Heeger, H. Shirakawa, E. J. Louis, S. C. Gau, and A. G. McDiarmid. Electrical conductivity in doped polyacetylene. *Phys. Rev. Lett.*, 39:1098, 1977.

[32] Nobelprize.org. Nobel Media AB 2014. The Nobel Prize in Chemistry 2000. `http://www.nobelprize.org/nobel_prizes/chemistry/laureates/2000`.

[33] A. J. Heeger. Semiconducting and metallic polymers: The fourth generation of polymeric materials. *J. Phys. Chem. B*, 105(36):8475–8491, 2001.

[34] G. Inzelt. *Conducting Polymers - A New Era in Electrochemistry*. Springer, 2nd edition, 2012.

[35] G. G. Malliaras and R. Friend. An organic electronics primer. *Phys. Today*, 58(5):53, 2005.

[36] M. Berggren and A. Richter-Dahlfors. Organic bioelectronics. *Adv. Mater.*, 19:3201–3213, 2007.

[37] A. S. Andersson, F. Bäckhed, A. von Euler, A. Richter-Dahlfors, D. Sutherland, and B. Kasemo. Nanoscale features influence epithelial cell morphology and cytokine production. *Biomaterials*, 24(20):3427–36, 2003.

[38] M. J. Higgins, P. J. Molino, Z. L. Yue, and G. G. Wallace. Organic conducting polymer-protein interactions. *Chem. Mater.*, 24(5):828–839, 2012.

[39] S. C. Luo, E. M. Ali, N. C. Tansil, H. H. Yu, S. Gao, E. A. B. Kantchev, and J. Y. Ying. Poly(3,4-ethylenedioxythiophene) (PEDOT) nanobiointerfaces:

Thin, ultrasmooth, and functionalyzed PEDOT films with in vitro and in vivo biocompatibility. *Langmuir*, 24(15):8071–8077, 2008.

[40] X. D. Wang, X. S. Gu, C. W. Yuan, S. J. Chen, P. Y. Zhang, T. Y. Zhang, J. Yao, F. Chen, and G. Chen. Evaluation of biocompatibility of polypyrrole in vitro and in vivo. *J. Biomed. Mater. Res., Part A*, 68A(3):411–422, 2004.

[41] S. Kamalesh, P. C. Tan, J. J. Wang, T. Lee, E. T. Kang, and C. H. Wang. Biocompatibility of electroactive polymers in tissues. *J. Biomed. Mater. Res.*, 52(3):467–478, 2000.

[42] M. Nikolou and G. G. Malliaras. Applications of poly (3,4-ethylenedioxythiophene) doped with poly(styrene sulfonic acid) transistors in chemical and biological sensors. *Chem. Rec.*, 8:13–22, 2008.

[43] S. Kumar, A. Wandit, R. Kumar, and N. Dilbaghi. Graphene, carbon nanotubes, zinc oxide and gold as elite nanomaterials for fabrication of biosensors for healthcare. *Bioesens. Bioelectron.*, 70:498–503, 2015.

[44] L. C. Clark and G. Sachs. Bioelectrodes for tissue metabolism. *Ann. N. Y. Acad. Sci.*, 148:133–153, 1968.

[45] L. Basiricò, P. Cosseddu, B. Fraboni, and A. Bonfiglio. Inkjet printing of transparent, flexible, organic transistors. *Thin solid films*, 520:1291–1294, 2011.

[46] L. Kergoat, B. Piro, M. Berggren, G. Horowitz, and M. C. Pham. Advances in organic transistor-based biosensors: from organic electrochemical transistors to electrolyte-gated organic field-effect transistors. *Anal. Bioanal. Chem.*, 402:1813–1826, 2012.

[47] F. Ebisawa, T. Kurokawa, and S. Nara. Electrical properties of polyacetylene/polysiloxane interface. *J. Appl. Phys.*, 54:3255–3259, 1983.

[48] C. Wang, H. Dong, W. Hu, Y. Liu, and D. Zhu. Semiconducting π-conjugated systems in field-effect transistors: a material odyssey for organic electronics. *Chem. Rev.*, 112:2208–2267, 2012.

[49] R. Ponce Ortiz, A. Facchetti, and T. J. Marks. High-k organic, inorganic, and hybrid dielectrics for low-voltage organic field-effect transistors. *Chem. Rev.*, 110(1):205–239, 2010.

[50] A. Dodabalapur, L. Torsi, and H. E. Katz. Organic transistors: two-dimensional transport and improved electrical characteristics. *Science*, 268(5208):270–271, 1995.

[51] M. Erouel, K. Diallo, J. Tardy, P. Blanchard, J. Roncali, P. Frere, and N. Jaffrezic. Stability and 2, 4-dinitrotoluene response of organic field effect transistors based on π-conjugated thiophene oligomers. *Mater. Sci. Eng., C*, 28:965–970, 2008.

[52] S. Tiwari, A. K. Singh, L. Joshi, P. Chakrabarti, W. Takashima, and R. Kaneto, K. andPrakash. Poly-3-hexylthiophene based organic field-effect transistor: Detection of low concentration of ammonia. *Sens. Actuators, B*, 171-172:962–968, 2012.

[53] A. M. Andringa, M. J. Spijkman, E. C. Smits, S. G. Mathijssen, P. A. van Hal, S. Setayesh, N. P. Willard, O. V. Borshchev, S. A. Ponomarenko, P. W. M. Blom, and D. M. de Leeuw. Gas sensing with self-assembled monolayer field-effect transistors. *Org. Electron.*, 11(5):895–898, 2010.

[54] E. D. Royer, J. E. andKappe, C. Zhang, D. T. Martin, W. C. Trogler, and A. C. Kummel. Organic thin-film transistors for selective hydrogen peroxide and organic peroxide vapor detection. *J. Phys. Chem. C*, 116(46):2456624572, 2012.

[55] P. Bergveld. Thirty years of ISFETOLOGY: what happened in the past 30 years and what may happen in the next 30 years. *Sens. Actuators, B*, 88(1):1–20, 2003.

[56] S. Lai, M. Demelas, G. Casula, P. Cosseddu, M. Barbaro, and A. Bonfiglio. Ultralow voltage, OTFT-based sensor for label-free DNA detection. *Adv. Mater.*, 25(1):103107, 2013.

[57] M. J. Panzer, C. R. Newman, and C. D. Frisbie. Low-voltage operation of a pentacene field-effect transistor with a polymer electrolyte gate dielectric. *Appl. Phys. Lett.*, 86:103503, 2005.

[58] M. J. Panzer and C. D. Frisbie. Exploiting ionic coupling in electronic devices: electrolyte-gated organic field-effect transistors. *Adv. Mater.*, 20:3177–3180, 2008.

[59] J-C. Lassègues, J. Grondin, T. Becker, L. Servant, and M. Hernandez. Supercapacitor using a proton conducting polymer electrode. *Solid State Ionics*, 77:311–317, 1995.

[60] G. Tarabella, F. M. Mohammadi, N. Coppedè, F. Barbero, S. Iannotta, C. Santato, and F. Cicoira. New opportunities for organic electronics and bioelectronics: ions in action. *Chem. Sci.*, 4:1395–1409, 2013.

[61] J. H. Cho, J. Lee, Y. He, B. S. Kim, T. P. Lodge, and C. D. Frisbie. High-capacitance ion gel gate dielectrics with faster polarization response times for organic thin film transistors. *Adv. Mater.*, 20(4):686–690, 2008.

[62] M. J. Panzer and C. D. Frisbie. Polymer electrolyte-gated organic field-effect transistors: Low-voltage, high-current switches for organic electronics and testbeds for probing electrical transport at high charge carrier density. *J. Am. Chem. Soc.*, 129:6599–6607, 2007.

[63] M. Hamedi, L. Herlogsson, X. Crispin, R. Marcilla, M. Berggren, and O. Inganäs. Fiber-embedded electrolyte-gated field-effect transistors for e-textiles. *Adv. Mater.*, 21(5):573–577, 2008.

[64] T. G. Bäcklund, H. G. O. Sandberg, R. Österbacka, and H. Stubb. Current modulation of hygroscopic insulator organic field-effect transistors. *Appl. Phys. Lett.*, 85:3887–3889, 2004.

[65] L. Herlogsson, M. Cölle, S. Tierney, X. Crispin, and M. Berggren. Low-voltage ring oscillators based on polyelectrolyte-gated polymer thin-film transistors. *Adv. Mater.*, 22(1):72–76, 2009.

[66] P. Stoliar, E. Bystrenova, S. D. Quiroga, P. Annibale, M. Facchini, M. Spijkman, S. Setayesh, D. de Leeuw, and F. Biscarini. DNA adsorption measured with ultra-thin film organic field effect transistor. *Biosens. Bioelectron.*, 24(9):29352938, 2009.

[67] F. Buth, A. Donner, M. Sachsenhauser, M. Stutzmann, and J. A. Garrido. Biofunctional electrolyte-gated organic field-effect transistor. *Adv. Mater.*, 24(33):45114517, 2012.

[68] S. Casalini, F. Leonardi, T. Cramer, and F. Biscarini. Organic field-effect transistor for label-free dopamine sensing. *Org. Electron.*, 14(1):156–163, 2013.

[69] T. Cramer, B. Chelli, M. Murgia, M. Barbalinardo, E. Bystrenova, D. M. de Leeuw, and F. Biscarini. Organic ultra-thin film transistors with a liquid gate for extracellular stimulation and recording of electric activity of stem cell-derived neuronal networks. *Phys. Chem. Chem. Phys.*, 15:38973905, 2013.

[70] X. Strakosas, M. Bongo, and R. M. Owens. The organic electrochemical transistor for biological applications. *J. Appl. Polym. Sci.*, 132(15):41735, 2015.

[71] D. Khodagholy, J. Rivnay, M. Sessolo, M. Gurfinkel, P. Leleux, L. H. Jimison, E. Stavrinidou, T. Herve, S. Sanaur, R. M. Owens, and G. G. Malliaras. High transconductance organic electrochemical transistors. *Nat. Commun.*, 4:2133, 2013.

[72] F. Lin and M. C. Lonergan. Gate electrode processes in an electrolyte-gated transistor: Non-faradaically versus faradaically coupled conductivity modulation of a polyacetylene ionomer. *Appl. Phys. Lett.*, 88(13):133507, 2006.

[73] P. Lin, F. Yan, and L. W. Chan. Ion-sensitive properties of organic electrochemical transistors. *ACS Appl. Mater. Interfaces*, 2(6):1637–1641, 2010.

[74] F. Cicoira, M. Sessolo, O. Yaghmazadeh, J. A. DeFranco, S. Y. Yang, and G. G. Malliaras. Influence of device geometry on sensor characteristics of planar organic electrochemical transistors. *Adv. Mater.*, 22(9):1012–1016, 2010.

[75] L. Basiricò, P. Cosseddu, A. Scidà, B. Fraboni, G. G. Malliaras, and A. Bonfiglio. Electrical characteristics of ink-jet printed, all-polymer electrochemical transistors. *Org. Electron.*, 13(2):244–248, 2012.

[76] I. Gualandi, M. Marzocchi, E. Scavetta, M. Calienni, A. Bonfiglio, and B. Fraboni. A simple all-PEDOT:PSS electrochemical transistor for ascorbic acid sensing. *J. Mater. Chem. B*, 3:6753–6762, 2015.

[77] J. Rivnay, P. Leleux, M. Ferro, M. Sessolo, A. Williamson, D. A. Koutsouras, D. Khodagholy, M. Ramuz, X. Strakosas, R. M. Owens, C. Benar, J. M. Badier, C. Bernard, and G. G. Malliaras. High-performance transistors for bioelectronics through tuning of channel thickness. *Sci. Adv.*, 1(4):e1400251, 2015.

[78] J. Rivnay, P. Leleux, M. Sessolo, D. Khodagholy, T. Hervé, M. Fiocchi, and G. G. Malliaras. Organic electrochemical transistors with maximum transconductance at zero gate bias. *Adv. Mater.*, 25(48):7010–7014, 2013.

[79] M. Sessolo, J. Rivnay, E. Bandiello, G. G. Malliaras, and H. J. Bolink. Ion-selective organic electrochemical transistors. *Adv. Mater.*, 26(28):4803–4807, 2014.

[80] M. Nishizawa, T. Matsue, and I. Uchida. Penicillin sensor based on a microarray electrode coated with pH-responsive polypyrrole. *Anal. Chem.*, 64(21):2642–2644, 1992.

[81] Z. T. Zhu, J. T. Mabeck, C. Zhu, N. C. Cady, C. A. Batt, and G. G. Malliaras. A simple poly(3,4-ethylene dioxythiophene)/poly(styrene sulfonic acid) transistor for glucose sensing at neutral pH. *Chem. Commun.*, 13:1556–1557, 2004.

[82] D. J. Macaya, M. Nikolou, S. Takamatsu, J. T. Mabeck, R. M. Owens, and G. G. Malliaras. Simple glucose sensors with micromolar sensitivity based on organic electrochemical transistors. *Sens. Actuators B: Chem.*, 123(1):374–378, 2007.

[83] N. Y. Shim, D. A. Bernards, D. J. Macaya, J. A. DeFranco, M. Nikolou, R. M. Owens, and G. G. Malliaras. All-plastic electrochemical transistor for glucose sensing using a ferrocene mediator. *Sensors*, 9(12):9896–9902, 2009.

[84] N. Coppedè, G. Tarabella, M. Villani, D. Calestani, S. Iannotta, and A. Zappettini. Human stress monitoring through an organic cotton-fiber biosensor. *J. Mater. Chem. B*, 2(34):5620–5626, 2014.

[85] G. Tarabella, A. Pezzella, A. Romeo, P. DAngelo, N. Coppedè, M. Calicchio, M. dIschia, R. Mosca, and S. Iannotta. Irreversible evolution of eumelanin redox states detected by an organic electrochemical transistor: en route to bioelectronics and biosensing. *J. Mater. Chem. B*, 1(31):3843–3849, 2013.

[86] H. Tang, P. Lin, H. L. W. Chan, and F. Yan. Highly sensitive dopamine biosensors based on organic electrochemical transistors. *Biosens. Bioelectron.*, 26(11):4559–4563, 2011.

[87] K. Tybrandt, S. B. Kollipara, and M. Berggren. Organic electrochemical transistors for signal amplificationin fast scan cyclic voltammetry. *Sens. Actuators, B*, 195:651–656, 2014.

[88] L. Kergoat, B. Piro, D. T. Simon, M. C. Pham, V. Noël, and M. Berggren. Detection of glutamate and acetylcholine with organic electrochemical transistors based on conducting polymer/platinum nanoparticle composites. *Adv. Mater.*, 26(32):5658–5664, 2014.

[89] D. Khodagholy, V. F. Curto, K. J. Fraser, M. Gurfinkel, R. Byrne, D. Diamond, G. G. Malliaras, F. Benito-Lopez, and R. M. Owens. Organic electrochemical transistor incorporating an ionogel as a solid state electrolyte for lactate sensing. *J. Mater. Chem.*, 22:4440–4443, 2012.

[90] P. Lin, X. Luo, I. M. Hsing, and F. Yan. Organic electrochemical transistors integrated in flexible microfluidic systems and used for label-free DNA sensing. *Adv. Mater.*, 23:4035–4040, 2011.

[91] L. H. Jimison, S. Tria, D. Khodagholy, M. Gurfinkel, E. Lanzarini, A. Hama, G. G. Malliaras, and R. M. Owens. Measurement of barrier tissue integrity with an organic electrochemical transistor. *Adv. Mater.*, 24:5919–5923, 2012.

[92] S. Tria, L. H. Jimison, A. Hama, M. Bongo, and R. M. Owens. Sensing of EGTA mediated barrier tissue disruption with an organic transistor. *Biosensors*, 3(1):44–57, 2013.

[93] S. Tria, M. Ramuz, M. Huerta, P. Leleux, J. Rivnay, L. H. Jimison, A. Hama, G. G. Malliaras, and R. M. Owens. Dynamic monitoring of salmonella typhimurium infection of polarized epithelia using organic transistors. *Adv. Health. Mater.*, 3:1053–1060, 2014.

[94] A. Romeo, G. Tarabella, P. D'Angelo, C. Caffarra, D. Cretella, R. Alfieri, Petronini P. G., and S. Iannotta. Drug-induced cellular death dynamics monitored by a highly sensitive organic electrochemical system. *Biosens. Bioelectron.*, 68:791–797, 2015.

[95] D. Khodagholy, T. Doublet, P. Quilichini, M. Gurfinkel, P. Leleux, A. Ghestem, E. Ismailova, T. Hervé, S. Sanaur, C. Bernard, and G. G. Malliaras. In vivo recordings of brain activity using organic transistors. *Nat. Commun.*, 4:1575, 2013.

[96] A. Campana, T. Cramer, D. T. Simon, M. Berggren, and F. Biscarini. Electrocardiographic recording with conformable organic electrochemical transistor fabricated on resorbable bioscaffold. *Adv. Mater.*, 26(23):3874–3878, 2014.

[97] P. Leleux, J. Rivnay, T. Lonjaret, J. M. Badier, C. Benar, T. Hervé, P. Chauvel, and G. G. Malliaras. Organic electrochemical transistor for clinical applications. *Adv. Health. Mater.*, 4(1):142–147, 2015.

[98] R. L. Williams and P. J. Doherty. A preliminary assessment of poly(pyrrole) in nerve guide studies. *J. Mater. Sci.: Mater. Med.*, 5(6):429–433, 1994.

[99] D. Khodagholy, T. Doublet, M. Gurfinkel, P. Quilichini, E. Ismailova, P. Leleux, T. Herve, S. Sanaur, C. Bernard, and G. G. Malliaras. Highly conformable conducting polymer electrodes for in vivo recordings. *Adv. Mater.*, 23:H268–H272, 2011.

[100] M. Bolin, K. Svennersten, X. Wang, I. S. Chronakis, A. Richter-Dahlfors, E. Jager, and M. Berggren. Nano-fiber scaffold electrodes based on pedot for cell stimulation. *Sens. Actuators*, 142:451–456, 2009.

[101] A. F. Quigley, J. M. Razal, B. C. Thompson, S. E. Moulton, M. Kita, E. L. Kennedy, G. M. Clark, G. G. Wallace, and R. M. Kapsa. A conducting-polymer platform with biodegradable fibers for stimulation and guidance of axonal growth. *Adv. Mater.*, 21:4393–4397, 2009.

[102] D. H. Kim, S. M. Richardson-Burns, J. L. Hendricks, C. Sequera, and D. C. Martin. Effect of immobilized nerve growth factor on conductive polymers: Electrical properties and cellular response. *Adv. Funct. Mater.*, 17:79–86, 2007.

[103] F. Cicchetti and R. A. Barker. The glial response to intracerebrally delivered therapies for neurodegenerative disorders: Is this a critical issue? *Front. Pharmacol.*, 5:139, 2014.

[104] X. Cui, V. A. Lee, Y. Raphael, J. A. Wiler, J. F. Hetke, D. J. Anderson, and D. C. Martin. Surface modification of neural recording electrodes with conducting polymer/biomolecule blends. *J. Biomed. Mater. Res.*, 56:261–272, 2001.

[105] W. R. Stauffer and X. T. Cui. Polypyrrole doped with 2 peptide sequences from laminin. *Biomaterials*, 27:2405–2413, 2006.

[106] S. M. Richardson-Burns, J. L. Hendricks, B. Foster, L. K. Povlich, D. H. Kim, and D. C. Martin. Polymerization of the conducting poly-

mer poly(3,4-ethylenedioxythiophene) (PEDOT) around living neural cells. *Biomaterials*, 28:1539–1552, 2007.

[107] S. M. Richardson-Burns, J. L. Hendricks, and D. C. Martin. Electrochemical polymerization of conducting polymers in living neural tissue. *J. Neural Eng.*, 4:L6–L13, 2007.

[108] H. H. Jasper, G. Arfel-Capdeville, and T. Rasmussen. Evaluation of EEG and cortical electrographic studies for prognosis of seizures following surgical excision of epileptogenic lesions. *Epilepsia*, 2(2):130–137, 1961.

[109] D. R. Kipke, W. Shain, G. Buzsáki, E. Fetz, J. M. Henderson, J. F. Hetke, and G. Schalk. Advanced neurotechnologies for chronic neural interfaces: new horizons and clinical opportunities. *J. Neurosci.*, 28(46):11830–11838, 2008.

[110] D. A. Bernards, G. G. Malliaras, G. E. S. Toombes, and S. M. Gruner. Gating of an organic transistor through a bilayer lipid membrane with ion channels. *Appl. Phys. Lett.*, 89:053505, 2006.

[111] D. Nilsson, T. Kugler, P. O. Svensson, and M. Berggren. An all-organic sensor-transistor based on a novel electrochemical transducer concept printed electrochemical sensors on paper. *Sens. Act. B*, 86:193–197, 2002.

[112] D. Khodagholy, J. N. Gelinas, T. Thesen, W. Doyle, O. Devinsky, G. G. Malliaras, and G. Buzsáki. NeuroGrid: recording action potentials from the surface of the brain. *Nat. Neurosci.*, 18:310–315, 2015.

[113] J. Isaksson, C. Tengstedt, M. Fahlman, N. Robinson, and M. Berggren. A solid-state organic electronic wettability switch. *Adv. Mater.*, 16(4):316–320, 2004.

[114] A. Gelmi, M. J. Higgins, and G. G. Wallace. Physical surface and electromechanical properties of doped polypyrrole biomaterials. *Biomaterials*, 31(8):1974–1983, 2010.

[115] M. Marzocchi, I. Gualandi, M. Calienni, I. Zironi, E. Scavetta, G. Castellani, and B. Fraboni. Physical and electrochemical properties of PEDOT:PSS as a tool for controlling cell growth. *ACS Appl. Mater. Interfaces*, 7(32):17993–18003, 2015.

[116] A. M. D. Wan, R. M. Schur, C. K. Ober, C. Fischbach, D. Gourdon, and G. G. Malliaras. Electrical control of protein conformation. *Adv. Mater.*, 24(18):2501–2505, 2012.

[117] A. M. D. Wan, E. M. Chandler, M. Madhavan, D. W. Infanger, C. K. Ober, D. Gourdon, G. G. Malliaras, and C. Fischbach. Fibronectin conformation regulates the proangiogenic capability of tumor-associated adipogenic stromal cells. *Biochim. Biophys. Acta, Gen. Subj.*, 1830(9):4314–4320, 2013.

[118] A. Gelmi, M. J. Higgins, and G. G. Wallace. Resolving sub-molecular binding and electrical switching mechanisms of single proteins at electroactive conducting polymers. *Small*, 9(3):393–401, 2013.

[119] A. G. MacDiarmid, R. J. Mammone, R. B. Kaner, S. J. Porter, R. Pethig, A. J. Heeger, and D. R. Rosseinsky. The concept of "doping" of conducting polymers: The role of reduction potentials (and discussion). *Philos. Trans. R. Soc. A Math. Phys. Eng. Sci.*, 314:3–15, 1985.

[120] M. Liu, F. Q. Nie, Z. Wei, Y. Song, and L. Jiang. In situ electrochemical switching of wetting state of oil droplet on conducting polymer films. *Langmuir*, 26:3993–3997, 2010.

[121] S. Boduroglu, M. Cetinkaya, W. J. Dressick, A. Singh, and M. C. Demirel. Controlling the wettability and adhesion of nanostructured poly-(p-xylylene) films. *Langmuir*, 23:11391–11395, 2007.

[122] M. H. Bolin, K. Svennersten, D. Nilsson, A. Sawatdee, E. W. H. Jager, A. Richter-Dahlfors, and M. Berggren. Active control of epithelial cell-density gradients grown along the channel of an organic electrochemical transistor. *Adv. Mater.*, 21(43):4379–4382, 2009.

[123] M. Ramuz, A. Hama, M. Huerta, J. Rivnay, P. Leleux, and R. M. Owens. Combined optical and electronic sensing using planar organic transistors. *Adv. Mater.*, 26(41):7083–7090, 2014.

[124] E. W. Neuse. Synthetic polymers as drug-delivery vehicles in medicine. *Metal-based Drugs*, 2008:469531, 2008.

[125] B. Zinger and L. L. Miller. Timed release of chemicals from polypyrrole films. *J. Am. Chem. Soc.*, 106:6861–6863, 1984.

[126] L. Poole-Warren and J. Goding. Challenges of therapeutic delivery using conducting polymers. *Ther. Deliv.*, 3:421–427, 2012.

[127] D. Svirskis, J. Travas-Sejdic, A. Rodgers, and S. Garg. Electrochemically controlled drug delivery based on intrinsically conducting polymers. *J. Control. Release*, 146:6–15, 2010.

[128] D. Svirskis, M. Sharma, Y. Yu, and S. Garg. Electrically switchable polypyrrole film for the tunable release of progesterone. *Ther. Deliv.*, 4:307–313, 2013.

[129] M. Sharma, G. I. N. Waterhouse, S. W. C. Loader, S. Garg, and D. Svirskis. High surface area polypyrrole scaffolds for tunable drug delivery. *Int. J. Pharm.*, 443:163–168, 2013.

[130] S. Jiang, Y. Sun, X. Cui, X. Huang, Y. He, S. Ji, W. Shi, and D. Ge. Enhanced drug loading capacity of polypyrrole nanowire network for controlled drug release. *Synth. Met.*, 163:19–23, 2013.

[131] L. M. Lira and S. I. C. de Torresi. Conducting polymer-hydrogel composites for electrochemical release devices: Synthesis and characterization of semi-interpenetrating polyaniline-polyacrylamide networks. *J. Electrochem. Commun.*, 7(7):717–723, 2005.

[132] D. Mawad, E. Stewart, D. L. Officer, T. Romeo, P. Wagner, K. Wagner, and G. G. Wallace. A single component conducting polymer hydrogel as a scaffold for tissue engineering. *Adv. Funct. Mater.*, 22(13):2692–2699, 2012.

[133] K. Keiichi, F. Hisashi, K. Masakatsu, and T. Wataru. Conducting polymer soft actuators based on polypyrrole films - energy conversion efficiency. *Smart Mater. Struct.*, 16:S250, 2007.

[134] K. Kaneto, H. Somekawa, and W. Takashima. Soft actuators based on conducting polymers: Recent progress. *SPIE Proc.*, 5051, 2003.

[135] K. Kaneto, M. Nakashima, and W. Takashima. Improvement of electrochemical deformation of conducting polymers: Strain, force, and response. *SPIE Proc.*, 5385, 2004.

[136] K. Kaneto, M. Nakashima, and W. Takashima. Electroactive performances of conductive polythiophene/hydrogel hybrid artificial muscle. *Energy Procedia*, 34:673–681, 2013.

[137] J. D. Madden. Polypyrrole actuators: Properties and initial applications. In K. Kim and S. Tadokoro, editors, *Electroactive Polymers for Robotic Applications*, pages 121–152. Springer: London, UK, 2007.

[138] X. Wang and E. Smela. Color and volume change in PPy(DBS). *J. Phys. Chem. C*, 113:359–368, 2009.

[139] T. F. Otero, J. G. Martinez, and J. Arias-Pardilla. Biomimetic electrochemistry from conductive polymers. a review: Artificial muscles, smart membranes, smart drug/delivery and computer/neuron interfaces. *Electrochim. Acta*, 84:112–128, 2012.

[140] L. Valero, J. Arias-Pardilla, J. Cauich-Rodriguez, M. A. Smit, and T. F. Otero. Characterization of the movement of polypyrrole-dodecylbenzenesulfonate-perchlorate/tape artificial muscles. Faradaic control of reactive artificial molecular motors and muscles. *Electrochim. Acta*, 56(10):3721–3726, 2011.

[141] K. Svennersten, M. Berggren, A. Richter-Dahlfors, and E. W. H. Jager. Mechanical stimulation of epithelial cells using polypyrrole microactuators. *Lab Chip*, 11:3287–3293, 2011.

[142] M. Hiraoka, P. Fiorini, J. O'Callaghan, I. Yamashita, C. van Hoof, and M. Op de Beeck. Miniature conductive polymer actuators for high pressure generation in lab on chip systems. *Sens. Actuators A Phys.*, 133:23–29, 2012.

[143] L. V. Conzuelo, J. Arias-Pardilla, J. V. Cauich-Rodriguez, M. A. Smit, and T. F. Otero. Sensing and tactile artificial muscles from reactive materials. *Sensors*, 10:2638–2674, 2010.

[144] P. Schroeder, J. Schotter, A. Shoshi, M. Eggeling, O. Bethge, A. Hutten, and H. Bruckl. Artificial cilia of magnetically tagged polymer nanowires for biomimetic mechanosensing. *Bioinspiration Biomimicry*, 6:046007, 2011.

[145] K. M. Persson, R. Karlsson, K. Svennersten, S. Löffler, E. W. H. Jager, A. Richter-Dahlfors, P. Konradsson, and M. Berggren. Electronic control of cell detachment using a self-doped conducting polymer. *Adv. Mater.*, 23:4403–4408, 2011.

[146] A. Elschner, S. Kirchmeyer, W. Lövenich, U. Merker, and K. Reuter. *PEDOT - Principles and Applications of an Intrinsically Conductive Polymer*. CRC Press, 2011.

[147] R. Hoffmann, C. Janiak, and C. Kollmar. A chemical approach to the orbitals of organic polymers. *Macromolecules*, 24(13):3725–3746, 1991.

[148] J. H. Davies. *The Physics of Low Dimensional Semiconductors: An Introduction*. Cambridge University Press, 6th edition, 2006.

[149] B. E. Kohler and I. D. W. Samuel. Experimental determination of conjugation lengths in long polyene chains. *J. Chem. Phys.*, 103(14):6248–6252, 1995.

[150] R. E. Peierls. *Quantum Theory of Solids*. Oxford University Press, 1955.

[151] M. Grundmann. *The Physics of Semiconductors - An Introduction including Devices and Nanophysics*. Springer, 2006.

[152] J. L. Brédas and G. B. Street. Polarons, bipolarons, and solitons in conducting polymers. *Acc. Chem. Res.*, 18:309–315, 1985.

[153] E. M. Conwell. *Handbook of Organic Conductive Molecules and Polymers*, volume 4. John Wiley & Sons, 2000.

[154] P. W. Anderson. Model for the electronic structure of amorphous semiconductors. *Phys. Rev. Lett.*, 34(15):953–955, 1975.

[155] J. L. Brédas, R. R. Chance, and R. Silbey. Theoretical studies of charged defect states in doped polyacetylene and polyparaphenylene. *Mol. Cryst. Liq. Cryst.*, 77:319, 1981.

[156] J. L. Brédas, R. R. Chance, and R. Silbey. Comparative theoretical study of the doping of conjugated polymers: polarons in polyacetylene and polyparaphenylene. *Phys. Rev. B: Condens. Matter*, 26:5843, 1982.

[157] J. L. Brédas, J. C. Scott, K. Yakushi, and G. B. Street. Polarons and bipolarons in polypyrrole: Evolution of the band structure and optical spectrum upon doing. *Phys. Rev. B: Condens. Matter*, 30:1023, 1984.

[158] J. C. Scott, M. Kronubi, P. Pfluger, and G. B. Street. Electron-spin resonance studies of pyrrole polymers: Evidence for bipolarons. *Phys. Rev. B: Condens. Matter*, 28:2140, 1983.

[159] W. P. Su, J. R. Schrieffer, and A. J. Heeger. Solitons in polyacetylene. *Phys. Rev. Lett.*, 42:1698, 1979.

[160] C. Rebbi. Solitons. *Sci. Am.*, 240:92–99, 1979.

[161] S. Kivelson. Electron hopping conduction in the soliton model of polyacetylene. *Mol. Cryst. Liq. Cryst.*, 77(1-4):65–79, 1981.

[162] J. L. Brédas, J. G. Thémans, J. G. Fripiat, J. M. André, and R. R. Chance. Highly conducting polyparaphenylene, polypyrrole, and polythiophene chains: An ab initio study of the geometry and electronic-structure modifications upon doping. *Phys. Rev. B: Condens. Matter*, 29:6761, 1984.

[163] N. W. Ashcroft and N. D. Mermin. *Solid State Physics*. Holt Rinehart & Winston, 1976.

[164] A. B. Kaiser. Systematic conductivity behavior in conducting polymers: Effects of heterogeneous disorder. *Adv. Mater.*, 13(12-13):927–941, 2001.

[165] J. S. Dugdale. *The electical properties of metals and alloys*. Edward Arnold, 1977.

[166] A. B. Kaiser. Electronic transport properties of conducting polymers and carbon nanotubes. *Rep. Prog. Phys.*, 64(1):1, 2001.

[167] A. B. Kaiser. Thermoelectric power and conductivity of heterogeneous conducting polymers. *Phys. Rev. B*, 40(5):2806, 1989.

[168] H. C. F. Martens, J. A. Reedijk, H. B. Brom, D. M. de Leeuw, and R. Menon. Metallic state in disordered quasi-one-dimensional conductors. *Phys. Rev. B*, 63(7):073203, 2001.

[169] A. N. Aleshin, S. R. Williams, and A. J. Heeger. Transport properties of poly(3,4- ethylenedioxythiophene)/ poly(styrenesulfonate). *Synth. Met.*, 94(2):173–177, 2001.

[170] J. Joo, Z. Oblakowski, G. Du, J. P. Pouget, E. J. Oh, J. M. Wiesinger, Y. Min, A. G. MacDiarmid, and A. J. Epstein. Microwave dielectric response of mesoscopic metallic regions and the intrinsic metallic state of polyaniline. *Phys. Rev. B*, 49(4):2977–2980, 1994.

[171] V. Percec, C. H. Ahn, W. D. Cho, A. M. Jamieson, J. Kim, T. Leman, M. Schmidt, M. Gerle, M. Möller, S. A. Prokhorova, S. S. Sheiko, S. Z. D. Cheng, A. Zhang, G. Ungar, and D. J. P. Yeardley. Visualizable cylindrical macromolecules with controlled stiffness from backbones containing libraries of self-assembling dendritic side groups. *J. Am. Chem. Soc.*, 120(34):8619–8631, 1998.

[172] V. N. Prigodin and K. B. Efetov. Metal-insulator transition in an irregular structure of metallic chains. *Synth. Met.*, 65(2-3):195–201, 1994.

[173] Y. W. Park, A. J. Heeger, M. A. Druy, and A. G. MacDiarmid. Electrical transport in doped polyacetylene. *J. Chem. Phys.*, 73(2):946, 1980.

[174] L. Pietronero. Ideal conductivity of carbon π polymers and intercalation compounds. *Synth. Met.*, 8(3):225–231, 1983.

[175] S. Kivelson and A. J. Heeger. Intrinsic conductivity of conducting polymers. *Synth. Met.*, 22(4):371–384, 1988.

[176] A. B. Kaiser. Metallic behaviour in highly conducting polymers. *Synth. Met.*, 45(2):183–196, 1991.

[177] P. Sheng. Fluctuation-induced tunneling conduction in disordered materials. *Phys. Rev. B*, 21(6):2180, 1980.

[178] A. B. Kaiser, C. J. Liu, P. W. Gilberd, B. Chapman, N. T. Kemp, B. Wessling, A. C. Partridge, W. T. Smith, and J. S. Shapiro. Comparison of electronic transport in polyaniline blends, polyaniline and polypyrrole. *Synth. Met.*, 84(1):699–702, 1997.

[179] N. F. Mott. Conduction in non-crystalline systems: III. localized states in a pseudogap and near extremities of conduction and valence bands. *Phylos. Mag.*, 19(160):835–852, 1969.

[180] A. L. Efros and B. I. Shklovskii. Coulomb gap and low temperature conductivity of disordered systems. *J. Phys. C*, 8(4):L49, 1975.

[181] P. Sheng. Electronic transport in granular metal films. *Philos. Mag. B*, 65(3):357–384, 1992.

[182] Ö. Rapp, S. M. Bhagat, and H. Gudmusson. Evidence for correlation effects:$-\sqrt{\mathrm{T}}$ behaviour in the low temperature electrical resistance of disordered metals. *Solid State Commun.*, 42(10):741–744, 1982.

[183] Y. Wang. Research progress on a novel conductive polymer poly(3,4-ethylenedioxythiophene) (PEDOT) by a change of solvents. *J. Phys.: Conf. Ser.*, 152:012023, 2009.

[184] D. Mecerreyes, R. Marcilla, E. Ochoteco, H. Grande, J. A. Pomposo, R. Vergaz, and J. M. Sánchez Pena. A simplified all-polymer flexible electrochromic device. *Electrochim. Acta*, 49(21):3555–3559, 2004.

[185] R. Kiebooms, A. Aleshin, K. Hutchison, and F. Wudl. Thermal and electromagnetic behavior of doped poly(3,4-ethylenedioxythiophene) films. *J. Phys. Chem. B*, 101(51):11037, 1997.

[186] Q. Pei, G. Zuccarello, M. Ahskog, and O. Inganäs. Electrochromic and highly stable poly(3,4-ethylenedioxythiophene) switches between opaque blue-black and transparent sky blue. *Polymer*, 35(7):1347, 1994.

[187] G. Heywang and F. Jonas. Poly(alkylenedioxythiophene)s new, very stable conducting polymers. *Adv. Mater.*, 4(2):116–118, 1992.

[188] M. Dietrich, J. Heinze, G. Heywang, and F. Jonas. Electrochemical and spectroscopic characterization of polyalkylenedioxythiophenes. *J. Electroanal. Chem.*, 369(1-2):87–92, 1994.

[189] S. Kirchmeyer and K. Reuter. Scientific importance, properties and growing applications of poly(3,4-ethylenedioxythiophene). *J. Mater. Chem.*, 15(21):2077–2088, 2005.

[190] Sigma-Aldrich Co. LLC. Poly(styrenesulfonate)(PSS). `http://www.sigmaaldrich.com`.

[191] L. S. C. Pingree, B. A. MacLeod, and D. S. Ginger. The changing face of PEDOT:PSS films: substrate, bias, and processing effects on vertical charge transport. *J. Phys. Chem. C*, 112:7922–7927, 2008.

[192] S. K. M. Jönsson, J. Birgerson, X. Crispin, G. Greczynski, W. Osikowicz, A. W. Denier van der Gon, W. R. Salaneck, and M. Fahlman. The effects of solvents on the morphology and sheet resistance in poly(3,4-ethylenedioxythiophene)-polystyrenesulfonic acid (PEDOT-PSS) films. *Synth. Met.*, 139(1):1–10, 2003.

[193] F. C. Krebs. Fabrication and processing of polymer solar cells: A review of printing and coating techniques. *Sol. Energy. Mater. Sol. Cells*, 93(4):394–412, 2009.

[194] D. Honholz and A. G. MacDiarmid. Line patterning of conducting polymers: new horizons for inexpensive, disposable electronic devices. *Synth. Met.*, 121(1):1327–1328, 2001.

[195] J. A. DeFranco, B. S. Schmidt, M. Lipson, and G. G. Malliaras. Photolithographic patterning of organic electronic materials. *Org. Electron.*, 7(1):22–28, 2006.

[196] Heraeus Deutschland GmbH & Co. KG. Conductive Polymers. `http://www.heraeus-clevios.com`.

[197] Sigma-Aldrich Co. LLC. Poly(3,4-ethylenedioxythiophene)-poly(styrenesulfonate). `http://www.sigmaaldrich.com`.

[198] A. F. Diaz, K. K. Kanazawa, and G. P. Gardini. Electrochemical polymerization of pyrrole. *J.C.S. Chem. Commun.*, 14:635–636, 1979.

[199] E. Scavetta, R. Mazzoni, F. Mariani, R. G. Margutta, A. Bonfiglio, M. Demelas, S. Fiorilli, M. Marzocchi, and B. Fraboni. Dopamine amperometric detection at a ferrocene clicked PEDOT:PSS coated electrode. *J. Mater. Chem. B*, 2(19):2861–2867, 2014.

[200] X. Cui and D. C. Martin. Electrochemical deposition and characterization of poly (3, 4-ethylenedioxythiophene) on neural microelectrode arrays. *Sens. Actuators, B*, 89(1):92–102, 2003.

[201] G. Li and P. G. Pickup. Ion transport in poly(3, 4-ethylenedioxythiophene)-poly (styrene-4-sulfonate) composites. *Phys. Chem. Chem. Phys.*, 2(6):1255–1260, 2000.

[202] J. Bobacka, A. Lewenstam, and A. Ivaska. Electrochemical impedance spectroscopy of oxidized poly(3, 4-ethylenedioxythiophene) film electrodes in aqueous solutions. *J. Electroanal. Chem.*, 489(1):17–27, 2000.

[203] D. Han, G. Yang, J. Song, L. Niu, and A. Ivaska. Morphology of electrodeposited poly(3, 4-ethylenedioxythiophene)/poly (4-styrene sulfonate) films. *J. Electroanal. Chem.*, 602(1):24–28, 2007.

[204] U. Lang, N. Naujoks, and J. Dual. Mechanical characterization of PEDOT:PSS thin films. *Synth. Met.*, 159(5-6):473–479, 2009.

[205] L. A. A. Pettersson, S. Ghosh, and O. Inganäs. Optical anisotropy in thin films of poly(3,4-ethylenedioxythiophene) - poly(4-styrenesulfonate). *Org. Electron.*, 3(3-4):143–148, 2002.

[206] G. Gustafsson, B. Liedberg, and O. Inganäs. In situ spectroscopic investigations of electrochromism and ion transport in a poly(3,4-ethylenedioxythiophene) electrode in a solid state electrochemical cell. *Solid State Ionics*, 69(2):145–152, 1994.

[207] J. Ouyang, Q. Xu, C. Chu, Y. Yang, G. Li, and J. Shinar. On the mechanism of conductivity enhancement in poly(3,4-ethylenedioxythiophene): poly(styrenesulfonate) film through solvent treatment. *Polymer*, 45:8443–8450, 2004.

[208] A. M. Nardès, R. A. J. Janssen, and M. Kemerink. A morphological model for the solvent-enhanced conductivity of PEDOT:PSS thin films. *Adv. Funct. Mater.*, 18(6):865–871, 2008.

[209] A. G. MacDiarmid and A. J. Epstein. The concept of secondary doping as applied to polyaniline. *Synth. Met.*, 65(2-3):103–106, 1994.

[210] B. D. Martin, N. Nikolov, S. K. Pollack, A. Saprigin, R. Shashidhar, F. Zhang, and P. A. Heiney. Hydroxylated secondary dopants for surface resistance enhancement in transparent poly(3,4-ethylenedioxythiophene)-poly(styrenesulfonate) thin films. *Synth. Met.*, 142(1):187–193, 2004.

[211] A. Elschner and W. Lövenich. Solution-deposited PEDOT for transparent conductive applications. *MRS Bull.*, 36(10):794–798, 2011.

[212] X. Crispin, F. L. E. Jakobsson, A. Crispin, P. C. M. Grim, P. Andersson, A. Volodin, C. van Haesendonck, M. Van der Auweraer, W. R. Salaneck, and M. Berggren. The origin of the high conductivity of poly(3,4-ethylenedioxythiophene)- poly(styrenesulfonate) (PEDOT-PSS) plastic electrodes. *Chem. Mater.*, 18(18):4354–4360, 2006.

[213] N. Kim, S. Kee, S. H. Lee, B. H. Lee, Y. H. Kahng, Y. R. Jo, B. J. Kim, and K. Lee. Highly conductive PEDOT:PSS nanofibrils induced by solution-processed crystallization. *Adv. Mater.*, 26(14):2268–2272, 2014.

[214] J. Y. Kim, J. H. Jung, D. E. Lee, and J. Joo. Enhancement of electrical conductivity of poly(3,4- ethylenedioxythiophene)/poly(4- styrenesulfonate) by a change of solvents. *Synth. Met.*, 126(2-3):311–316, 2002.

[215] S. Zhang, P. Kumar, A. S. Nouas, L. Fontaine, H. Tang, and F. Cicoira. Solvent-induced changes in PEDOT:PSS films for organic electrochemical transistors. *APL Mater.*, 3(1):014911, 2015.

[216] S. Timpanaro, M. Kemerink, F. J. Touwslager, M. M. De Kok, and S. Schrader. Morphology and conductivity of PEDOT/PSS films studied by scanning-tunneling microscopy. *Chem. Phys. Lett.*, 394(4-6):339–343, 2004.

[217] A. M. Nardès, M. Kemerink, M. De Kok, E. Vinken, K. Maturová, and R. A. J. Janssen. Conductivity, work function, and environmental stability of PEDOT:PSS thin films treated with sorbitol. *Org. Electron.*, 9(5):727–734, 2008.

[218] H. S. White, G. P. Kittlesen, and M. S. Wrighton. Chemical derivatization of an array of three gold microelectrodes with polypyrrole: fabrication of a molecule-based transistor. *J. Am. Chem. Soc.*, 106(18):5375–5377, 1984.

[219] O. Yaghmazadeh, F. Cicoira, D. A. Bernards, S. Y. Yang, Y. Bonnassieux, and G. G. Malliaras. Optimization of organic electrochemical transistors for sensor applications. *J. Polym. Sci. B Polym. Phys.*, 49(1):34–39, 2011.

[220] D. A. Bernards and G. G. Malliaras. Steady-state and transient behavior of organic electrochemical transistors. *Adv. Funct. Mater.*, 17(17):3538–3544, 2007.

[221] A. J. Bard and L. R. Faulkner. *Electrochemical Methods: Fundamentals and Applications*. Wiley, 2000.

[222] G. A. Snook, P. Kao, and A. S. Best. Conducting-polymer-based supercapacitor devices and electrodes. *J. Power Sources*, 196(1):1–12, 2011.

[223] D. A. Bernards, D. J. Macaya, M. Nikolou, J. A. DeFranco, S. Takamatsu, and G. G. Malliaras. Enzymatic sensing with organic electrochemical transistors. *J. Mater. Chem.*, 18(1):116–120, 2007.

[224] S. Zhang, E. Hubis, C. Girard, P. Kumar, J. DeFranco, and F. Cicoira. Water stability and orthogonal patterning of flexible micro-electrochemical transistors on plastic. *J. Mater. Chem. C.*, 2016.

[225] D. Nilsson, N. Robinson, M. Berggren, and R. Forchheimer. Electrochemical logic circuits. *Adv. Mater.*, 17(3):353–358, 2005.

[226] V. L. Mironov. *Fundamentals of scanning probe microscopy*. NT-MDT, 2004.

[227] R. García, R. Magerle, and R. Pérez. Nanoscale compositional mapping with gentle forces. *Nat. Mater.*, 6:405–411, 2007.

[228] I. N. Sneddon. The relation between load and penetration in the axisymmetric boussinesq problem for a punch of arbitrary profile. *Int. J. Eng. Sci.*, 3:47–57, 1965.

[229] P. H. Mott and M. C. Roland. Limits to poisson's ratio in isotropic materials. *Phys. Rev. B*, 80(13):132104, 2009.

[230] T. Young. An essay on the cohesion of fluids. *Philos. Trans. R. Soc. Lond.*, 95:65–87, 1805.

[231] D. Li and A. W. Neumann. A reformulation of the equation of state for interfacial tensions. *J. Colloid Interface Sci.*, 137:304–307, 1990.

[232] N. B. Vargaftik, B. N. Volkov, and L. D. Voljiak. International tables of the surface tension of water. *J. Phys. Chem. Ref. Data*, 12(3):817–820, 1983.

[233] Y. Yuan and T. L. Randall. Contact angle and wetting properties. In G. Bracco and B. Holst, editors, *Surface Science Techniques*, pages 3–34. Springer-Verlag, 2013.

[234] S. M. Sze and Kwok K. Ng. *Physics of semicondutor devices*. Wiley, 2007.

[235] K. B. Oldham and J. C. Myland. *Fundamentals of electrochemical science*. Academic Press, London, 1994.

[236] A. Molleman. *Patch Clamping: An Introductory Guide To Patch Clamp Electrophysiology*. Wiley, 2003.

[237] M. Demelas, E. Scavetta, L. Basiricò, R. Rogani, and A. Bonfiglio. A deeper insight into the operation regime of all-polymeric electrochemical transistors. *Appl. Phys. Lett.*, 102(19):193301, 2013.

[238] P. A. Esrman, D. Nilsson, J. Kawahara, G. Gustafsson, and M. Berggren. Fast-switching all-printed organic electrochemical transistors. *Org. Electron.*, 14(5):1276–1280, 2013.

[239] S. K. Kanakamedala, H. T. Alshakhouri, M. Agarwal, and DeCoster M. A. A simple polymer based electrochemical transistor for micromolar glucose sensing. *Sens. Actuators B*, 157(1):92–97, 2011.

[240] C. Zanardi, F. Terzi, and R. Seeber. Polythiophenes and polythiophene-based composites in amperometric sensing. *Anal. Bioanal. Chem.*, 405(2-3):509–531, 2013.

[241] J. Du, J. J. Cullen, and G. R. Buettner. Ascorbic acid: chemistry, biology and the treatment of cancer. *Biochim. Biophys. Acta*, 1826(2):443–457, 2012.

[242] A. M. Pisoschi, A. Pop, A. I. Serban, and C. Fafaneata. Electrochemical methods for ascorbic acid determination. *Electrochim. Acta*, 121:443–460, 2014.

[243] D. Gardner and D. Shoback. Normal hormone reference ranges (appendix). In *Greenspan's Basic & Clinical Endocrinology, Ninth Edition*. McGraw-Hill Education, 2011.

[244] P.A. LeWitt and D. Nyholm. New developments in levodopa therapy. *Neurology*, 62:S9–16, 2004.

[245] T. Müller, J. Welnic, D. Woitalla, and S. Muhlack. Endurance exercise modulates levodopa induced growth hormone release in patients with Parkinson's disease. *Neurosci. Lett.*, 422:119–122, 2007.

[246] R. E. Wrolstad. Determination of total phenolics. In A. L. Waterhouse, editor, *Current Protocols in Food Analytical Chemistry*. Wiley, 2001.

[247] Y. S. Velioglu, G. Mazza, L. Gao, and B. D. Oomah. Antioxidant activity and total phenolics in selected fruits, vegetables, and grain products. *J. Agric. Food Chem.*, 46:4113–4117, 1998.

[248] M Naczka and F. Shahidi. Extraction and analysis of phenolics in food. *J. Chromatogr. A*, 1054(1-2):95–111, 2004.

[249] P. Pignatelli, A. Ghiselli, B. Buchetti, R. Carnevale, F. Natella, G. Germanó, F. Fimognari, S. Di Santo, L. Lenti, and F. Violi. Polyphenols synergistically inhibit oxidative stress in subjects given red and white wine. *Atherosclerosis*, 188(1):77–83, 2006.

[250] F. Natella, M. Nardini, F. Belelli, and C. Scaccini. Coffee drinking induces incorporation of phenolic acids into ldl and increases the resistance of ldl to ex vivo oxidation in humans. *Am. J. Clin. Nutr.*, 86(3):604–609, 2007.

[251] N. Landrault, P. Poucheret, J. Azay, M. Krosniak, F. Gasc, C. D. Jenin, G. Cros, and P. L. Teissedre. Effect of a polyphenols-enriched chardonnay white wine in diabetic rats. *J. Agric. Food Chem.*, 51:311–318, 2003.

[252] A. Ivanova-Petropulos, A. Ricci, D. Nedelkovski, V. Dimovska, G. P. Parpinello, and A. Versari. Targeted analysis of bioactive phenolic compounds and antioxidant activity of macedonian red wines. *Food Chem.*, 171:412–420, 2015.

[253] D. De Beer, J. F. Harbertson, P. A. Kilmartin, V. Roginsky, T. Barsukova, D. O. Adams, and A. L. Waterhouse. Phenolics: A comparison of diverse analytical methods. *Am. J. Enol. Vitic.*, 55(4):389–400, 2004.

[254] O. P. Sharma and T. K. Bha. DPPH antioxidant assay revisited. *Food Chem.*, 113:1202–1205, 2009.

[255] M. Barbaro, A. Caboni, P. Cosseddu, G. Mattana, and A. Bonfiglio. Active devices based on organic semiconductors for wearable applications. *IEEE Trans. Inf. Technol. Biomed.*, 14:758–766, 2010.

[256] G. Matzeu, L. Florea, and D. Diamond. Advances in wearable chemical sensor design for monitoring biological fluids. *Sens. Actuators B*, 211:403–418, 2015.

[257] I. Tonazzini, E. Bystrenova, B. Chelli, P. Greco, P. Stoliar, A. Calò, A. Lazar, F. Borgatti, P. D'Angelo, C. Martini, and F. Biscarini. Multiscale morphology of organic semiconductor thin films controls the adhesion and viability of human neural cells. *Biophys. J.*, 98:2804–2812, 2010.

[258] S. Baek, R. A. Green, and L. A. Poole-Warren. Electrical trade-offs related to the thickness of conducting polymers for neural applications. *Acta Biomater.*, 10:3048–3058, 2014.

[259] C. J. Bettinger, R. Langer, and J. T. Borenstein. Engineering substrate topography at the micro- and nanoscale to control cell function. *Angew. Chem., Int. Ed.*, 48:5406–5415, 2009.

[260] S. Baek, R. A. Green, and L. A. Poole-Warren. Electrically tunable organic bioelectronics for spatial and temporal manipulation of neuron-like pheochromocytoma (PC-12) cells. *Biochim. Biophys. Acta, Gen. Subj.*, 1830:4321–4328, 2013.

[261] F. Pires, Q. Ferreira, C. A. V. Rodrigues, J. Morgado, and F. Castelo Ferreira. Neural stem cell differentiation by electrical stimulation using a cross-linked PEDOT substrate: Expanding the use of biocompatible conjugated conductive polymers for neural tissue engineering. *Biochim. Biophys. Acta, Gen. Subj.*, 1850:1158–1168, 2015.

[262] T. A. Skotheim and J. R. Reinolds. *Conjugated Polymers: Theory, Synthesis, Properties, and Characterization*. CRC Press, 2007.

[263] N. Massonnet, A. Carella, O. Jaudouin, P. Rannou, G. Laval, C. Cellea, and J. Simonato. Improvement of the Seebeck coefficient of PEDOT:PSS by chemical reduction combined with a novel method for its transfer using free-standing thin films. *J. Mater. Chem. C*, 2:1278–1283, 2014.

[264] S. Garreau, J. L. Duvail, and G. Louarn. Spectroelectrochemical studies of poly(3,4-ethylenedioxythiophene) in aqueous medium. *Synth. Met.*, 125:325–329, 2001.

[265] C. Kvarnström, H. Neugebauer, S. Blomquist, H. J. Ahonen, J. Kankare, and A. Ivaska. In situ spectroelectrochemical characterization of poly(3,4-ethylenedioxythiophene). *Electrochim. Acta*, 44:2739–2750, 1999.

[266] G. Greczynski, T. Kugler, and W. R. Salaneck. Characterization of the PEDOT-PSS system by means of X-ray and ultraviolet photoelectron spectroscopy. *Thin Solid Films*, 354:129–135, 1999.

[267] A. R. Hillman, S. J. Daisley, and S. Bruckenstein. Kinetics and mechanism of the electrochemical p-doping of PEDOT. *Electrochem. Commun.*, 9:1316–1322, 2007.

[268] Q. Wei, M. Mukaida, Y. Naitoh, and T. Ishida. Morphological change and mobility enhancement in PEDOT:PSS by adding co-solvents. *Adv. Mater.*, 25(20):28312836, 2013.

[269] F. Yan, E. P. J. Parrott, B. S. Y. Ung, and E. Pickwell-MacPherson. Solvent doping of PEDOT/PSS: Effect on terahertz optoelectronic properties

and utilization in terahertz devices. *J. Phys. Chem. C*, 119(12):6813–6818, 2015.

[270] E. Hoffmann and S. Pedersen. Sensors and signal transduction pathways in vertebrate cell volume regulation. *Contrib Nephrol. Basel*, 152:54–104, 2006.

[271] F. Lang, M. Föller, K. S. Lang, P. A. Lang, M. Ritter, E. Gulbins, A. Vereninov, and S. M. Huber. Ion channels in cell proliferation and apoptotic cell death. *J. Membr. Biol.*, 205(3):147–157, 2005.

[272] D. Urrego, A. P. Tomczak, F. Zahed, W. Stühmer, and L. A. Pardo. Potassium channels in cell cycle and cell proliferation. *Philos. Trans. R. Soc., B*, 369(1638):20130094, 2014.

[273] H. Ouadid-Ahidouch, X. Le Bourhis, M. Roudbaraki, R. A. Toillon, P. Delcourt, and N. Prevarskaya. Changes in the K^+ current-density of MCF-7 cells during progression through the cell cycle: possible involvement of a h-ether. a-gogo K^+ channel. *Recept. Channels*, 7(5):345–356, 2000.

[274] H. Ouadid-Ahidouch, M. Roudbaraki, P. Delcourt, A. Ahidouch, N. Joury, and N. Prevarskaya. Functional and molecular identification of intermediate-conductance Ca^{2+}-activated K^+ channels in breast cancer cells: association with cell cycle progression. *Am. J. Physiol.*, 287(1):C125–C134, 2004.

[275] D. J. Blackiston, K. A. McLaughlin, and M. Levin. Bioelectric controls of cell proliferation: Ion channels membrane voltage and the cell cycle. *Cell Cycle*, 8(21):3527–3536, 2009.

List of Publications and conference presentations

Publications

- M. Marzocchi, E. Scavetta, A. Bonfiglio, I. Zironi, G. Castellani, and G. Malliaras, R. Owens, and B. Fraboni. *Conducting polymer thin films as substrates for cell cultures*. Mater. Res. Soc. Symp. Proc., Vol. 1624, 2014.

- E. Scavetta, R. Mazzoni, F. Mariani, R. G. Margutta, A. Bonfiglio, M. Demelas, S. Fiorilli, M. Marzocchi, and B. Fraboni. *Dopamine amperometric detection at a ferrocene clicked PEDOT:PSS coated electrode*. J. Mater. Chem. B, 2(19):2861-2867, 2014.

- I. Gualandi, M. Marzocchi, E. Scavetta, M. Calienni, A. Bonfiglio, and B. Fraboni. *A simple all-PEDOT:PSS electrochemical transistor for ascorbic acid sensing*. J. Mater. Chem. B, 3(33):6753-6762, 2015.

- M. Marzocchi, I. Gualandi, M.Calienni, I. Zironi, E. Scavetta, G. Castellani, and B. Fraboni. *Physical and Electrochemical Properties of PEDOT:PSS as a Tool for Controlling Cell Growth*. ACS Appl. Mater. Interfaces, 7(32):17993-18003, 2015.

- I. Gualandi, M. Marzocchi, J. F. Saenz-Cogollo, A. Bonfiglio, and B. Fraboni. *Textile organic electrochemical transistors as a platform for wearable sensors*. Submitted.

- F. Amorini, I. Zironi, M. Marzocchi, I. Gualandi, M. Calienni, B. Fraboni, and G. Castellani. *Cells electrical properties driven by the PEDOT:PSS nano-sponge effect on ions*. Submitted.

- M. Marzocchi, I. Gualandi, T. Cramer, E. Scavetta, and B. Fraboni. *Sensing mechanism in PEDOT:PSS-based amperometric sensors and OECTs*. Submitted.

Conference presentations

- E. Moyen, M. Marzocchi, L. Assaud, A. Hama, B. Fraboni, and R. M. Owens. *Effect of nanoscale substrate patterning on cell differentiation*. Oral contribution at the Third Bilateral Cornell-EMSE Workshop on Bioelectronics, June 2013, Porquerolles, France.

- M. Marzocchi, E. Scavetta, A. Bonfiglio, I. Zironi, G. Castellani, G. Malliaras, R. Owens, and B. Fraboni. *Cell adhesion and proliferation on conducting polymer thin films*. Oral contribution at the MRS Fall Meeting, December 2013, Boston, USA.

- M. Marzocchi, I. Gualandi, E. Scavetta, I. Zironi, M.Calienni, G. Castellani, and B. Fraboni. *Control of cell adhesion by a change in the redox state of PEDOT:PSS substrates*. Poster presented at the International School of Solid State Physics "Biomaterials: Principles, Materials and Processes", May 2014, Erice and at the 10th International Conference on Organic Electronics, June 2014, Modena.

- M. Marzocchi, I. Gualandi, E. Scavetta, M.Calienni, I. Zironi, G. Castellani, and B. Fraboni. *Control of cell adhesion by a change in the redox state of PEDOT:PSS substrates*. Oral contribution at the XIX International Conference on Mechanics in Medicine and Biology, September 2014, Bologna.

- M. Marzocchi, I. Gualandi, M. J. Higgins, G. G. Wallace, and B. Fraboni. *In-situ AFM analysis of redox-induced modifications in PEDOT-based thin*

films. Poster presented at the MRS Fall Meeting, December 2015, Boston, USA.

- M. Marzocchi, I. Gualandi, M.Calienni, I. Zironi, F. Amorini, E. Scavetta, G. Castellani, and B. Fraboni. *A closer look on the physical and electrochemical properties of PEDOT:PSS as a tool for controlling cell growth*. Poster presented at the MRS Fall Meeting, December 2015, Boston, USA.

Acknowledgements

First of all, I would like to thank my supervisor, Prof. Beatrice Fraboni, for her help, patience and kind encouragement. Her advice was fundamental for overcoming the many problems that every PhD student has to face during his research.

In an interdisciplinary research field such as Bioelectronics, collaboration with researchers with different background is crucial. For this reason, I would like to thank the collaborators that gave their contribution to the realization of this thesis, starting from Prof. Gastone Castellani and his group from the Department of Physics and Astronomy of the University of Bologna, in particular Dr. Isabella Zironi and Fabrizio Amorini, for their help on all the aspects regarding the biological part of my research, from the experimental part to our scientific discussions. Another critical contribution regarding the electrochemical characterization of our devices has been given by Prof. Erika Scavetta from the Department of Industrial Chemistry of the University of Bologna. Thanks also to Prof. Annalisa Bonfiglio and her research group from the University of Cagliari, in particular Dr. Jose Francisco Saenz Cogollo, Dr. Piero Cosseddu, Dr. Monia Demelas and Silvia Conti, for their help on OECTs and on textile electronics. I would also like to thank all the undergraduate students that worked on this project for their contribution.

I am very grateful to Prof. George Malliaras and Prof. Roisin Owens, from the École de Mines de Saint-Étienne in Gardanne, France, and to Prof. Gordon Wallace and Prof. Michael Higgins from the University of Wollongong, Australia, for giving me the opportunity to work in their laboratories as a visiting student. I would also like to thank the amazing people I had the luck to meet there, especially Agostino, Xenofon, Adel, Esma, Manue, Cassandre, Eleni, Jonathan, Marc, Dion, Pierre, Michele and Eric at BEL, and Christina, Jay, Lei, Tania, Sina, George, Brandon, Miina and Andres at IPRI, for their kindness and helpfulness both inside

and outside the lab.

I would like to acknowledge the PRIN Project MiND that provided the financial support, and the Spinner 2013 Project of the Emilia-Romagna region and the Marco Polo project of the Department of Physics and Astronomy of the University of Bologna for the financial support of my research periods abroad.

A very special thanks to my present and former colleagues in Bologna, Martina, Laura, Andrea, Marco II, Giacomo, Maria Antonietta, Maria, Tobias, Lucia, Alberto, Stefania, Geeta, Shankar, and to our Best student Maria. An even more special thanks to Isacco for his continuous help and advice and for teaching me almost everything I know about electrochemistry. I consider myself very lucky for working with people like the ones I have found here.

Finally, I gratefully thank my family for supporting me in every choice I make, and to Alice, for always being by my side.